

**ESTABLISHING THE OPTOELECTRONIC INTERACTIONS BETWEEN
CONJUGATED POLYMERS AND ORGANIC RADICALS**

by

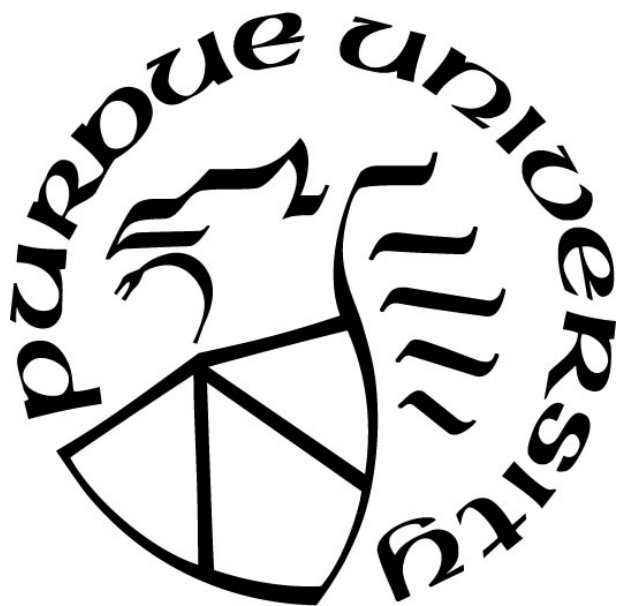
Daniel A. Wilcox

A Dissertation

Submitted to the Faculty of Purdue University

In Partial Fulfillment of the Requirements for the degree of

Doctor of Philosophy



Davidson School of Chemical Engineering

West Lafayette, Indiana

August 2020

**THE PURDUE UNIVERSITY GRADUATE SCHOOL
STATEMENT OF COMMITTEE APPROVAL**

Dr. Bryan Boudouris, Chair

Charles D. Davidson School of Chemical Engineering

Dr. Jianguo Mei

Department of Chemistry

Dr. Brett Savoie

Charles D. Davidson School of Chemical Engineering

Dr. Letian Dou

Charles D. Davidson School of Chemical Engineering

Approved by:

Dr. John Morgan

*Dedicated to my wife Liz, my family, my friends,
and everyone who was there for me on this journey*

ACKNOWLEDGMENTS

I would first like to thank my advisor, Professor Bryan Boudouris. Thank you for all the support, guidance, and mentorship you have given me during my time here, as well as the many opportunities for professional development. Your industriousness, attention to detail, and leadership are qualities I strive to emulate, and I am grateful that you were always willing to make yourself available whenever I needed it. I would also like to thank all of the members of my committee: Professor Jianguo Mei, Professor Letian Dou, and Professor Brett Savoie, as well as Professor Rakesh Agrawal and Professor James Caruthers for their many helpful discussions and feedback over the years. Professor Brett Savoie, in particular, I would like to thank you for sharing your expertise with me. You gave me the opportunity to develop my skills in a new direction, and I am grateful for the mentorship.

I would also like to thank all of our collaborators: Dr. Jordan Snaider, Dr. Long Yuan, Professor Libai Huang, Dr. Yelin Ni, Hosup Song and Dr. Grigori Medvedev. My success could not have happened without your efforts, and I have learned so much from working with you all. A huge thanks goes to Dr. Robert Everly, Dr. Patricia Bishop, Dr. Hartmut Hedderich, and Janis Vanderpool at the Amy Facility in the Department of Chemistry, as well as Bill Rowe, Tim Miller, and the rest of the staff at Birck Nanotechnology Center for making my experimental work possible. To Beverly Johnson, Corwin Green, Robin Wailing, Jeff Valley, Nick Humphrey, Jason Davenport, Jill Vigar, Dr. Gabriela Nagy, and everyone else keeping everything running behind the scenes, I appreciate everything you do for us.

I would also like to thank the diverse group of individuals in the POWER Lab that I have had the pleasure of working with. Liz, Ryan, Aditya, Seung, Ned, Jenny, Darby, Jess, Martha, Adam, Si, Nick, Noelia, Jaeyub, Stephen, Junfeng, Sanjoy, Varad, Teng, Yongho, Sid, John, Kuluni, Roy, Po, Gabriel, Sheng-Ning, Ying, Femi, Wenchao, Hongguang, Xinping, Diana, Ning, Connie, Carsten, and Aaron, all of you have made this process so much more enjoyable, and I have enjoyed getting to know you all both professionally and personally. I hope you have learned from me as much as I have from all of you. To all future students, remember that success is a group effort. Seek out help from your peers, and always be willing to offer guidance in return. I would also like to thank all of the students I have had the opportunity to mentor over the years. Dan,

Akash, John, and Leyla, I appreciate having the chance to mentor you all, and I wish all of you the best of luck in all your future endeavors.

I would also like to thank all of my friends in the department: Michael, David, Garrett, Arthur, Juan-Carlos, Stephen, Ryan, Jeremiah, and Zihao. Good friends can be hard to come by, and I am thankful that we got to share this journey together and build each other up along the way. Finally, I would like to thank all of my friends, members of my community, and my family for being there all these years. Mom and Dad, thank you both for always pushing me to strive for excellence and always giving me support when I needed it the most. To my brother Michael, my grandparents, my stepparents Keith and Bethany, and all my extended family, I am forever grateful for your love and support. And to my wonderful wife Liz, I couldn't ask for a better partner to take this journey with. Your determination and drive to succeed is truly admirable, and your big heart inspires me to keep focused on the things that truly matter in this life. Thank you.

TABLE OF CONTENTS

LIST OF TABLES	10
LIST OF FIGURES	11
ABSTRACT	20
1. INTRODUCTION	22
1.1 Dissertation Overview	23
1.2 References	25
2. INTRODUCTION TO ORGANIC ELECTRONICS	27
2.1 General Introduction	27
2.2 Charge Transport in Organic Materials	29
2.2.1 Wave Nature of Electrons	29
2.2.2 Inorganic Materials	33
2.2.3 Organic Materials	38
2.2.4 Charge Transport in Radical Polymers	42
2.3 Photoexcited Interactions	44
2.4 Organic Electronic Devices	48
2.4.1 Organic Photovoltaics (OPVs)	48
2.4.2 Organic Light-Emitting Diodes (OLEDs)	53
2.4.3 Organic Thermoelectric Devices	55
2.4.4 Organic Field-Effect Transistors (OFETs)	57
2.5 References	63
3. STABLE RADICAL MATERIALS FOR ENERGY APPLICATIONS	70
3.1 Abstract	70
3.2 Introduction	70
3.3 Radical-Containing Materials for Energy Storage Applications	73
3.3.1 Organic Radical Batteries	74
3.3.2 Flow Batteries	78
3.4 Radicals in Energy Conversion Technologies	82
3.5 Towards a Unity 'Internal Quantum Efficiency' in Light-Emitting Devices	88
3.6 Summary and Outlook	90

3.7	Acknowledgements.....	91
3.8	References.....	91
4.	TUNING THE INTERFACIAL AND ENERGETIC INTERACTIONS BETWEEN A PHOTOEXCITED CONJUGATED POLYMER AND OPEN-SHELL SMALL MOLECULES ..	
	97
4.1	Abstract.....	97
4.2	Introduction.....	98
4.3	Materials and Methods.....	100
4.3.1	Materials	100
4.3.2	Solution Phase Fluorescence Quenching.....	100
4.3.3	Quencher Anion Absorbance Measurements	102
4.3.4	Thin Film Preparation.....	102
4.3.5	Thin Film Fluorescence Quenching.....	103
4.3.6	Ensemble Transient Absorption Spectroscopy Measurements.....	103
4.3.7	Atomic Force Microscopy (AFM) Imaging	104
4.3.8	X-ray Diffraction	104
4.3.9	Computational Methods.....	104
4.4	Results and Discussion	107
4.5	Conclusions.....	118
4.6	Acknowledgements.....	119
4.7	Electronic Supplementary Information.....	120
4.7.1	Derivation of the Inner Filter Effect Correction Formula	124
4.8	Notes and References.....	126
5.	MODIFYING FIELD-EFFECT TRANSISTOR RESPONSE IN A CONJUGATED POLYMER UPON THE ADDITION OF RADICAL DOPANTS.....	129
5.1	Abstract.....	129
5.2	Introduction.....	129
5.3	Experimental Details.....	131
5.3.1	Materials	131
5.3.2	OFET Fabrication	132
5.4	Results and Discussion	133

5.5	Conclusions.....	140
5.6	Acknowledgements.....	140
5.7	References.....	140
6.	INTRODUCTION TO BROADBAND DIELECTRIC SPECTROSCOPY.....	143
6.1	Relaxation.....	143
6.2	Mathematical Models of Dielectric Relaxation.....	153
6.3	Model Dielectric Materials.....	156
6.4	References.....	157
7.	RELAXATION MAP OF GLYCEROL AND SORBITOL IN THE GLASS AND LIQUID STATES.....	160
7.1	Abstract.....	160
7.2	Introduction.....	160
7.3	Experimental.....	165
7.4	Method of Analysis.....	166
7.5	Results.....	169
7.5.1	Glycerol.....	170
7.5.2	Sorbitol.....	180
7.6	Discussion.....	192
7.6.1	Possible Arrhenian Model.....	195
7.6.2	Possible origin of the processes emerging at short times.....	197
7.6.3	Some final questions.....	198
7.7	Acknowledgments.....	199
7.8	Supplementary Material.....	200
7.8.1	Glycerol (Schneider et al data).....	200
7.8.2	Glycerol (Dielectric data reported in this paper).....	201
7.8.3	Sorbitol (Dielectric data reported in this paper).....	201
7.8.4	Sorbitol (Geirhos et al data).....	203
7.9	References.....	204
8.	CONCLUSIONS, ONGOING, AND FUTURE WORK.....	207
8.1	Protected PTEO Copolymers.....	208
8.1.1	Materials and Methods.....	210

8.1.2 Results and Discussion	215
8.2 Dielectric Spectroscopy of Model Compounds	219
8.3 Impedance Spectroscopy of PTEO	220
8.4 Intramolecular Fluorescence Quenching Experiments	221
8.5 Protecting P3HT Transistors from Photodegradation with the PTIO Radical.....	222
8.6 References.....	223
VITA.....	225
PUBLICATIONS.....	227

LIST OF TABLES

Table 4.1. Calculated Charge Transfer Parameters and Rates for the Radical Species.....	117
Table 4.2. Calculated FRET Parameters and Rates for P3HT-Radical Blends.	118
Table 5.1. Arrhenius Fitting Parameters for Doped and Undoped P3HT OFETs.	139
Table 8.1. Summary of Synthesis Information.	217

LIST OF FIGURES

Figure 2.1. (a) Example of orbital energy level diagram of a molecule in the ground state. Here, all orbitals are filled in order of increasing energy. (b) Examples of different spin states of a molecule. Excited states involving one electron can have either singlet or triplet character. In the ground state, radicals exist as a doublet state. Triplet ground states can exist in the case where the highest-occupied molecular orbital is degenerate. 31

Figure 2.2. (a) Real part of a Bloch wave in a 1D crystal lattice, showing it as the product of a periodic function $u(x)$ and a plane wave e^{ikx} . (b) Sample band diagram for a 1D system, showing how a state's energy (E) relates to its wavevector (k) in differing bands. Blue boxes depict allowed energy levels, all others are disallowed. Based on ref 50. 35

Figure 2.3. Examples of hole transporting and electron transporting polymers and small molecules commonly seen in the literature. BBL is short for poly(benzobisimidazobenzophenanthroline).^{60,61} Shown here are the conjugated cores; often times solubilizing side chains will be included (particularly for polythiophene, pentacene, perylene diimide, and fullerenes). Of note are the metal phthalocyanines, which illustrate how addition of electron-withdrawing substituents leads to a change in character from p-type to n-type. 40

Figure 2.4. Schematic of charge transport in radical polymers. (a) Oxidation and reduction reactions for a nitroxide radical. Both reactions are shown although typically only one proceeds reversibly for a given species. A schematic of the molecular orbital energies is shown as well, depicting the shift in energies that occurs on oxidation or reduction, as well as why the potential for both reactions differs. (b) Schematic of a p-type radical polymer film. Charges are localized to radical pendant groups and move through a series of one-electron transfers between neutral (grey) and charged (red) species. 43

Figure 2.5. Schematic showing different possible quenching mechanisms between a conjugated fluorophore (red) and a quencher (blue). Electrons are indicated with black circles. Holes (represented by white circles) are included for clarity. (a) Photoinduced charge transfer occurs when an electron is transferred from the excited fluorophore to the quencher. (b) Excited state transfer occurs when the excited state is transferred from the fluorophore to the quencher. It can go by the FRET mechanism (blue) where coupling between the dipoles of the excited states lead to a transfer of energy or by the Dexter mechanism (red) where simultaneous concerted electron transfer occurs. (c) Enhanced intersystem crossing occurs when an exchange interaction between the unpaired electron on an open-shell quencher and one of the electrons in the fluorophore leads to the conversion of the singlet excited state to a triplet state. (d) Static quenching occurs when the fluorophore and quencher form a nonfluorescent supramolecular complex in the ground state. . 47

Figure 2.6. Schematic of organic solar cell operation, with the electron donor depicted as red and the acceptor depicted as blue. (a) A photon is absorbed by a donor molecule, promoting an electron to an unoccupied orbital and leaving a hole in the HOMO. The electron is depicted as at a lower energy than the LUMO to account for the exciton binding energy. (b) Through a series of excited state transfer steps, the exciton diffuses through the donor. (c) Upon reaching the donor/acceptor interface, the promoted electron transfers to an acceptor molecule, forming a Coulombically-bound charge transfer state. $E_{B,CT}$ represents the binding energy. (d) Thermal energy dissociates the bound

charges. (e) Through a series of one-electron transfer reactions, the charges diffuse through the donor/acceptor bulk and eventually leave the solar cell. 50

Figure 2.7. Schematic of (a) planar heterojunction, (b) bulk heterojunction, and (c) ordered heterojunction OPV active layer architectures. 51

Figure 2.8. Examples of materials used in organic photovoltaics. 53

Figure 2.9. (a) Typical structure of an OLED device, showing the anode, hole injection layer (HIL), hole transport layer (HTL), emissive layer (EML) consisting of a host molecule doped with an emitter, hole blocking layer (HBL), electron transport layer (ETL), and cathode. Holes are injected from the anode, while electrons are injected from the cathode. (b) A far-from-exhaustive list of molecules used in in OLEDs. Abbreviations are poly(3,4-ethylenedioxythiophene):poly(styrenesulfonic acid) (PEDOT:PSS);¹²⁹ Copper Phthalocyanate (CuPc);¹³⁰ α -NPD;¹³¹ N,N'-bis(3-methylphenyl)-N,N'-diphenylbenzidine (TPD);^{131,132} *fac* tris(2-phenylpyridine) iridium (Ir(ppy)₃);¹³³ poly(phenylene vinylene) (PPV); 9,10-(2-naphthyl)anthracene (ADN);¹³⁴ 2,4,5,6-Tetra(9H-carbazol-9-yl)isophthalonitrile (4CzIPN);¹³⁵ 4,4'-di(N-carbazole)biphenyl (CBP);¹³⁶ bis(10-hydroxybenzo[h]quinolinato)beryllium (Be(bq)₂);¹³⁷ tris-(8-hydroxyquinolato)aluminum (Alq₃);¹³⁸ and Bathocuproine (BCP).¹³⁹ 55

Figure 2.10. (a) Schematic depicting the Seebeck effect. In a p-type material, heating one side leads to increased thermal energy causing the holes to diffuse more rapidly, which lowers their density. Cooling the other side likewise leads to an increase in density. The buildup of charges increases the electrical potential at the cold side, generating a voltage. In an n-type material, the opposite sign of the charge carriers lead to a reversal of the voltage. (b) An appreciable voltage can be produced by linking multiple thermoelectric modules in series. As the p- and n-type materials produce opposite voltages, they can be connected at the hot or cold side and their voltages will add..... 56

Figure 2.11. Schematic of field-effect transistor operation. (a) With no applied gate voltage (off), conductivity is low as only intrinsic charges are present between the source and drain. (b) An applied gate voltage attracts more charges to the channel, which greatly increases the conductivity. 58

Figure 2.12. Sample characteristics for an ideal FET, showing (a) output characteristics, i.e. I_{DS} vs. V_{DS} , and (b) transfer characteristics, i.e. I_{DS} vs V_{GS} 59

Figure 2.13. Examples of CMOS logic circuits. (a) Circuit diagram of a CMOS inverter, which produces a low voltage output if the voltage input is high, and vice-versa. (b) Relationship between V_i and V_o for an inverter consisting of ideal FETs with equal values of $\mu C_{ox}WL$. (c) Circuit diagram of a CMOS NAND gate, where the output voltage is low only if both input voltages are high, and high otherwise. This serves as a universal building block for any digital circuit. 60

Figure 2.14. (a) A non-zero threshold voltage results in a horizontal displacement of the transfer curve, meaning that it turns on at higher voltages. (b) Extracting mobility and threshold voltage from a plot of I_{DS} vs V_{GS} . Here, the slope is proportional to the mobility, and the x-intercept is equal to the threshold voltage. Note that a smooth transition below V_T is illustrated. 61

Figure 3.1. (a) Schematic of a radical polymer, which consists of pendant stable radical sites along the backbone of a macromolecular architecture. (b) Representative chemical structures of the most

commonly-reported stable radical moieties. The open-shell groups that are marked with green ovals have been reported as pendant units in radical polymers, and the small molecule-only radical materials (i.e., those not marked in green) also have been important in energy-related efforts. (c) Example redox reactions associated with the nitroxyl radical show that the compound can access three distinct redox states. (d) Example chemical structures of a few radical polymers that have been described to a large degree in the literature..... 72

Figure 3.2. (a) Charging of an ORB. The nitroxyl radical is oxidized to the oxoammonium cation causing a flow of electrons through the outer circuit. This causes the electrolyte anions to migrate towards the newly-formed oxoammonium cations of the radical polymer, thus compensating their charge, while lithium cations migrate towards the graphite anode. Here, the lithium ions are reduced to lithium metal. (b) Discharging of an ORB. The intercalated lithium metal undergoes oxidation to form lithium ions, which migrate to the central electrolyte cavity. The free electrons travel through the outer circuit and reach the cathode reducing the oxoammonium cations back to nitroxyl moiety. The arrows within the battery show the movement of the electrolyte ions. 75

Figure 3.3. Working principle of a polymer-based RFB. The anolyte and catholyte are pumped into respective chambers, which are divided by a membrane separator in order to prevent inter-mixing of solutions. The TEMPO- and viologen-based copolymers serve as the catholyte and anolyte redox-active material, respectively. The quaternary ammonium moieties, included in the second block for both copolymers, help to induce water solubility in the copolymers as they are applied to aqueous RFBs. 79

Figure 3.4. (a) Schematic of a dye-sensitized solar cell in operation. (1) A photon is absorbed by a dye molecule, promoting an electron from the HOMO to the LUMO energy level. (2) The electron is then transferred to the conduction band of the TiO₂ nanoparticle layer (3) where it then enters the external circuit. (4) Redox-active molecules are reduced at the counter electrode by electrons from the external circuit. (5) The reduced redox-active molecules then diffuse to the dye and transfer the electron to the dye, regenerating the dye and completing the circuit. (b) Schematic showing how the galvinoxyl radical acts as a spin-flip center at the interface of a heterojunction organic solar cell. The dashed circles indicate the charge transfer states at the donor-acceptor interface. The red species is the electron-donating material, and the blue species is the electron-accepting material. 84

Figure 3.5. (a) Schematic diagram for the spin configuration of an open-shell doublet system. Figures (b-e) show a set of properties for an OLED [Device Structure: ITO/ N,N'-di-1-naphthyl-N,N'-diphenylbenzidine (NPB) (30 nm) / 4,4-bis(carbazol-9-yl)biphenyl (CBP) (10 nm) / TTM-1Cz:CBP (5wt%, 40 nm) / 1,3,5-tri(phenyl-2-benzimidazolyl)-benzene (TPBi) (35 nm) / lithium fluoride (LiF) (0.8 nm) / aluminum (100 nm)] made from the doublet emitting TTM-1Cz and a conventional fluorescent material (NPB). (b) The time-dependent magnetic field applied in the Magneto-electroluminescence (MEL) experiments. (c) The EL intensity of the blue emission of NPB from the OLED at 7 V when the magnetic field was applied. (d) The EL intensity of the red emission of TTM-1Cz from the OLED at 7 V when the magnetic field was applied. Figure (e) shows photographs of the OLEDs [Device Structure: (ITO)/ NPB (30 nm)/TTM-1Cz:CBP (5wt%, 40 nm)/ (TPBi) (35 nm)/ LiF (0.8 nm)/aluminum (100 nm)] driving voltages ranging from 7 V to 11 V. The blue emission at higher voltages arises from NPB and CBP. Figures are adapted with permission from ¹²³(© 2015, Wiley-VCH Verlag GmbH & Co. KGaA, Weinheim). 89

Figure 4.1. (a) Stern-Volmer plots of the corrected fluorescence intensity of P3HT solutions in chloroform (60 μ M of thiophene repeat units) and small molecules that serve as quenching sites for the photoexcited P3HT. The vertical axis represents the intensity of a P3HT-only solution divided by the corrected intensity of a solution consisting of P3HT and the quencher at a specific concentration. These data demonstrate that the galvinoxyl and PTIO radical species have nearly the same quenching ability for P3HT as PCBM does in solution; conversely, TEMPO does not demonstrate this property. Error bars show the range of values measured for each concentration of quencher. The excitation and emission wavelengths for all of the measurements were 500 nm and 578 nm, respectively. The raw data were corrected for the inner filter effect. (b) Molecular structures of species used in this work. Electron-donating (p-type) species are indicated in red, while electron-accepting (n-type) species are indicated with blue labels. 108

Figure 4.2. Reduction in intensity of fluorescence spectra of P3HT thin films with increasing loadings of (a) PCBM, (b) the galvinoxyl radical, (c) the PTIO radical, and (d) the TEMPO radical. As with the solution-state measurements, the PTIO and galvinoxyl radicals show a reduction in the P3HT fluorescence intensity in the solid state while the TEMPO radical does not. The excitation wavelength was 500 nm. 109

Figure 4.3. Absorbance spectra of P3HT thin films with increasing amounts of (a) PCBM, (b) the galvinoxyl radical, (c) the PTIO radical, and (d) the TEMPO radical. These data demonstrate that no supramolecular complexes are forming in the ground state between P3HT and the radical species, as the peak locations for P3HT and the radical species are unchanged [see inset of (c)]. Moreover, there is no appearance of a lower energy absorption band. PCBM, by contrast, shows a blue-shifting in the P3HT absorption peak [see inset of (a)], most likely because the PCBM disrupts the crystalline packing of the P3HT. The insets show the blue-shift for P3HT-PCBM in greater detail, as compared to P3HT-PTIO, which shows no shift. 110

Figure 4.4. XRD data of P3HT thin films with small molecule additives of (a) PCBM, (b) the galvinoxyl radical, (c) the PTIO radical, and (d) the TEMPO radical present at a loading of 10% (on a molar basis), compared to those of pristine P3HT and the pristine small molecule species. For the radical species, peaks corresponding to those seen for pristine P3HT appear in the XRD spectra of the combined films (blue) with minimal shift in peak locations, indicating the existence of a pure P3HT phase in the film. This is in contrast with the P3HT-PCBM film, which shows no (010) peak corresponding to the π - π stacking, most likely because the PCBM disrupts the crystalline packing of the P3HT. The spectra are shifted vertically and the small molecule signals are scaled in order to provide clarity in data presentation. 111

Figure 4.5. Overlap of the P3HT emission spectrum (green line) with the absorbance spectra of the quencher molecules. (a) The emission spectrum of a 60 μ M P3HT solution in chloroform, and (b) the emission spectrum of a P3HT thin film. The inset shows the frontier orbital (HOMO and LUMO) energies of P3HT and the reduction potentials, in units of eV removed from free vacuum, of the two n-type open-shell species: the PTIO and galvinoxyl radicals. 113

Figure 4.6. Representative transient absorption spectra of a (a) pristine P3HT film, (b) P3HT-PCBM blend, (c) P3HT-Galvinoxyl blend, (d) P3HT-PTIO blend, and (e) P3HT-TEMPO blend at selected delay times. The negative signal from 500 to 625 nm corresponds to the ground-state bleaching of the P3HT film, while the positive signal from 625 to 700 nm corresponds to delocalized polarons in the P3HT film. The pump wavelength was 400 nm. All quencher species were added to the thin films at a 10 mol% loading. 115

Figure 4.7. Comparison of the dynamics of the transient absorption signals of the P3HT-quencher blends at a probe wavelength of (a) 550 nm (ground-state bleach) and (b) 650 nm (polaron). Each of the radical-containing composites shows a faster decay of both signals over the pristine sample. This is in contrast to the P3HT-PCBM blend, which shows a persistent signal over the course of the measurement that reaches a maximum long after the P3HT-radical blends, due to persistent charge separation. A 10 mol% loading of quencher species was used for the films. 116

Figure 4.S1. (a) Binding curves for the neutral quaterthiophene (4T) and radical quencher species. Geometries of the (b) 4T-GxMe pair, (c) 4T-PTIO pair, and (d) 4T-TEMPO pair at the equilibrium distances seen looking down on the x-z plane. (e) Orientations of the individual species seen looking down the x-y plane (red: x, green: y, blue: z). The species were aligned in a co-facial orientation in the following manner. For 4T, the 2- and 5- carbons of the thiophene ring nearest the geometric center of the molecule were aligned along the x-axis, and the plane of this thiophene ring was aligned with the x-y plane by orienting the cross product of the x-axis and the C-S bond with the positive z-axis. For GxMe, the C2 axis was aligned with the y-axis, and the two carbons closest to the C2 axis were aligned with the x-axis. For PTIO, the C2 axis was aligned with the x-axis, and the phenyl ring was aligned with the x-y plane by orienting the 3- and 5- carbons of the phenyl ring with the y-axis. For TEMPO, the mirror plane, or the vector between the nitrogen and the 4-carbon, was aligned with the x-axis, and the 2- and 6-carbons were aligned with the y-axis. The TEMPO molecule was oriented so the less sterically-hindered face was facing the negative z-direction. All molecules were translated such that their centroids were aligned with the origin. To generate the 4T-radical pairs, the two molecules were superimposed with their centroids overlapping, and the radical species was displaced a given distance along the positive z-axis.. 120

Figure 4.S2. Absorbance spectra of P3HT in solution (60 μ M of repeat units in chloroform) blended with varying concentrations of (a) PCBM, (b) the galvinoxyl radical, (c) the PTIO radical, and (d) the TEMPO radical. The absorbance spectra of solutions with 0.1 mM of small molecule and no P3HT are indicated with a dashed line. The spectra are the sum of the spectra of the individual components, indicating that no supramolecular complexes are forming in the ground state when the materials are co-dissolved in solution. 121

Figure 4.S3. Reduction of the intensity of fluorescence spectra of P3HT in solution (60 μ M of repeat units in chloroform) upon addition of up to 1 mM of (a) PCBM, (b) the galvinoxyl radical, (c) the PTIO radical, and (d) the TEMPO radical, showing that the galvinoxyl and PTIO radical species act as fluorescence quenchers with nearly the same quenching ability as PCBM, while the TEMPO radical does not show this effect. The excitation wavelength was 500 nm. All spectra were corrected for the inner filter effect. 122

Figure 4.S4. Absorbance spectra of the neutral galvinoxyl and PTIO radicals and the reduced galvinylate and PTIO anions. The galvinoxyl species were measured at a 0.01 mM concentration in ethanol, and the PTIO species were measured at a 0.1 mM concentration in water. These concentrations were chosen so that the samples would have similar optical densities for comparison purposes. The galvinylate anion shows a strong absorbance near 560 nm, while the PTIO anion shows a broad absorbance near 325 nm. 123

Figure 4.S5. Atomic Force Microscopy (AFM) phase images of P3HT thin films with small molecule additives present at a loading of 10%, on a molar basis. Scale bars represent 50 nm. 123

Figure 4.S6. Illustrations for the inner filter effect derivation. (a) Depiction of how the light going to and coming from an infinitesimal area element is attenuated and (b) the definition of the coordinates used in the derivation..... 124

Figure 5.1. Output curves for (a) pristine P3HT transistor and (b) a P3HT-Gx blend transistor with a 5% galvinoxyl (by weight) loading. The corresponding transfer curves are shown in (c) and (d). In the pristine film, the current saturates at high voltage, and the saturation point increases with gate voltage. In the doped film, the current is roughly linear with voltage, and the conductivity dependence on gate voltage is reduced. The differing scale between (a) and (b) vs. (c) and (d) is due to hysteresis..... 133

Figure 5.2. Output curves for P3HT transistors with loadings of 2.5% (by weight) of the (a) PTIO and (b) TEMPO radicals. The corresponding transfer curves are shown in (c) and (d). These loadings were selected to have approximately the same molar concentration as the galvinoxyl radical-containing device shown in Figure 5.1b. The qualitative shift in behavior is not observed for these radicals, which contrasts with what was observed for the galvinoxyl radical. 134

Figure 5.3. (a) Chemical structures of the conjugated polymer (P3HT), radical polymer (PGSt), and small molecule open-shell materials implemented in this work. Radicals are classified according to whether they preferentially reduce (n-type), preferentially oxidize (p-type), or are capable of being oxidized or reduced under normal conditions (ambipolar). (b) Oxidation (red) and reduction (blue) potentials of all molecular species implemented in this work. For P3HT these values are identified with the HOMO and lowest-unoccupied molecular orbital (LUMO) energy. For the radical species, these are identified with the SOMO energy. This identification is ambiguous for ambipolar species, such as the PTIO radical; thus, both its oxidation and reduction potentials are shown..... 135

Figure 5.4. Electronic conductivity of the P3HT-PGSt active layer blends as a function of the PGSt loading. Though an increase is seen from 0 to 5% PGSt loadings, the conductivity does not change for loadings from 25% to 75%. No conductivity is observed for blends with extremely high PGSt loadings. 136

Figure 5.5. Mobility as a function of the galvinoxyl/PGSt loading, ranging from 0 to 100% loading (by weight). (a) Results for low loading. (b) Results for loadings used in Figure 5.4. The mobilities were extracted from the transfer curves assuming saturation for 0% loading and linear regime for higher values. The mobility can be seen to increase slightly at low loadings but decrease at high loadings. At the highest loadings, the mobility decreases dramatically. 137

Figure 5.6. Charge carrier concentration found by dividing the conductivity by the mobility as a function of the PGSt fraction. A modest increase is seen at higher loadings. 138

Figure 5.7. (a) Plot of on (orange) and off (blue) currents of a pristine P3HT OFET (circles) and a P3HT OFET blended with 5% PGSt by weight (squares). The current decreases with temperature, but the qualitative behavior does not change. Arrhenius plots of (b) mobility and (c) ON current for undoped P3HT OFETs (black circles and red squares) and a P3HT OFET blended with 5% PGSt by weight (blue triangles). A similar slope can be seen for both undoped devices, despite the difference in magnitude, while the doped device shows a slightly greater slope. 139

Figure 6.1. Example of mechanical stress (σ) generated in a viscoelastic material in response to a small sinusoidal strain (ϵ). For a complex modulus $G^* = G^{e^{i\delta}}$, the magnitude of the complex

modulus $|G|$ is equal to the ratio of the amplitudes of the stress and strain functions, while the argument δ is equal to the phase difference between the two. 147

Figure 6.2. Schematic of dielectric relaxation (a) storage and (b) loss response, demonstrating many of the signals often seen in relaxation spectra. The α -process corresponds to the glass transition, while the β - and γ -processes correspond to more localized motions. The infinite-frequency dielectric response is included in each component in (a), while the response due to conductivity is included in (b). 151

Figure 6.3. Schematic of the effect of increasing temperature on the illustrative dielectric response shown in Figure 6.2. Increasing the temperature causes the individual peaks of the response to shift to higher frequencies. However, the peaks do not all shift by the same amount, nor does their shape necessarily stay fixed as they shift. 153

Figure 6.4. Havriliak-Negami function illustration, showing the effects of the stretching exponents α and β on the (a) storage and (b) loss permittivity. Decreasing α leads to a broadening of the response, while decreasing β skews the response towards higher frequencies. The black line is equivalent to a Debye function. 155

Figure 6.5. Illustrations of model compounds for dielectric spectroscopy. (a) Chemical structure of diglycidylether of bisphenol-A (DGEBA) and of phenoxy, a DGEBA linear polymer. (b) Chemical structure of 4,4'-methylenedianiline (MDA), a commonly used crosslinking agent for DGEBA, and chemical structure of the crosslink between one functional end of an MDA molecule and two DGEBA molecules. (c) Chemical structures of other materials commonly studied with dielectric spectroscopy, including poly(methylmethacrylate) (PMMA), poly(dimethylsiloxane) (PDMS), and *ortho*-terphenyl (OTP). 156

Figure 7.1. Effect of the process strength magnitude H . (A) Relaxation spectrum used to fit the loss dielectric permittivity shown in the right panel; $H=10^{-2}$ – blue, $H=2 \cdot 10^{-2}$ – magenta. (B) Sorbitol data for 120 K – markers, solid lines – fits produced by the spectra shown in the left panel. 168

Figure 7.2. Storage (A) and loss (B) dielectric permittivity data of Schneider et al. Symbols corresponds to temperatures (left-to-right): 184 K – magenta squares and stars, 195 K – blue stars, 204 K – cyan stars, 213 K – green stars, 223 K – orange stars, 234 K – red stars, 253 K – magenta circles, 273 K – blue circles, 295 K – cyan circles, 323 K – green circles, 363 K – orange circles, 413 K – red circles. Solid lines – fit using the VASESS method of this paper. 170

Figure 7.3. Spectral density of processes vs relaxation times of the processes obtained from fitting the dielectric permittivity data of Schneider et al³³ from Figure 7.2. Temperatures are the same as in Figure 7.2, i.e. from 184 K to 413 K going right-to-left. Colors correspond to colors in Figure 7.2. 172

Figure 7.4. Relaxation map for glycerol obtained from fitting the Schneider et al. data in Figure 7.2. Relaxation times for processes from the longest (i.e. at the long-time edge of the spectra in Figure 7.3) to shortest (i.e. at the short-time edge of the spectra in Figure 7.3) are shown, where for clarity only every 500th process (out of the maximum number of 7144 processes) is plotted. Black diamond markers indicate locations of the loss peaks in Figure 7.2 after their conversion from the frequency domain to the time domain. 175

Figure 7.5. Storage (A, C) and loss (B, D) dielectric permittivity for glycerol. Symbols corresponds to temperatures: (A) and (B) (left-to-right) 180 K – red circles, 190 K – magenta stars, 200 K – blue stars, 210 K – cyan stars, 220 K – green stars, 230 K – yellow stars, 240 K – red stars, 250 K – magenta diamonds; (C) and (D) (left-to-right) 120 K – red hexagram, 130 K – magenta circles, 140 K – blue circles, 150 K – cyan circles, 160 K – green circles, 170 K – yellow circles. Solid lines – fits using the spectra shown in Figure 7.6. 176

Figure 7.6. Spectra (density of processes vs relaxation times of these processes) obtained from fitting the dielectric permittivity data in Figure 7.5. Temperatures are the same as in Figure 7.5 from 120 K (rightmost curve) to 250 K (leftmost curve) going right-to-left. Colors correspond to those in Figure 7.5..... 177

Figure 7.7. Relaxation map for glycerol obtained from fitting the data in Figure 7.5. Relaxation times for processes from the longest (i.e. at the long-time edge of the spectra in Figure 7.6) to shortest (i.e. at the short-time edge of the spectra in Figure 7.6) are shown; processes No 5 to No 45 with an increment of 5 – green, processes No 50 to No 200 with an increment of 50 – orange, No 700 to No 7200 with an increment of 500 – red. Vertical black line indicates T_g 179

Figure 7.8. Combined relaxation map for glycerol, including results of Figure 7.4 (based on Schneider et al. data) and Figure 7.7 (based on this paper data). Extrapolation of data to shorter relaxation times is shown as dashed lines (see text for details). 180

Figure 7.9. Storage and loss dielectric permittivity for sorbitol. Symbols corresponds to temperatures: (A) and (B) (left-to-right) 275 K – blue circles, 277.5 K – cyan circles, 280 K – green circles, 285 K – orange circles, 290 K – red circles, 295 K – magenta plusses, 300 K – blue plusses, 305 K – cyan plusses, 310 K – green plusses, 315 K – orange plusses, 320 K – red plusses; (C) and (D) (left-to-right) 255 K – magenta stars, 260 K – blue stars, 262.5 K – cyan stars, 265 K – green stars, 267.5 K – orange stars, 270 K – red stars, 272.5 K – magenta circles; (E) and (F) (left-to-right) 150 K – blue pentagrams, 160 K – cyan pentagrams, 170 K – green pentagrams, 180 K – orange pentagrams, 190 K – red pentagrams, 200 K – magenta squares, 210 K – blue squares, 220 K – cyan squares, 230 K – green squares, 240 K – orange squares, 250 K – red squares. Solid lines – fits using the spectra shown in Figure 7.10. 182

Figure 7.10. Spectra (density of processes vs relaxation times of these processes) obtained from fitting the dielectric permittivity data in: (A) – Figure 7.9A and Figure 7.9B, (B) – Figure 7.9C and Figure 7.9D, (C) – Figure 7.9E and Figure 7.9F. Temperatures are the same as in Figure 7.9 going right-to-left. Colors correspond to those in Figure 7.9. 185

Figure 7.11. Storage (A, C) and loss (B, D) dielectric permittivity data for sorbitol of Geirhos et al.⁴¹ Symbols corresponds to temperatures: (A) and (B) (left-to-right) 190 K – magenta squares, 200 K – blue squares, 210 K – cyan squares, 220 K – green squares, 230 K – orange squares, 240 K – red squares, 250 K – magenta triangles, 260 K – blue triangles; (C) and (D) (left-to-right) 10 K – cyan circles, 70 K – green circles, 100 K – orange circles, 120 K – red circles, 130 K – magenta plusses, 140 K – blue plusses, 150 K – cyan plusses, 160 K – green plusses, 170 K – orange plusses, 180 K – red plusses. Solid lines – fits using the spectra shown in Figure 7.12. 187

Figure 7.12. Spectral density of processes vs relaxation times of the processes obtained from fitting the dielectric permittivity data of Geirhos et al⁴¹ from Figure 7.11. All curves have been shifted

vertically by -1 to facilitate comparison with Figure 7.10. Temperatures are the same as in Figure 7.11, i.e. from 10 K to 260 K going right-to-left. Colors correspond to colors in Figure 7.11. . 188

Figure 7.13. (A) Relaxation map for sorbitol obtained from fitting the data in Figure 7.9 and Figure 7.11. Relaxation times from the shortest to the longest (right-to-left): this paper data – blue lines, processes No 50 to No 3450 (total 3517) with an increment of 100; Geirhos et al data – red lines, processes No 500 to No 14500 (total 14600) with an increment of 500. Cyan circles – compilation of literature data for the α -relaxation $\log aT$ shift factor using various experimental techniques, including viscosity, mechanical relaxation, dielectric relaxation, light scattering, and NMR.^{18,22,26,41,42,58-60} Black squares – mechanical relaxation data of Faivre et al⁵⁸; black plusses – dielectric relaxation data of Geirhos et al⁴¹ and Kastner et al⁴³ for the β -relaxation $\log aT$ shift factor. Vertical black line indicates Tg. (B) Magnified portions of (A) above and near Tg region; (C) β -relaxation region, relaxation times (right-to-left) for processes No 50 to No 400 with an increment of 10 are shown. (D) Relaxation map obtained from Geirhos et al⁴¹ data at the lowest temperatures. The relaxation strength is set at $H=10^{-2}$ for fitting this paper data and at $H=10^{-3}$ for fitting Geirhos et al data..... 190

Figure 7.14. A sketch of a relaxation map for the Arrhenian model (see text for details) as an alternative to fit the relaxation data. Vertical solid line is Tg. Vertical dashed line separates high and low temperature regions. 196

Figure 8.1. H1-NMR Spectra of (a) TEMPO-M and (b) TEO-M. 216

Figure 8.2. (a) Molecular weight distributions of all PTEO copolymers derived from SEC traces. (b) Number-average and weight-average molecular weights (Mn and Mw, respectively) and dispersity (\mathcal{D}) values of all copolymers. 216

Figure 8.3. Differential Scanning Calorimetry data of PTEO copolymer blends. (a) full data range showing heat flow between -40 °C and 100 °C. (b) Zoomed in data showing glass transition temperature (Tg). 217

Figure 8.4. (a) EPR derivative spectra of the PTEO copolymers. Here, the transition from a primarily Lorentzian lineshape of the polymer to the triple Lorentzian lineshape of the monomer can be observed. The inset shows the monomer signal is visible as a shoulder on the main polymer peak at nominal concentrations below 80%, with some seen in 90% due to monomer impurity. (b) Integrated EPR spectra normalized to the integration of an equimolar TEMPO solution..... 218

ABSTRACT

Design rules and application spaces for closed-shell conjugated polymers have been well established in the field of organic electronics, and this has allowed for significant breakthroughs to occur in myriad device platforms [e.g., organic field-effect transistors (OFETs) and organic light-emitting devices (OLEDs)]. Conversely, organic electronic materials that are based on the emerging design motif that includes open-shell stable radicals have not been evaluated in such detail, despite the promise these materials show for charge transfer, light-emission, and spin manipulation platforms. Moreover, recent results have demonstrated that the materials performance of hybrid systems will allow for future applications to harness both of these platform design archetypes to generate composites that combine the performance of current state-of-the-art conjugated polymer systems with the novel functions provided by open-shell species. Thus, establishing the underlying physical phenomena associated with the interactions between both classes of materials is imperative for the effective utilization of these soft materials.

In the first part of this work, Förster resonance energy transfer (FRET) is demonstrated to be the dominant mechanism by which energy transfer occurs from a common conjugated polymer to various radical species using a combination of experimental and computational approaches. Specifically, this is determined by monitoring the fluorescence quenching of poly(3-hexylthiophene) (P3HT) in the presence of three radical species: (1) the galvinoxyl; (2) the 2-phenyl-4,4,5,5-tetramethylimidazoline-3-oxide-1-oxyl (PTIO); and (3) the 4-hydroxy-2,2,6,6-tetramethylpiperidine-1-oxyl (TEMPO) radicals. Both in solution and in the solid-state, the galvinoxyl and PTIO radicals show quenching on par with that of a common fullerene electron-accepting derivative. Conversely, the TEMPO radical shows minimal quenching at similar concentrations. Using both ultrafast transient absorption spectroscopy and computational studies, FRET is shown to occur at a significantly faster rate than other competing processes. These findings suggest that long-range energy transfer can be accomplished in applications when radicals that can act as FRET acceptors are utilized, forming a new design paradigm for future applications involving both closed- and open-shell soft materials.

Following this, addition of the galvinoxyl radical to P3HT is shown to alter the thin film transistor response from semiconducting to conducting. This is accompanied by a modest enhancement in electrical conductivity. This interaction is not seen with either the TEMPO or

PTIO radicals. While an increase in charge carrier concentration is observed, the interaction is not otherwise consistent with a simple charge-transfer doping mechanism, due to the mismatched reduction and oxidation potentials of the two species. Additionally, no freeze-out of charge carriers is observed at reduced temperatures. It is also not due to parallel conduction through the radical fraction of the bulk composite, as the radical species is non-conductive. Hole mobility is enhanced at lower concentrations of the radical, but it decreases at higher concentrations due to the reduced fraction of conductive material in the polymer bulk. Despite the increase in mobility at lower concentrations, the activation energy for charge transport is increased by the presence of the radical. This suggests that the radical is not improving the charge transport through filling of deep trap states or by reducing the activation energy for the charge transport reaction; however, the galvinoxyl radical is likely filling shallow trap states within the P3HT for the composite thin film.

Finally, a novel analysis technique for polymer relaxation is investigated through dielectric spectroscopy of model polyalcohols. An understanding of relaxation phenomena and the physics of amorphous solids in general remains one of the grand open challenges in the field of condensed matter physics. This problem is particularly relevant to organic electronics as many organic electronic materials are found in the amorphous state, and their physical relaxation can lead to undesirable effects such as hysteresis and instability. Current procedures describe relaxation phenomena in terms of empirical functions, but the physical insights provided by this representation are limited. The new approach instead represents the dielectric response as a spectrum of Debye processes. Rather than varying the spectral strength at fixed time points as traditional spectral analysis implicitly does, this approach instead varies the characteristic time of each spectral element while the strength remains fixed. This allows the temperature dependence on relaxation time of each spectral element to be determined, and the α - and β -relaxation are interpreted in light of this analysis.

1. INTRODUCTION

Significant academic and industrial research has been performed with respect to organic electronic devices over the past few decades.¹⁻³ The primary goal of the field is to establish optoelectronically-active organic molecules as a practical alternative to inorganic conductors and semiconductors. While the performance may be lower than conventional technologies in some instances,⁴ the reduced cost, ease of fabrication through solution-based coating methods,^{5,6} and potential for flexible and transparent devices⁷⁻¹⁰ make these materials appealing for a wide range of applications. The most commercially-relevant application of organic electronics at present is the organic light-emitting diode (OLED),¹¹ which is widely utilized in television and smartphone displays.¹² Additionally, organic photovoltaics (OPVs),¹³ thermoelectric modules,¹⁴ and field-effect transistors (OFETs)¹⁵ represent potential application spaces where organic electronic materials can be utilized. Low performance is often the barrier to commercialization of these technologies. As such, a significant amount of effort in organic electronics research is focused on both developing better-performing materials for use in these devices and understanding what enables these new materials to perform at a high level.¹⁶⁻¹⁸

The standard class of materials used in organic electronic devices are π -conjugated polymers and small molecules. Benefitting from the bulk of the research, conjugated materials have achieved a highly sophisticated range of molecular designs. However, the need for still higher-performing materials has motivated the exploration of alternative classes of materials. One such class are stable organic radicals.¹⁹⁻²¹ These open-shell molecules can undergo either a reduction or oxidation reaction to form a closed-shell anion or cation, and ion/radical pairs can transfer an electron between each other, enabling charge transport through the bulk material. These materials have demonstrated their value in battery and charge-storage applications,^{22,23} as interfacial modifying layers in conventional organic devices,²⁴⁻²⁶ and have shown impressive intrinsic solid-state electrical conductivity.²⁷ Additionally, the open-shell nature of the molecules makes them well-suited for spin-manipulation platforms, which are not well-addressed by conventional closed-shell conjugated polymers.²⁸⁻³⁰ While these reports highlight the promise of this emerging class of materials, it is unlikely that they will entirely supplant standard conjugated polymers. Rather, future applications will likely utilize both materials in combination to harness the complementary strengths of each class of material. For this reason, it is essential that the

interactions between these two classes of materials be established, so that conjugated-radical composite systems can be appropriately chosen and tailored towards their intended applications.

In contrast to the often-crystalline inorganic electronic materials, organic electronic materials typically show a significant degree of disorder, with many materials being completely amorphous. While the theoretical treatment of crystalline materials is well-established by modern solid-state physics,³¹ a robust theoretical treatment of disordered solids remains an open challenge.³² Much of the behavior of these materials, such as viscoelasticity and the glass transition, are understood as relaxation phenomena. These can be studied using a variety of techniques, such as dielectric spectroscopy. However, the results of this analysis are primarily described using empirical relationships, whose physical significance is tenuous.³³ Therefore, there is a need to explore new theoretical models and data analysis techniques in order to uncover the principles behind the macroscopic behavior that is observed for amorphous solids.

1.1 Dissertation Overview

The motivation for this work is to study the optoelectronic interactions between conjugated polymers and stable radicals, with the goal of establishing these interactions to provide guidelines for the incorporation of radicals into conjugated polymer devices. To that end, the studies herein look at the interactions of the model conjugated polymer poly(3-hexylthiophene) with three stable organic radicals: the galvinoxyl, 2-phenyl-4,4,5,5-tetramethylimidazoline-1-oxyl-3-oxide (PTIO), and 4-hydroxy-2,2,6,6-tetramethylpiperidin-1-oxyl (TEMPO) radicals. This dissertation also includes work done on acquiring data with model compounds to demonstrate new analysis techniques for dielectric spectroscopy. While not immediately concerned with the field of organic electronics, advances in the study of amorphous solids will benefit the field by providing insights into the macro- and microscopic behavior of oft-used organic electronic materials.

Chapter 2 of this document focuses on a general introduction to organic electronics. After a brief introduction and overview, the chapter discusses a theoretical treatment of charge transport phenomena. The relevant concepts from quantum mechanics are highlighted, and the theory of charge transport in crystalline materials is summarized. How these concepts translate to organic electronic materials is then discussed, as well as the electronic excited-state behavior of these materials. Following the theoretical introduction, the primary device application spaces of

conjugated polymers are introduced with a description of the relevant device physics, device architecture, and common materials used in each application space.

Chapter 3 has been published as “Stable radical materials for energy applications,” by D. A. Wilcox; V. Agarkar; S. Mukherjee; and B. W. Boudouris, *Annu. Rev. Chem. Biomol. Eng.* **2018**, *9*, 83–103. This review article covers the primary device application spaces of organic radicals for energy storage and conversion technologies. In particular, the use of organic radicals in batteries, dye-sensitized solar cells, and OLEDs is highlighted.

Chapter 4 has been published as “Tuning the interfacial and energetic interactions between a photoexcited conjugated polymer and open-shell small molecules,” by D. A. Wilcox; J. Snaider; S. Mukherjee; L. Yuan; L. Huang; B. M. Savoie; and B. W. Boudouris, *Soft Matter* **2019**, *15*, 1413–1422. This article establishes the mechanism by which P3HT interacts with stable organic radicals in the excited state. Specifically, the galvinoxyl and PTIO radicals act as fluorescence quenchers for P3HT both in solution and in thin films, while the TEMPO radical shows minimal quenching. This is explained through a Förster Resonance Energy Transfer (FRET) mechanism, the determination of which is supported through both ultrafast spectroscopy measurements and computational studies.

Chapter 5 explores the ground-state electronic interactions between P3HT and the same radical species through a field-effect transistor device geometry. Specifically, P3HT OFETs that are doped with the galvinoxyl radical show a shift in behavior from semiconducting to conducting, while the PTIO and TEMPO radicals show no effect. The nature of this interaction is explored by measuring the conductivity and charge-carrier mobility as a function of radical loading and observing the effect of varying temperature. A modest increase in carrier concentration is seen, but the data appear to be consistent with a filling of shallow trap states in the P3HT bulk by the galvinoxyl radical.

Chapter 6 discusses relaxation phenomena in amorphous materials. An overview of relaxation, particularly with regards to the glass transition, is given, and how this relaxation manifests in the viscoelastic properties of materials is described. The closely related phenomenon of dielectric relaxation is also introduced, along with a general qualitative description of the phenomena captured by the experimental technique of dielectric spectroscopy. Mathematical models and empirical functions used to describe dielectric relaxation are also introduced, as well as model compounds studied in dielectric spectroscopy.

Chapter 7, “Relaxation Map of Glycerol and Sorbitol in the Glass and Liquid States,” was carried out in collaboration with G. A. Medvedev and J. M. Caruthers. This work looks at applying a new analysis technique towards understanding the dielectric relaxation of the small-molecule glass-formers glycerol and sorbitol, using a combination of literature data and data gathered in our laboratory. Specifically, the dielectric response at varying temperatures is fit with a spectrum of Debye processes, where the spectral strength for each process is constant but the characteristic time for each process is allowed to vary with temperature. This approach allows the temperature dependence of each individual relaxation time to be determined, and maps of these relaxation times are used to describe the various features of the dielectric response.

Chapter 8 briefly summarizes the results and significance of the previous works, particularly to the field of organic electronics, and describes a number of ongoing and future projects that build off of the results presented. Preliminary data are presented concerning the synthesis of radical polymers with deactivated radical sites, which are designed to study the charge transport through conductivity measurements and electron paramagnetic resonance (EPR) spectroscopy. Additionally, further materials for study with dielectric spectroscopy and the analysis method presented in Chapter 7 are proposed, as well as the use of dielectric spectroscopy to study charge transport in radical polymers. Next, the synthesis of covalently-linked conjugated-radical hybrids is proposed to further expand upon the results from Chapter 4. Finally, the use of the PTIO radical to protect P3HT from photodegradation is proposed based on the results outlined in Chapters 4 and 5.

1.2 References

- (1) Meller, G.; Grasser, T. *Organic Electronics*; Springer: Heidelberg/New York, 2010.
- (2) Li, G.; Zhu, R.; Yang, Y. *Nat. Photonics* **2012**, *6* (February), 153–161.
- (3) Skotheim, T.; Reynolds, J. *Handbook of Conducting Polymers*, 3rd ed.; CRC Press, 2007.
- (4) Forrest, S. R. *Nature* **2004**, *428* (6986), 911–918.
- (5) Søndergaard, R. R.; Hösel, M.; Krebs, F. C. *J. Polym. Sci. B Polym. Phys.* **2013**, *51* (1), 16–34.
- (6) de Gans, B.-J.; Duineveld, P. C.; Schubert, U. S. *Adv. Mater.* **2004**, *16* (3), 203–213.
- (7) OLED introduction and basic OLED information | OLED-Info <https://www.oled-info.com/oled-introduction> (accessed Jun 11, 2020).
- (8) Ultra-Thin, Organic and Flexible Solar Energy Solution | Heliatek <http://www.heliatek.com/product> (accessed Jun 17, 2020).

- (9) Savagatrup, S.; Printz, A. D.; O'Connor, T. F.; Zaretski, A. V.; Lipomi, D. J. *Chem. Mater.* **2014**, *26* (10), 3028–3041.
- (10) Savagatrup, S.; Printz, A. D.; Rodriguez, D.; Lipomi, D. J. *Macromolecules* **2014**, *47* (6), 1981–1992.
- (11) Ma, R. In *Handbook of Visual Display Technology*; Chen, J., Cranton, W., Fihn, M., Eds.; Springer, 2016; pp 1799–1820.
- (12) Hayase, H. OLED Display Market Tracker - Q1 2016 - IHS Technology <https://technology.ihs.com/572845/oled-display-market-tracker-q1-2016> (accessed Sep 30, 2016).
- (13) Brabec, C.; Dyakonov, V.; Scherf, U. *Organic Photovoltaics*; Wiley-VCH, 2008.
- (14) Russ, B.; Glaudell, A.; Urban, J. J.; Chabinyk, M. L.; Segalman, R. A. *Nat. Rev. Mater.* **2016**, *1* (10).
- (15) Bao, Z.; Locklin, J. *Organic Field-Effect Transistors*; CRC Press: Boca Raton, FL, 2007.
- (16) Boudouris, B. W. *Curr. Opin. Chem. Eng.* **2013**, *2* (3), 294–301.
- (17) Son, H. J.; He, F.; Carsten, B.; Yu, L. *J. Mater. Chem.* **2011**, *21* (47), 18934–18945.
- (18) Zhou, H.; Yang, L.; You, W. *Macromolecules* **2012**, *45*, 607–632.
- (19) Tomlinson, E. P.; Hay, M. E.; Boudouris, B. W. *Macromolecules* **2014**, *47* (18), 6145–6158.
- (20) Wingate, A. J.; Boudouris, B. W. *J. Polym. Sci. A Polym. Chem.* **2016**, *54*, 1875–1894.
- (21) Oyaizu, K.; Nishide, H. *Adv. Mater.* **2009**, *21* (22), 2339–2344.
- (22) Nakahara, K.; Oyaizu, K.; Nishide, H. *Chem. Lett.* **2011**, *40* (3), 222–227.
- (23) He, J.; Mukherjee, S.; Zhu, X.; You, L.; Boudouris, B. W.; Mei, J. *ACS Appl. Mater. Interfaces* **2018**, *10* (22), 18956–18963.
- (24) Rostro, L.; Galicia, L.; Boudouris, B. W. *J. Polym. Sci. B Polym. Phys.* **2015**, *53* (5), 311–316.
- (25) Sung, S. H.; Bajaj, N.; Rhoads, J. F.; Chiu, G. T.; Boudouris, B. W. *Org. Electron.* **2016**, *37*, 148–154.
- (26) Zheng, L.; Mukherjee, S.; Wang, K.; Hay, M. E.; Boudouris, B. W.; Gong, X. *J. Mater. Chem. A* **2017**, *5*, 23831–23839.
- (27) Joo, Y.; Agarkar, V.; Sung, S. H.; Savoie, B. M.; Boudouris, B. W. *Science* **2018**, *359* (6382), 1391–1395.
- (28) Zhang, Y.; Gautam, B. R.; Basel, T. P.; Mascaro, D. J.; Vardeny, Z. V. *Synth. Met.* **2013**, *173*, 2–9.
- (29) Basel, T. P.; Huynh, U.; Zheng, T.; Xu, T.; Yu, L.; Vardeny, Z. V. *Adv. Funct. Mater.* **2015**, *25*, 1895–1902.
- (30) Gallagher, N. M.; Olankitwanit, A.; Rajca, A. *J. Org. Chem.* **2015**, *80*, 1291–1298.
- (31) Kittel, C. *Introduction to Solid-State Physics*, 8th ed.; Wiley: Hoboken, NJ, 2005.
- (32) Cavagna, A. *Phys. Rep.* **2009**, *476* (4–6), 51–124.
- (33) Schönhals, A.; Kremer, F. In *Broadband Dielectric Spectroscopy*; Kremer, F., Schönhals, A., Eds.; Springer-Verlag Berlin Heidelberg: New York, 2003; pp 59–98.

2. INTRODUCTION TO ORGANIC ELECTRONICS

2.1 General Introduction

It is hard to dispute that electronic devices are of prime importance to modern society. With each passing day, our world grows more interconnected as decreasing costs and increasing performance lead to the integration of devices in every available sphere. The increasing prevalence of smart appliances is a testament to this trend. As such, the development of materials for electronic applications is crucial. Most electronic devices utilize inorganic materials such as metals (e.g., gold, silver, and copper) or metalloids (e.g., silicon and germanium), due to their high performance in terms of charge transport and energy conversion. However, this approach is not always optimal, particularly when looking at applications where maximum performance is not the top priority. Typically, devices based on inorganic systems require high-purity materials and expensive production methods.¹ Materials used in semiconductor fabrication typically must be purified to less than one impurity per ten billion atoms, and fabrication of such devices requires high temperatures, the use of aggressive chemicals, and complex multi-step procedures. Additionally, these materials tend to be mechanically rigid, forcing most applications to either be rigid as well or to utilize thin (i.e., < 500 nm) materials² or multiple rigid pieces connected together to allow for mechanical flexibility. Furthermore, inorganic devices present sustainability concerns. Many inorganic materials are relatively rare, and due to the presence of toxic heavy metals in devices, there is a growing concern over the safe disposal of these. While recycling efforts can mitigate these concerns, there is still much work to do in order to devise and implement a fully closed product lifecycle. Therefore, to further the ubiquitous integration of electronic devices, there is a need to explore alternative classes of materials, especially for applications where concerns other than the highest possible performance are key.

One such class is comprised of organic electronic materials, which have been the subject of an increasing amount of academic and industrial research over the past few decades,³⁻⁶ particularly after the discovery in 1977 of relatively high electrical conductivity in polyacetylene films oxidized by iodine vapors.^{7,8} These consist of primarily carbon-based molecules, which are designed such that they are stable in both neutral and charged states. Organic materials allow for the possibility of inexpensive roll-to-roll production through solution processing methods such as

doctor blade coating and inkjet printing.^{9,10} Additionally, organic materials can be designed on the molecular level to be both intrinsically flexible and conductive, enabling widespread new applications for electronic materials that are also mechanically flexible and elastic.¹¹ While many applications are still in the experimental stage,¹² organic electronics have made headway into the commercial market in the form of organic light-emitting diode (OLED) displays in televisions and smartphones.¹³ Potential applications in the near future also include flexible and transparent OLED displays¹⁴ and solar cells.¹⁵ Despite the promises offered by organic electronics, however, organic materials in general have poor electronic properties compared to their inorganic counterparts.¹⁶ Thus, a significant amount of effort in organic electronics research is focused on developing new high-performing materials for use in these devices, as well as understanding what enables these new materials to perform at a high level in order to guide future development efforts.¹⁷⁻¹⁹

To date, work regarding organic electronics has been dominated by conjugated materials, which are materials with extensive π -orbital conjugation throughout their structure. This electron delocalization stabilizes ionized states on the molecule, and electronic conduction is achieved through the transfer of ionization states between adjacent molecules. While the behavior of these materials is mostly well-understood, they too have some fundamental limitations. The mechanical properties and electronic properties are both determined by the conjugated structure encompassing most of the molecule, and there is often, but not always, a trade-off between the two.^{11,20} That is, in many cases, improving the flexibility of the material results in a reduction in electrical performance. Additionally, materials with extensive π -conjugation typically absorb light in the visible spectrum, limiting their application for transparent electronics.

While many efforts have focused on improving the properties of conjugated materials, an alternate class of conductive materials based on stable organic radicals have recently emerged.²¹⁻²³ These open-shell molecules can undergo either a reduction or oxidation to form a closed-shell anion or cation, and ion/radical pairs can transfer an electron between each other, enabling charge transport through the bulk material. In recent years, the potential value of this new class of materials has been demonstrated both with small molecules and with non-conjugated polymers bearing radical side chains. A description of many of the applications of these materials in energy storage and energy conversion applications is given in Chapter 3 of this document. Additionally, relatively high intrinsic conductivity in these materials has been demonstrated if the system can be thermally annealed.²⁴ While many examples exist of the unique utility of open-shell species

relative to closed-shell conjugated polymers, they highlight the need to elucidate the behavior of these emerging materials such that the community can allow them to reach their full potential.

As conjugated materials benefit from the significantly greater maturity of the field while radical materials show many unique application spaces not well addressed by conjugated materials, it is important to not see either material as being potentially superior to the other. Rather, both classes of materials will simply serve as a wide toolbox for future uses, and future applications will likely involve both materials being used in conjunction with each other. Indeed, many reports in the literature describe approaches that utilize both conjugated and radical functionalities together. For instance, radical polymers have been used to improve the performance of devices that used conjugated polymers as the active semiconductor layer, specifically as interfacial modifying layers in organic and perovskite solar cells^{25,26} and organic field effect transistors²⁷ and as an ion storage layer in organic electrochromic devices.²⁸ Additionally, materials with both conjugated and radical character are being explored for a variety of applications. In particular, conjugated polymers bearing stable radical pendant groups promise improved organic battery performance provided the energetics of both electroactive species are properly tuned.²⁹⁻³⁶ Additionally, pendant radical groups have been utilized to stabilize conjugated small molecules such as pentacene, protecting them from degradation.³⁷⁻⁴² One final example are conjugated polymers that themselves have open-shell character in the conjugated backbone. These are distinct from radical polymers in that the radicals can interact and are coupled through the conjugated network. Through proper molecular design, the molecule can be structured such that the ground state is of triplet or even higher character.⁴³ Such materials are being examined for applications in organic magnets^{44,45} and in low bandgap polymers.^{46,47} With all these application spaces, it is important that a thorough understanding of the interactions between both classes of materials is developed.

2.2 Charge Transport in Organic Materials

2.2.1 Wave Nature of Electrons

A material's optoelectronic and chemical properties ultimately result from the motion of electrons, for which a precise theory was developed in the 1920s with the advent of quantum mechanics. According to this theory, electrons and all elementary particles behave as waves, the

square of whose amplitude at a given point in space and time determines the probability of a particle being found there. Because of this, electrons do not have a specific fixed position and are understood to be delocalized over all space, albeit with fuzzy regions where they have a higher probability of being found. Additionally, they show wave phenomena such as interference and diffraction, as demonstrated by the famous double-slit experiment.⁴⁸ Finally, this implies that electrons are indistinguishable. A simple example of what this means is that if we imagine two electrons coming towards each other and diverging, it is impossible to determine if the electrons collided or passed by each other, as the distinction is meaningless for waves. Indistinguishability implies a number of surprising, non-intuitive phenomena, particularly with regards to the interaction of spin.

The way a particle's wavefunction evolves in time is given by the Schrödinger equation.

$$-\frac{\hbar^2}{2m}\nabla^2\Psi(\vec{r},t) + U(\vec{r},t)\Psi(\vec{r},t) = i\hbar\frac{\partial}{\partial t}\Psi(\vec{r},t) \quad (2.1)$$

Here, $\Psi(\vec{r},t)$ is the complex-valued wavefunction at a given point in space and time, $U(\vec{r},t)$ is the potential energy experienced by the electron at a given point, m is the mass of the particle, \hbar is the reduced Planck constant, and $i = \sqrt{-1}$. In general, the potential energy itself depends on the wavefunction due to Coulombic repulsions of the electrons, and thus, the equation cannot be exactly solved. However, single-electron models as well as numerical solutions of multi-particle models still provide considerable insight into the behavior of the system. For stationary states, where the system is not evolving with time beyond the sinusoidal oscillation of the wave function (referred to as a standing wave), the right-hand side of Equation 2.1 is equal to the total energy of the system times the wavefunction. Thus, the total energy of a given state of the system can be obtained by solving an eigenvalue problem.

One of the implications of this is that only certain discrete energy values are allowed. An example is the classic particle in a box, where only square integer multiples (e.g., 1, 4, 9, and so on) of the lowest energy are permitted. This is because only specific wavefunctions work as solutions to Equation 2.1, and each wavefunction has a single defined energy. Continuous variation between them is not possible, in principle, for most forms of the potential energy. One consequence of this fact is the existence of discrete wavefunctions for the electrons in an atom or molecule.

The wavefunctions of an atom or molecule can be found using the sum of the Coulombic potentials of point charges corresponding to the nuclei as the potential energy term, along with a term describing the electrons' mutual repulsion. The solutions in all cases are also a limited selection of wavefunctions with discrete energies, known as orbitals. Due to the Pauli exclusion principle, which arises from the requirement of particle indistinguishability, no two electrons can have the same quantum state, which in a molecule corresponds to the orbitals. Thus, the lowest-energy state of an atom or molecule is one where the lowest energy orbital is filled, followed by the second-lowest energy orbital, and so on until all electrons are in place (Figure 2.1a).

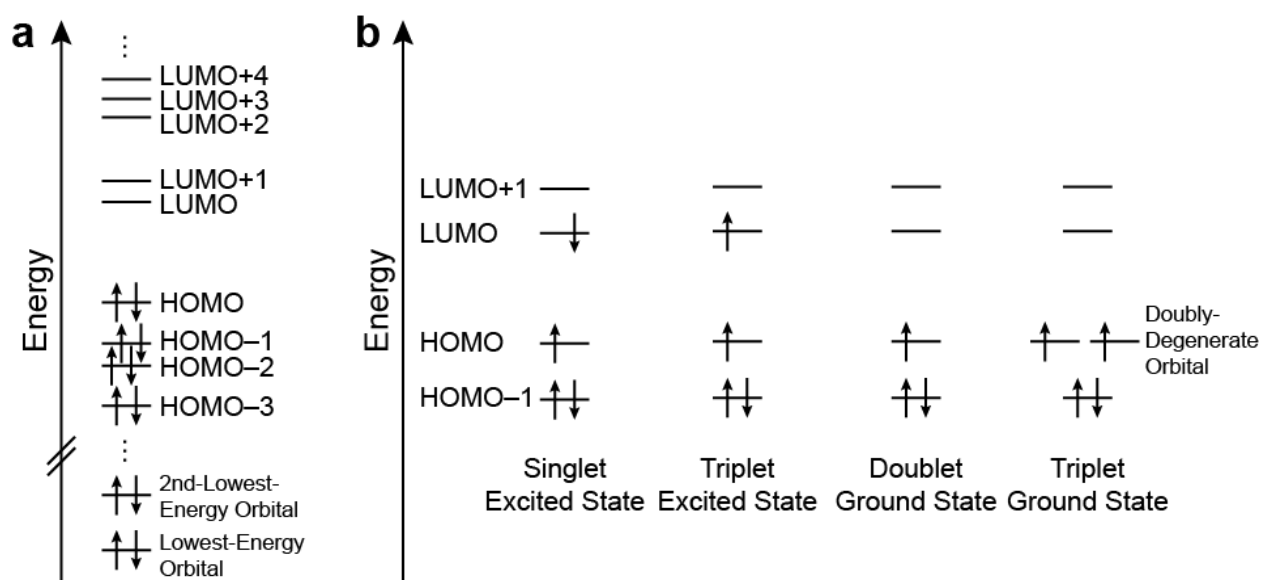


Figure 2.1. (a) Example of orbital energy level diagram of a molecule in the ground state. Here, all orbitals are filled in order of increasing energy. (b) Examples of different spin states of a molecule. Excited states involving one electron can have either singlet or triplet character. In the ground state, radicals exist as a doublet state. Triplet ground states can exist in the case where the highest-occupied molecular orbital is degenerate.

One aspect that has been neglected is that of spin. Electrons have an intrinsic magnetic moment, known as their spin, which can take on one of two values. A classical picture is that of a charged particle of finite size spinning, where the circular motion of charge results in a magnetic field. This suggests that, when a magnetic field is applied, some electrons will be attracted to it and some will be repelled, depending on the direction of their spin. Being a quantum property, spin is quantized and can only take on one of two values with equal but opposite angular momenta and magnetic moments for an electron. These states are commonly referred to as “up” and “down”.

However, the mathematical formalism suggests that these states are orthogonal, rather than opposite. The ultimate result is that a quantum state can be inhabited by both a spin-up and spin-down electron before the Pauli exclusion principle is violated. Thus, in an atom or molecule in its lowest energy state, it is common for most orbitals to be doubly-occupied. However, if multiple orbitals have the same energy (referred to as degenerate states), then the degenerate orbitals can be singly-occupied. Also, if there are an odd number of electrons in the system, then at least one orbital must be singly-occupied.

Systems with unpaired electrons are classified based upon the number of electrons with like spins. In this case, it is referred to as a (number of unpaired spins plus one)-let. A simple case is that of two electrons. Intuition suggests that the four possible states are $\uparrow\uparrow$, $\downarrow\downarrow$, $\uparrow\downarrow$, and $\downarrow\uparrow$. However, the indistinguishability requirement disallows the two unmatched states, which can be made compliant in the form $\frac{1}{\sqrt{2}}(\uparrow\downarrow + \downarrow\uparrow)$ and $\frac{1}{\sqrt{2}}(\uparrow\downarrow - \downarrow\uparrow)$. Thus, there are three matched states (i.e. $\uparrow\uparrow$, $\downarrow\downarrow$, and $\frac{1}{\sqrt{2}}(\uparrow\downarrow + \downarrow\uparrow)$), and one unmatched state (i.e. $\frac{1}{\sqrt{2}}(\uparrow\downarrow - \downarrow\uparrow)$). The state where the spins are matched is referred to as a triplet, and that of the unmatched spins is called a singlet. Similar rules govern systems with higher numbers of spins. In common organic molecules, the ground state is a singlet as all orbitals are doubly-occupied. In these systems, triplets and higher-order spin states are seen only for electronically excited molecules, where electrons occupy higher-energy orbitals. In systems with degenerate highest-energy occupied orbitals, however, ground states with triplet or higher character can be observed. Systems with an odd number of electrons, such as radicals, will show a doublet ground state in general (one unpaired spin) excluding the case of degeneracy (Figure 2.1b).

The electrons in the lowest-energy occupied orbitals are bound sufficiently tightly that they are functionally inactive. Most of the interesting behavior occurs with the electrons in the highest-occupied orbital (HOMO), and those immediately below it, referred to as HOMO-1, HOMO-2, etc., as these require the least energy to move into an unoccupied state. Higher energy orbitals exist mathematically as solutions to the Schrödinger equation and are referred to as the lowest unoccupied molecular orbital (LUMO), LUMO+1, LUMO+2, etc. The unoccupied molecular orbitals are only virtual states, meaning that an electron is never actually in the state. As the shape of the orbitals in space is different, moving an electron from an occupied orbital to the LUMO would change the charge distribution and thus the potential energy term in the Schrödinger

equation, resulting in a slightly different set of orbitals than the ground state molecule. However, the now-occupied orbital is still identified with the LUMO for simplicity, as are all the occupied orbitals with their ground state counterparts. This identification is further kept for charged molecules, despite the even more dramatic impact of adding or removing a charge on the potential energy term.

While only single molecules have been described thus far, all these behaviors apply to systems of multiple molecules as well. In groups of molecules referred to as supramolecular complexes, there are multiple interacting molecules that all share a single electronic structure. This is because electrons cannot tell whether nuclei belong to one molecule or the other; all that affects them is how far away the nuclei are. Thus, if two molecules come close together, the electrons in one will feel the Coulombic potential from the nuclei, and thus the orbital structure will change, with some orbitals spatially extending over both molecules. This leads to a “splitting” of energy levels, as the new frontier orbitals will resemble the symmetric and antisymmetric additions of those of the constituent molecules, much as with diatomic molecules.

One commonly seen interaction in organic electronics is π -stacking.⁴⁹ For conjugated molecules, the relatively exposed π electrons allow loose bonding between multiple of these molecules. This is an attractive effect that leads to aggregation. Several phenomena in organic electronics are related to this interaction. Charge transportation through π -stacked complexes is facilitated as the frontier electrons are delocalized across all the π orbitals, and crystallization is driven in part by the interaction. Additionally, the splitting of energy levels leads to sometimes significant changes in the optical properties of the material, specifically red-shifting of the photoabsorbance of the material due to the shrinking HOMO-LUMO gap. These interactions can of course occur between dissimilar materials as well. While it is often tempting to look at single molecules to describe a system, the interactions between them lead to a significantly more complex picture of what is occurring at the most fundamental level in a material.

2.2.2 Inorganic Materials

When describing charge transport in organic electronic materials, it is common to make use of the terminology developed for inorganic crystalline materials, as the theory is significantly more robust. However, it is worth noting that while many parallels can be drawn, the underlying mechanisms are different. Organic materials will frequently deviate so far from the ideal state that

the similarity with the inorganic is tenuous. Nevertheless, understanding the terminology and theory associated with inorganic crystalline materials provides a conceptual framework for applying organic materials in areas where inorganic ones are commonly used.

The previous section described quantum mechanics and its implications for the electronic structure of single molecules. Most inorganic materials, however, are not well described by a molecular picture. Indeed, for most metals, one tends to think of all the nuclei surrounded by a “sea” of electrons, which are not bound to any one nucleus but free to move throughout the entire bulk of the material. Nevertheless, the same concept applies, where the allowable wavefunctions can be calculated from the Schrödinger equation knowing the arrangement of the nuclei.^{1,50,51} For a crystalline material, the translational symmetry of the nuclei allows for the equation to be solved exactly within a unit cell with periodic boundary conditions. Solutions take on the following form, referred to as a Bloch wave.

$$\psi(\vec{r}) = e^{i\vec{k}\cdot\vec{r}}u(\vec{r}) \quad (2.2)$$

Here, \vec{r} is the position, $u(\vec{r})$ is a function sharing the same translational symmetry as the crystal, and \vec{k} is the wavevector, a vector quantity whose magnitude is equal to $\frac{2\pi}{\lambda}$, where λ is the wavelength of the wave, and whose direction corresponds to the direction of travel of the wave. A 1-dimensional illustration is given in Figure 2.2. If the crystal is assumed to be infinite in extent, the energies of the allowed wavefunctions range continuously, albeit with separate regions of allowed and disallowed energy levels. The regions of allowed energies are called “bands”. For a finite crystal, the energy is still discretized. However, as crystals are several orders of magnitude greater in extent than the unit cell being considered, the difference between energies in a single band is still small enough that assuming a continuous distribution is valid. While the number of states in the entire crystal is infinite, the number of states in a band per unit volume of crystal is not, and thus the extent to which bands are filled can be determined from the density of states and the density of electrons.

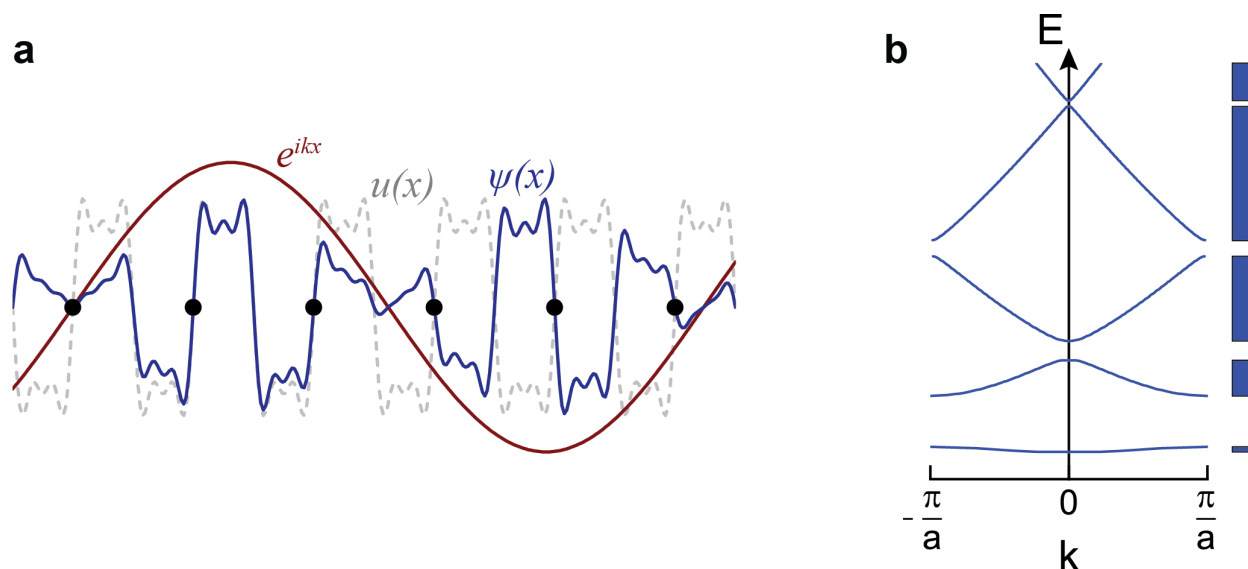


Figure 2.2. (a) Real part of a Bloch wave in a 1D crystal lattice, showing it as the product of a periodic function $u(x)$ and a plane wave e^{ikx} . (b) Sample band diagram for a 1D system, showing how a state's energy (E) relates to its wavevector (k) in differing bands. Blue boxes depict allowed energy levels, all others are disallowed. Based on ref 50.

The electrons are (mostly) free to move about the crystal, and they do so in the direction of the wavevector of their state. If a force acts upon an electron, the effect will be the electron changing from one state to another whose wavevector points in a different direction. For this to occur, there must be an empty state for the electron to occupy. This leads to an interesting result that if a band is completely filled, the electrons in it will be unable to change states and thus applying a force will not cause a net movement. In the case of a filled band, the electrons are still moving, but each state with a given wavevector has one with a wavevector pointing the opposite direction. Thus, no net motion of electrons occurs.

As with molecules, the most important bands for understanding electronic properties are the highest-energy occupied bands and the lowest-energy unoccupied "virtual" bands. In a crystal these are referred to as the valence and conduction bands. As with the HOMO and LUMO of a single molecule, most of the action happens in these two bands. One common distinction when talking about electronic materials is the distinction between conductors, semiconductors, and insulators. This distinction comes from the valence band. In a semiconductor, all energy states in the valence band are filled, while in a conductor, the valence band is half-filled. This difference is significant, as filled bands do not allow for a net transport of charge to occur. In a conductor, as the band is only half-filled, there are ample empty states infinitesimally close to the occupied ones

that can become occupied in response to an applied force. However, for a semiconductor, the nearest available state is in the conduction band. Therefore, semiconductors naturally act as insulators (in practice, the term insulator is used for a semiconductor with high bandgap).

In a semiconductor at 0 K, all valence band states are filled while all conduction band states are empty. At a finite temperature, some electrons will have sufficient thermal energy to populate the conduction band states. As neither band is completely filled, some degree of charge transport can occur. For the nearly full valence band, only a small portion of the electrons will be missing a partner with the opposite wavevector, and only these contribute to the charge transport. It is often easier to consider the vacancies left behind as their own particles, which are referred to as “holes”. These holes also can adopt k values of their own and move about the crystal relatively independently of the electron that previously occupied them. An intuitive picture of hole motion can be understood as adjacent electrons moving to fill a vacancy in real space, thus leaving behind a new hole. A sequence of these electron motions thus results in the hole moving in the opposite direction. However, it should be emphasized that for all intents and purposes, the holes behave like positively-charged electrons moving relatively unimpeded, as opposed to the clunky motion that the previous description may inspire.

The population of holes and electrons in a semiconductor at a given temperature can be directly computed using Boltzmann statistics, with the formula $n = p = \sqrt{N_C N_V} e^{-\frac{E_g}{2k_B T}}$, where N_C and N_V are the effective densities of states (i.e., the number of quantum states in each band per unit volume of semiconductor crystal) in the conduction and valence bands, and E_g is the bandgap energy, or difference in energy between the highest energy state in the valence band and the lowest energy state in the conduction band. In a silicon crystal at room temperature, this is equivalent to one free charge carrier per trillion atoms. By contrast, for a metal there is one free charge carrier per atom in the lattice. As conductivity is proportional to the density of charge carriers, the conductivity can be increased by introducing more charge carriers. This is done using dopants, which are intentionally introduced impurities. For a tetravalent atom such as silicon, more free electrons can be introduced using an atom such as phosphorous, where each phosphorous atom has five valence electrons instead of four. Four of these valence electrons participate in bonds with adjacent silicon atoms, and the extra electron is only weakly bound to the phosphorus nucleus due to dielectric screening; thus, it is easily liberated at room temperature by thermal energy. This is referred to as n-doping. In the band picture, this corresponds to an additional occupied state at an

energy slightly lower than the conduction band for each donor atom, which can be promoted to the conduction band with energy on the order of thermal energy ($k_B T$). Even the presence of phosphorous at a concentration of one part-per-million will result in a million-times higher conductivity, while having essentially no other impact on the material properties. Likewise, the concentration of holes can be increased via a trivalent atom such as boron, which introduces an empty state at energies around $k_B T$ above the valence band. This is referred to as p-doping. Typically, concentrations of dopants do not start affecting the properties until reaching concentrations of one part-per-thousand or even per-hundred.

In a doped material, the population of the charge carriers are no longer equal. An n-doped material is referred to as n-type while a p-doped material is referred to as p-type. From an electrical conductivity standpoint, the identity of the charge carriers does not matter; however, for most device applications there will be an effect. For example, both the Hall effect (deflection of moving charge carriers by a magnetic field) and Seebeck effect (gradient of charge carriers induced by a temperature difference) will change direction with oppositely charged carriers. Additionally, as charges travel at the energy of the band they are in, holes and electrons have different energies, which can affect the charge transport across the interface between two dissimilar materials. For example, joining a p-type material with an n-type material will create a pn-junction, which only allows for unidirectional charge transport due to the charge gradient inside.

Holes are an example of a quasiparticle, which is a particle that does not truly exist on its own but is composed of interactions between many other particles. There are many other quasiparticles that are relevant to electronic devices. One example is the phonon, which is understood as a unit of lattice vibration. In other words, the vibronic modes of the crystal are ultimately quantized, meaning that an atom vibrating in its unit cell can only have a certain discrete energy. Because of this, units of vibration can travel between atoms. When a hole or electron's travel is frustrated by thermally-induced lattice distortions, this is commonly interpreted as the charge carrier scattering off of a phonon. One other quasiparticle is the polaron. In a polarizable medium, free charge carriers will induce polarization that follows them as they travel. They effectively are dragging along a cloud of polarization that acts as a frictional force. The charge carrier plus the cloud of polarization are what make up the polaron. Finally, when an electron is photoexcited from the valence band to the conduction band, it remains Coulombically bound to the hole left behind in the valence band. Binding energies tend to be very weak in inorganic

materials, but the bound hole-electron pair is called an exciton. Quasiparticles offer a useful conceptual framework that clarifies some of the behaviors observed in these materials.

2.2.3 Organic Materials

In principle, band theory depends only on the existence of a periodic potential described by a crystal lattice. What occupies those lattice sites is irrelevant. Inorganic crystals have single atoms or small clusters of atoms as their crystal elements, but if the crystal elements were instead organic molecules, the same concepts should apply. Indeed, for carefully prepared samples at low temperatures, band transport in organic materials has been observed.^{52,53} In practice, however, the assumption of an infinite periodic lattice is almost always broken. In contrast to the atomic nuclei in a silicon crystal, the forces holding the molecules together in an organic material are relatively weak. Thus, even small amounts of thermal energy are sufficient to disrupt the lattice, meaning that charges are necessarily more localized in nature.⁵⁴ This naturally assumes that a crystal even exists. While single crystals of organic small molecules can be produced, polymer materials are necessarily polycrystalline simply due to the size and flexibility of the molecules. Therefore, the electronic properties must be described by looking at individual molecules, or small groups of them.* Because of the more localized nature of the charges, the picture of charge transport changes from one of plane waves travelling through a crystal to one of charges jumping from one localized site to another.

Despite this crucial difference, terminology from band transport and inorganic crystals is still utilized. Holes and electrons now refer to positively- and negatively-charged states that move from one molecule to another. In this framework, the HOMO and LUMO of the molecule are described as analogous to the valence and conduction bands for a crystal, respectively.⁴ One key difference arises when drawing this analogy, however, which is illustrated by what happens when a charge is added or removed. For a crystal, the electrons are delocalized over a large region relative to the crystal unit cell. Therefore, adding or removing an electron does little to impact the potential energy felt by the other electrons, so the band structure and thus the energies of the other states in the crystal are almost entirely unaffected. By contrast, when charges are localized, adding

* One important note is that interactions such as π - π stacking allow for electrons to be delocalized across more than one molecule. Additionally, for polymers, the delocalization tends to be over multiple repeat units, rather than the entire macromolecule. For sake of generality, “molecule” will refer to a structure over which an electron is delocalized.

or removing one from the molecule has a significant impact, both due to that charge's repulsion with the other electrons and due to a change in molecular equilibrium geometry caused by the change in force acting on the nuclei. More robust descriptions of the relevant energy levels are given by the ionization energy (IE) and electron affinity (EA) of the molecules, which refer to the minimum energy required to remove an electron from the molecule, and the energy released when an electron is added to the molecule, respectively. If one ignored the effect ionization has on the other states in the molecule (referred to as the frozen orbital approximation), the energy of the HOMO/LUMO states would equal the IE/EA values. Of course, this effect cannot be ignored.⁵⁵ Thus, while literature reports often describe holes as having energy equal to that of the HOMO state of a neutral molecule and electrons as having energy equal to the LUMO state (and that convention will be utilized at various points throughout this document for simplicity), it is important to remember that the actual energy landscape of an organic semiconductor is significantly more complex.

While significant progress has been made towards developing low-bandgap organic semiconductors, organic materials typically have higher bandgap energies than their inorganic counterparts. Thus, the intrinsic charge carrier concentration is much lower. Additionally, due to their more disordered nature, organic electronic materials generally have a lower charge mobility; thus, the electrical conductivity is significantly lower. While the terms p-type and n-type can refer to the nature of a doped material, organic semiconductors typically can only support one form of charge carrier. That is, organic molecules can be reversibly oxidized or reduced, but not usually both. For this reason, the terms p-type and n-type are usually used to classify intrinsic materials relative to their preferred redox behavior. Materials capable of undergoing both are referred to as ambipolar. Examples of these materials are illustrated in Figure 2.3. Interestingly, p-type materials are significantly more common. This is, in part, because the reduction potential of most organic materials is much lower than that of oxygen in the presence of water or another proton source, which will cause most organic anions to react in all but the most tightly controlled environments (inorganic single crystals are less permeable and thus more stable).^{56,57} Furthermore, the electron affinity of these materials tends to be significantly higher than the work function of most metals used for contacts, resulting in significant contact resistance. Most reported n-type materials require extensive delocalization or many electron-withdrawing substituents to increase the electron affinity and thus stabilize the negative charge.⁵⁸ With more stringent molecular design rules, the

search for better n-type materials remains one of the significant focus areas for organic electronics research.⁵⁷⁻⁵⁹

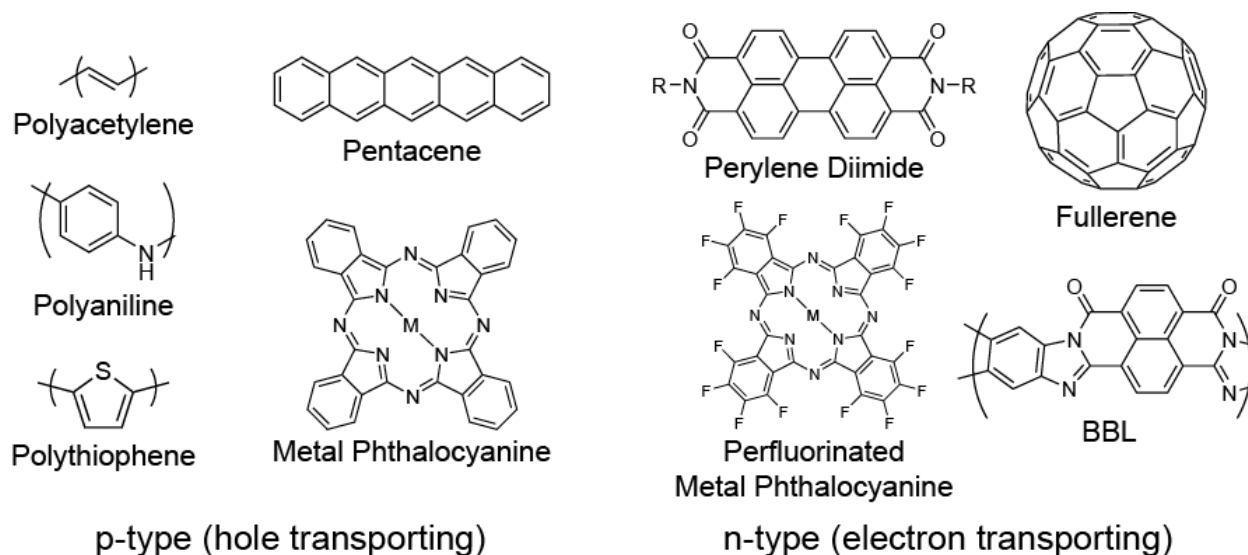


Figure 2.3. Examples of hole transporting and electron transporting polymers and small molecules commonly seen in the literature. BBL is short for poly(benzobisimidazobenzophenanthroline).^{60,61} Shown here are the conjugated cores; often times solubilizing side chains will be included (particularly for polythiophene, pentacene, perylene diimide, and fullerenes). Of note are the metal phthalocyanines, which illustrate how addition of electron-withdrawing substituents leads to a change in character from p-type to n-type.

Doping in organic materials is typically accomplished using powerful oxidizing or reducing agents.⁶² Initial studies used iodine vapor as a p-dopant,⁷ and commonly-used ones today include both strong acids (as with PEDOT:PSS)^{63,64} and molecules such as tetrafluorotetracyanoquinodimethane (F4TCNQ),⁶⁵⁻⁶⁸ which is itself an n-type semiconductor with a high electron affinity. For organic materials, the general concept of doping is similar; charge transfer from the organic semiconductor to the dopant occurs and is driven by the difference in IE of the donor and EA of the acceptor. However, doping tends to be less efficient in organic materials than inorganic materials. A number of explanations have been proposed, ranging from the formation of charge transfer states that alter the energetics of doping,^{68,69} the preferential filling of trap states by dopants,⁷⁰ and the strong Coulombic attraction between the charge and the ionized dopant.^{65,67} For these reasons combined with the already low conductivity of organic materials, it is common to see dopant concentrations in the percent range for organic materials. Despite the

issues seen with doping, it can be widely utilized to provide stable high conductivities of greater than $1,000 \text{ S cm}^{-1}$,⁷¹ and can be utilized to alter the majority charge carrier type in normally p-type materials.^{72,73}

Being able to measure the charge transport energy for a material is important for proper selection of dopants. More importantly, if the transport levels of two materials in contact are not aligned, contact resistance and non-ohmic behavior can arise,⁷⁴⁻⁷⁶ which in many cases is detrimental to device performance. IE and EA can be measured directly, albeit only on the surface of the sample, by utilizing ultraviolet photoemission spectroscopy (UPS) and inverse photoemission spectroscopy (IPES). UPS involves shining ultraviolet light on a sample and measuring the current while varying the photon energy.⁷⁷ IPES is the reverse process, where the sample is bombarded with electrons and ultraviolet photons are measured.⁷⁸ While these procedures directly measure the IE and EA of a molecule, they require highly-specialized equipment to carry out. Thus, they are often approximated by the oxidation and reduction potentials, which are measured using electrochemical techniques.⁷⁹ However, while the techniques should in principle measure the same quantity, the combination of different chemical environments (i.e., vacuum vs. a polar solvent) and electrode contact effects conspire to make the results significantly different, with some literature reports relating oxidation potential to ionization energy by a slope of 1.4.⁸⁰ While approximate pictures of the energy landscape in organic systems can be drawn up using these data, it is important to remember that the fact that charges are localized to a single molecule results in an energy landscape that is much less robustly determined.

The localization of charges means that different theoretical models must be utilized in order to describe the charge transport. For band theory, charges are free to move around the crystal while occasionally running into obstacles such as lattice distortions caused by thermal energy. The degree to which charges are scattered can be encapsulated along with other parameters into a factor called mobility (μ). Conductivity is proportional to the mobility and the number of charge carriers. For band-like transport, mobility decreases with increasing temperature, as more thermal energy leads to greater lattice distortions which act as obstacles to charge transport.⁵⁰ In this framework, organic materials can be thought of materials where the mean free path of charge carriers is smaller than the dimensions of the molecules. In this situation, the charge is confined to a single site by potential energy barriers that it must surpass to move to another site. This is referred to as hopping transport, and it predicts that mobility will increase with higher temperature, as increased thermal

energy allows the potential energy barriers to be more easily surpassed.^{81,82} Therefore, when probing materials, the temperature dependence of their mobility can be utilized to determine the charge transport mechanism.⁸³

2.2.4 Charge Transport in Radical Polymers

While closed-shell conjugated polymers do show many parallels to inorganic semiconductors, less is known about how to treat open-shell radical polymers. Charge is transported at the energy corresponding to the ionization energy or electron affinity of the radical species, depending on which mode of charge transport is occurring.^{21,23} Typically, this is equated to the energy of the singly-occupied molecular orbital (SOMO), which leads to the picture of many half-filled molecular orbitals that charges move between. Based upon this picture, it seems as though radical polymers should be analogous to inorganic metals. However, this picture relies on the erroneous frozen orbital assumption, which would give equal values for electron affinity and ionization energy. Indeed, for ambipolar radicals such as nitronyl nitroxide, it is known that the reduction and oxidation potentials differ by 1.3 V,⁸⁴ indicating that this assumption is significantly flawed (Figure 2.4a). Additionally, as with conjugated polymers, many radical species are unipolar, meaning they can be reversibly oxidized or reduced, but not both. If the IE and EA for a radical species were equal in general, this would not make sense. With these facts in mind, it seems as though radicals should behave closer to closed-shell semiconductors, with the half-filled SOMO still being analogous to a filled band.

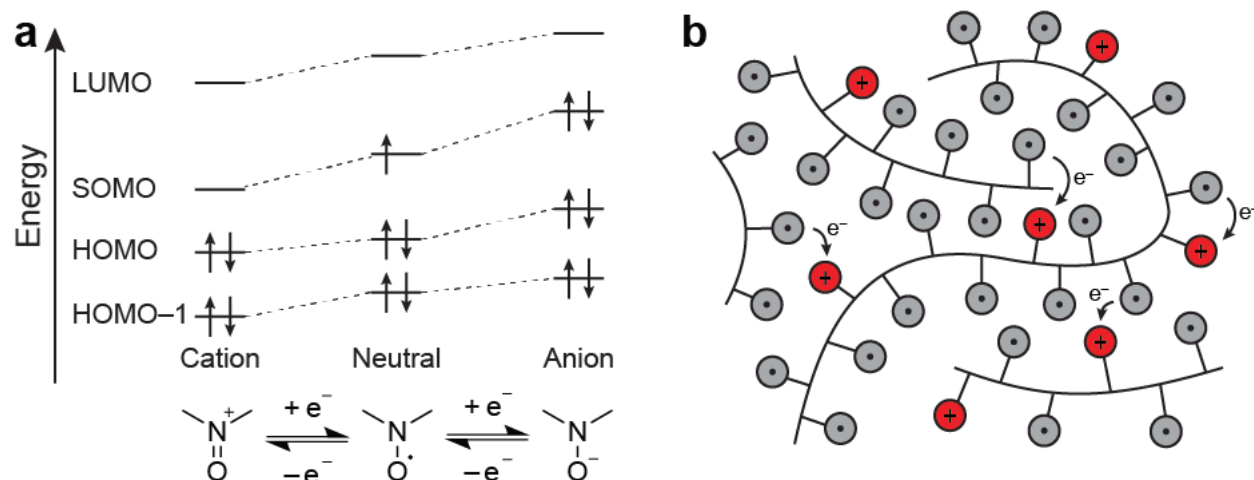


Figure 2.4. Schematic of charge transport in radical polymers. (a) Oxidation and reduction reactions for a nitroxide radical. Both reactions are shown although typically only one proceeds reversibly for a given species. A schematic of the molecular orbital energies is shown as well, depicting the shift in energies that occurs on oxidation or reduction, as well as why the potential for both reactions differs. (b) Schematic of a p-type radical polymer film. Charges are localized to radical pendant groups and move through a series of one-electron transfers between neutral (grey) and charged (red) species.

A number of differences present themselves between charge transport in radical polymers and conjugated polymers, however. In general, radical polymers in the solid state show minimal dependence of conductivity or mobility on temperature,^{24,85–87} which is inconsistent with the predictions of a hopping model. This is unique for radical polymers and suggests that new models must be developed to describe their charge transport. One interesting feature is the high intrinsic conductivity observed in a highly flexible radical polymer after annealing, which is theorized to be related to aggregation of radical sites.²⁴ An understanding of charge transport within the aggregates and how that differs from transport outside the aggregates is lacking as well. Aside from the mechanical properties afforded by selection of differing backbones, the electrical conduction is mostly unrelated to the polymer backbone. Indeed, computational studies suggest that the majority of charge transport is between pendant groups on different chains.⁸⁸ In contrast to conjugated polymers, where some delocalization along the backbone occurs, charges in radical systems are truly localized. Finally, doping in radical polymers is still not well understood. In theory, doping should be facile due to the fact that both the charged and neutral versions of the radical species are stable. A half-filled “band” could be engineered by blending equal parts charged and neutral radical species. Current studies however show only modest increases in conductivity

when this doping is performed,^{24,85,89,90} in contrast to the orders-of-magnitude variation seen for conjugated polymers and inorganic crystals. This difference further highlights the difference in charge transport mechanisms between these two classes of organic electronic materials and the importance of further study.

2.3 Photoexcited Interactions

For applications such as solar cells and light-emitting devices, understanding the excited state interactions between different materials is of crucial importance. The excited state in this case refers to electronic excited states, where electrons are found in higher-energy orbitals than the lowest-energy configuration. A molecule in an excited state is referred to as an exciton, analogous to the quasiparticle in inorganic systems. A molecule can be promoted from the ground state to an excited electron state via a photon whose energy is equal or greater than the difference in energy between the two states (greater energies will cause the molecule to enter an excited vibronic state as well). Typically, the lowest-energy excited state involves a single electron transition from the HOMO to the LUMO. The photon energy required for this transition can be approximated as the difference between the IE and EA of the molecule, which in organic electronics is referred to as the electronic bandgap. As has been established, however, the IE/EA are only crude approximations of the HOMO and LUMO energy, as they include the coulombic potential difference experienced by the other electrons in the molecule. Therefore, the electronic bandgap tends to be an overestimation of the photon energy. The actual photon energy required to excite the molecule is referred to as the optical bandgap. The difference between the electronic and optical bandgap is referred to as the exciton binding energy, as it corresponds to the energy that would be required to separate the hole and electron into free charge carriers.

Many conjugated polymers have bandgap energies corresponding to photons within the visible spectrum.^{91,92} Therefore, the transitions between these excited states can be studied using visible light techniques, including absorbance and fluorescence spectroscopy. Absorbance and fluorescence are inverse processes. Absorbance occurs when a photon is absorbed, resulting in the molecule entering a higher energy electronic state, and fluorescence occurs when a molecule in an excited electronic state decays to a lower energy one, emitting a photon whose energy is equal to the difference in energy between the two states. The energy of the emitted photon tends to be less than that of the absorbed photon, a phenomenon known as the Stokes shift. This occurs because

the electronic transition often results in a change in vibronic state as well, which relaxes faster than the excited state lifetime. Thus, the transition during fluorescence is lower in energy than the one occurring during absorption. How absorbance and fluorescence change in samples containing multiple different materials can shed light on the electronic interactions between the materials. One such signature is through fluorescence quenching.⁹³ If a fluorescent molecule, or fluorophore, is in close proximity to another molecule, the other molecule can introduce pathways leading to the fluorophore's ground state that do not involve photon emission, or it will prevent excitation in the first place. This will result in fewer photons being emitted and thus a reduction in fluorescence intensity. The precise mechanism by which this occurs provides key insights into the electronic interactions between both molecules.

One such distinction between mechanisms is between static and dynamic quenching. Dynamic quenching occurs when the quencher interacts with the excited molecule leading to non-radiative relaxation of the excitation. The other is static quenching, where the fluorophore interacts with the quencher in the ground state to form a complex that is not fluorescent. If fluorescence quenching is observed in a system, then it is important to establish that dynamic quenching is occurring. Fortunately, the difference between the two is straightforward to detect, as outlined below.

Both static and dynamic quenching obey the Stern-Volmer relationship, which is described by the following equation.

$$\frac{I_0}{I} = 1 + K[Q] \quad (2.3)$$

Here, I_0 is the intensity in the absence of quencher, I is the intensity with quencher, $[Q]$ is the molar concentration of quencher, and K is the Stern-Volmer constant, which indicates the strength of the quenching interaction. For dynamic quenching, this is equal to the product of the bimolecular rate constant for the quenching process (k_q) and the excited state lifetime in the absence of quencher (τ_0). For static quenching, this is equal to the equilibrium constant for complex formation. If both static and dynamic quenching occur, the end result is the product of two terms in the form of Equation 2.3, leading to a quadratic dependence of the reciprocal of the intensity on concentration. The behavior of the two different mechanisms differs for time-resolved fluorescence, where the fluorescence intensity, after a brief excitation pulse, is measured as a

function of time. Excited states relax through a first-order process, so fluorescence naturally decays exponentially with time. Dynamic quenching, by offering an alternate route for relaxation, hastens this process, lowering the time constant for the decay. Static quenching, on the other hand, prevents the initial excitation entirely, so while the initial intensity will be lower, the actual relaxation dynamics are unaffected as the excited state still only has one route by which to decay. In the case of dynamic quenching, the time constant also obeys the Stern-Volmer relationship, so by performing time-resolved studies, the nature of the quenching can be established in a ready manner.

Absorption spectroscopy is used to establish the nature of these interactions. In the case of static quenching, the ground state complex would likely have a different electronic structure than the two molecules separately, owing to interaction of the molecular orbitals. Thus, the optical absorption spectrum would be different than simply the sum of the absorption spectra of the two materials separately. That is, additional peaks corresponding to the complex would be expected to appear in the spectrum. With only dynamic quenching, the absorbance of the mixed solution should simply be a sum of the individual spectra, as per the Beer-Lambert law.

Even once the question of static vs. dynamic quenching in a system has been answered, multiple mechanisms for dynamic quenching exist, and it is essential to distinguish amongst them (Figure 2.5). These include electron transfer, excited state transfer, and enhanced intersystem crossing as potential mechanisms. Electron transfer is where an electron transfers from the excited fluorophore to the quencher and it can occur if the electron affinity of the quencher is greater than the ionization energy of the fluorophore minus the excited state energy (an analogous mechanism involving hole transfer is also possible). Excited state transfer, wherein the fluorophore decays to the ground state at the same time as the quencher is excited, can occur through one of two mechanisms. The first is Förster resonance energy transfer (FRET), in which coupling between the ground to excited state dipole transitions results in non-radiative transfer of energy from the fluorophore to the quencher.⁹⁴ The other is Dexter energy transfer, which results from a simultaneous concerted electron transfer from the LUMO of the fluorophore to that of the quencher and from the HOMO of the quencher to that of the fluorophore due to the overlap of their respective wavefunctions.⁹⁵ These mechanisms both result in a net transfer of energy without a transfer of charge. Enhanced intersystem crossing can occur when the quencher is an open-shell species. In this case, exchange interactions between the excited electron on the fluorophore and the unpaired electron on the quencher results in both electrons flipping their spins, which leads to the singlet

exciton on the fluorophore converting to a triplet exciton. If the fluorophore is not phosphorescent, i.e. cannot decay radiatively from the triplet state, then the fluorescence will effectively be quenched.

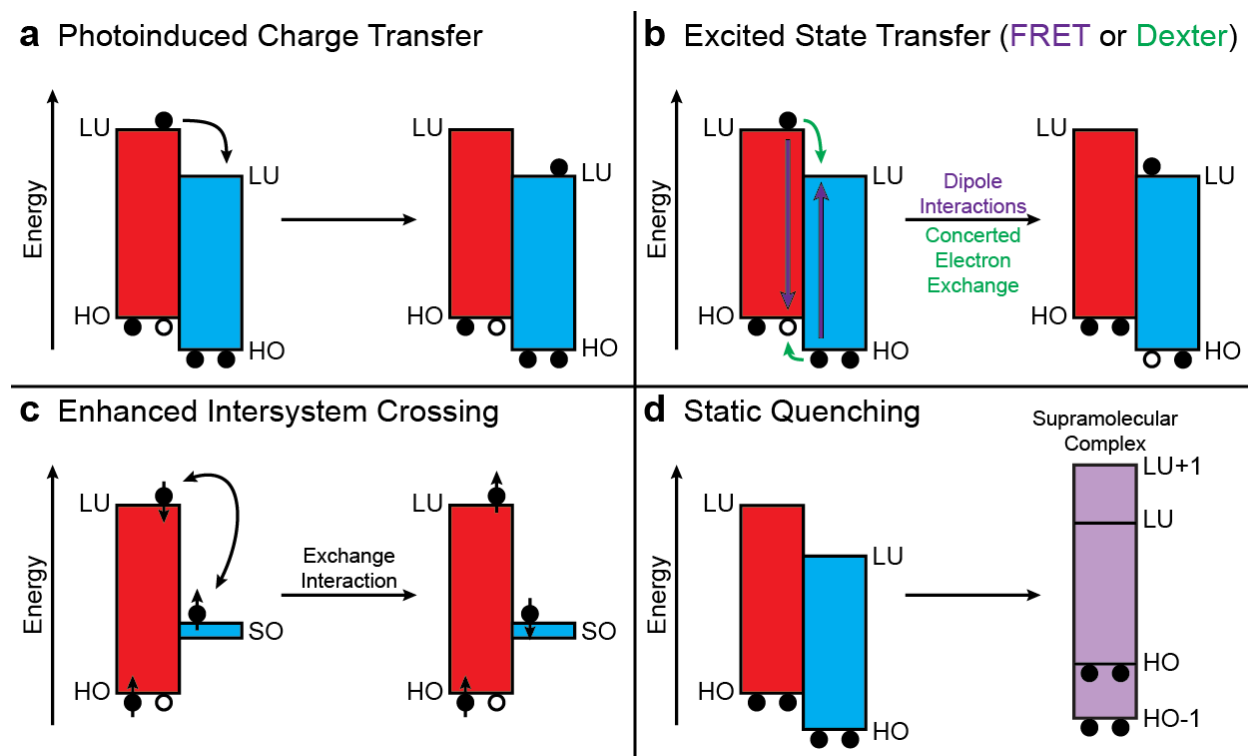


Figure 2.5. Schematic showing different possible quenching mechanisms between a conjugated fluorophore (red) and a quencher (blue). Electrons are indicated with black circles. Holes (represented by white circles) are included for clarity. (a) Photoinduced charge transfer occurs when an electron is transferred from the excited fluorophore to the quencher. (b) Excited state transfer occurs when the excited state is transferred from the fluorophore to the quencher. It can go by the FRET mechanism (blue) where coupling between the dipoles of the excited states lead to a transfer of energy or by the Dexter mechanism (red) where simultaneous concerted electron transfer occurs. (c) Enhanced intersystem crossing occurs when an exchange interaction between the unpaired electron on an open-shell quencher and one of the electrons in the fluorophore leads to the conversion of the singlet excited state to a triplet state. (d) Static quenching occurs when the fluorophore and quencher form a nonfluorescent supramolecular complex in the ground state.

Steady-state absorbance and fluorescence spectroscopy cannot readily distinguish these mechanisms. Therefore, other experimental techniques can be used to gain more insight into the processes occurring. One such technique is transient absorption spectroscopy, wherein the sample is photoexcited by a brief ($\sim 10^{-13}$ s) laser pulse, and then the absorbance spectrum of the sample

is taken after a delay. By measuring at multiple time delays and comparing the excited state absorbance spectra to the ground state, a clear picture of the evolution of the excited state can be observed. If the absorbances of the species corresponding to the intermediates can be identified, such as the charged quencher species for electron transfer, the photoexcited quencher for excited state transfer, or the fluorophore triplet for intersystem crossing, then a determination of the mechanism can be made.

Electron paramagnetic resonance spectroscopy can, in some circumstances, provide useful information about mechanisms in cases where unpaired electrons are encountered. In particular, it is widely utilized for studying photoinduced charge transfer mechanisms between closed-shell species.⁹⁶ In this case, an electron transfer will lead to the generation of two open-shell species, which can be detected by comparing the signals from the samples under illumination and in the dark. If performed at cryogenic temperatures, where the electron dynamics are slowed enough for a population of excited state intermediates to build up, then this technique can be performed at steady-state. However, more information, and evidence of intersystem crossing, can be obtained using time-resolved electron paramagnetic resonance, which as with transient absorption looks specifically at the excited state as a function of time.⁹⁷ As all of these mechanisms play relevant roles in device applications, understanding which are at play can allow for material systems to be optimized for a particular device application.

2.4 Organic Electronic Devices

Many classes of device can be fabricated using organic electronic materials. Some of the main applications for conjugated materials are outlined below. Applications for radicals, such as for batteries and for dye-sensitized solar cells, are discussed further in Chapter 3 of this document.

2.4.1 Organic Photovoltaics (OPVs)

Transitioning from fossil fuel-based energy sources to renewable ones requires reducing the cost of technologies that gather renewable energy. One clear case is with solar cell technology. Much of the energy available to humanity ultimately comes from the sun, and with 9,000 TW of solar energy reaching the Earth's surface, there is more than sufficient amounts to meet the current global consumption of 18 TW. At present, however, solar modules are more expensive than fossil

fuels, which limits their implementation. Most commercial solar cells use doped silicon, but processing the material is an expensive process. Organic solar cells are part of a larger class of solution-processable solar cells, wherein the active layers are deposited from solution, which is a more scalable process in terms of cost.^{98–103} While there are still hurdles to be cleared in terms of efficiency, it is hoped that organic solar cells can provide a means of producing solar cells at a much lower cost when the technology is commercially scaled.

Solar cells, in general, use energy from incident photons to directly drive an electrical current. Organic solar cells do this using a heterojunction between a p-type and n-type material, referred to as the electron donor and electron acceptor.¹⁰⁴ In the prototypical case, a five-step procedure is followed (Figure 2.6). First, a photon is absorbed by a molecule in either layer, which excites it to a higher electronic state. As previously mentioned, this is referred to as an exciton, which more formally describes a bound hole-electron pair. Second, through excited-state transfer mechanisms, an excited molecule can transfer the excitation to a nearby one, which allows the exciton to move through the material. Excitons on average last as long as the excited state on a molecule does. For the prototypical donor poly(3-hexylthiophene) (P3HT), the exciton lifetime is approximately 600 ps, which means an exciton can typically diffuse about 10 nm before recombining.¹⁰⁵ If it does arrive at the interface between the two materials, a charge transfer from an excited donor molecule to an acceptor molecule can occur. This forms a charge-transfer state consisting of a positively-charged donor molecule and a negatively-charged acceptor, which can be seen as a Coulombically bound hole and electron pair. Fourth, thermal energy allows the hole and electron to separate creating a free hole and electron that diffuse through the bulk material. Finally, these charges diffuse to the electrodes driven by the concentration gradient, where they are extracted and travel through the connected circuit.

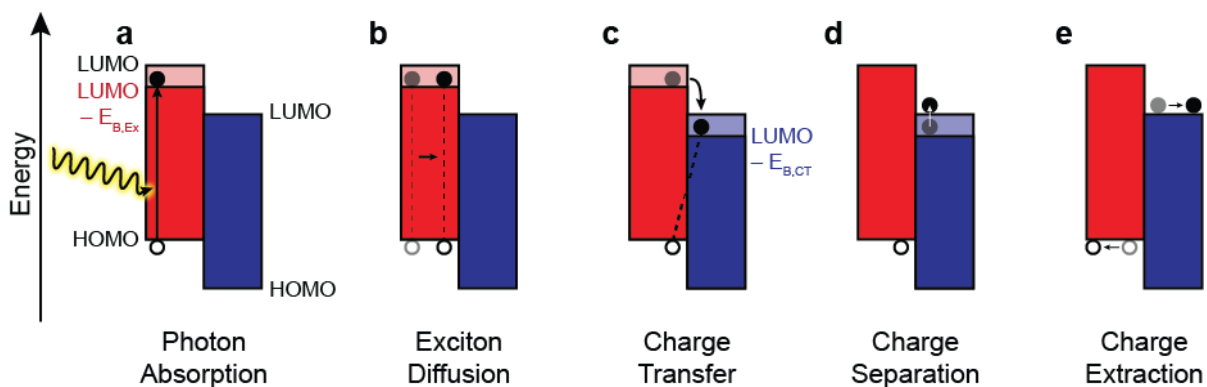


Figure 2.6. Schematic of organic solar cell operation, with the electron donor depicted as red and the acceptor depicted as blue. (a) A photon is absorbed by a donor molecule, promoting an electron to an unoccupied orbital and leaving a hole in the HOMO. The electron is depicted as at a lower energy than the LUMO to account for the exciton binding energy. (b) Through a series of excited state transfer steps, the exciton diffuses through the donor. (c) Upon reaching the donor/acceptor interface, the promoted electron transfers to an acceptor molecule, forming a Coulombically-bound charge transfer state. $E_{B,CT}$ represents the binding energy. (d) Thermal energy dissociates the bound charges. (e) Through a series of one-electron transfer reactions, the charges diffuse through the donor/acceptor bulk and eventually leave the solar cell.

There are many concerns that limit the efficiency of a given solar cell, and the previously-described processes do not occur with 100% efficiency. As mentioned, excitons have a limited lifetime, which means that unless they are generated within around 10 nm of an interface, the energy absorbed in producing them is wasted. Therefore, the structure of the solar cell should be such that this is always the case. However, no material can absorb 100% of the photons that are incident upon it at thicknesses of that scale. Therefore, the active layer of the solar cell must be thick enough, on the order of 1000 nm, so that photons do not pass through unabsorbed. Initial experiments on heterojunction OPVs utilized a planar heterojunction structure (Figure 2.7a), wherein the donor and acceptor layers were deposited in separate layers.¹⁰⁶ With such a structure, any layer thicker than 10 nm does not contribute to charge generation, but the number of photons actually absorbed in that 10 nm slice are minimal, which greatly limits the efficiency. An ideal situation would utilize an ordered heterojunction structure (Figure 2.7c), where a jagged interface has been created such that no exciton is further than 10 nm away from it, while the thickness is still sufficient to allow most of the incident photons to be absorbed.¹⁰⁷ Unfortunately, fabrication of such a nanostructure is difficult. A compromise is the bulk heterojunction (Figure 2.7b), wherein the donor and acceptor are simply blended before solution casting, and phase separation allows for

the creation of distinct domains within the material.¹⁰⁸ While there is poor control over the nanostructure using this technique, it is far superior to a planar heterojunction in terms of performance, and significantly easier to implement than an ordered heterojunction. Therefore, the bulk heterojunction is the most commonly-utilized active-layer architecture for OPVs.

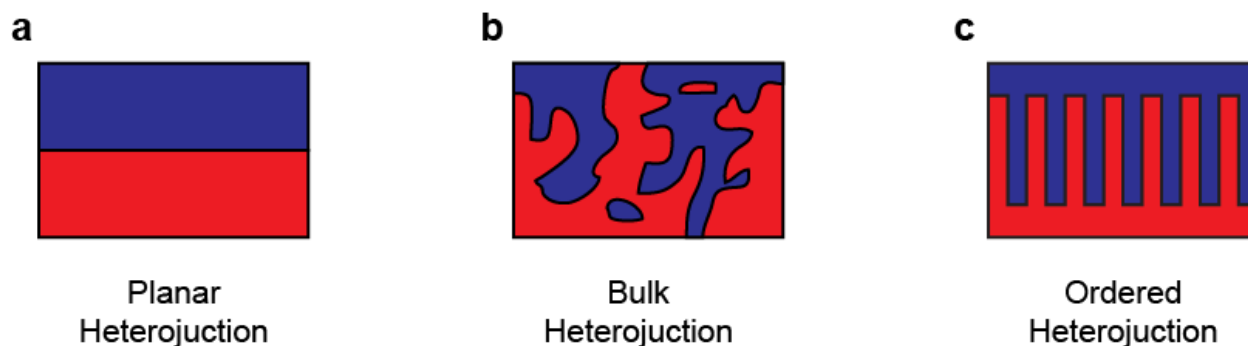


Figure 2.7. Schematic of (a) planar heterojunction, (b) bulk heterojunction, and (c) ordered heterojunction OPV active layer architectures.

One other factor that limits the efficiency is the fact that the exciton energy is a fixed value for a given material. To excite a molecule to a higher electronic state requires a photon with energy equal to the energy of that excited state. If the energy is less, then no absorption occurs. Therefore, any photons with energy less than the bandgap of the material are not absorbed. Photons with a greater energy may be absorbed by promoting the molecule to higher vibronic states. However, this energy is quickly dissipated as heat, meaning that photons with energy greater than the bandgap are partially wasted. Given the photon energy distribution of the solar spectrum, this consideration alone puts a limit of 44% on the efficiency of a material with an optimized bandgap of 1.1 eV.¹⁰⁹ One way to avoid this issue is to stack two solar cells on top of each other, each with different bandgaps. The high-bandgap material is placed on top, which allows a larger portion of the energy to be collected from high-energy photons, and the low-bandgap material on the bottom collects all the low-energy photons that pass through. This is referred to as a tandem solar cell. While the processing becomes significantly more complicated for such a structure, tandem OPVs have recorded some of the highest efficiencies in the literature.^{110,111}

Aside from the efficiency, OPV performance can be broken down into three parameters. These are the short-circuit current (J_{SC}), open-circuit voltage (V_{OC}), and fill factor (FF). J_{SC} is the current produced if the two contacts of the solar cell are shorted together, corresponding to one

electron produced per dissociated exciton. If the solar cell is operated as an open-circuit, charge will build up at both electrodes until a potential is generated that neutralizes the driving force for exciton dissociation. That potential is equal to V_{OC} . As the voltage drop across the external circuit varies from 0 to V_{OC} , the current will decrease gradually, and the extent to which it does is given by FF . Formally, it is defined as the power generated by the solar cell (current times voltage) at the point of maximal output, divided by the power obtained from multiplying J_{SC} by V_{OC} . A solar cell with FF equal to 1 would be one where the cell produces current equal to J_{SC} for any load with a voltage drop less than V_{OC} . This definition allows the efficiency (η) of the solar cell to be described as follows, where P_{in} is the power from the light incident on the solar cell.

$$\eta = \frac{J_{SC}V_{OC}FF}{P_{in}} \quad (2.4)$$

The most-studied donor-acceptor pair for OPVs is P3HT blended with a fullerene such as C₆₀ or phenyl-C₆₁-butyric acid methyl ester (PCBM), due to the reasonably high hole mobility of P3HT combined with the high density of LUMO states for fullerenes.^{18,112} However, the efficiency of this pair maximizes around 5%, which is too low for commercial applications. One limitation is the high bandgap of P3HT (2 eV), which has spurred the development of low-bandgap polymers. Use of both electron-rich and electron-poor moieties within the molecule, referred to as donor-acceptor materials, is a popular strategy. Many examples are shown in Figure 2.8. Materials can be further optimized through the use of multiple donors or acceptors, which synergistically combine the effects of multiple components. The simplest case is a ternary solar cell, which uses either two donors or two acceptors.^{113,114} This can be used to improve the absorbance range of the solar cell, improve charge transport, or improve morphology. One special case is that of the cascade solar cell, which uses a series of donors or acceptors with staggered HOMO or LUMO levels improve charge separation.^{115–117}

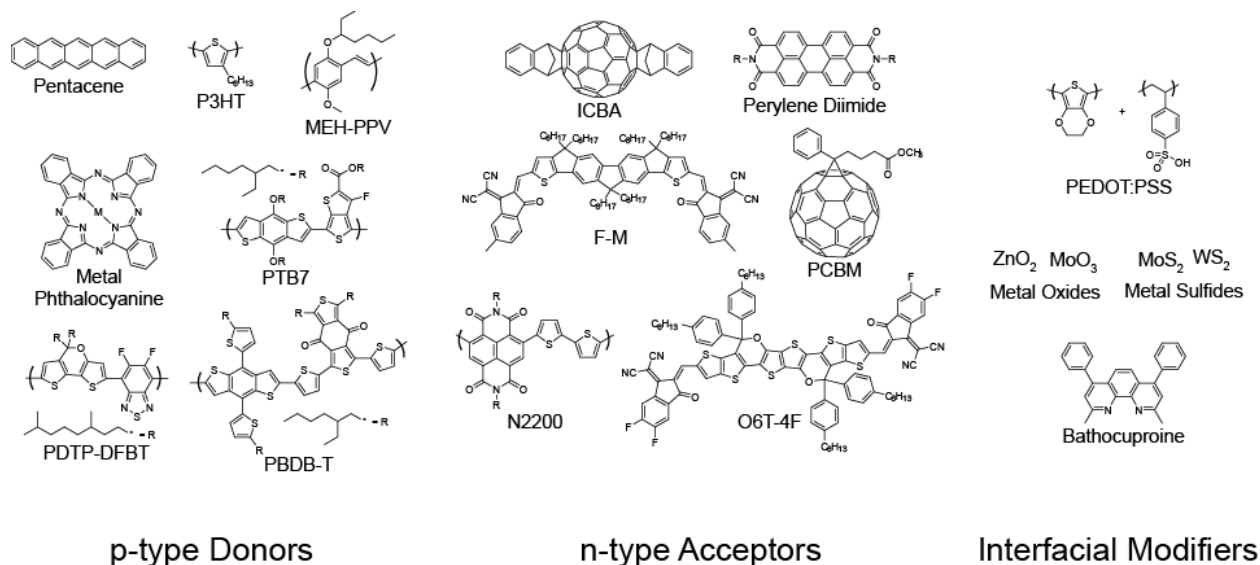


Figure 2.8. Examples of materials used in organic photovoltaics.

Also important for OPVs are their interfacial modifying layers. These are used to facilitate charge extraction from the solar cell, minimize recombination at the electrodes, improve device morphology and stability, and protect the organic layers during subsequent deposition steps. The ones listed in Figure 2.8 are ubiquitous, though much research has looked at developing more efficient interfacial modifying layers to bring about incremental improvements in existing active layer technologies.⁷⁶

2.4.2 Organic Light-Emitting Diodes (OLEDs)

In contrast to the other applications, organic light-emitting diodes (OLEDs) are one area where the performance of organic materials currently exceeds their inorganic counterparts, and where the specific technology outperforms comparable ones.^{13,14,118} Thus, they represent the most commercially-relevant application of organic electronics at this time. More specifically, OLED displays in televisions and smartphones offer significantly improved color and contrast as well as lower power consumption versus conventional backlit displays, all in a thinner profile, and while some promising inorganic LED technologies exist,^{119–121} OLEDs currently are the most mature LED display technology.

An LED can be thought of as the inverse of a solar cell from a simplistic perspective. Here, a current is driven across a semiconductor to inject charges that will subsequently generate photons.

In this case, both holes and electrons are injected at opposite ends of the material, then meet to form excitons that radiatively recombine to emit photons, in a process known as electroluminescence. In this case, aside from ensuring efficient charge injection and transport, the primary concern is to maximize the fluorescent and phosphorescent yield of the molecule. This key metric influences the development of OLED materials, and results in very different molecular designs than what are used for other applications.

One obstacle to achieving high fluorescent yields from OLED materials is spin statistics. When an exciton is formed, the quantum spin state of the two unpaired electrons is randomized, with a 75% chance of creating a triplet state (matching spins) and a 25% chance of creating a singlet state (unmatched spins). Due to the Pauli exclusion principle preventing two electrons with the same spin from occupying the same orbital, radiative recombination of the triplet excited state is forbidden. Thus, the efficiency is limited to 25% for most organic materials unless this issue can be circumvented.

One technique is through a process called spin-orbit coupling. For smaller atoms, electrons cannot readily change their spin as angular momentum must be conserved. However, for a larger atom with open d- or f-orbitals, the electron can change its orbital angular momentum to counteract the change in spin angular momentum. Therefore, most OLED emitters consist of organic ligands bound to a metal atom such as Iridium,¹²² which has strong spin-orbit coupling and therefore allows ready interconversion between singlet and triplet states. Similarly, metal-organic ligands often show phosphorescence, which is direct radiative recombination of a triplet excited state. These remove the issue of spin statistics; however, the use of rare metals adds considerable expense to the material. Therefore, one area of considerable research is producing metal-free electroluminescent materials that still manage to avoid the issue of spin statistics. Some techniques include triplet-triplet annihilation,¹²³ thermally-activated delayed fluorescence,¹²⁴ and doublet emission.^{125,126}

The simplest OLED structure consists of an emissive layer sandwiched between two electrodes. Such a design, however, leads to poor efficiency due to poor charge transport and non-radiative recombination. Therefore, typical designs will also include multiple interfacial modifying layers (Figure 2.9a). At the anode will be a hole injection layer (HIL) and hole transport layer (HTL) to facilitate charge injection from the electrode to the active layer. An analogous electron transport layer (ETL) is incorporated between the cathode and the emissive layer, along with a

small hole-blocking layer (HBL) with a HOMO energy that is far from vacuum to prevent holes from entering the ETL.⁷⁶ The emissive layer typically consists of a conductive host material that is doped with emitters, allowing the charge transport properties and luminescence to be decoupled.¹²⁷ Figure 2.9b shows examples of different materials used in the different layers.¹²⁸

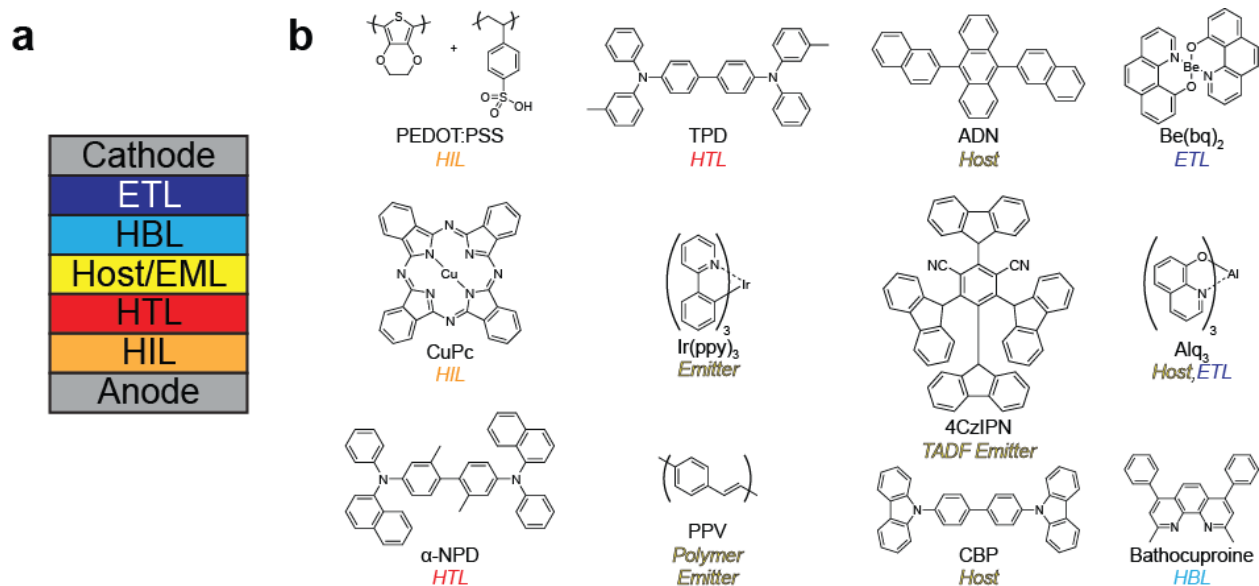


Figure 2.9. (a) Typical structure of an OLED device, showing the anode, hole injection layer (HIL), hole transport layer (HTL), emissive layer (EML) consisting of a host molecule doped with an emitter, hole blocking layer (HBL), electron transport layer (ETL), and cathode. Holes are injected from the anode, while electrons are injected from the cathode. (b) A far-from-exhaustive list of molecules used in in OLEDs. Abbreviations are poly(3,4-ethylenedioxythiophene):poly(styrenesulfonic acid) (PEDOT:PSS);¹²⁹ Copper Phthalocyanate (CuPc);¹³⁰ α -NPD;¹³¹ N,N'-bis(3-methylphenyl)-N,N'-diphenylbenzidine (TPD);^{131,132} fac tris(2-phenylpyridine) iridium (Ir(ppy)₃);¹³³ poly(phenylene vinylene) (PPV); 9,10-(2-naphthyl)anthracene (ADN);¹³⁴ 2,4,5,6-Tetra(9H-carbazol-9-yl)isophthalonitrile (4CzIPN);¹³⁵ 4,4'-di(N-carbazole)biphenyl (CBP);¹³⁶ bis(10-hydroxybenzo[h]quinolinato)beryllium (Be(bq)₂);¹³⁷ tris-(8-hydroxyquinolinato)aluminum (Alq₃);¹³⁸ and Bathocuproine (BCP).¹³⁹

2.4.3 Organic Thermoelectric Devices

When energy is transformed, a significant amount is wasted in the production of heat. While thermodynamics dictate that this is unavoidable, there is considerable interest in trying to recapture some of this thermal energy in a usable form. Thermoelectric devices allow thermal energy to be converted directly into electrical energy with no moving parts.¹⁴⁰ While such a

prospect is highly appealing, the cost efficiency of conventional thermoelectric materials is minimal. Therefore, the development of new materials is essential.

Thermoelectric devices exploit the Seebeck effect to generate electricity. A qualitative explanation is as follows. In a conductor or semiconductor with free charges, an increase in temperature will increase the kinetic energy of those charge carriers. If a region of the material is heated relative to the rest of the material, the increased kinetic energy will cause those charge carriers to move away more quickly, reducing the carrier density in that area. As the charge is no longer balanced, this will result in an electrical potential build-up that is proportional to the temperature difference (Figure 2.10a). If the two ends are joined with an ideal wire, then a current will flow. The sign of the voltage depends on that of the charge carriers. Electrons in a metal or n-doped material result in a positive $\Delta V/\Delta T$, while holes in a p-doped material show a negative $\Delta V/\Delta T$. Alternating p- and n-doped legs connected in series allow for a consistent voltage to be built up (Figure 2.10b).

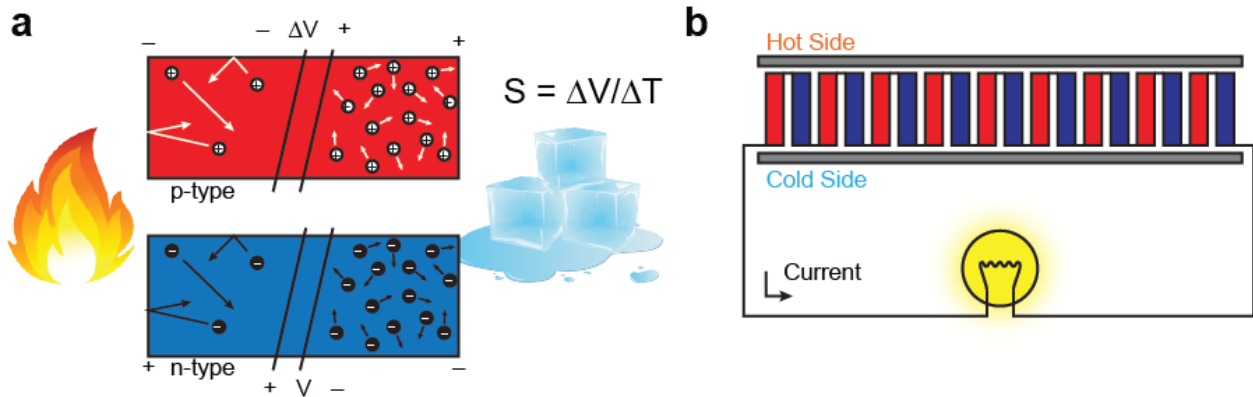


Figure 2.10. (a) Schematic depicting the Seebeck effect. In a p-type material, heating one side leads to increased thermal energy causing the holes to diffuse more rapidly, which lowers their density. Cooling the other side likewise leads to an increase in density. The buildup of charges increases the electrical potential at the cold side, generating a voltage. In an n-type material, the opposite sign of the charge carriers lead to a reversal of the voltage. (b) An appreciable voltage can be produced by linking multiple thermoelectric modules in series. As the p- and n-type materials produce opposite voltages, they can be connected at the hot or cold side and their voltages will add.

The figure of merit for a thermoelectric material is given by the following equation:

$$zT = \frac{S^2 \sigma}{\kappa} T \quad (2.5)$$

Here, S is the Seebeck coefficient, which is equal to $\Delta V/\Delta T$, σ is the electrical conductivity, κ is the thermal conductivity, and T is the average absolute temperature between the hot and cold sides. These parameters are not entirely independent, as tuning one often leads to changes in the others. For example, the conductivity can be increased through doping, but the increased charge carrier density leads to greater thermal conductivity, and the resulting shift in chemical potential of the carriers leads to a reduction in the Seebeck coefficient. Therefore, there is a considerable optimization process. While organic thermoelectric materials often show lower conductivity than their inorganic counterparts, one potential advantage is that organic materials have significantly lower thermal conductivities than the metals that are typically used.

All conjugated polymers show some degree of thermopower, but the current highest-performing p-type materials include PEDOT, polyacetylene, and polyaniline,^{140,141} with some reports indicating thermopower on par with that of bismuth telluride, the champion inorganic material. As with other organic electronic devices, high-performance n-type materials are less common, but the most common ones seen include fullerenes,¹⁴² perylene diimides,¹⁴³ naphthalene-diimide-based donor-acceptor polymers,^{144,145} and ladder polymers.¹⁰⁰ Composites with inorganic materials and carbon nanotubes are also utilized.^{146,147} While most thermoelectric applications make use of closed-shell conjugated polymers, radicals can be utilized for charge filtering to improve the Seebeck coefficient with minimal impact on conductivity.¹⁴⁸ Ultimately, thermoelectric generators are still very much an experimental technology, but organic electronic materials with their competitive performance offer a potential path towards commercial viability.

2.4.4 Organic Field-Effect Transistors (OFETs)

Of crucial importance to digital electronic devices is the transistor. This simple device makes possible every calculation and manipulation done by a computer. While OFETs differ from the other devices presented here in that they are not used for energy conversion, they are nevertheless critical for the implementation of organic materials in all but the most basic electronic applications.⁵³ A transistor is effectively a solid-state switch, where application of a voltage at one terminal of the device controls the amount of current that can flow between the other two terminals. Field-effect transistors accomplish this by using a semiconductor with low charge carrier density but high mobility placed against a thin insulating layer. Application of an electric potential across

the insulating layer attracts charge carriers to the interface between the semiconductor and insulator, which results in a significantly higher conductance at the interface (Figure 2.11).

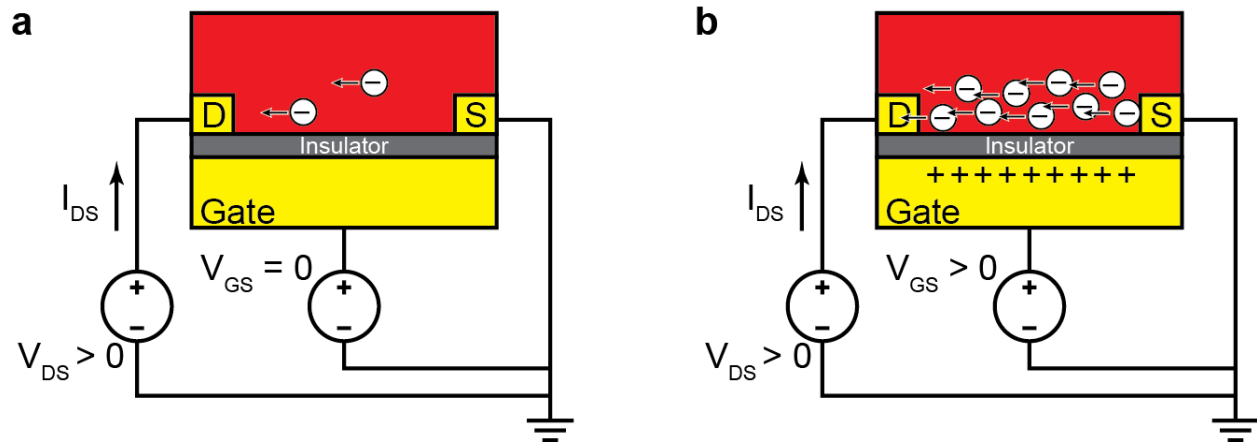


Figure 2.11. Schematic of field-effect transistor operation. (a) With no applied gate voltage (off), conductivity is low as only intrinsic charges are present between the source and drain. (b) An applied gate voltage attracts more charges to the channel, which greatly increases the conductivity.

A more quantitative description of the behavior is as follows.¹ As a FET is a three-terminal device, the source-drain current (I_{DS}) will depend on both the drain-source voltage (V_{DS}) and the gate-source voltage (V_{GS}). For an ideal FET with a perfect gate insulator, the gate-source current (I_{GS}) at steady-state is zero. At a constant value of V_{GS} , increasing V_{DS} will result in a linear increase in current for $V_{DS} \ll V_{GS}$, but as V_{DS} approaches V_{GS} in value, the slope will decrease and saturate when $V_{DS} = V_{GS}$. Past this point, the current will increase no further. This is due to the fact that the charge concentration is non-uniform along the channel. It will be proportional to V_{GS} at the source electrode and $V_{GS} - V_{DS}$, or the gate-drain voltage (V_{GD}) at the drain electrode. If $V_{DS} > V_{GS}$, the charge on the gate will be negative close to the drain electrode. Therefore, charge will effectively be pinched off at some point along the channel, which counteracts the effect of increased driving force and results in saturation. If V_{GS} is instead varied while V_{DS} is held constant, there will be a quadratic increase in current for $V_{GS} < V_{DS}$ due to the combined effects of increasing the carrier concentration and negating the pinch-off effect. For $V_{GS} > V_{DS}$, the increase in I_{DS} will be linear.

When I_{DS} is plotted against V_{DS} at a fixed V_{GS} , this is referred to as an output characteristic (Figure 2.12a). If V_{DS} is instead fixed with V_{GS} allowed to vary, this is referred to as a transfer characteristic (Figure 2.12b). The exact formula for an ideal FET is as follows.

$$I_{DS} = \begin{cases} 0 & \text{if } V_{GS} < 0 \\ \mu C_{ox} \frac{W}{L} \left(V_{GS} V_{DS} - \frac{V_{DS}^2}{2} \right) & \text{if } V_{DS} < V_{GS} \\ \mu C_{ox} \frac{W}{L} \left(\frac{V_{GS}^2}{2} \right) & \text{if } V_{DS} \geq V_{GS} \end{cases} \quad (2.6)$$

Here, μ is the charge carrier mobility, C_{ox} is the capacitance of the insulator per unit area, and W and L are the width and length of the channel, which in Figure 2.11 correspond to the distance into the page and the distance horizontally, respectively. All of these equations are for an n-type (i.e. electron transporting) FET. For a p-type FET, the same quantitative behavior is seen, except the signs are reversed. Thus, the results in Figure 2.12 still hold except with the graph rotated 180° into the third quadrant.

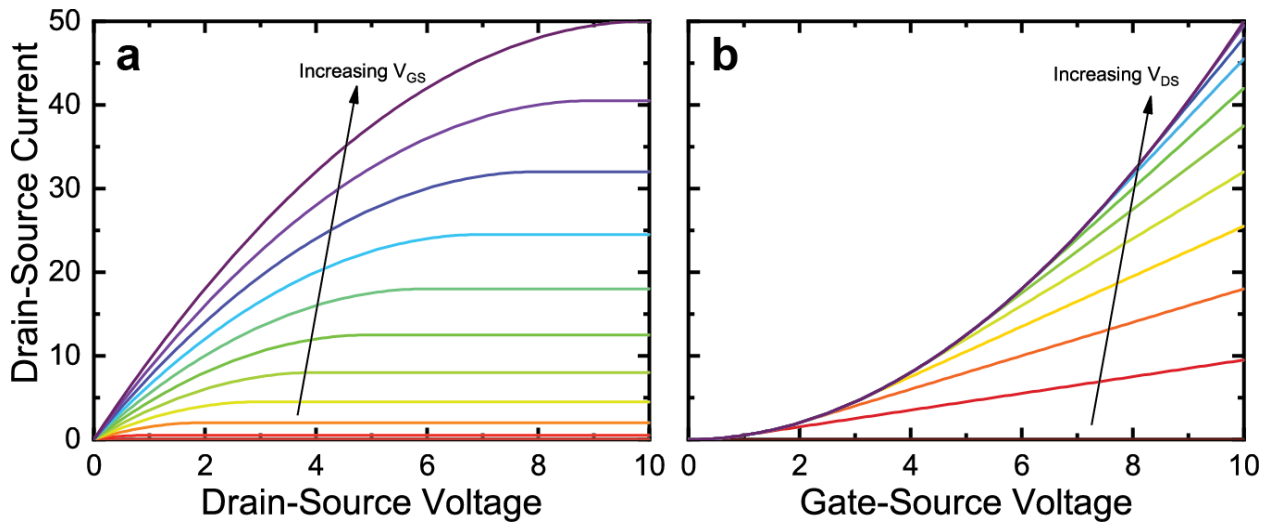


Figure 2.12. Sample characteristics for an ideal FET, showing (a) output characteristics, i.e. I_{DS} vs. V_{DS} , and (b) transfer characteristics, i.e. I_{DS} vs. V_{GS} .

The power of a transistor is achieved in a device design that pairs of p- and n-type FETs, referred to as a complimentary circuit, as logic elements for binary calculations can be constructed. An example is shown in Figure 2.13a, where both a p- and n-type FET in series with a common

gate connection are used. The relationship between input and output voltage for this circuit is shown in Figure 2.13b. What is seen here is an inverter, as V_{out} is low when V_{in} is high, and vice-versa. The approximately sigmoidal nature of the transfer function benefits a binary application, as the saturation at low and high voltages means that, for multiple inverters in series, the voltage at each stage will tend to get closer to the saturation values. Figure 2.13c shows a similar setup for a NAND gate, where V_{out} is low if both inputs are high, and high otherwise. This structure allows any binary logic circuit to be implemented. Thus, achieving complimentary FETs is essential for pursuing digital logic applications.

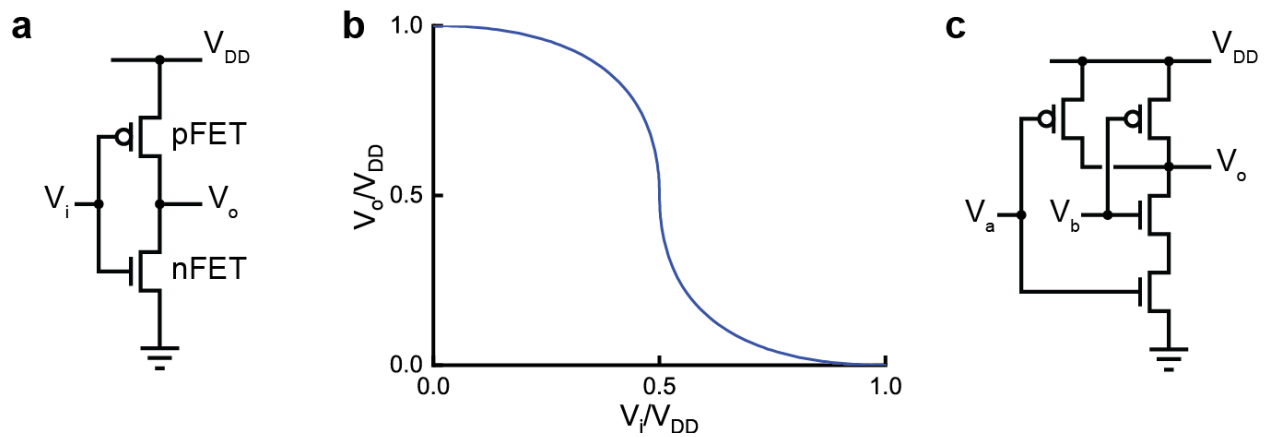


Figure 2.13. Examples of CMOS logic circuits. (a) Circuit diagram of a CMOS inverter, which produces a low voltage output if the voltage input is high, and vice-versa. (b) Relationship between V_i and V_o for an inverter consisting of ideal FETs with equal values of $\mu C_{ox} \frac{W}{L}$. (c) Circuit diagram of a CMOS NAND gate, where the output voltage is low only if both input voltages are high, and high otherwise. This serves as a universal building block for any digital circuit.

Equation 2.6 describes an ideal FET. Most practically implemented FETs, particularly OFETs, will show some degree of nonideal behavior. One assumption that is only an idealization is the fact that the current passed when $V_{GS} < 0$ is equal to zero. All materials will have some residual conductivity such that some current will flow as long as V_{DS} is nonzero. For the transistor to fulfill its role as a switch, it is desirable that this current be as low as possible. The relevant figure of merit is the on-off ratio, defined as the ratio between the current when $V_{GS} = V_{DS}$ and when $V_{GS} = 0$ for a fixed V_{DS} . MOSFETs and state-of-the-art OFETs show on-off ratios up to 10^9 . The second nonideality is that the FET will not turn on exactly when V_{GS} becomes positive. Rather, some threshold voltage (V_T) must be surpassed before current will begin to flow. A reasonable

approximation simply substitutes V_{GS} with $V_{GS} - V_T$ in Equation 2.6, which is illustrated in Figure 2.14a. This is accurate far above V_T , but the transition at V_T tends to be smoother than what Equation 2.6 would imply (see Figure 2.14b).

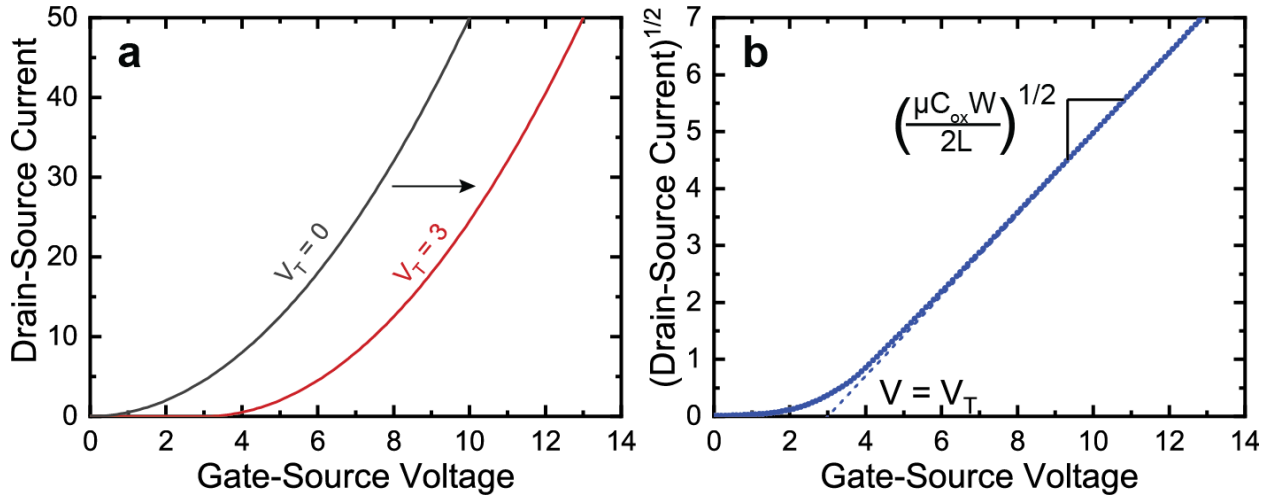


Figure 2.14. (a) A non-zero threshold voltage results in a horizontal displacement of the transfer curve, meaning that it turns on at higher voltages. (b) Extracting mobility and threshold voltage from a plot of $\sqrt{I_{DS}}$ vs V_{GS} . Here, the slope is proportional to the mobility, and the x-intercept is equal to the threshold voltage. Note that a smooth transition below V_T is illustrated.

Extraction of these parameters, as well as the mobility (μ), can be done by appropriate fitting of the transfer characteristics. The on-off ratio can simply be found by reading the current at the appropriate values of V_{GS} . To fit μ and V_T requires linearizing Equation 2.6. Substituting $V_{GS} - V_T$ for V_{GS} in the equation for the saturated regime and taking the square root of both sides yields the following.

$$\sqrt{I_{DS}} = \sqrt{\mu \frac{C_{ox} W}{2L}} (V_{GS} - V_T) \quad (2.7)$$

Fitting the data in this form with a straight line will yield μ and V_T from the slope and x-intercept, respectively, as seen in Figure 2.14b. Data gathered in the linear regime can also be fit in a similar manner. Typically for OFETs, however, the mobility is not constant with V_{GS} , and contact resistance effects can increase the perceived variability.^{149,150} Additionally, hysteresis is often seen in the transfer characteristics when the voltage is swept in both directions. Thus, some judgement must be exercised in fitting the parameters. Ultimately, the primary targets when synthesizing

high-performance materials are to increase mobility (which allows for lower-voltage operation) and to reduce the off current (which reduces power dissipation in the off state).

Materials used for OFETs include many of those also used for OPVs (Figure 2.8).¹⁵¹ Thiophene-containing materials such as oligothiophenes¹⁵² and P3HT¹⁵³ are widely utilized, as well as more complex thiophene structures such as poly(2,5-bis(3-alkylthiophen-2-yl)thieno[3,2-b]thiophene) (pBTTT).¹⁵⁴ Acenes such as pentacene^{155,156} and rubrene¹⁵⁷ are common, particularly for single-crystal studies, as are soluble derivatives such as triisopropylsilyl (TIPS)-Pentacene.¹⁵⁸ Benzothieno[3,2-b]benzothiophene (BTBT) derivatives offer some of the highest mobilities recorded in the literature.^{159,160} n-Type materials include fullerenes,^{161–164} naphthalene and parylene diimides,^{165–168} tetracyanoquinodimethane (TCNQ),¹⁶⁹ and fluorinated derivatives of p-type materials.⁵⁷ The gap in performance between polymers and small molecules was very significant for much of the history of OFETs, due to the impeded crystallinity of the polymers. As of recently, however, the mobilities of polymers and solution-processed small molecules have caught up with those of crystalline small molecules, an important milestone in achieving both high performance and low processing cost.¹⁷⁰

A brief mention must also be made of organic electrochemical transistors (OECTs).¹⁷¹ These consist of a conducting polymer immersed in an electrolyte solution, where the carrier density in the channel is modulated through electrochemical oxidation/reduction of the conductive polymer upon application of a gate voltage. As ions must migrate through the material, switching is slower than for an OFET. However, the main advantage is that the current can be modulated to an even greater degree than for an OFET. The relevant figure of merit is the transconductance (g_T), defined as the slope of the transfer characteristic.

$$g_T = \frac{\partial I_D}{\partial V_G} \quad (2.8)$$

As the transfer characteristic is nonlinear, the maximal value of transconductance is typically used to characterize a transistor. For an OECT, the transconductance is several orders of magnitude higher than for an OFET. The reason for this higher transconductance is the increased capacitance. For an OFET, charge accumulates only at the interface between the gate and the channel. In other words, it occurs only on the surface. However, for an OECT, as the electrolyte permeates the entire channel, charge is accumulated throughout the bulk material. This makes them ideally suited for

sensing applications due to the much greater sensitivity of the measured current to changes in the gate voltage.

2.5 References

- (1) Pierret, R. F. *Semiconductor Device Fundamentals*; Pearson, 1996.
- (2) Menard, E.; Lee, K. J.; Khang, D. Y.; Nuzzo, R. G.; Rogers, J. A. *Appl. Phys. Lett.* **2004**, *84* (26), 5398–5400.
- (3) Yang, Y.; Wudl, F. *Adv. Mater.* **2009**, *21* (14–15), 1401–1403.
- (4) Meller, G.; Grasser, T. *Organic Electronics*; Springer: Heidelberg/New York, 2010.
- (5) Li, G.; Zhu, R.; Yang, Y. *Nat. Photonics* **2012**, *6* (February), 153–161.
- (6) Skotheim, T.; Reynolds, J. *Handbook of Conducting Polymers*, 3rd ed.; CRC Press, 2007.
- (7) Shirakawa, H.; Louis, E. J.; MacDiarmid, A. G.; Chiang, C. K.; Heeger, A. J. *J. Chem. Soc. Chem. Commun.* **1977**, No. 16, 578–580.
- (8) Heeger, A. J.; MacDiarmid, A. G.; Shirakawa, H. *Stock. Sweden R. Swedish Acad. Sci.* **2000**, 1–16.
- (9) Søndergaard, R. R.; Hösel, M.; Krebs, F. C. *J. Polym. Sci. B Polym. Phys.* **2013**, *51* (1), 16–34.
- (10) de Gans, B.-J.; Duineveld, P. C.; Schubert, U. S. *Adv. Mater.* **2004**, *16* (3), 203–213.
- (11) Savagatrup, S.; Printz, A. D.; O'Connor, T. F.; Zaretski, A. V; Lipomi, D. J. *Chem. Mater.* **2014**, *26* (10), 3028–3041.
- (12) Nielsen, T. D.; Cruickshank, C.; Foged, S.; Thorsen, J.; Krebs, F. C. *Sol. Energy Mater. Sol. Cells* **2010**, *94* (10), 1553–1571.
- (13) Hayase, H. OLED Display Market Tracker - Q1 2016 - IHS Technology <https://technology.ihs.com/572845/oled-display-market-tracker-q1-2016> (accessed Sep 30, 2016).
- (14) OLED introduction and basic OLED information | OLED-Info <https://www.oled-info.com/oled-introduction> (accessed Jun 11, 2020).
- (15) The Flexible Solar Film from Heliatek - Heliatek - The future is light <http://www.heliatek.com/en/heliafilm> (accessed Sep 30, 2016).
- (16) Forrest, S. R. *Nature* **2004**, *428* (6986), 911–918.
- (17) Boudouris, B. W. *Curr. Opin. Chem. Eng.* **2013**, *2* (3), 294–301.
- (18) Son, H. J.; He, F.; Carsten, B.; Yu, L. *J. Mater. Chem.* **2011**, *21* (47), 18934–18945.
- (19) Zhou, H.; Yang, L.; You, W. *Macromolecules* **2012**, *45*, 607–632.
- (20) Savagatrup, S.; Printz, A. D.; Rodriguez, D.; Lipomi, D. J. *Macromolecules* **2014**, *47* (6), 1981–1992.
- (21) Tomlinson, E. P.; Hay, M. E.; Boudouris, B. W. *Macromolecules* **2014**, *47* (18), 6145–6158.
- (22) Wingate, A. J.; Boudouris, B. W. *J. Polym. Sci. A Polym. Chem.* **2016**, *54*, 1875–1894.
- (23) Oyaizu, K.; Nishide, H. *Adv. Mater.* **2009**, *21* (22), 2339–2344.
- (24) Joo, Y.; Agarkar, V.; Sung, S. H.; Savoie, B. M.; Boudouris, B. W. *Science* **2018**, *359* (6382), 1391–1395.
- (25) Rostro, L.; Galicia, L.; Boudouris, B. W. *J. Polym. Sci. B Polym. Phys.* **2015**, *53* (5), 311–316.
- (26) Zheng, L.; Mukherjee, S.; Wang, K.; Hay, M. E.; Boudouris, B. W.; Gong, X. *J. Mater. Chem. A* **2017**, *5*, 23831–23839.

- (27) Sung, S. H.; Bajaj, N.; Rhoads, J. F.; Chiu, G. T.; Boudouris, B. W. *Org. Electron.* **2016**, *37*, 148–154.
- (28) He, J.; Mukherjee, S.; Zhu, X.; You, L.; Boudouris, B. W.; Mei, J. *ACS Appl. Mater. Interfaces* **2018**, *10* (22), 18956–18963.
- (29) Li, F.; Zhang, Y.; Kwon, S. R.; Lutkenhaus, J. L. *ACS Macro Lett.* **2016**, *5*, 337–341.
- (30) Casado, N.; Hernández, G.; Veloso, A.; Devaraj, S.; Mecerreyes, D.; Armand, M. *ACS Macro Lett.* **2016**, *5*, 59–64.
- (31) Li, F.; Gore, D. N.; Wang, S.; Lutkenhaus, J. L. *Angew. Chem. Int. Ed.* **2017**, *56*, 9856–9859.
- (32) Zhang, Y.; Park, A. M.; McMillan, S. R.; Harmon, N. J.; Flatté, M. E.; Fuchs, G. D.; Ober, C. K. *Chem. Mater.* **2018**, *30* (14), 4799–4807.
- (33) Schwartz, P. O.; Pejic, M.; Wachtler, M.; Bäuerle, P. *Synth. Met.* **2018**, *243* (January), 51–57.
- (34) Wang, P.; Lin, S.; Lin, Z.; Peeks, M. D.; Van Voorhis, T.; Swager, T. M. *J. Am. Chem. Soc.* **2018**, *140* (34), 10881–10889.
- (35) Li, F.; Wang, S.; Zhang, Y.; Lutkenhaus, J. L. *Chem. Mater.* **2018**, *30* (15), 5169–5174.
- (36) Xie, Y.; Zhang, K.; Monteiro, M. J.; Jia, Z. *ACS Appl. Mater. Interfaces* **2019**, *11* (7), 7096–7103.
- (37) Kawanaka, Y.; Shimizu, A.; Shinada, T.; Tanaka, R.; Teki, Y. *Angew. Chem. Int. Ed.* **2013**, *52* (26), 6643–6647.
- (38) Ito, A.; Shimizu, A.; Kishida, N.; Kawanaka, Y.; Kosumi, D.; Hashimoto, H.; Teki, Y. *Angew. Chem. Int. Ed.* **2014**, *53* (26), 6715–6719.
- (39) Chernick, E. T.; Casillas, R.; Zirzmeier, J.; Gardner, D. M.; Gruber, M.; Kropp, H.; Meyer, K.; Wasielewski, M. R.; Guldi, D. M.; Tykwinski, R. R. *J. Am. Chem. Soc.* **2015**, *137*, 857–863.
- (40) Ito, A.; Hinoshita, M.; Kato, K.; Teki, Y. *Chem. Lett.* **2016**, *45* (11), 1324–1326.
- (41) Shimizu, A.; Ito, A.; Teki, Y. *Chem. Commun.* **2016**, *52* (14), 2889–2892.
- (42) Huang, Y.; Egap, E. *Polym. J.* **2018**, *50* (8), 603–614.
- (43) Abe, M. *Chem. Rev.* **2013**, *113* (9), 7011–7088.
- (44) Rajca, A. **2002**, No. 21, 4834–4841.
- (45) Gallagher, N. M.; Olankitwanit, A.; Rajca, A. *J. Org. Chem.* **2015**, *80*, 1291–1298.
- (46) Joo, Y.; Huang, L.; Eedugurala, N.; London, A. E.; Kumar, A.; Wong, B. M.; Boudouris, B. W.; Azoulay, J. D. *Macromolecules* **2018**, *51* (10), 3886–3894.
- (47) London, A. E.; Chen, H.; Sabuj, M. A.; Tropp, J.; Saghayezhian, M.; Eedugurala, N.; Zhang, B. A.; Liu, Y.; Gu, X.; Wong, B. M.; Rai, N.; Bowman, M. K.; Azoulay, J. D. *Sci. Adv.* **2019**, *5*, eaav2336.
- (48) Merli, P. G.; Missiroli, G. F.; Pozzi, G. *Am. J. Phys.* **1976**, *44* (3), 306–307.
- (49) Hunter, C. A.; Sanders, J. K. M. *J. Am. Chem. Soc.* **1990**, *112* (14), 5525–5534.
- (50) Pierret, R. F. *Advanced Semiconductor Fundamentals*, 2nd ed.; Pearson, 2003.
- (51) Kittel, C. *Introduction to Solid-State Physics*, 8th ed.; Wiley: Hoboken, NJ, 2005.
- (52) Karl, N.; Marktanner, J.; Stehle, R.; Warta, W. *Synth. Met.* **1991**, *41–43*, 2473–2481.
- (53) Bao, Z.; Locklin, J. *Organic Field-Effect Transistors*; CRC Press: Boca Raton, FL, 2007.
- (54) Duke, C. B.; Schein, L. B. *Phys. Today* **1980**, *33* (2), 42–48.
- (55) Savoie, B. M.; Jackson, N. E.; Marks, T. J.; Ratner, M. A. *Phys. Chem. Chem. Phys.* **2013**, *15* (13), 4538–4547.

- (56) de Leeuw, D. M.; Simenon, M. M. J.; Brown, A. R.; Einerhand, R. E. F. *Synth. Met.* **1997**, *87*, 53–59.
- (57) Newman, C. R.; Frisbie, C. D.; Da Silva Filho, D. A.; Brédas, J. L.; Ewbank, P. C.; Mann, K. R. *Chem. Mater.* **2004**, *16* (23), 4436–4451.
- (58) Anthony, J. E.; Facchetti, A.; Heeney, M.; Marder, S. R.; Zhan, X. *Adv. Mater.* **2010**, *22* (34), 3876–3892.
- (59) Wang, Y.; Hasegawa, T.; Matsumoto, H.; Michinobu, T. *J. Am. Chem. Soc.* **2019**, *141* (8), 3566–3575.
- (60) Hong, S. Y.; Kertesz, M.; Lee, Y. S.; Kim, O. K. *Macromolecules* **1992**, *25* (20), 5424–5429.
- (61) Babel, A.; Jenekhe, S. A. *J. Am. Chem. Soc.* **2003**, *125* (45), 13656–13657.
- (62) Lüssem, B.; Keum, C.-M.; Kasemann, D.; Naab, B.; Bao, Z.; Leo, K. *Chem. Rev.* **2016**, *acs.chemrev.6b00329*.
- (63) Hatchett, D. W.; Josowicz, M.; Janata, J. *J. Phys. Chem. B* **1999**, *103* (50), 10992–10998.
- (64) Sun, K.; Zhang, S.; Li, P.; Xia, Y.; Zhang, X.; Du, D.; Isikgor, F. H.; Ouyang, J. *J. Mater. Sci. Mater. Electron.* **2015**, *26* (7), 4438–4462.
- (65) Mityashin, A.; Olivier, Y.; Van Regemorter, T.; Rolin, C.; Verlaak, S.; Martinelli, N. G.; Beljonne, D.; Cornil, J.; Genoe, J.; Heremans, P. *Adv. Mater.* **2012**, *24* (12), 1535–1539.
- (66) Duong, D. T.; Wang, C.; Antono, E.; Toney, M. F.; Salleo, A. *Org. Electron. physics, Mater. Appl.* **2013**, *14* (5), 1330–1336.
- (67) Pingel, P.; Neher, D. *Phys. Rev. B - Condens. Matter Mater. Phys.* **2013**, *87* (11), 1–9.
- (68) Méndez, H.; Heimel, G.; Winkler, S.; Frisch, J.; Opitz, A.; Sauer, K.; Wegner, B.; Oehzelt, M.; Röthel, C.; Duhm, S.; Töbrens, D.; Koch, N.; Salzmänn, I. *Nat. Commun.* **2015**, *6*, 1–11.
- (69) Salzmänn, I.; Heimel, G.; Duhm, S.; Oehzelt, M.; Pingel, P.; George, B. M.; Schnegg, A.; Lips, K.; Blum, R. P.; Vollmer, A.; Koch, N. *Phys. Rev. Lett.* **2012**, *108* (3), 1–5.
- (70) Olthof, S.; Mehraeen, S.; Mohapatra, S. K.; Barlow, S.; Coropceanu, V.; Brédas, J. L.; Marder, S. R.; Kahn, A. *Phys. Rev. Lett.* **2012**, *109* (17), 1–5.
- (71) Kim, G. H.; Shao, L.; Zhang, K.; Pipe, K. P. *Nat. Mater.* **2013**, *12* (8), 719–723.
- (72) Ahonen, H. J.; Lukkari, J.; Kankare, J. *Macromolecules* **2000**, *33* (18), 6787–6793.
- (73) Al-Shadeedi, A.; Liu, S.; Keum, C. M.; Kasemann, D.; Hoßbach, C.; Bartha, J.; Bunge, S. D.; Lüssem, B. *ACS Appl. Mater. Interfaces* **2016**, *8* (47), 32432–32439.
- (74) Cahen, D.; Kahn, A.; Umbach, E. *Mater. Today* **2005**, *8* (7), 32–41.
- (75) Ishii, H.; Sugiyama, K.; Ito, E.; Seki, K. *Adv. Mater.* **1999**, *11*, 605–625.
- (76) Ma, H.; Yip, H.-L.; Huang, F.; Jen, A. K.-Y. *Adv. Funct. Mater.* **2010**, *20* (9), 1371–1388.
- (77) Ozawa, K. In *Compendium of Surface and Interface Analysis*; The Surface Science Society of Japan, Ed.; Springer Nature Singapore Pte Ltd.: Tokyo, Japan, 2018; pp 783–790.
- (78) Kanai, K. In *Compendium of Surface and Interface Analysis*; The Surface Science Society of Japan, Ed.; Springer Nature Singapore Pte Ltd.: Tokyo, Japan, 2018; pp 307–312.
- (79) Elgrishi, N.; Hammon, K.; McCarthy, B.; Eisenhart, T.; Dempsey, J. *J. Chem. Educ.* **2017**.
- (80) D’Andrade, B. W.; Datta, S.; Forrest, S. R.; Djurovich, P.; Polikarpov, E.; Thompson, M. E. *Org. Electron. physics, Mater. Appl.* **2005**, *6* (1), 11–20.
- (81) Mott, N. F. *Philos. Mag.* **1969**, *19* (160), 835–852.
- (82) Hill, R. M. *Phys. Status Solidi A* **1976**, *34*, 601–613.
- (83) Kaiser, A. B. *Reports Prog. Phys.* **2001**, *64*, 1–49.
- (84) Sukegawa, T.; Kai, A.; Oyaizu, K.; Nishide, H. *Macromolecules* **2013**, 1361–1367.

- (85) Baradwaj, A. G.; Wong, S. H.; Laster, J. S.; Wingate, A. J.; Hay, M. E.; Boudouris, B. W. *Macromolecules* **2016**, *49* (13), 4784–4791.
- (86) Baradwaj, A. G.; Rostro, L.; Alam, M. A.; Boudouris, B. W. *Appl. Phys. Lett.* **2014**, *104*, 213306.
- (87) Hay, M. E.; Wong, S. H.; Mukherjee, S.; Boudouris, B. W. *J. Polym. Sci. Part B* **2017**, *55*, 1516–1525.
- (88) Kemper, T. W.; Larsen, R. E.; Gennett, T. *J. Phys. Chem. C* **2014**, *118*, 17213–17220.
- (89) Rostro, L.; Wong, S. H.; Boudouris, B. W. *Macromolecules* **2014**, *47* (11), 3713–3719.
- (90) Chan, H.; Wang, Y.; Boudouris, B. W. *Thin Solid Films* **2015**, *577*, 56–61.
- (91) Friend, R. H.; Gymer, R. W.; Holmes, A. B.; Burroughes, J. H.; Marks, R. N.; Taliani, C.; Bradley, D. D. C.; Santos, D. A. Dos; Bredas, J. L.; Logdlund, M.; Salaneck, W. R. *Nature* **1999**, *397* (6715), 121–128.
- (92) Vezie, M. S.; Few, S.; Meager, I.; Pieridou, G.; Dörling, B.; Ashraf, R. S.; Goñi, A. R.; Bronstein, H.; McCulloch, I.; Hayes, S. C.; Campoy-Quiles, M.; Nelson, J. *Nat. Mater.* **2016**, *15* (7), 746–753.
- (93) Lakowicz, J. R. *Principles of Fluorescence Spectroscopy*, 3rd ed.; Springer: New York, 2010.
- (94) Förster, T. *Radiat. Res. Suppl.* **1960**, *2*, 326–339.
- (95) Dexter, D. L. *J. Chem. Phys.* **1953**, *21* (5), 836–850.
- (96) Niklas, J.; Poluektov, O. G. *Adv. Energy Mater.* **2017**, *7*, 1602226.
- (97) Forbes, M. D. E.; Jarocho, L. E.; Sim, S.; Tarasov, V. F. In *Advances in Physical Organic Chemistry, Volume 47*; 2013; pp 1–83.
- (98) Dou, L.; You, J.; Hong, Z.; Xu, Z.; Li, G.; Street, R. A.; Yang, Y. *Adv. Mater.* **2013**, *25* (46), 6642–6671.
- (99) Romanyuk, Y. E.; Hagendorfer, H.; Stücheli, P.; Fuchs, P.; Uhl, A. R.; Sutter-Fella, C. M.; Werner, M.; Haass, S.; Stüchelberger, J.; Broussillou, C.; Grand, P. P.; Bermudez, V.; Tiwari, A. N. *Adv. Funct. Mater.* **2015**, *25* (1), 12–27.
- (100) Wang, S.; Sun, H.; Ail, U.; Vagin, M.; Persson, P. O. Å.; Andreasen, J. W.; Thiel, W.; Berggren, M.; Crispin, X.; Fazzi, D.; Fabiano, S. *Adv. Mater.* **2016**, *28*, 10764–10771.
- (101) Habibi, M.; Zabihi, F.; Ahmadian-Yazdi, M. R.; Eslamian, M. *Renew. Sustain. Energy Rev.* **2016**, *62*, 1012–1031.
- (102) Shi, E.; Gao, Y.; Finkenauer, B. P.; Akriti; Coffey, A. H.; Dou, L. *Chem. Soc. Rev.* **2018**, *47* (16), 6046–6072.
- (103) Miskin, C. K.; Deshmukh, S. D.; Vasiraju, V.; Bock, K.; Mittal, G.; Dubois-Camacho, A.; Vaddiraju, S.; Agrawal, R. *ACS Appl. Nano Mater.* **2019**, *2* (3), 1242–1252.
- (104) Brabec, C.; Dyakonov, V.; Scherf, U. *Organic Photovoltaics*; Wiley-VCH, 2008.
- (105) Cook, S.; Furube, A.; Katoh, R. *Energy Environ. Sci.* **2008**, *1* (2), 294.
- (106) Tang, C. W. *Appl. Phys. Lett.* **1986**, *48* (2), 183–185.
- (107) Kim, J.; Kim, K.; Hwan Ko, S.; Kim, W. *Sol. Energy Mater. Sol. Cells* **2011**, *95* (11), 3021–3024.
- (108) Yu, G.; Gao, J.; Hummelen, J. C.; Wudl, F.; Heeger, A. J. *Science* **1995**, *270* (5243), 1789.
- (109) Shockley, W.; Queisser, H. J. *J. Appl. Phys.* **1961**, *32* (3), 510–519.
- (110) Meng, L.; Zhang, Y.; Wan, X.; Li, C.; Zhang, X.; Wang, Y.; Ke, X.; Xiao, Z.; Ding, L.; Xia, R.; Yip, H.; Cao, Y.; Chen, Y. *Science* **2018**, *2612*, 1–10.
- (111) Di, D.; Rasi, C.; Janssen, R. A. J. *Adv. Mater.* **2018**, 1806499.
- (112) Dang, M. T.; Hirsch, L.; Wantz, G. *Adv. Mater.* **2011**, *23* (31), 3597–3602.

- (113) Lu, H.; Xu, X.; Bo, Z. *Sci. China Mater.* **2016**, *59* (6), 444–458.
- (114) Xiao, Z.; Jia, X.; Ding, L. *Sci. Bull.* **2017**, *62* (23), 1562–1564.
- (115) Cnops, K.; Rand, B. P.; Cheyns, D.; Heremans, P. *Appl. Phys. Lett.* **2012**, *101*, 143301.
- (116) Huang, J.-S.; Goh, T.; Li, X.; Sfeir, M. Y.; Bielinski, E. A.; Tomasulo, S.; Lee, M. L.; Hazari, N.; Taylor, A. D. *Nat. Photonics* **2013**, *7* (6), 479–485.
- (117) Goh, T.; Huang, J.-S.; Bartolome, B.; Sfeir, M. Y.; Vaisman, M.; Lee, M. L.; Taylor, A. D. *J. Mater. Chem. A* **2015**, *3* (36), 18611–18621.
- (118) Ma, R. In *Handbook of Visual Display Technology*; Chen, J., Cranton, W., Fihn, M., Eds.; Springer, 2016; pp 1799–1820.
- (119) Dai, X.; Zhang, Z.; Jin, Y.; Niu, Y.; Cao, H.; Liang, X.; Chen, L.; Wang, J.; Peng, X. *Nature* **2014**, *515* (7525), 96–99.
- (120) Jin, S. X.; Li, J.; Li, J. Z.; Lin, J. Y.; Jiang, H. X. *Appl. Phys. Lett.* **2000**, *76* (5), 631–633.
- (121) MicroLED introduction and basic microLED information | MicroLED-Info <https://www.microled-info.com/introduction> (accessed Jun 11, 2020).
- (122) Lamansky, S.; Djurovich, P.; Murphy, D.; Abdel-Razzaq, F.; Lee, H. E.; Adachi, C.; Burrows, P. E.; Forrest, S. R.; Thompson, M. E. *J. Am. Chem. Soc.* **2001**, *123* (18), 4304–4312.
- (123) Hu, J. Y.; Pu, Y. J.; Satoh, F.; Kawata, S.; Katagiri, H.; Sasabe, H.; Kido, J. *Adv. Funct. Mater.* **2014**, *24* (14), 2064–2071.
- (124) Adachi, C. *Jpn. J. Appl. Phys.* **2014**, *53*, 060101.
- (125) Peng, Q.; Obolda, A.; Zhang, M.; Li, F. *Angew. Chem. Int. Ed.* **2015**, *54*, 7091–7095.
- (126) Neier, E.; Arias, R.; Rady, N.; Venkatesan, S.; Hudnall, T. W.; Zakhidov, A. *Org. Electron.* **2017**, *44*, 126–131.
- (127) Tang, C. W.; Vanslyke, S. A.; Chen, C. H. *J. Appl. Phys.* **1989**, *65* (9), 3610–3616.
- (128) Jou, J.-H.; Kumar, S.; Agrawal, A.; Li, T.-H.; Sahoo, S. *J. Mater. Chem. C* **2015**, *3*, 2974–3002.
- (129) Groenendaal, L.; Jonas, F.; Freitag, D.; Pielartzik, H.; Reynolds, J. R. *Adv. Mater.* **2000**, *12* (7), 481–494.
- (130) Van Slyke, S. A.; Chen, C. H.; Tang, C. W. *Appl. Phys. Lett.* **1996**, *69* (15), 2160–2162.
- (131) Goushi, K.; Kwong, R.; Brown, J. J.; Sasabe, H.; Adachi, C. *J. Appl. Phys.* **2004**, *95* (12), 7798–7802.
- (132) Strohriegel, P.; Grazulevicius, J. V. *Adv. Mater.* **2002**, *14* (20), 1439–1452.
- (133) Baldo, M. A.; Thompson, M. E.; Forrest, S. R. *Nature* **2000**, *403* (6771), 750–753.
- (134) Shi, J.; Tang, C. W. *Appl. Phys. Lett.* **2002**, *80* (17), 3201–3203.
- (135) Uoyama, H.; Goushi, K.; Shizu, K.; Nomura, H.; Adachi, C. *Nature* **2012**, *492* (7428), 234–238.
- (136) Kozlov, V. G.; Parthasarathy, G.; Burrows, P. E.; Forrest, S. R.; You, Y.; Thompson, M. E. *Appl. Phys. Lett.* **1998**, *72* (2), 144–146.
- (137) Fukagawa, H.; Shimizu, T.; Hanashima, H.; Osada, Y.; Suzuki, M.; Fujikake, H. *Adv. Mater.* **2012**, *24* (37), 5099–5103.
- (138) Kepler, R. G.; Beeson, P. M.; Jacobs, S. J.; Anderson, R. A.; Sinclair, M. B.; Valencia, V. S.; Cahill, P. A. *Appl. Phys. Lett.* **1995**, *66* (26), 3618–3620.
- (139) O’Brien, D. F.; Baldo, M. A.; Thompson, M. E.; Forrest, S. R. *Appl. Phys. Lett.* **1999**, *74* (3), 442–444.

- (140) Beretta, D.; Neophytou, N.; Hodges, J. M.; Kanatzidis, M. G.; Narducci, D.; Martin-Gonzalez, M.; Beekman, M.; Balke, B.; Cerretti, G.; Tremel, W.; Zevalkink, A.; Hofmann, A. I.; Müller, C.; Dörling, B.; Campoy-Quiles, M.; Caironi, M. *Mater. Sci. Eng. R Reports* **2019**, *138* (July 2018), 210–255.
- (141) Russ, B.; Glauddell, A.; Urban, J. J.; Chabiny, M. L.; Segalman, R. A. *Nat. Rev. Mater.* **2016**, *1* (10).
- (142) Sumino, M.; Harada, K.; Ikeda, M.; Tanaka, S.; Miyazaki, K.; Adachi, C. *Appl. Phys. Lett.* **2011**, *99* (9), 1–4.
- (143) Russ, B.; Robb, M. J.; Brunetti, F. G.; Miller, P. L.; Perry, E. E.; Patel, S. N.; Ho, V.; Chang, W. B.; Urban, J. J.; Chabiny, M. L.; Hawker, C. J.; Segalman, R. A. *Adv. Mater.* **2014**, *26* (21), 3473–3477.
- (144) Naab, B. D.; Zhang, S.; Vandewal, K.; Salleo, A.; Barlow, S.; Marder, S. R.; Bao, Z. *Adv. Mater.* **2014**, *26* (25), 4268–4272.
- (145) Schlitz, R. A.; Brunetti, F. G.; Glauddell, A. M.; Miller, P. L.; Brady, M. A.; Takacs, C. J.; Hawker, C. J.; Chabiny, M. L. *Adv. Mater.* **2014**, *26* (18), 2825–2830.
- (146) Yee, S. K.; Coates, N. E.; Majumdar, A.; Urban, J. J.; Segalman, R. A. *Phys. Chem. Chem. Phys.* **2013**, *15* (11), 4024–4032.
- (147) Blackburn, J. L.; Ferguson, A. J.; Cho, C.; Grunlan, J. C. *Adv. Mater.* **2018**, *30* (11), 1–35.
- (148) Tomlinson, E. P.; Willmore, M. J.; Zhu, X.; Hilsmier, S. W. A.; Boudouris, B. W. *ACS Appl. Mater. Interfaces* **2015**, *7* (33), 18195–18200.
- (149) Choi, H. H.; Cho, K.; Frisbie, C. D.; Sirringhaus, H.; Podzorov, V. *Nat. Mater.* **2017**, *17* (1), 2–7.
- (150) Paterson, A. F.; Singh, S.; Fallon, K. J.; Hodsdon, T.; Han, Y.; Schroeder, B. C.; Bronstein, H.; Heeney, M.; McCulloch, I.; Anthopoulos, T. D. *Adv. Mater.* **2018**, *30* (36), 1–33.
- (151) Horowitz, G. *Adv. Mater.* **1998**, *10* (5), 365–377.
- (152) Garnier, F.; Yassar, A.; Hajlaoui, R.; Horowitz, G.; Deloffre, F.; Servet, B.; Ries, S.; Alnot, P. *J. Am. Chem. Soc.* **1993**, *115* (19), 8716–8721.
- (153) Sirringhaus, H.; Brown, P. J.; Friend, R. H.; Nielsen, M. M.; Bechgaard, K.; Langeveld-Voss, B. M. W.; Spiering, A. J. H.; Janssen, R. A. J.; Meijer, E. W.; Herwig, P.; De Leeuw, D. M. *Nature* **1999**, *401* (6754), 685–688.
- (154) McCulloch, I.; Heeney, M.; Bailey, C.; Genevicius, K.; MacDonald, I.; Shkunov, M.; Sparrowe, D.; Tierney, S.; Wagner, R.; Zhang, W.; Chabiny, M. L.; Kline, R. J.; McGehee, M. D.; Toney, M. F. *Nat. Mater.* **2006**, *5* (4), 328–333.
- (155) Lin, Y. Y.; Gundlach, D. J.; Nelson, S. F.; Jackson, T. N. *IEEE Electron Device Lett.* **1997**, *18* (12), 606–608.
- (156) Butko, V. Y.; Chi, X.; Lang, D. V.; Ramirez, A. P. *Appl. Phys. Lett.* **2003**, *83* (23), 4773–4775.
- (157) Podzorov, V.; Pudalov, V. M.; Gershenson, M. E. *Appl. Phys. Lett.* **2003**, *82* (11), 1739–1741.
- (158) Payne, M. M.; Parkin, S. R.; Anthony, J. E.; Kuo, C. C.; Jackson, T. N. *J. Am. Chem. Soc.* **2005**, *127* (14), 4986–4987.
- (159) Yuan, Y.; Giri, G.; Ayzner, A. L.; Zoombelt, A. P.; Mannsfeld, S. C. B.; Chen, J.; Nordlund, D.; Toney, M. F.; Huang, J.; Bao, Z. *Nat. Commun.* **2014**, *5*, 1–9.
- (160) Minemawari, H.; Yamada, T.; Matsui, H.; Tsutsumi, J. Y.; Haas, S.; Chiba, R.; Kumai, R.; Hasegawa, T. *Nature* **2011**, *475* (7356), 364–367.

- (161) Haddon, R. C.; Perel, A. S.; Morris, R. C.; Palstra, T. T. M.; Hebard, A. F.; Fleming, R. M. *Appl. Phys. Lett.* **1995**, *67* (1995), 121.
- (162) Haddon, R. C. *J. Am. Chem. Soc.* **1996**, *118* (12), 3041–3042.
- (163) Jarrett, C. P.; Pichler, K.; Newbould, R.; Friend, R. H. *Synth. Met.* **1996**, *77* (1–3), 35–38.
- (164) Kobayashi, S.; Takenobu, T.; Mon, S.; Fujiwara, A.; Iwasa, Y. *Appl. Phys. Lett.* **2003**, *82* (25), 4581–4583.
- (165) Malenfant, P. R. L.; Dimitrakopoulos, C. D.; Gelorme, J. D.; Kosbar, L. L.; Graham, T. O.; Curioni, A.; Andreoni, W. *Appl. Phys. Lett.* **2002**, *80* (14), 2517–2519.
- (166) Guo, X.; Watson, M. D. *Org. Lett.* **2008**, *10* (23), 5333–5336.
- (167) Yan, H.; Chen, Z.; Zheng, Y.; Newman, C.; Quinn, J. R.; Dötz, F.; Kastler, M.; Facchetti, A. *Nature* **2009**, *457* (7230), 679–686.
- (168) Kim, Y.; Long, D. X.; Lee, J.; Kim, G.; Shin, T. J.; Nam, K. W.; Noh, Y. Y.; Yang, C. *Macromolecules* **2015**, *48* (15), 5179–5187.
- (169) Brown, A. R.; de Leeuw, D. M.; Lous, E. J.; Havinga, E. E. *Synth. Met.* **1994**, *66* (3), 257–261.
- (170) Zhang, X.; Bronstein, H.; Kronemeijer, A. J.; Smith, J.; Kim, Y.; Kline, R. J.; Richter, L. J.; Anthopoulos, T. D.; Siringhaus, H.; Song, K.; Heeney, M.; Zhang, W.; McCulloch, I.; Delongchamp, D. M. *Nat. Commun.* **2013**, *4*.
- (171) Rivnay, J.; Inal, S.; Salleo, A.; Owens, R. M.; Berggren, M.; Malliaras, G. G. *Nat. Rev. Mater.* **2018**, *3*, 17806.

3. STABLE RADICAL MATERIALS FOR ENERGY APPLICATIONS*

3.1 Abstract

Although less studied than their closed-shell counterparts, materials containing stable open-shell chemistries have played a key role in many energy storage and energy conversion devices. In particular, the oxidation-reduction (redox) properties of these stable radicals have made them a substantial contributor to the progress of organic batteries. Moreover, the use of radical-based materials in photovoltaic devices and thermoelectric systems has allowed for these emerging molecules to have impacts in the energy conversion realm. Additionally, the unique doublet states of radical-based materials provide access to otherwise inaccessible spin states in optoelectronic devices, offering many new opportunities for efficient usage of energy in light-emitting devices. Here, we review the current state of the art regarding the molecular design, synthesis, and application of stable radicals in these energy-related applications. Finally, we point to fundamental and applied arenas of future promise for these designer open-shell molecules, which have only just begun to be evaluated in full.

3.2 Introduction

From biological systems, to a functioning civilization, and to the observable universe, the transport and transformation of energy is the essence of everything. Although the conservation of energy is dictated by physical laws, the struggle has been to find the most efficient manner by which to convert, use, and store energy. In modern electronic applications, electrons serve as the fundamental carriers of charge and energy. Thus, many functional materials involved with aspects of energy research are associated with either charge transport or storage. From a chemical perspective, electron transfer reactions can be broadly described as oxidation-reduction (redox) processes.¹ Thus, organic materials having active redox behavior associated with them are of immense import in the realms of energy transport or storage.²

In fact, the previous decades have witnessed significant progress in the development of optoelectronically-active organic materials.^{3,4} In addition to the potentially lower cost and

* Reproduced from Wilcox, D. A.; Agarkar, V.; Mukherjee, S.; Boudouris, B. W. *Annu. Rev. Chem. Biomol. Eng.* **2018**, *9*, 83–103. Copyright 2018 Annual Reviews.

mechanical flexibility of devices associated with organic materials relative to many of their inorganic counterparts, organic-based systems often compete with or surpass the capabilities of inorganic materials in functioning applications (e.g., display technologies).^{5,6} As only loosely bound electrons of organic compounds are accessible from an energetic standpoint, π -conjugated systems have found significant attention as active layer materials in organic electronic devices and impressive progress has been made in this arena.⁷ However, the notion that a highly-conjugated π -system is required to access loosely bound electrons (and valence orbitals) of organic compounds is strictly untrue.^{8,9} In this report, we will instead focus on an alternative class of materials, organic molecules bearing stable radical groups.¹⁰

We define radicals as open-shell organic compounds, where the valence unpaired electron either resides on a localized orbital or on a conjugated system.¹¹ Having a singularly occupied molecular orbital (SOMO) energy level, radical species can either accept or donate an electron to form a closed-shell anion or cation, respectively. Depending on the relative stability of these species, a redox-active radical can be preferentially reduced (n-type), preferentially oxidized (p-type), or can be capable of undergoing either oxidation or reduction (ambipolar).¹² A radical species can have several accessible stable redox states, allowing for the radical to experience multiple consecutive or independent redox processes. Such redox behavior can be a simple tool for storing and releasing electrons at will, potentially allowing for reaction-based charge storage and memory applications.^{13,14} Similar chemistry can be beneficial to form active redox couples as auxiliary components in electronic devices (e.g., photovoltaic cells). Using analogous principles, redox-active radical based materials with high radical densities can form conductive networks where the neighboring radicals transport charge through a cooperative self-exchange process.¹⁴ Additionally, the unpaired electrons can allow access to uncommon spin states (e.g., the doublet state) of a material, which can have beneficial consequences with respect to the optoelectronic properties of the material.¹⁵ To date, the synthetic community has only scratched the surface of potential radical-containing materials, and organic radical materials are dominated by only a few specific chemical structures, such as sterically protected nitroxyl and phenolic radicals (Figure 3.1). Fortunately, with the continued progress of modern synthetic tools, a considerable variety of radical-based materials are emerging. There is no shortage of potential avenues to develop and fine-tune the chemistry of these materials for advanced energy-related applications, which allows us to expect an ever-increasing progress in this regard.¹⁶ Thus, through the appropriate

combination of chemistry, materials science, and engineering, we anticipate that large strides will be had in the stable radical community in the near future.

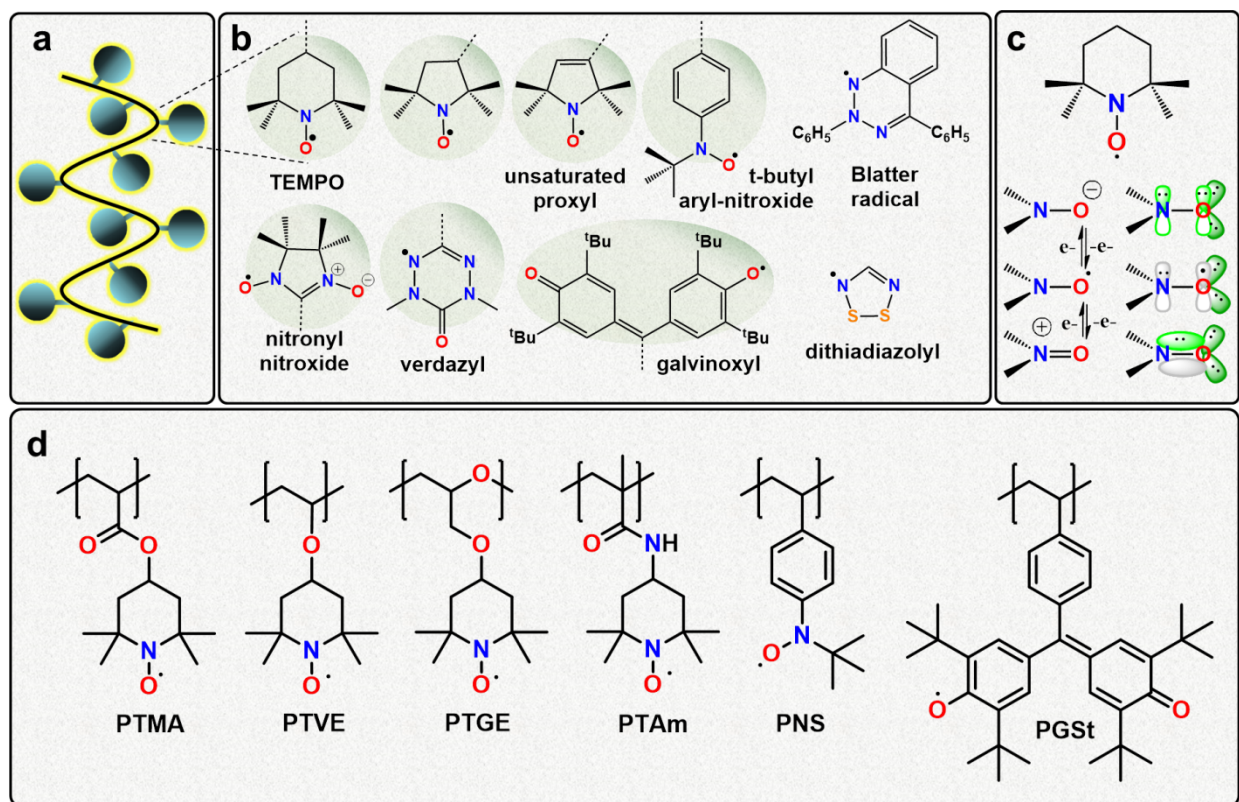


Figure 3.1. (a) Schematic of a radical polymer, which consists of pendant stable radical sites along the backbone of a macromolecular architecture. (b) Representative chemical structures of the most commonly-reported stable radical moieties. The open-shell groups that are marked with green ovals have been reported as pendant units in radical polymers, and the small molecule-only radical materials (i.e., those not marked in green) also have been important in energy-related efforts. (c) Example redox reactions associated with the nitroxyl radical show that the compound can access three distinct redox states. (d) Example chemical structures of a few radical polymers that have been described to a large degree in the literature.

Materials based on organic radicals can be broadly classified as either small molecules or macromolecules. Small molecules prove advantageous due to: (1) their ability to be deposited at high purity from the vapor phase [e.g., using physical vapor deposition (PVD)] and (2) the finer synthetic tunability and exact reproducibility of their molecular architectures.¹⁷ On the other hand, polymers provide numerous opportunities for different physical processing methods (e.g., solution-processing and crosslinking).¹⁸ In particular, radical polymers, which are defined as non-conjugated macromolecules with pendant radical sites, have attracted significant attention.^{13,14} We

do note that polyradical species (i.e., molecules that contain multiple radical sites which interact through a conjugated framework) are of immense interest in a number of application fields;^{19–21} however, they are not the focus here as they have not been implemented in energy-related devices. While the choice between the utilization of small molecules and macromolecules must be weighed against the final end-use energy application, the basic functions of radical moieties are independent of this distinction. These key functions can be classified as: (1) electron exchange (charge flow); (2) reversible redox processes (charge storage); and (3) the residual spin of the unpaired electron. In particular, radical materials have made a significant mark on the fields of organic batteries and organic conductors due to their charge storage and charge transport abilities. While the first and second functions have been the primary means by which radical materials have impacted technology to this point, the third avenue is one of great promise as well. As the reaches of this field grow into specific applications, it is important to collectively ground the fundamental ideas of these unique, energy-related materials in a common platform, and that is the purpose of this report.

3.3 Radical-Containing Materials for Energy Storage Applications

Rechargeable batteries are instrumental in common portable electronic devices today; however, many current inorganic cathode active materials in these batteries are relatively expensive and emerging inorganic materials are hampered with long-term cyclability and stability issues.²² Furthermore, next-generation electronic devices (e.g., rollup displays and wearable devices) will require batteries that are mechanically robust and flexible.^{23,24} As such, soft electrodes with active polymeric materials, particularly radical polymers, offer great promise in this particular application area. Their mechanical and chemical robustness, as well as the fact that the polymer architectures and electrochemical properties of these materials can be tuned in a relatively straightforward manner, mean that radical polymers have altered, and will continue to impact, the battery market.²⁴ To date, molecules containing stable radicals have been implemented in organic radical batteries, flow batteries, and composite batteries and supercapacitors. The following subsections detail the impressive progress and opportunities for radical polymers in the first two examples of these energy storage technologies, which are less-frequently reviewed in the literature, and the reader is referred to other publications^{25–37} and reviews^{3,38–42} for details regarding radical-based moiety implementation in composite batteries and supercapacitors.

3.3.1 Organic Radical Batteries

This category encompasses both purely organic radical batteries (ORBs) and carbon composite batteries that contain open-shell entities. Thus, we will discuss batteries where radical polymers are one of the major constituents of the cathode,^{22,24,43–63} or both electrodes^{64–70} in the battery (Figure 3.2). The electron transfer in an ORB occurs in two stages with both heterogeneous (current collector-to-radical moiety) and homogeneous (between two distinct radical-bearing sites) charge transfer steps being present.⁴⁴ Among the open-shell moieties, the nitroxyl radical is the most widely-studied in the ORB field.^{22,46,47,49,51–53,57,59–63,71,72} This radical moiety is robust and has exceptional stability due to potential resonance structures.⁵³ Moreover, the nitroxyl radical reversibly oxidizes to the oxoammonium cation, making it suitable as a cathode material in ORBs. Experimental ORB reports demonstrate that nitroxyl radical cathodes are characterized by a high charge capacity (~100 Ah/kg), high charging and discharging rate performance (up to 50 C)⁵⁷ owing to rapid electron-transfer of the nitroxyl group, and a long cycle life (>1,000 cycles). Nitroxyl-based polymer cathodes and lithium metal anodes have been the most common redox-active materials used in ORBs since the first report by Nakahara et al.,^{22,46,49,52,53,59–61,63,66,72} and poly(2,2,6,6-tetramethylpiperidinyloxy methacrylate) (PTMA) is one of the variants that has been extensively employed for cathode fabrication in ORBs due to its ease of synthesis.

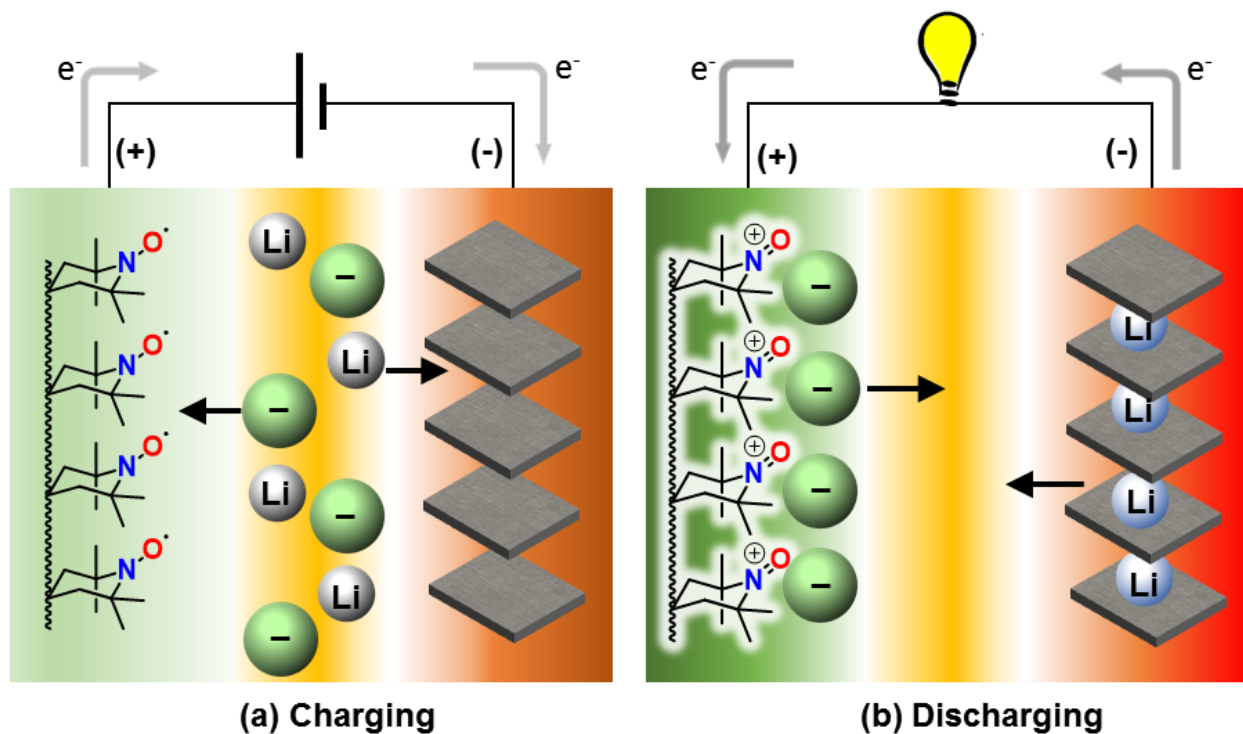


Figure 3.2. (a) Charging of an ORB. The nitroxyl radical is oxidized to the oxoammonium cation causing a flow of electrons through the outer circuit. This causes the electrolyte anions to migrate towards the newly-formed oxoammonium cations of the radical polymer, thus compensating their charge, while lithium cations migrate towards the graphite anode. Here, the lithium ions are reduced to lithium metal. (b) Discharging of an ORB. The intercalated lithium metal undergoes oxidation to form lithium ions, which migrate to the central electrolyte cavity. The free electrons travel through the outer circuit and reach the cathode reducing the oxoammonium cations back to nitroxyl moiety. The arrows within the battery show the movement of the electrolyte ions.

PTMA has a discharge cell voltage of ~ 3.5 V, which corresponds to its redox potential vs. Li/Li^+ , and is indicative of the oxidation of the nitroxyl moieties in PTMA to oxoammonium cations at the cathode during charging. The corresponding reverse reaction occurs while discharging.⁵² Based on the molecular structure and the fact that each PTMA repeat unit can store one electron, the theoretical discharge capacity of PTMA is 111 Ah/kg. Nakahara's first ORB displayed a discharge capacity of 70% of this theoretical value (77 Ah/kg), which was retained over 500 charge and discharge cycles.^{52,53} While this initial result was impressive, a significant advance with regards to the discharge capacity was achieved through the addition of an aluminum-laminated battery with thinner electrodes.⁵⁹ This system exhibited an enhanced discharge capacity of ~ 100 Ah/kg, which approached the theoretical value for PTMA. Furthermore, a thinner electrode caused relatively quick electron transfer in the polymer bulk, decreasing the charging

time. In even more recent work, the capacity of a PTMA-based ORB was further improved to 100% of the theoretical value by fabricating an ORB with an electrospun fluorinated copolymer suffused with electrolyte to serve as the ion-transporting phase. These landmark publications demonstrate that alterations in the battery design can be the key to achieving close to theoretical discharge capacities in ORBs.⁶⁰

Owing to the modular nature of the radical polymers, the backbone moieties are not limited to acrylate-based structures. In fact, radical polymers with polynorbornene backbones, such as poly(2,3-bis(2',2',6',6'-tetramethylpiperidiny-*N*-oxyl-4'-oxycarbonyl)-5-norbornene) (PTNB), have been used to increase the specific capacity of the battery. Additionally, the chemistry of polynorbornene is advantageous in some regards as it permits ready cross-linking sites for azide-based click chemistry. Crosslinking of these types of polymers, which are also used as cathode materials due to the same nitroxyl functionality of the pendant groups, can avoid their dissolution in the battery electrolyte. In turn, this prevents self-discharge of the battery.⁵⁸ Because of this key design motif, a specific capacity of 106 Ah/kg (theoretical value: 109 Ah/kg) with no decrease in performance up to 1,000 cycles was exhibited by an ORB made from a PTNB-based radical polymer.

Of course, the design of the radical polymers systems is not limited to hydrophobic materials either. For instance, poly(2,2,6,6-tetramethylpiperidiny-*N*-oxyl vinyl ether) (PTVE) is hydrophilic, which facilitates electrochemical processes in an ORB in the presence of protic electrolytes. Additionally, PTVE has a higher theoretical capacity (135 Ah/kg) than PTMA and PTNB.²² Thus, a PTVE coin-type cell exhibited a discharge voltage of 3.51 V and a discharge capacity of 114 Ah/kg. A rapid and reversible electrochemical response enabled an ultrafast charging of the cell (< 3 seconds) when a PTVE cathode was used in combination with an aqueous electrolyte.⁴³ The Zn/PTVE test cell, with an aqueous solution of 0.1 M ZnCl₂ and 0.1 M NH₄Cl serving as the electrolyte, displayed a plateau voltage at 1.73 V and a capacity of 124 Ah/kg. In addition to this macromolecule, hydrophilic polyethers like poly(2,2,6,6-tetramethylpiperidiny-*N*-oxyl glycidyl ether) (PTGE) helped to increase the amount of polymer material in the electrode without compromising its redox-activity, thus improving the ORB performance as compared to similar configuration PTMA ORBs.⁷²

Along similar lines of thinking, various attempts at altering the polymer design have been made to increase the theoretical capacity of the redox-active cathode material with moieties like

2,2,5,5-tetramethyl-3-oxiranyl-3-pyrrolin-1-oxyl and spiro-*bis*(nitroxide).^{45,47} Other alteration attempts, such as the replacement of toxic transition metal oxides with earth abundant silicones (for cathode-active polymer backbones), moved towards the reduction of electrode material toxicity and cost.⁶³ Another polymer design modification away from polyethers and towards water-insoluble polyacrylamide backbones resulted in long life-high capacity aqueous ORBs.⁴⁶ For instance, poly(2,2,6,6-tetramethylpiperidinyloxy-4-yl acrylamide) (PTAm) was designed to be used with an aqueous electrolyte. A test-cell was fabricated in which PTAm was used as the redox-active material for the cathode, poly(N-4,4'-bipyridinium-*N*-decamethylene dibromide) (PV10) served as the anode, and 0.1 M NaBF₄ was the aqueous electrolyte. The cell demonstrated a 1.2 V discharge voltage, exceeded 2,000 charging–discharging cycles, and had a high charging rate performance. Additionally, the report demonstrated the concept of an all-organic ORB, where both electrodes are composed of radical polymers; however, it was not the first all-radical polymer report.^{64–69}

In fact, the Nishide laboratory was the first group to report the synthesis of n-type radical polymers through the development of poly(nitroxyl styrene) (PNS) derivatives bearing different substituent groups.⁶⁹ The redox switch between the n-type and the p-type polymer was attributed to the addition of an electron-withdrawing trifluoromethyl group. While this report demonstrated the switch in the redox behavior of polymers and the potential of these moieties as electrode materials, the same team subsequently fabricated a completely organic ORB employing PTNB and poly(galvinoxyl styrene) (PGSt) as the cathode and anode, respectively.⁶⁸ The observed charge capacity was 32 Ah/kg, 92% of the theoretical value of 34.8 Ah/kg, with no significant deterioration in performance after 250 cycles. This was a key advance in the field as an all-organic ORB would lower the cost of the battery by avoiding use of metal-containing electrodes and would be superior in terms of electrode material capacity⁶⁹ and battery performance⁴⁶ relative to its hybrid counterparts.

In contrast to the previous batteries described, an ambipolar battery material would be advantageous due to the possibility of the reversal of battery polarity and the use of a single redox-active material. A report of an ambipolar electrode-active material and its application in batteries led to the development of two types of ORBs, which were deemed the pole-less and “rocking-chair-type” configurations.⁶⁷ The pole-less battery configuration consisted of both the cathode and the anode being fabricated from an ambipolar electrode material, poly(nitronylnitroxyl styrene)

(PNNS). The battery showed plateau voltages of +1.3 V and of -1.3 V, thus indicating the dual functionality of the polymer as a cathode and an anode material. The exhibited charge capacity was 44 Ah/kg (86% of the theoretical capacity) and a good cycle performance was exhibited, even after 250 cycles. The “rocking-chair-type” configuration consisted of a PNNS cathode and a PGSt anode. Owing to the n-type redox activity in both the PNNS and PGSt polymers, only the counter cation of the electrolyte was exchanged at both electrodes. This led to the migration of cations in “rocking-chair” fashion. The cell exhibited a charge capacity of 29 Ah/kg (90% of theoretical value) and good cycle stability over 250 cycles.

In this subsection, the highlights and successes of ORB energy storage devices have been highlighted, and there has been a great deal of progress made in these systems to date. In fact, detailed efforts have been made to increase various battery parameters (e.g., theoretical charge capacity and device cyclability) and decrease electrode material dissolution in the electrolyte. However, as potentially noted by the reader, batteries based upon nitroxyl-containing polymers possessing myriad backbones have dominated the ORB field. Thus, we note that a careful and novel stable radical design coupled with a robust battery design can lead to further improvement in ORBs, and this direction of work would be promising for future efforts in the field (*vide infra*). Next, we turn away from portable energy storage systems and towards energy storage platforms where pumping is involved.

3.3.2 Flow Batteries

In flow batteries, the chemical moieties that undergo the redox reactions are dissolved in a suitable electrolyte and pumped through the battery. In a manner that is distinct from many batteries used in portable and transportation applications, the redox-active chemical components are stored in separate reservoirs outside of the actual redox chamber. Because the oxidative and reductive species are dissolved species, the solutions which contain them are known as the catholyte (instead of cathode) and the anolyte (instead of anode) depending on their role in the flow battery. These solutions are then pumped into a chamber (i.e., the energy conversion area) where they are separated by a membrane, which allows for the passage of ions across the barrier while preventing the intermixing of the anolyte and catholyte (Figure 3.3).

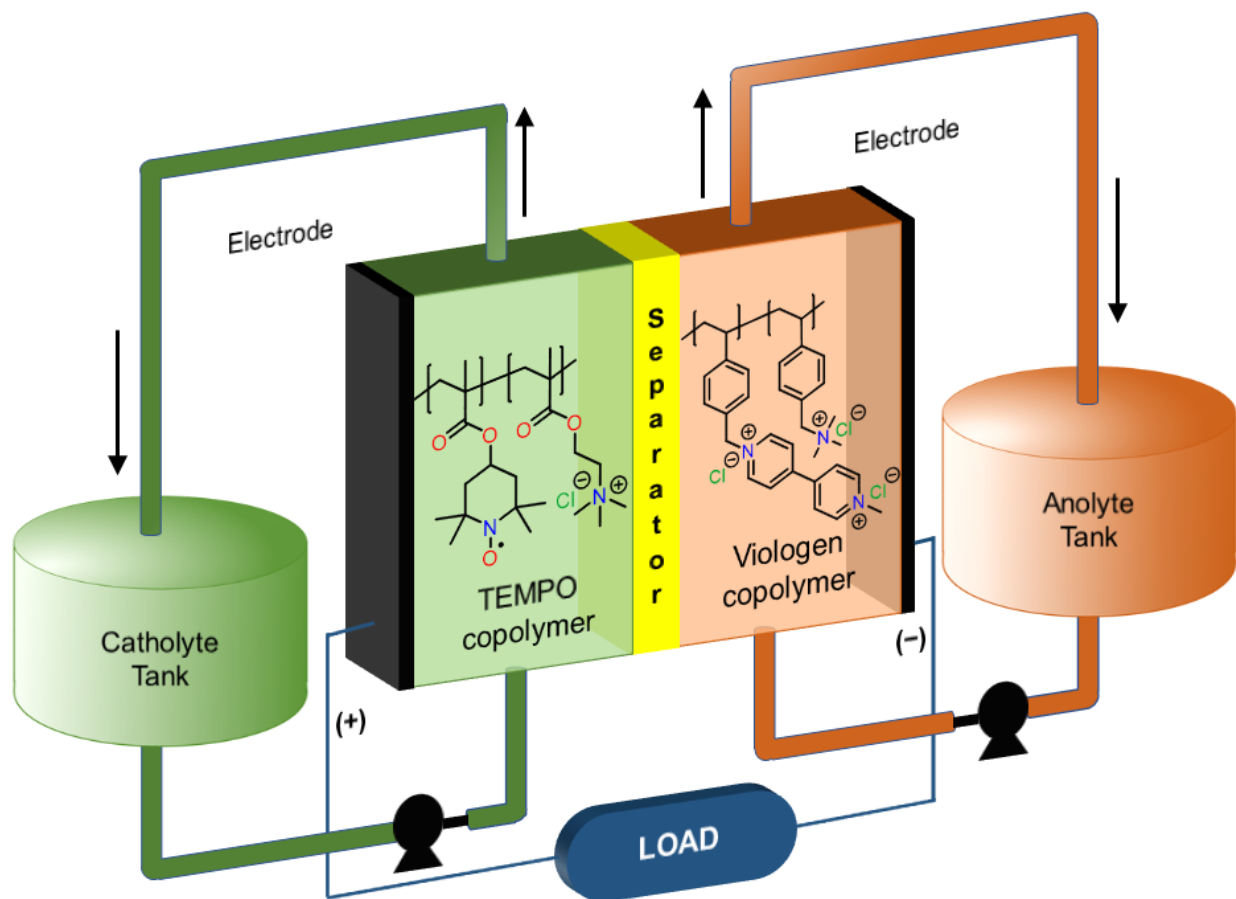


Figure 3.3. Working principle of a polymer-based RFB. The anolyte and catholyte are pumped into respective chambers, which are divided by a membrane separator in order to prevent inter-mixing of solutions. The TEMPO- and viologen-based copolymers serve as the catholyte and anolyte redox-active material, respectively. The quaternary ammonium moieties, included in the second block for both copolymers, help to induce water solubility in the copolymers as they are applied to aqueous RFBs.

The first redox flow battery, reported in the 1970s, used the Fe/Cr redox system.⁷³ Despite their scalability and quick regeneration, flow batteries have been accompanied by both safety and environmental issues owing to use of inorganic salts and metal/halogen redox couples.⁷⁴ As a result, a relatively safer alternative is an all-organic or a metal/organic redox flow battery,⁷⁵ and efforts focused on organic-based systems have gained significant momentum. Further development resulted in the incorporation of organic radical compounds as a redox-active material into the flow battery. The redox flow batteries have a few additional advantages over other types of batteries, such as the tunability of the properties of redox-active components, their relatively safe and environmentally benign nature, and an increased output voltage for non-aqueous RFBs.^{75,76}

Typical hybrid RFBs are comprised of a metal salt in the anolyte phase and a radical polymer in the catholyte solution. Again, to date, the radical moiety of these polymers has been exclusively those based on the TEMPO entity. Xu, Wang, and co-workers reported a hybrid RFB that was superior with respect to the cell voltage, electrolyte concentration, and discharge volumetric energy density relative to other aqueous and non-aqueous RFBs.⁷⁶ The test flow cell consisted of an anode fabricated by using lithium metal/graphite and TEMPO-LiPF₆ electrolyte/graphite felt at the cathode side with a polyethylene-based porous separator. The battery demonstrated an 84% coulombic efficiency (CE), 82% voltaic efficiency (VE), 69% energy efficiency (EE), and good cyclability along with a superior discharge volumetric energy density of 126 Wh/L.⁷⁶ Replacement of Li with Zn, for the design of an aqueous hybrid RFB, resulted in a cell that exhibited a voltage of 2 V, a large value for an aqueous flow battery.⁷⁷ The cell was comprised of a zinc anode and a TEMPO-based copolymer catholyte with a cellulose-based membrane separator. The copolymers were specifically designed to ensure water solubility by incorporation of hydrophilic moieties [e.g., poly(ethylene glycol methyl ether methacrylate) (PEGMA) and 2-(methacryloyloxy)-N,N,N-trimethylethane ammonium chloride (METAC)]. The cellulose membrane and water-soluble redox-active polymers lowered the battery cost and the potential environmental impact. In this example, rheological analysis revealed that micelle formation resulted in lowering of the viscosity of the polymer catholyte used in the battery as compared to the linear PEGMA copolymer solutions.⁷⁸ Specifically, polystyrene (PS) was utilized as the second moiety of the block copolymer. Owing to a polarity difference between the polar TEMPO block and the non-polar PS block, self-assembled micellar structure copolymers were obtained in the battery electrolytes. The PS formed the core of the micelles while TEMPO-based moieties formed the corona. The Zn/PTMA-PS battery exhibited a maximum 99% CE with 93% utilization of the catholyte and was stable over 1,000 charging-discharging cycles in the +0.5 V to +2 V range. Such alterations in the chemical architecture of the polymer enabled comparatively higher performance in terms of the battery efficiency and life owing to low catholyte viscosity.

The first all-organic radical redox flow battery was reported by Liu and co-workers in 2011.⁷⁹ The battery used *N*-methyl phthalimide and TEMPO as the anolyte and catholyte, respectively. The battery exhibited 90% CE over the first 20 cycles and demonstrated charge-discharge plateaus of +1.65 V and -1.36 V, respectively. An improvement over the TEMPO/*N*-methyl phthalimide RFB, in terms of battery voltage and temperature stability, was

TEMPO/benzophenone (BP) RFB with a cell voltage of 2.41 V, owing to low redox potential and temperature stability (up to 45°C) of BP.⁸⁰

Water-based RFBs are environmentally benign as they consist of non-toxic polymers and water; however, it should be noted that they have a limited open-circuit voltage relative to their non-aqueous counterparts. Such an aqueous RFB based on TEMPO- and viologen-containing copolymers acting as the catholyte and anolyte materials, respectively, was reported recently (see inset of Figure 3.3 for chemical structures).⁷⁴ Quaternary ammonium salts were introduced by using METAC moieties in one of the blocks in these copolymers to ensure solubility in the aqueous supporting electrolyte.⁸¹ The TEMPO- and viologen-based redox-active electrolyte solutions were pumped into a cell where they were separated by a cellulose-based membrane.⁷⁴ The battery exhibited an output voltage of 1.1 V with a discharge energy density of 8.0 Wh/L and retained 80% of its initial capacity after 10,000 charging-discharging cycles. Wang and co-workers reported a similar battery comprised of methyl viologen (MV) as the anolyte and 4-hydroxy-TEMPO as the catholyte with aqueous sodium chloride as the supporting electrolyte.⁸² The battery demonstrated nearly 100% CE with a discharge voltage of 0.9 V and retained around 89% of its original capacity after 100 cycles. The reports mentioned until now involve the use of different redox-active materials as anolyte and catholyte; however, RFBs with identical catholyte and anolyte materials also exist.

This is because redox-active molecules and polymers that exhibit an ambipolar nature can be employed as both n-type and p-type materials; thus, they can give rise to RFBs that are referred to as symmetric RFBs. Brushett, Wei, and co-workers reported such an RFB based on 2-phenyl-4,4,5,5-tetramethylimidazoline-1-oxyl-3-oxide (PTIO) in 2016.⁸³ In addition to being ambipolar, PTIO also exhibited high solubility in organic solvents. The RFB demonstrated a voltage of 1.73 V along with 90% CE, 67% VE, 60% EE, and exhibited charging and discharging energy densities of 9 Wh/L and 5 Wh/L respectively. Schubert and co-workers developed a similar symmetric RFB, but with improved efficiencies.⁸⁴ In this case, a tetraethylene glycol spacer was introduced between two PTIO moieties. The RFB exhibited 95% CE, 86% VE, and 82% EE. Another recently reported strategy is one that covalently bonds the individual n-type and p-type redox moieties, thereby imparting an ambipolar nature to the resulting molecule.^{75,85} The Schubert group reported an flow battery based on a covalently-bonded TEMPO-phenazine molecule.⁸⁵ Phenazine exhibits n-type behavior suited for an anolyte material whereas TEMPO demonstrates p-type behavior, thus

making it a suitable material for catholyte. The battery had a voltage of 1.2 V with around 98% CE. and achieved 60% of its theoretical capacity and retained it over 1800 charge-discharge cycles. Schubert and co-workers followed the same concept and very recently proposed an RFB employing covalently bonded TEMPO and viologen units.⁷⁵ This report was aimed at demonstrating the ability of the TEMPO-viologen combination molecule as a potential candidate for ORFBs.

Redox flow batteries have undergone significant transitions from Fe/Cr to metal/halogen redox systems and, finally, to all-organic RFBs. In this way, they have become progressively more environmental-friendly, safe, and cost-effective. While small molecule-based RFBs used several redox-active moieties, polymer-based RFBs were found to be restricted to nitroxyl-containing polymers as the catholyte. A valuable addition to RFBs employing ambipolar redox-active molecules was the novel concept of tethering two opposite nature redox-active species to each other by means of a suitable chemical rope. It propelled research in ambipolar RFBs, thus indicating that a careful design of redox-active molecules and polymers will pave the way for improved battery performance (compared to existing reports).

3.4 Radicals in Energy Conversion Technologies

Dye-sensitized solar cells (DSSCs) have gained a significant amount of attention since 1991 when the Grätzel team initially reported these energy conversion devices with an efficiency of ~7.5% under direct illumination and up to 12% in diffuse daylight.⁸⁶ A typical DSSC consists of a transparent electrode with a thin, porous layer of fused titanium dioxide nanoparticles. The porous oxide is coated with a dye and placed in an electrolyte with a redox couple, commonly I^-/I_3^- , and a counter electrode (Figure 3.4a).⁸⁷⁻⁹⁰

As the open-circuit voltage (V_{OC}) of the cell is determined primarily by the difference between the electron quasi-Fermi energy of the semiconducting species and the redox potential of the redox couple, one of the most promising means by which to increase the efficiency of these systems is to replace the I^-/I_3^- redox couple with one having a lower redox potential. Additionally, while iodide works well for most DSSC applications, it has several qualities that make it undesirable for solar cell operation. First, molecular iodine (I_2) absorbs strongly in the visible spectrum, reducing the amount of light available for charge generation. Second, iodide is corrosive. Furthermore, the oxidation of I^- to I_3^- is a two-step reaction, where two I^- ions are oxidized by the

dye to form I_2^- , and two of these species react to form I_3^- and I^- .⁹¹ While a two-step reaction reduces parasitic charge recombination between the dye and the semiconductor, the large energy difference between the I^-/I_2^- and I_2^-/I_3^- step results in wasted energy within the cell. Alternative redox couples based on other halogens,⁹² pseudohalogens,⁹³ disulfide bonds,⁹⁴⁻⁹⁷ transition metal complexes,⁹⁸⁻¹⁰¹ and small molecule organic radicals (e.g., TEMPO) have been proposed. Here, we will focus on the use of organic radicals for this purpose. The possibility of being able to tune the redox potential of these molecules through judicious molecular design makes them an attractive option. Additionally, many organic radicals are water-soluble, non-toxic, non-corrosive, and demonstrate low absorption coefficients in the visible spectrum,¹⁴ making them ideal for DSSC applications. In spite of these advantages, however, TEMPO derivatives cause traditionally-used ruthenium dyes to degrade in solution, thus necessitating research into other classes of sensitizers for DSSCs that utilize organic redox mediators.¹⁰²

The first report of an organic radical, specifically TEMPO, being used as a redox mediator was from the Grätzel team in 2008.¹⁰³ Inspired by the use of radicals in organic batteries, the authors fabricated cells with TEMPO as the redox electrolyte and an indoline dye (D-149) as a sensitizer, resulting in an efficiency of 5.4% and a V_{OC} of 830 mV, compared to 720 mV for a cell employing an iodide redox mediator. While the improvement in the V_{OC} by 110 mV was notable, the redox potential of TEMPO was 310 mV further below vacuum than I^-/I_3^- . Therefore, the predicted gains in V_{OC} that would come from using a redox couple with a lower potential were not fully realized. Both a larger dark current and a shorter electron lifetime, as measured by photovoltage transient decay, were observed for TEMPO than for I^-/I_3^- , which suggested significantly higher parasitic recombination between the TiO_2 electrode and the oxidized TEMPO species, ultimately leading to a lower V_{OC} than predicted.

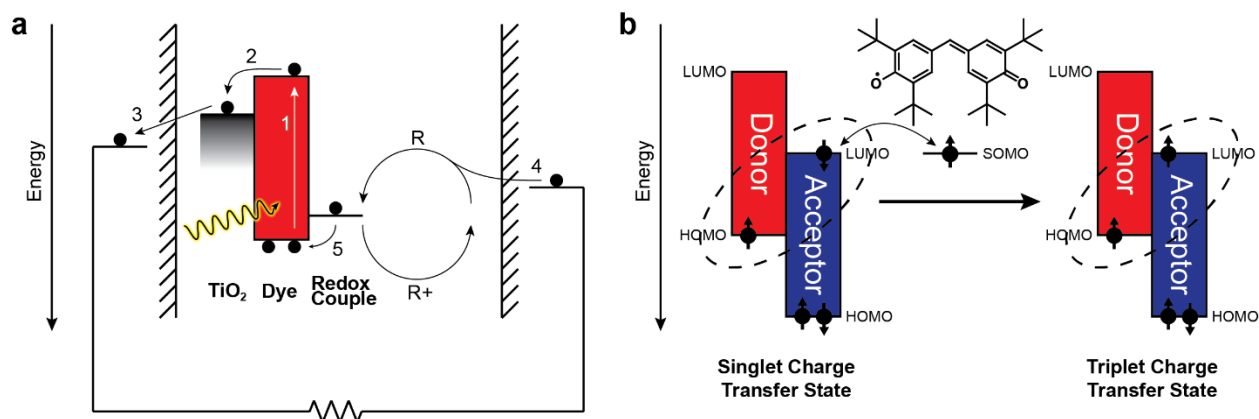


Figure 3.4. (a) Schematic of a dye-sensitized solar cell in operation. (1) A photon is absorbed by a dye molecule, promoting an electron from the HOMO to the LUMO energy level. (2) The electron is then transferred to the conduction band of the TiO₂ nanoparticle layer (3) where it then enters the external circuit. (4) Redox-active molecules are reduced at the counter electrode by electrons from the external circuit. (5) The reduced redox-active molecules then diffuse to the dye and transfer the electron to the dye, regenerating the dye and completing the circuit. (b) Schematic showing how the galvinoxyl radical acts as a spin-flip center at the interface of a heterojunction organic solar cell. The dashed circles indicate the charge transfer states at the donor-acceptor interface. The red species is the electron-donating material, and the blue species is the electron-accepting material.

A later report found that, for a series of TEMPO-based radicals with different substituents in the 4- position (namely -H, -OH, and -NHCOCH₃), the V_{OC} was linearly correlated with the redox potential in a cell using an indoline sensitizer (D-131). This suggested that the V_{OC} could indeed be tuned by varying the redox potential of the redox mediator.¹⁰⁴ However, as before, the TEMPO derivatives showed lower gains than expected in the V_{OC} compared to iodide, indicating that increased recombination was occurring in these systems as well. Iodide showed lower recombination because both forms of the iodide redox pair are negatively-charged, causing electrostatic repulsion from the TiO₂ surface. As TEMPO is positively-charged in its oxidized state, the opposite effect occurs. The authors suggested that TEMPO with negatively-charged substituents, such as -COO⁻, could help mitigate the effect. However, a separate extensive computational study showed that introducing charged substituents onto the TEMPO radical would greatly lower the redox potential to below the HOMO level of typical sensitizers, preventing the dye from being regenerated.¹⁰⁵

Further efforts sought to improve the short-circuit current density (J_{SC}) and fill factor (FF) of the device by enhancing the reactivity of the radical species. To this end, 2-azaadamantan-N-oxyl (AZA) was reported as an alternate redox mediator.¹⁰⁶ Reducing the steric hindrance around

the nitroxyl group led to an eleven-fold enhancement of the electron self-exchange rate (k_{ex}) between the radical molecules in solution for AZA compared to TEMPO. Additionally, AZA showed significantly higher values for the diffusion coefficient (D_0) and the heterogeneous electron-transfer rate constant (k_0) (i.e., the rate of electron transfer from the counter electrode to the redox couple) than for either TEMPO or iodide. An optimized solar cell using a combination of indoline sensitizers D-205 and D-131 yielded an efficiency of 8.1%, with a V_{OC} of 0.85 V, a J_{SC} of 13.3 mA cm⁻², and a FF of 0.75. Though the iodide cells showed a higher J_{SC} of 14.7 mA cm⁻², the cells with AZA performed better overall, due to the higher V_{OC} from the lower redox potential of the nitroxyl radical and the higher fill factor due to the high k_{ex} and diffusion coefficient.

As mentioned previously, regeneration of the dye via the iodide redox couple consists of two steps: formation of I_2^- from two I^- ions, and dissociation of two of these to form I_3^- and I^- . A significant energy loss occurs during the second step. By replacing this step with one involving a TEMPO derivative, an increase in the V_{OC} can be achieved while maintaining the attractive qualities of the iodide regeneration, such as the low recombination rate. In one report, the ionic liquid 1-butyl-3-{2-oxo-2-[(2,2,6,6-tetramethylpiperidin-1-oxyl-4-yl)amino]ethyl}-1H-imidazol-3-ium iodide (JC-IL) was synthesized, with a TEMPO group on the cationic portion of the room temperature salt.¹⁰⁷ This ionic liquid showed greatly improved diffusion coefficients and k_0 values relative to either TEMPO or iodide, and unlike iodide, maintained optical transparency. When incorporated into solar cells using the dye CR147, an efficiency of 8.12% was achieved, versus 5.42% for TEMPO and 6.90% for iodide. A later report further improved the efficiency to 8.38% by replacing the iodide anion with selenocyanate ($SeCN^-$).¹⁰⁸ The V_{OC} values were maximized with both ionic liquids, and while iodide gave higher J_{SC} values, the ionic liquids still performed far better than TEMPO alone in that regard. To further understand the nature of the improvements, the authors measured the charge transfer resistance at both electrodes as well as the recombination resistance. At the photoanode-electrolyte interface, ITSeCN (the selenocyanate-containing ionic liquid) showed a charge transfer resistance of 15.78 ohms, compared to 12.25 ohms for iodide and 31.43 ohms for TEMPO. Thus, the charge transfer resistances played a large role in determining the J_{SC} values for each of the cells. ITSeCN also showed the highest recombination resistance, suggesting that the high V_{OC} values were, in part, obtained due to minimized recombination in the cell. This demonstrated, once again, that suppressing recombination is essential for fully achieving the gains in the V_{OC} that nitroxyl radicals promise.

The highest reported efficiency for a dye-sensitized solar cell with an organic radical redox couple came from the Nishide group in 2016. They reported that, through proper tuning of the dye, they could achieve over 10% efficiency with TEMPO as a redox mediator in a gel electrolyte.¹⁰⁹ By using a fluorene-based dye with long alkyl side chains (MD-153), the dye molecules could selectively-attract the uncharged TEMPO molecules, but not the charged TEMPO⁺ cations. Thus, the dye itself acted as a barrier preventing recombination from the TiO₂ to the redox couple, allowing for high photocurrents and V_{OC}s to be achieved. Solar cells fabricated with MD-153 and TEMPO in a gel electrolyte achieved efficiencies of 10.1%, with a V_{OC} of 0.93 V, a J_{SC} of 15.5 mA cm⁻², and a FF of 0.70. The same device structure with a liquid electrolyte showed a marginally higher efficiency of 10.4%. As a gel-based electrolyte reduces the risk of solvent leakage from the cell, this report also demonstrated that a less hazardous DSSC could be fabricated with a minimal decrease in performance. Overall, organic radical-based redox couples show strong promise for use in DSSC applications due to their high V_{OC} values, and further improvements in the J_{SC} through improved transport properties would allow organic radicals to provide record efficiencies in these devices.

Work regarding organic radicals within solar cells has not been limited only to DSSCs. The Vardeny group has reported that the galvinoxyl radical acts as a spin-flip mediator in bulk-heterojunction (BHJ) solar cells when phenyl-C₆₁-butyric acid methyl ester (PCBM) is used as the electron acceptor and poly(3-hexylthiophene) (P3HT) is utilized as the electron donor. They reported that an optimal loading of 3% galvinoxyl (by weight) in an optimized P3HT:PCBM BHJ device lead to an improvement in efficiency from 3.4% to 4.0%, primarily due to an improvement in J_{SC}.¹¹⁰ When tested in a P3HT-rich device, no such improvement was found. However, in PC₆₀BM rich devices, a much greater improvement was seen upon galvinoxyl doping, with maximum device performance occurring at greater loadings of the galvinoxyl radical. Therefore, the improvements were ascribed to favorable interactions between the galvinoxyl moiety and PCBM. The improvements were specific to those two species; tests with other acceptors, such as bis(1-[3-(methoxycarbonyl)propyl]-1-phenyl)-[6,6]C₆₂ (bis-PCBM) and indene-C₆₀ bisadduct (ICBA), and other radicals, such as TEMPO and 1,3-bisdiphenylene-2-phenylallyl (BDPA), showed no improvement in the ultimate device performance. However, similar experiments with different electron donors, such as regiorandom P3HT and poly[2-methoxy-5-(2-ethylhexyloxy)-1,4-phenylenevinylene] (MEH-PPV), showed similar improvements. Due to a reduction in the

magneto-photocurrent in films containing galvinoxyl, it was concluded that the unpaired electron in galvinoxyl was promoting intersystem crossing in the interfacial charge transfer states. In other words, the singlet charge transfer states were converted into triplet states, which had a longer lifetime due to recombination being spin-forbidden (Figure 3.4b). The spin-exchange mechanism was allowable due to the energy levels of the galvinoxyl radical and the PCBM LUMO being close to one another, which was thought to be the reason that improvements were only seen for this particular system.

The same group later reported on improvements to a poly({4,8-bis[(2-ethylhexyl)oxy]benzo[1,2-b:4,5-b']dithiophene-2,6-diyl}{3-fluoro-2-[(2-ethylhexyl)carbonyl]thieno[3,4-b]thiophenediyl}) (PTB7):PCBM BHJ solar cell with a 2% (by weight) galvinoxyl loading.¹¹¹ This report demonstrated, as before, that galvinoxyl was behaving as a spin-flip center in the BHJ cell. However, in this particular situation, triplet charge transfer states were undesirable, as PTB7 had a lower triplet exciton energy than that of the charge-transfer states. As such, triplet states would lead to increased back transfer of electrons from the acceptor to the donor. Addition of the galvinoxyl radical led to a reduction in triplet excitons, as measured by photo-induced absorption; this is consistent with the idea that the radical moiety was increasing the number of singlet CT states, thus preventing the decay of the triplet CT state. As observed previously, when a different electron acceptor was used, no improvement in performance was seen upon addition of galvinoxyl. Moreover, no reduction in the number of triplet excitons in the PTB7 was observed, suggesting that the spin exchange interaction could only occur between two species with similar energy levels (e.g., galvinoxyl radical and PCBM). This fact is an important design criterion when trying to match open-shell and closed-shell moieties in charge, spin, and energy transfer scenarios.

Previous efforts by our group have demonstrated the ability for small molecule radicals and radical polymers to be used elsewhere in organic energy conversion devices. In thermoelectric devices utilizing poly(3,4-ethylenedioxythiophene):poly(styrene sulfonate) (PEDOT:PSS), the thermoelectric power factor can be nearly doubled by the addition of 2% TEMPO, by weight.¹¹² The TEMPO radicals acted as a filter for low-energy charges in the PEDOT:PSS, allowing for the thermopower to be improved without a significant reduction in conductivity at low loadings. Another report examined inverted organic photovoltaic devices fabricated with the structure ITO/ZnO/PCBM:P3HT/PTMA/Ag, which showed significantly higher power conversion

efficiencies (2.08%) than devices without the PTMA interlayer (0.56%).¹¹³ Additionally, the performance of the device with the interlayer showed greater stability over time, primarily because the PTMA layer maintained an ohmic contact with the P3HT even as the silver contacts oxidized. Unlike PEDOT:PSS, which is commonly used as a polymeric hole transporting layer in organic photovoltaics, PTMA is not acidic, making it a practical alternative for an interfacial-modifying layer (IML). PTMA has also been successfully used as an IML in a pentacene field-effect transistor, reducing the contact resistance and improving the crystallinity of the deposited pentacene.¹¹⁴

The favorable redox and optoelectronic properties of organic radicals, as well as their spin-active nature, have allowed them to be used in synergy with traditional materials in energy conversion devices such as solar cells and thermoelectric devices. While there are still hurdles to overcome for their practical implementation in next-generation devices, the synthetic flexibility of the materials offers the promise that these hurdles can be overcome by judicious molecular design. With the ever-growing library of modern synthetic methods, there will be no shortage of organic radical materials that can be tailored for specific energy conversion device applications.

3.5 Towards a Unity ‘Internal Quantum Efficiency’ in Light-Emitting Devices

The recent revolution in lighting display technologies has been aided by the progress that occurred with respect to organic light-emitting diodes (OLEDs).^{115–117} The emission of light in the emissive layers of OLEDs occurs when electrons and holes that are injected from the cathode and anode, respectively, recombine to emit photons of a wavelength determined by the band structure of the light-emitting organic molecule.¹¹⁸ However, according to the principles of spin statistics, only one in four electron-hole pairs forms a singlet exciton. The other three form triplet excitons, capping the theoretical upper limit of internal quantum efficiency (IQE) to only 25% in fluorescent materials.¹¹⁹ Although phosphorescent materials are used to harvest the remaining 75% triplet excitons,¹²⁰ the ambiguous nature of the intersystem crossing process, potential non-radiative decay events, and thermal inversion phenomena result in complex trade-offs, restricting a straightforward pathway towards achieving desired targets with traditional phosphorescent materials.¹²¹ Recent efforts towards solving this problem have involved the utilization of thermally-activated delayed fluorescence (TADF) emissive layer materials.¹²² However, the problem associated with spin statistics can be more elegantly avoided with the use of open-shell

luminescent materials.^{123,124} For example, in 2015, Li and co-workers used this simple principle to develop a neutral conjugated radical-based emitter (Figure 3.5).¹²³ The compound, (4-N-carbazolyl-2,6-dichlorophenyl)bis(2,4,6-trichlorophenyl) methyl (TTM-1Cz), is an emissive radical with a photoluminescence lifetime of 25 ns. Because of this, the authors were able to fabricate active OLEDs using TTM-1Cz as an emissive layer. Importantly, the emission from a doublet state was confirmed as the material does not show any magneto-electroluminescence (MEL) effect. That is, as shown in Figure 3.5, unlike a derivative with a similar closed-shell structure, [N,N'-Di(1-naphthyl)-N,N'-diphenyl-(1,1'-biphenyl)-4,4'-diamine] (NPB), TTM-1Cz does not show any measurable MEL effect, which indicates the absence of any triplet-state formation for the radical component. Although it can be regarded as the first step towards a broader opportunity, the scope of this design principle is significant towards the development of OLEDs with even higher energy efficiencies than those of available devices. Thus, the usage of radical based emitters as forthcoming energy efficient materials alters the principles and ideas of OLED devices from a fundamental perspective, with significant practical potentials.

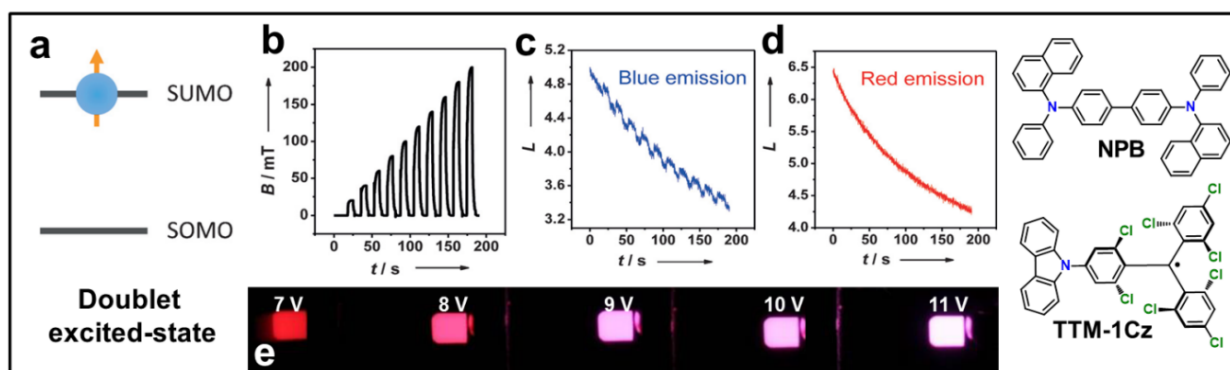


Figure 3.5. (a) Schematic diagram for the spin configuration of an open-shell doublet system. Figures (b-e) show a set of properties for an OLED [Device Structure: ITO/ N,N'-di-1-naphthyl-N,N'-diphenylbenzidine (NPB) (30 nm) / 4,4-bis(carbazol-9-yl)biphenyl (CBP) (10 nm) / TTM-1Cz:CBP (5wt%, 40 nm) / 1,3,5-tri(phenyl-2-benzimidazolyl)-benzene (TPBi) (35 nm) / lithium fluoride (LiF) (0.8 nm) / aluminum (100 nm)] made from the doublet emitting TTM-1Cz and a conventional fluorescent material (NPB). (b) The time-dependent magnetic field applied in the Magneto-electroluminescence (MEL) experiments. (c) The EL intensity of the blue emission of NPB from the OLED at 7 V when the magnetic field was applied. (d) The EL intensity of the red emission of TTM-1Cz from the OLED at 7 V when the magnetic field was applied. Figure (e) shows photographs of the OLEDs [Device Structure: (ITO)/ NPB (30 nm)/TTM-1Cz:CBP (5wt%, 40 nm)/(TPBi) (35 nm)/ LiF (0.8 nm)/aluminum (100 nm)] driving voltages ranging from 7 V to 11 V. The blue emission at higher voltages arises from NPB and CBP. Figures are adapted with permission from ¹²³(© 2015, Wiley-VCH Verlag GmbH & Co. KGaA, Weinheim).

3.6 Summary and Outlook

Radical-containing small molecules and polymers recently have been successfully implemented in energy conversion and energy storage technologies due to their synthetic tunability, open-shell nature, and unique and rapid redox properties. While the majority of the work has focused on energy storage applications, there is also a clear possibility in using radical-based materials in photovoltaic, thermoelectric, and light-emitting devices. Moreover, there are clear design paradigms for radical-based materials that are at the very early stages of development. For instance, an emerging class of materials is that of conjugated radical polymers (CRPs). In these materials, the macromolecular backbone of the polymer is conjugated (e.g., a polythiophene-based backbone), and the substituent groups are open-shell species that can either be electrically-separated from the conjugated backbone or be bound to the backbone in a manner that preserves conjugation. By making these hybrid closed-shell–open-shell macromolecules, initial efforts have been able to implement them as electrode materials in batteries^{125,126} and identify key design aspects that must be considered in order to have high-performance materials.¹²⁷ This simple example highlights the true potential of radical-based materials. Moreover, the fact that small molecule radical species have been well-characterized by the chemistry community previously,^{128,129} allows for the next generation of researchers to exploit this solid foundation in order to synthesize designer materials for specific energy applications in a fairly straightforward manner. However, there is one avenue of work that has not been addressed in this review as it has not been given the attention it deserves by the community as a whole.

Specifically, the computational design of radical-based energy conversion materials and the usage of simulation packages to elucidate fundamental charge transfer properties has not occurred to a great extent in the open-shell community. While excellent efforts from the National Renewable Energy Laboratory (NREL) have begun to address these opportunities,^{130–133} creating a larger base of researchers dedicated to these critical challenges is key for the continued success of radical-containing materials. For example, the predictive design of never-before-developed stable radical species and their inclusion in either traditional radical polymers or conjugated radical polymers would allow chemists and chemical engineers clear synthetic targets that have not been envisioned to date. While many other fields of chemistry, chemical engineering, and materials science have benefited from the combined interactions of theory, simulation, and experiment, energy storage and conversion applications based upon radical-containing systems have not joined

in this effort. Thus, addressing this opportunity could lead to significant and wide-ranging strides of progress. Despite this current gap in the community, the future of radical-based materials for energy conversion applications is quite promising. As noted above frequently, the primary chemical motifs utilized in application have been relatively narrow in scope; thus, there is a clear opportunity to make better devices through better chemical designs. Moreover, as the operational physics of the materials and devices continues to be elucidated in full, it is anticipated that the unique properties associated with lone-spin molecules will afford them a special place in being able to revolutionize the energy landscape across the globe.

3.7 Acknowledgements

The work of D.A.W. and V.A. was graciously supported by the National Science Foundation (NSF) through the CAREER Award in the Polymers Program (Award Number: 1554957, Program Manager: Dr. Andrew Lovinger), and the work of S.M. was kindly provided by the Air Force Office of Scientific Research (AFOSR) through the Organic Materials Chemistry Program (Grant Number: FA9550-15-1-0449, Program Manager: Dr. Kenneth Caster). We thank these organizations for this generous support.

3.8 References

- (1) Nishinaga, T. *Organic Redox Systems: Synthesis, Properties, and Applications*; Wiley, 2015.
- (2) Casado, N.; Hernández, G.; Sardon, H.; Mecerreyes, D. *Prog. Polym. Sci.* **2016**, *52*, 107–135.
- (3) Gracia, R.; Mecerreyes, D. *Polym. Chem.* **2013**, *4*, 2206–2214.
- (4) Ostroverkhova, O. *Handbook of Organic Materials for Optical and (Opto)Electronic Devices: Properties and Applications*; Woodhead Publishing, 2013.
- (5) Boudouris, B. W. *Curr. Opin. Chem. Eng.* **2013**, *2* (3), 294–301.
- (6) Root, S. E.; Savagatrup, S.; Printz, A. D.; Rodriquez, D.; Lipomi, D. J. *Chem. Rev.* **2017**, *117*, 6467–6499.
- (7) Skotheim, T. A.; Reynolds, J. *Conjugated Polymers: Theory, Synthesis, Properties, and Characterization*; CRC Press, 2006.
- (8) Baradwaj, A. G.; Rostro, L.; Alam, M. A.; Boudouris, B. W. *Appl. Phys. Lett.* **2014**, *104*, 213306.
- (9) Rostro, L.; Wong, S. H.; Boudouris, B. W. *Macromolecules* **2014**, *47* (11), 3713–3719.
- (10) Mukherjee, S.; Boudouris, B. W. *Organic Radical Polymers: New Avenues in Organic Electronics*; Springer, 2017.

- (11) McNaught, A. D.; Wilkinson, A. *IUPAC. Compendium of Chemical Terminology, 2nd ed.*; Blackwell Scientific Publications, Oxford, 1997.
- (12) Castellanos, S.; Gaidelis, V.; Jankauskas, V.; Grazulevicius, J. V.; Brillas, E.; López-Calahorra, F.; Juliá, L.; Velasco, D. *Chem. Commun.* **2010**, *46*, 5130–5132.
- (13) Tomlinson, E. P.; Hay, M. E.; Boudouris, B. W. *Macromolecules* **2014**, *47* (18), 6145–6158.
- (14) Rostro, L.; Baradwaj, A. G.; Boudouris, B. W. *ACS Appl. Mater. Interfaces* **2013**, *5* (20), 9896–9901.
- (15) Dediu, V. A.; Hueso, L. E.; Bergenti, I.; Taliani, C. *Nat. Mater.* **2009**, *8* (9), 707–716.
- (16) Wingate, A. J.; Boudouris, B. W. *J. Polym. Sci. A Polym. Chem.* **2016**, *54*, 1875–1894.
- (17) Roncali, J.; Leriche, P.; Blanchard, P. *Adv. Mater.* **2014**, *26* (23), 3821–3838.
- (18) Halary, J. L.; Laupretre, F.; Monnerie, L. *Polymer Materials: Macroscopic Properties and Molecular Interpretations*; Wiley, 2011.
- (19) Rajca, A. *Chem. Rev.* **1994**, *94* (4), 871–893.
- (20) Gallagher, N. M.; Olankitwanit, A.; Rajca, A. *J. Org. Chem.* **2015**, *80*, 1291–1298.
- (21) Rajca, A.; Wongsriratanakul, J.; Rajca, S.; Cerny, R. L. *Chem. Eur. J.* **2004**, *10*, 3144–3157.
- (22) Suguro, M.; Iwasa, S.; Kusachi, Y.; Morioka, Y.; Nakahara, K. *Macromol. Rapid Commun.* **2007**, *28*, 1929–1933.
- (23) Mike, J. F.; Lutkenhaus, J. L. *ACS Macro Lett.* **2013**, *2*, 839–844.
- (24) Nishide, H.; Oyaizu, K. *Science* **2008**, *319*, 737–738.
- (25) Choi, W.; Ohtani, S.; Oyaizu, K.; Nishide, H.; Geckeler, K. E. *Adv. Mater.* **2011**, *23* (38), 4440–4443.
- (26) Guo, W.; Yin, Y.-X.; Xin, S.; Guo, Y.-G.; Wan, L.-J. *Energy Environ. Sci.* **2012**, *5* (1), 5221.
- (27) Wang, Y.-H.; Hung, M.-K.; Lin, C.-H.; Lin, H.-C.; Lee, J.-T. *Chem. Commun.* **2011**, *47* (4), 1249–1251.
- (28) Oyaizu, K.; Ando, Y.; Konishi, H.; Nishide, H. *J. Am. Chem. Soc.* **2008**, *130*, 14459–14461.
- (29) Vlad, A.; Singh, N.; Rolland, J.; Melinte, S.; Ajayan, P. M.; Gohy, J.-F. *Sci. Rep.* **2014**, *4*, 4315.
- (30) Huang, Q.; Choi, D.; Cosimbescu, L.; Lemmon, J. P. *Phys. Chem. Chem. Phys.* **2013**, *15* (48), 20921–20928.
- (31) Choi, W.; Endo, S.; Oyaizu, K.; Nishide, H.; Geckeler, K. E. *J. Mater. Chem. A* **2013**, *1* (9), 2999–3003.
- (32) Aqil, A.; Vlad, A.; Piedboeuf, M.-L.; Aqil, M.; Job, N.; Melinte, S.; Detrembleur, C.; Jérôme, C. *Chem. Commun.* **2015**, *51* (45), 9301–9304.
- (33) Kim, J.-K.; Kim, Y.; Park, S.; Ko, H.; Kim, Y. *Energy Environ. Sci.* **2015**, *9* (4), 1264–1269.
- (34) Ernould, B.; Devos, M.; Bourgeois, J.-P.; Rolland, J.; Vlad, A.; Gohy, J.-F. *J. Mater. Chem. A* **2015**, *3* (16), 8832–8839.
- (35) Li, Y.; Jian, Z.; Lang, M.; Zhang, C.; Huang, X. *ACS Appl. Mater. Interfaces* **2016**, *8* (27), 17352–17359.
- (36) Vlad, A.; Singh, N.; Melinte, S.; Gohy, J.-F.; Ajayan, P. M. *Sci. Rep.* **2016**, *6*, 22194.
- (37) Hung, M.-K.; Wang, Y.-H.; Lin, C.-H.; Lin, H.-C.; Lee, J.-T. *J. Mater. Chem.* **2012**, *22* (4), 1570.
- (38) Singh, V. K.; Rao, O. S.; Singh, R. A. *Indian J. Eng. Mater. Sci.* **1996**, *3* (5), 201–206.
- (39) Nakahara, K.; Oyaizu, K.; Nishide, H. *Chem. Lett.* **2011**, *40* (3), 222–227.
- (40) Suga, T.; Nishide, H. *ACS Symp. Ser.* **2012**, *1096*, 45–53.
- (41) Muench, S.; Wild, A.; Friebe, C.; Häupler, B.; Janoschka, T.; Schubert, U. S. *Chem. Rev.* **2016**, *116* (16), 9438–9484.

- (42) Schon, T. B.; McAllister, B. T.; Li, P.-F.; Seferos, D. S. *Chem. Soc. Rev.* **2016**, *45*, 6345–6404.
- (43) Koshika, K.; Sano, N.; Oyaizu, K.; Nishide, H. *Chem. Commun.* **2009**, *0*, 836–838.
- (44) Oyaizu, K.; Nishide, H. *Adv. Mater.* **2009**, *21* (22), 2339–2344.
- (45) Oyaizu, K.; Kawamoto, T.; Suga, T.; Nishide, H. *Macromolecules* **2010**, *43*, 10382–10389.
- (46) Koshika, K.; Chikushi, N.; Sano, N.; Oyaizu, K.; Nishide, H. *Green Chem.* **2010**, *12* (9), 1573.
- (47) Nesvadba, P.; Bugnon, L.; Maire, P.; Novák, P. *Chem. Mater.* **2010**, *22* (3), 783–788.
- (48) Komaba, S.; Tanaka, T.; Ozeki, T.; Taki, T.; Watanabe, H.; Tachikawa, H. *J. Power Sources* **2010**, *195* (18), 6212–6217.
- (49) Dai, Y.; Zhang, Y.; Gao, L.; Xu, G.; Xie, J. *J. Electrochem. Soc.* **2011**, *158* (3), A291–A295.
- (50) Janoschka, T.; Hager, M. D.; Schubert, U. S. *Adv. Mater.* **2012**, *24* (48), 6397–6409.
- (51) Cao, L.; Sadaf, S.; Beladi-Mousavi, S. M.; Walder, L. *Eur. Polym. J.* **2013**, *49* (8), 1923–1934.
- (52) Nakahara, K.; Iwasa, S.; Satoh, M.; Morioka, Y.; Iriyama, J.; Suguro, M.; Hasegawa, E. *Chem. Phys. Lett.* **2002**, *359*, 351–354.
- (53) Nishide, H.; Iwasa, S.; Pu, Y. J.; Suga, T.; Nakahara, K.; Satoh, M. *Electrochim. Acta* **2004**, *50*, 827–831.
- (54) Koshika, K.; Sano, N.; Oyaizu, K.; Nishide, H. *Macromol. Chem. Phys.* **2009**, *210* (22), 1989–1995.
- (55) Chae, I. S.; Koyano, M.; Oyaizu, K.; Nishide, H. *J. Mater. Chem. A* **2013**, *1* (4), 1326–1333.
- (56) Chae, I. S.; Koyano, M.; Sukegawa, T.; Oyaizu, K.; Nishide, H. *J. Mater. Chem. A* **2013**, *1* (34), 9608–9611.
- (57) Nishide, H.; Suga, T. *Electrochem. Soc. Interface* **2005**, *14* (4), 32–36.
- (58) Suga, T.; Konishi, H.; Nishide, H. *Chem. Commun.* **2007**, *0*, 1730.
- (59) Nakahara, K.; Iriyama, J.; Iwasa, S.; Suguro, M.; Satoh, M.; Cairns, E. J. *J. Power Sources* **2007**, *163* (2), 1110–1113.
- (60) Kim, J.-K.; Cheruvally, G.; Choi, J.-W.; Ahn, J.-H.; Choi, D. S.; Song, C. E. *J. Electrochem. Soc.* **2007**, *154* (9), A839–A843.
- (61) Bugnon, L.; Morton, C. J. H.; Novak, P.; Vetter, J.; Nesvadba, P. *Chem. Mater.* **2007**, *19* (15), 2910–2914.
- (62) Qu, J.; Katsumata, T.; Satoh, M.; Wada, J.; Igarashi, J.; Mizoguchi, K.; Masuda, T. *Chem. Eur. J.* **2007**, *13* (28), 7965–7973.
- (63) Suguro, M.; Mori, A.; Iwasa, S.; Nakahara, K.; Nakano, K. *Macromol. Chem. Phys.* **2009**, *210* (17), 1402–1407.
- (64) Jähnert, T.; Hager, M. D.; Schubert, U. S. *Macromol. Rapid Commun.* **2016**, *37* (8), 725–730.
- (65) Jähnert, T.; Häupler, B.; Janoschka, T.; Hager, M. D.; Schubert, U. S. *Macromol. Rapid Commun.* **2014**, *35* (9), 882–887.
- (66) Jähnert, T.; Häupler, B.; Janoschka, T.; Hager, M. D.; Schubert, U. S. *Macromol. Chem. Phys.* **2013**, *214* (22), 2616–2623.
- (67) Suga, T.; Sugita, S.; Ohshiro, H.; Oyaizu, K.; Nishide, H. *Adv. Mater.* **2011**, *23* (6), 751–754.
- (68) Suga, T.; Ohshiro, H.; Sugita, S.; Oyaizu, K.; Nishide, H. *Adv. Mater.* **2009**, *21* (16), 1627–1630.
- (69) Suga, T.; Pu, Y. J.; Kasatori, S.; Nishide, H. *Macromolecules* **2007**, *40* (9), 3167–3173.

- (70) Sano, N.; Tomita, W.; Hara, S.; Min, C. M.; Lee, J. S.; Oyaizu, K.; Nishide, H. *ACS Appl. Mater. Interfaces* **2013**, *5* (4), 1355–1361.
- (71) Takahashi, Y.; Hayashi, N.; Oyaizu, K.; Honda, K.; Nishide, H. *Polym. J.* **2008**, *40* (8), 763–767.
- (72) Oyaizu, K.; Suga, T.; Yoshimura, K.; Nishide, H. *Macromolecules* **2008**, *41*, 6646–6652.
- (73) Weber, A. Z.; Mench, M. M.; Meyers, J. P.; Ross, P. N.; Gostick, J. T.; Liu, Q. *J. Appl. Electrochem.* **2011**, *41* (10), 1137–1164.
- (74) Janoschka, T.; Martin, N.; Martin, U.; Friebe, C.; Morgenstern, S.; Hiller, H.; Hager, M. D.; Schubert, U. S. *Nature* **2015**, *527* (7576), 78–81.
- (75) Janoschka, T.; Friebe, C.; Hager, M. D.; Martin, N.; Schubert, U. S. *ChemistryOpen* **2017**, *6* (2), 216–220.
- (76) Wei, X.; Xu, W.; Vijayakumar, M.; Cosimbescu, L.; Liu, T.; Sprenkle, V.; Wang, W. *Adv. Mater.* **2014**, *26* (45), 7649–7653.
- (77) Winsberg, J.; Janoschka, T.; Morgenstern, S.; Hagemann, T.; Muench, S.; Hauffman, G.; Gohy, J. F.; Hager, M. D.; Schubert, U. S. *Adv. Mater.* **2016**, *28* (11), 2238–2243.
- (78) Winsberg, J.; Muench, S.; Hagemann, T.; Morgenstern, S.; Janoschka, T.; Billing, M.; Schacher, F. H.; Hauffman, G.; Gohy, J.-F.; Hoepfener, S.; Hager, M. D.; Schubert, U. S. *Polym. Chem.* **2016**, *7* (9), 1711–1718.
- (79) Li, Z.; Li, S.; Liu, S.; Huang, K.; Fang, D.; Wang, F.; Peng, S. *Electrochem. Solid-State Lett.* **2011**, *14* (12), A171.
- (80) Xing, X.; Huo, Y.; Wang, X.; Zhao, Y.; Li, Y. *Int. J. Hydrogen Energy* **2017**, *42*, 17488–17494.
- (81) Janoschka, T.; Morgenstern, S.; Hiller, H.; Friebe, C.; Wolkersdörfer, K.; Häupler, B.; Hager, M. D.; Schubert, U. S. *Polym. Chem.* **2015**, *6* (45), 7801–7811.
- (82) Liu, T.; Wei, X.; Nie, Z.; Sprenkle, V.; Wang, W. *Adv. Energy Mater.* **2016**, *6*, 1501449.
- (83) Duan, W.; Vemuri, R. S.; Milshstein, J. D.; Laramie, S.; Dmello, R. D.; Huang, J.; Zhang, L.; Hu, D.; Vijayakumar, M.; Wang, W.; Liu, J.; Darling, R. M.; Thompson, L.; Smith, K.; Moore, J. S.; Brushett, F. R.; Wei, X. *J. Mater. Chem. A* **2016**, *4* (15), 5448–5456.
- (84) Hagemann, T.; Winsberg, J.; Häupler, B.; Janoschka, T.; Gruber, J. J.; Wild, A.; Schubert, U. S. *NPG Asia Mater.* **2017**, *9*, e340.
- (85) Winsberg, J.; Stolze, C.; Muench, S.; Liedl, F.; Hager, M. D.; Schubert, U. S. *ACS Energy Lett.* **2016**, *1* (5), 976–980.
- (86) Oregan, B.; Grätzel, M. *Nature* **1991**, *353* (6346), 737–740.
- (87) Grätzel, M. *Nature* **2001**, *414*, 338–344.
- (88) Hagfeldt, A.; Boschloo, G.; Sun, L.; Kloo, L.; Pettersson, H. *Chem. Rev.* **2010**, *110*, 6595–6663.
- (89) Li, C. T.; Lin, R. Y. Y.; Lin, J. T. *Chem. Asian J.* **2017**, *12*, 486–496.
- (90) Ye, M.; Wen, X.; Wang, M.; Iocozzia, J.; Zhang, N.; Lin, C.; Lin, Z. *Mater. Today* **2015**, *18* (3), 155–162.
- (91) Boschloo, G.; Hagfeldt, A. *Acc. Chem. Res.* **2009**, *42* (11), 1819–1826.
- (92) Teng, C.; Yang, X.; Yuan, C.; Li, C.; Chen, R.; Tian, H.; Li, S.; Hagfeldt, A.; Sun, L. *Org. Lett.* **2009**, *11* (23), 5542–5545.
- (93) Oskam, G.; Bergeron, B. V.; Meyer, G. J.; Searson, P. C. *J. Phys. Chem. B* **2001**, *105*, 6867–6873.
- (94) Liu, Y.; Jennings, J. R.; Wang, Q. *ChemSusChem* **2013**, *6* (11), 2124–2131.

- (95) Li, D.; Li, H.; Luo, Y.; Li, K.; Meng, Q.; Armand, M.; Chen, L. *Adv. Funct. Mater.* **2010**, *20* (19), 3358–3365.
- (96) Wang, M.; Chamberland, N.; Breau, L.; Moser, J.-E.; Humphry-Baker, R.; Marsan, B.; Zakeeruddin, S. M.; Grätzel, M. *Nat. Chem.* **2010**, *2* (5), 385–389.
- (97) Liu, Y.; Jennings, J. R.; Parameswaran, M.; Wang, Q. *Energy Environ. Sci.* **2011**, *4* (2), 564.
- (98) Kakiage, K.; Aoyama, Y.; Yano, T.; Oya, K.; Fujisawa, J.; Hanaya, M. *Chem. Commun.* **2015**, *51* (88), 15894–15897.
- (99) Daeneke, T.; Duffy, N. W.; Holmes, A. B. *Energy Environ. Sci.* **2012**, *5*, 7090–7099.
- (100) Bai, Y.; Yu, Q.; Cai, N.; Wang, Y.; Zhang, M.; Wang, P. *Chem. Commun.* **2011**, *47*, 4376–4378.
- (101) Li, T. C.; Spokoyny, A. M.; She, C.; Farha, O. K.; Mirkin, C. A.; Marks, T. J.; Hupp, J. T. *J. Am. Chem. Soc.* **2010**, *132*, 4580–4582.
- (102) Lee, J. Y.; Lee, C.; Lee, Y. M.; Cho, K. Y.; Choi, J. W.; Park, J. K. *J. Solid State Electrochem.* **2012**, *16* (2), 657–663.
- (103) Zhang, Z.; Chen, P.; Murakami, T. N.; Zakeeruddin, S. M.; Grätzel, M. *Adv. Funct. Mater.* **2008**, *18* (2), 341–346.
- (104) Kato, F.; Hayashi, N.; Murakami, T.; Okumura, C.; Oyaizu, K.; Nishide, H. *Chem. Lett.* **2010**, *39* (5), 464–465.
- (105) Gryn'ova, G.; Barakat, J. M.; Blinco, J. P.; Bottle, S. E.; Coote, M. L. *Chem. Eur. J.* **2012**, *18* (24), 7582–7593.
- (106) Kato, F.; Kikuchi, A.; Okuyama, T.; Oyaizu, K.; Nishide, H. *Angew. Chem. Int. Ed.* **2012**, *51* (40), 10177–10180.
- (107) Chu, T. C.; Lin, R. Y. Y.; Lee, C. P.; Hsu, C. Y.; Shih, P. C.; Lin, R.; Li, S. R.; Sun, S. S.; Lin, J. T.; Vittal, R.; Ho, K. C. *ChemSusChem* **2014**, *7* (1), 146–153.
- (108) Li, C. T.; Lee, C. P.; Lee, C. T.; Li, S. R.; Sun, S. S.; Ho, K. C. *ChemSusChem* **2015**, *8* (7), 1244–1253.
- (109) Suzuka, M.; Hayashi, N.; Sekiguchi, T.; Sumioka, K.; Takata, M.; Hayo, N.; Ikeda, H.; Oyaizu, K.; Nishide, H. *Sci. Rep.* **2016**, *6*, 28022.
- (110) Zhang, Y.; Basel, T. P.; Gautam, B. R.; Yang, X.; Mascaro, D. J.; Liu, F.; Vardeny, Z. V. *Nat. Commun.* **2012**, *3*, 1043.
- (111) Basel, T. P.; Huynh, U.; Zheng, T.; Xu, T.; Yu, L.; Vardeny, Z. V. *Adv. Funct. Mater.* **2015**, *25*, 1895–1902.
- (112) Tomlinson, E. P.; Willmore, M. J.; Zhu, X.; Hilsmier, S. W. A.; Boudouris, B. W. *ACS Appl. Mater. Interfaces* **2015**, *7* (33), 18195–18200.
- (113) Rostro, L.; Galicia, L.; Boudouris, B. W. *J. Polym. Sci. B Polym. Phys.* **2015**, *53* (5), 311–316.
- (114) Sung, S. H.; Bajaj, N.; Rhoads, J. F.; Chiu, G. T.; Boudouris, B. W. *Org. Electron.* **2016**, *37*, 148–154.
- (115) Gaspar, D. J.; Polikarpov, E. *OLED Fundamentals: Materials, Devices, and Processing of Organic Light-Emitting Diodes*; CRC Press, 2015.
- (116) Xu, R.-P.; Li, Y.-Q.; Tang, J.-X. *J. Mater. Chem. C* **2016**, *4*, 9116–9142.
- (117) Jou, J.-H.; Kumar, S.; Agrawal, A.; Li, T.-H.; Sahoo, S. *J. Mater. Chem. C* **2015**, *3*, 2974–3002.
- (118) Adachi, C. *Jpn. J. Appl. Phys.* **2014**, *53*, 060101.
- (119) Wohlgenannt, M.; Tandon, K.; Mazumdar, S.; Ramasesha, S. *Nature* **2001**, *409*, 494–497.

- (120) Baldo, M. A.; O'Brien, D. F.; You, Y.; Shoustikov, A.; Sibley, S.; Thompson, M. E.; Forrest, S. R. *Nature* **1998**, *395*, 151–154.
- (121) Minaev, B.; Baryshnikov, G.; Agren, H. *Phys. Chem. Chem. Phys.* **2014**, *16*, 1719–1758.
- (122) Yang, Z.; Mao, Z.; Xie, Z.; Zhang, Y.; Liu, S.; Zhao, J.; Xu, J.; Chi, Z.; Aldred, M. P. *Chem. Soc. Rev.* **2017**, *46*, 915–1016.
- (123) Peng, Q.; Obolda, A.; Zhang, M.; Li, F. *Angew. Chem. Int. Ed.* **2015**, *54*, 7091–7095.
- (124) Neier, E.; Arias, R.; Rady, N.; Venkatesan, S.; Hudnall, T. W.; Zakhidov, A. *Org. Electron.* **2017**, *44*, 126–131.
- (125) Li, F.; Zhang, Y.; Kwon, S. R.; Lutkenhaus, J. L. *ACS Macro Lett.* **2016**, *5*, 337–341.
- (126) Casado, N.; Hernández, G.; Veloso, A.; Devaraj, S.; Mecerreyes, D.; Armand, M. *ACS Macro Lett.* **2016**, *5*, 59–64.
- (127) Li, F.; Gore, D. N.; Wang, S.; Lutkenhaus, J. L. *Angew. Chem. Int. Ed.* **2017**, *56*, 9856–9859.
- (128) Koivisto, B. D.; Hicks, R. G. *Coord. Chem. Rev.* **2005**, *249*, 2612–2630.
- (129) Hicks, R. G. *Org. Biomol. Chem.* **2007**, *5*, 1321–1338.
- (130) Kemper, T. W.; Larsen, R. E.; Gennett, T. *J. Phys. Chem. C* **2014**, *118*, 17213–17220.
- (131) Kemper, T. W.; Larsen, R. E.; Gennett, T. *J. Phys. Chem. C* **2015**, *119*, 21369–21375.
- (132) Bobela, D. C.; Hughes, B. K.; Braunecker, W. A.; Kemper, T. W.; Larsen, R. E.; Gennett, T. *J. Phys. Chem. Lett.* **2015**, *6*, 1414–1419.
- (133) Kemper, T. W.; Gennett, T.; Larsen, R. E. *J. Phys. Chem. C* **2016**, *120*, 25639–25646.

4. TUNING THE INTERFACIAL AND ENERGETIC INTERACTIONS BETWEEN A PHOTOEXCITED CONJUGATED POLYMER AND OPEN-SHELL SMALL MOLECULES *

4.1 Abstract

Design rules and application spaces for closed-shell conjugated polymers have been well established in the field of organic electronics, but the emerging class of open-shell stable radicals have not been evaluated in such detail. Thus, establishing the underlying physical phenomena associated with the interactions between both classes of molecules is imperative for the effective utilization of these soft materials. Here, we establish that Förster Resonance Energy Transfer (FRET) is the dominant mechanism by which energy transfer occurs from a common conjugated polymer to various radical species using a combination of experimental and computational approaches. Specifically, we determined this fact by monitoring the fluorescence quenching of poly(3-hexylthiophene) (P3HT) in the presence of three radical species: (1) the galvinoxyl; (2) the 2-phenyl-4,4,5,5-tetramethylimidazoline-3-oxide-1-oxyl (PTIO); and (3) the 4-hydroxy-2,2,6,6-tetramethylpiperidine-1-oxyl (TEMPO) radicals. Both in solution and in the solid-state, the galvinoxyl and PTIO radicals showed quenching that was on par with that of a common fullerene electron-accepting derivative, due to the considerable overlap of their absorbance spectrum with the fluorescence spectrum of the P3HT species, which indicated that isoenergetic electronic transitions existed for both species. Conversely, TEMPO showed minimal quenching at similar concentrations due to the lack of such an overlap. Furthermore, computational studies demonstrated that FRET would occur at a significantly faster rate than other competing processes. These findings suggest that long-range energy transfer can be accomplished in applications when radicals that can act as FRET acceptors are utilized, forming a new design paradigm for future applications involving both closed- and open-shell soft materials.

* Reproduced from Wilcox, D. A.; Snaider, J.; Mukherjee, S.; Yuan, L.; Huang, L.; Savoie, B. M.; Boudouris, B. W. *Soft Matter* **2019**, *15*, 1413–1422. Copyright 2019 The Royal Society of Chemistry.

4.2 Introduction

The self-assembly and interfacial interactions of soft materials in the active layers of organic electronic devices are offering new perspectives on the modern energy conversion and energy storage landscape.¹ For example, the commercialization of organic light-emitting devices (OLEDs)² and the potential associated with the low-cost production of other electronic devices (e.g., batteries, sensors, thermoelectric modules, and photovoltaic cells) has resulted in significant interest in these materials from academic, military, and commercial entities.³ To date, most organic electronic devices utilize molecules and molecular blends with extensive π -conjugation, which allows for the stabilization of ionized states on the molecule, subsequently permitting the conduction of charge.^{3,4} Due to the significant research investments in this initial wave of organic electronics research, molecular design rules and defined structure-property relationships for closed-shell conjugated polymers as well as the structural, energetic, and electronic interactions between different conjugated species are relatively well understood. However, this same methodology has not been extended to radical-containing organic electronic systems. This is despite the promise that many of these materials show with respect to charge, energy, and spin transfer (e.g., spin-manipulating) platforms that are not always well-addressed by closed-shell conjugated polymers.^{5,6} Thus, there is a critical need to establish the key interactions of stable organic radicals with macromolecules and their role as charge and energy transfer moieties in organic electronic systems.

Stable organic radicals, which contain one or more unpaired electrons in their molecular structure, can undergo oxidation or reduction to form stable ionic species. Therefore, charge can be transferred to (or from) individual radical sites and transported within specific domains of these materials through electron self-exchange reactions in the solid state. As with conjugated materials, radicals are classified based upon whether they are preferentially oxidized (p-type) or reduced (n-type). Materials capable of readily undergoing both types of redox reactions (i.e., to form either a cationic or anionic species) are referred to as ambipolar. Radical materials are also frequently referred to as “open-shell” materials, indicating that they have partially-filled frontier molecular orbitals, to distinguish them from traditional “closed-shell” materials where these orbitals are completely filled. In recent years, the potential value of these radical-based materials has been demonstrated through conducting polymer⁷ applications and with their utilization as active interfacial-modifying layers in organic and perovskite solar cells,^{8,9} organic field-effect

transistors,¹⁰ and as dopants in thermoelectric applications.^{11–13} Additionally, the non-zero spin of the stable radical species makes them excellent candidates for applications where manipulation of the spin states within a given system are desired.¹⁴ While radical-based materials are now being used in conjunction with conjugated polymers, the fundamental interactions and energy transfer events in these closed-shell–open-shell hybrid composites have not been well illustrated in the literature. Indeed, recent results looking at radical moieties covalently linked to a conjugated polymer backbone illustrate the importance of tuning the energetic interactions between both functionalities to optimize the end behavior of the composite material, in this case, for organic radical battery applications.^{15–17} In order to more effectively establish the potential application space of this emerging class of materials, the interfacial and energetic interactions between conjugated materials and radical-based materials must be deciphered in full.

Specifically, the behavior of the excited states in conjugated polymer systems can be elucidated by evaluating the fluorescent behavior of the macromolecules. In a system of two different molecular species, the quenching of fluorescence is a direct reflection of the intermolecular interactions of the pair.¹⁸ Many conjugated polymer species are fluorescent, and recent studies have demonstrated that fluorescent radical species containing conjugated units exist, which are being actively researched for utilization in OLEDs as their emission from doublet excited states elegantly avoids the 75% loss in quantum efficiency caused by formation of triplet excited states in conventional closed-shell materials.^{19,20} Nevertheless, the vast majority of stable open-shell materials are non-fluorescent, owing to their open-shell electronic structure, which facilitates non-radiative decay of their excited states. Based on this concept, open-shell moieties such as the 2,2,6,6-tetramethylpiperidine-1-oxyl (TEMPO) radical have often been used as fluorescence quenchers for a variety of soft materials including both conjugated small molecules^{21–25} and quantum dots.^{26–28} In these studies, a variety of mechanisms, including electron transfer, resonance energy transfer, and enhanced intersystem crossing, have been proposed. Here, we establish the principal molecular interactions by which fluorescence quenching between a radical species and a specific conjugated polymer, poly(3-hexylthiophene) (P3HT) occurs, as P3HT has served as an oft-used material in many organic electronic applications.²⁹ Through a combination of experiment and simulation, we demonstrate that Förster Resonance Energy Transfer (FRET) is the primary mechanism by which the fluorescence quenching occurs in P3HT for radical species that absorb light strongly within the visible range, and that radical species with low optical

absorption coefficients do not show significant quenching behavior. Thus, certain interactions become improbable, which allows for the strategic design of systems that utilize both conjugated and radical species. This key point has significant implications in the development of coupled closed-shell conjugated polymer-radical molecule systems and interfaces with tunable directional energy transport.

4.3 Materials and Methods

4.3.1 Materials

The 4-hydroxy-2,2,6,6-tetramethylpiperidine-1-oxyl (TEMPO) radical (97%), galvinoxyl radical, L-ascorbic acid (99%), sodium hydride (95%), anhydrous chloroform (> 99%), and ethanol (200 proof) were purchased from Sigma-Aldrich. The 2-phenyl-4,4,5,5-tetramethylimidazoline-3-oxide-1-oxyl (PTIO) radical (> 98%) was purchased from TCI America, sodium hydroxide (> 98%) was purchased from Honeywell, poly(3-hexylthiophene) (P3HT) ($M_n \sim 60 \text{ kg mol}^{-1}$) was purchased from Rieke Metals, and phenyl- C_{61} -butyric acid methyl ester (PCBM) was purchased from Nano-C. All materials were used as received. Glass slides were purchased from Delta Technologies, and fused silica slides were purchased from Quartz Scientific, Inc.

4.3.2 Solution Phase Fluorescence Quenching

To generate the samples for the fluorescence quenching experiments, a solution of 0.01 mg of P3HT per 1 mL of chloroform was created (60 μM in terms of the number of thiophene repeat units). Quencher solutions composed of 3.4 mg mL⁻¹ TEMPO, 4.7 mg mL⁻¹ PTIO, 8.4 mg mL⁻¹ galvinoxyl, and 18.2 mg mL⁻¹ PCBM in chloroform were mixed in order to make each solution have a molar concentration of 20 mM. Using a transfer pipette, 3 mL of the P3HT solution were added to a cuvette for fluorescence measurements. A cap was placed over the cuvette to minimize solvent evaporation. The fluorescence spectrum of the solution was measured using a Cary Eclipse Fluorescence Spectrophotometer over a wavelength range of $525 \text{ nm} \leq \lambda \leq 900 \text{ nm}$ with an excitation wavelength of 500 nm. Afterwards, 15 μL of a specific quencher solution were added to the P3HT solution using a transfer pipette. This resulted in a quencher concentration of 0.1 mM. The pipette was pumped multiple times to ensure mixing, then the cuvette was capped. The

fluorescence spectrum was obtained, and the procedure was repeated, increasing the quencher concentration in 0.1 mM increments up to a concentration of 1.0 mM.

After acquiring the fluorescence spectra, the ultraviolet-visible (UV-Vis) absorbance spectra were acquired, using a Cary 60 Spectrometer over a wavelength range of $250 \text{ nm} \leq \lambda \leq 1,100 \text{ nm}$ with chloroform serving as a blank. This was done within three hours of taking the fluorescence spectra, using the same P3HT and quencher solutions that were prepared previously. To minimize degradation, as P3HT and the galvinoxyl radical (in solution) are air-sensitive, the solutions were divided in half after preparation. One half was used for the fluorescence measurements and the other half was kept under nitrogen atmosphere in a glovebox until the absorbance measurements were performed. The P3HT and quencher solutions were mixed using the same procedure as for the fluorescence measurements: 15 μL of quencher solution were added to the P3HT solution, increasing the concentration to 0.1 mM, and the absorbance spectra were taken. This was repeated up to a quencher concentration of 1.0 mM.

As the galvinoxyl and PTIO radicals and PCBM all have a high absorbance at the excitation and emission wavelengths, a significant decrease in the fluorescence signal occurred due to attenuation of the excitation beam and the emitted light. This apparent quenching, which is more accurately described as the inner-filter effect, was not caused by any actual interaction of the chemical species, and the raw data were corrected to account for this phenomenon. For a fluorimeter where the entire width of the sample is excited and the entire length is collected by the detector, as with the particular instrument used in the experiment,³⁰ the appropriate formula (see Section 4.7 - Electronic Supplementary Information for the derivation of this equation) is as follows.

$$I_{corr} = \frac{\ln(10)^2 A_{Ex} A_{Em}}{(1 - 10^{-A_{Ex}})(1 - 10^{-A_{Em}})} I_{obs} \quad (4.1)$$

Here, I_{corr} is the corrected intensity, I_{obs} is the measured (observed) intensity, and A_{ex} and A_{em} are the absorbance values of the solution over the entire cuvette length at the excitation and emission wavelengths, respectively.³¹

4.3.3 Quencher Anion Absorbance Measurements

To measure the absorbance spectrum of the galvinylate anion, a 4 mM (1.68 mg mL⁻¹) solution of galvinoxyl in ethanol was prepared, along with a 40 mM (7.0 mg mL⁻¹) solution of ascorbic acid and a 100 mM (2.4 mg mL⁻¹) solution of sodium hydride, both in ethanol. The galvinoxyl and ascorbic acid solutions were mixed in equal proportions to yield a quenched galvinoxyl solution, and this solution was mixed with a proportional amount of sodium hydride solution to yield a solution containing 1 mM of the galvinylate anion. Another solution consisting of 1 part ethanol, 1 part ascorbic acid solution, and 2 parts sodium hydride solution was also prepared to use as a baseline for absorbance measurements. After mixing, both solutions were diluted to 1/100th of their original concentration. The UV-Vis absorbance spectrum of the dilute galvinylate solution was acquired, using a Cary 60 Spectrometer over a wavelength range of 300 nm ≤ λ ≤ 1,100 nm with the dilute ascorbic acid/sodium hydride solution serving as a blank.

To measure the absorbance spectrum of the PTIO anion, a 4 mM (0.93 mg mL⁻¹) solution of PTIO in water was prepared, along with a 40 mM (7.0 mg mL⁻¹) solution of ascorbic acid and a 100 mM (4.0 mg mL⁻¹) solution of sodium hydroxide, both in water. As above, the PTIO solution was mixed with the ascorbic acid and sodium hydroxide solutions to yield a solution containing 1 mM of the PTIO anion. A baseline solution consisting of ascorbic acid and sodium hydroxide without the PTIO radical was also prepared. After mixing, both solutions were diluted to 1/10th of their original concentration. This dilution is different than what was used for the galvinylate anion, due to the weaker absorbance of the PTIO anion. The UV-Vis absorbance spectrum of the dilute PTIO solution was acquired in the same manner using the dilute ascorbic acid-sodium hydroxide solution as a blank.

4.3.4 Thin Film Preparation

All solutions were prepared with a P3HT concentration of 10 mg mL⁻¹ in chloroform (60 mM repeat units). Stock solutions of 6.7 mM of each small molecule quencher were prepared in chloroform. For each solution, the appropriate amounts of chloroform and stock solution were added to the P3HT powder to provide for molar loadings of quencher between 0 and 10% (on a molar basis) in 2% increments. After preparation of the solutions in a nitrogen atmosphere, the solutions were allowed to stir for at least 3 h. Depending on the experiment, either 13.6 mm × 15.6

mm borosilicate glass or 1-inch square fused silica substrates were cleaned by sonication for 10 minutes each in acetone, chloroform, and isopropyl alcohol, in a sequential manner. Afterwards, the appropriate solution was spun-coat on to the substrates at 1,500 rpm for 60 s in a nitrogen-filled glove box.

4.3.5 Thin Film Fluorescence Quenching

Thin films were cast onto fused silica slides using the above procedure. Once cast, the absorbance spectra of the films were measured using a Cary 60 Spectrometer over a wavelength range of $190 \text{ nm} \leq \lambda \leq 1,100 \text{ nm}$ with a clean fused silica slide as a blank. Within an hour of taking the absorbance spectra, the fluorescence spectra were acquired using an Edinburgh Instruments FLS980 steady-state fluorescence spectrometer over a wavelength range of $550 \text{ nm} \leq \lambda \leq 800 \text{ nm}$ with an excitation wavelength of 500 nm. A 550 nm colored glass long-pass filter purchased from ThorLabs Inc. was used as an emission filter.

4.3.6 Ensemble Transient Absorption Spectroscopy Measurements

Thin films were prepared on borosilicate glass substrates following the above procedure, except the concentrations of solids were doubled to yield thicker films with higher optical density values. The films were also encapsulated to prevent degradation during the measurements. This was achieved by placing the samples film side down on glass coverslips and sealing with a clear epoxy (JBWeld Clear Weld). Transient absorption spectra of the films were measured by a femtosecond pump-probe system with a home-built transient absorption spectrometer. Laser pulses at 1,030 nm with 250 fs duration were generated by a 400 kHz amplified Yb:KGW laser system (PHAROS, Light Conversion Ltd.). The probe beam was a white light continuum beam spanning the $450 \text{ nm} \leq \lambda \leq 950 \text{ nm}$ spectral region, created by focusing 5% of the 1,030 nm fundamental output onto an yttrium aluminum garnet (YAG) crystal (4.0 mm thick). The rest of the output pumps an optical parametric amplifier (OPA, TOPAS-Twins, Light Conversion Ltd.) to generate pump pulses with tunable photon energies for the transient absorption experiments.

4.3.7 Atomic Force Microscopy (AFM) Imaging

Thin films were prepared on borosilicate glass substrates following the same procedure that was used for the steady-state thin film absorption measurements. AFM images were acquired using a Veeco Dimension 3100 AFM operating in tapping mode with MikroMasch HQ:NSC15/Al BS tips.

4.3.8 X-ray Diffraction

Borosilicate glass substrates were cleaned and P3HT-quencher solutions were prepared as before. 1 mL of solution was drop-cast onto the clean substrates on a hot plate at 60 °C in order to form a thick, opaque film that contained no solvent. For the x-ray diffraction data of PCBM and the radical small molecules, the films were prepared in the same manner as above using solutions of the material in chloroform. The data were obtained using a Rigaku SmartLab X-ray diffractometer with a Cu K α radiation source. All diffraction data were collected in air at room temperature.

4.3.9 Computational Methods

Charge transfer rates were modeled via semi-classical Marcus theory, using density functional theory (DFT) to calculate the various Marcus parameters for each molecular species in combination with P3HT. The charge-transfer rate is given by the following expression.³²

$$k_{ET} = \frac{2\pi}{\hbar} (H_{AB})^2 \frac{1}{\sqrt{4\pi\lambda k_B T}} \exp\left(-\frac{(\Delta G_0 + \lambda)^2}{4\lambda k_B T}\right) \quad (4.2)$$

Here H_{AB} is the electronic coupling between the initial and final electronic states, λ is the reorganization energy, and ΔG_0 is the Gibbs free energy for the charge transfer. To reduce the computational time, quaterthiophene (4T) was used as a model for P3HT and the *tert*-butyl groups of the galvinoxyl radical were replaced with methyl groups, referred to hereafter as GxMe. The optimized ground state geometry for all the neutral species, the 4T cation, and the anions of the radical species were computed at the dispersion-corrected³³ B3LYP³⁴/def2-TZVP³⁵ level of theory,

as implemented in ORCA.³⁶ All geometries were confirmed by frequency calculations. For the calculation of the reorganization energy, additional single-point calculations were performed on each of the neutral species in the optimized charged geometries, and the charged species in the optimized neutral geometries. To determine the optimal separation of 4T with the individual radicals, a series of single-point calculations were performed on pairs of molecules to characterize the radial dependence of the ground state energy (Figure 4.S1). While the equilibrium vacuum separations for the pairs were not all equal, a representative value of 4.5 Å was used in all of the following calculations for direct comparison. Finally, the excited-state energy for 4T was also calculated using time-dependent DFT (TDDFT) at the same level of theory.³⁷

The Coulombic interaction of the cation and anion leads to a substantial stabilization of the final charge transfer state, which was calculated by computing the Coulomb potential between the nuclei on the cation and the anion, using the CHELPG point charges on each of the nuclei as computed by ORCA for the isolated 4T cation and various anions. The following formula was used.

$$E_{Coul} = \frac{1}{4\pi\epsilon_0} \sum_i^{4T \text{ Atoms}} \sum_j^{Quencher \text{ Atoms}} \frac{q_i q_j}{|\vec{r}_i - \vec{r}_j|} \quad (4.3)$$

Here ϵ_0 is the permittivity of free space, q_i and q_j are the CHELPG charges on the 4T cation and quencher anion nuclei, \vec{r}_i and \vec{r}_j are the position vectors of the 4T cation and quencher anion nuclei, and i and j are summed over the 4T cation and quencher anion atoms, respectively. From these calculations, the Gibbs free energy change was calculated using the following formula.

$$\Delta G_0 = (E_{4T^+,CG} + E_{Q^-,CG} + E_{Coul}) - (E_{4T,NG} + E_{Q,NG} + \Delta E_{Ex,4T}) \quad (4.4)$$

Here, the subscripts CG and NG refer to the single point energy of the optimized geometries of the charged and neutral species, respectively; $\Delta E_{Ex,4T}$ refers to the energy difference between the first singlet excited state and the ground state of 4T; and ΔE_{Coul} refers to the potential energy from the coulombic attraction between the two charged molecules. The reorganization energy was calculated from the following equations.

$$\lambda = \lambda_{inner} + \lambda_{outer} \quad (4.5)$$

$$\lambda_{inner} = \frac{1}{2} \left\{ [(E_{4T,CG} + E_{Q,CG}) - (E_{4T,NG} + E_{Q,NG})] + [(E_{4T^+,NG} + E_{Q^-,NG}) - (E_{4T^+,CG} + E_{Q^-,CG})] \right\} \quad (4.6)$$

$$\lambda_{outer} = \frac{1}{4\pi\epsilon_0} \left(\frac{1}{2r_{4T}} + \frac{1}{2r_Q} - \frac{1}{R} \right) \left(\frac{1}{n^2} - \frac{1}{\epsilon} \right) \quad (4.7)$$

Here ϵ is the static dielectric permittivity of the material, r_{4T} and r_Q are the radii of the 4T and quencher species, R is the distance between the 4T and quencher molecules, and n is the refractive index of the bulk material. For the inner reorganization energy (i.e., the energy difference due to the change in molecular geometry between products and reactants), Marcus theory assumes that the energy difference between the neutral molecules in the charged geometry and in the neutral geometry is the same as the energy difference between the charged molecules in the neutral geometry and in the charged geometry. In practice, these will not exactly be equal. Therefore, both differences were calculated and the average was taken. For the outer reorganization energy (i.e., the energy difference due to the relaxation of the surrounding media), the radii of the 4T and quencher species were calculated by measuring the volume of each species using the Chimera software package.^{38,39} The radius of a sphere with the equivalent volume as that of the chemical species was used as its radius. As before, 4.5 Å was used as the 4T-quencher distance. For the dielectric permittivity and refractive index, the values for P3HT, which are 3 and 1.4 respectively,^{40,41} were used.

Finally, the electronic coupling was calculated as the off-diagonal Fock matrix elements corresponding to the 4T LUMO ($\phi_{4T,LUMO}$) and radical SOMO orbitals ($\phi_{Q,SOMO}$) of the isolated molecules, with the Kohn-Sham Fock matrix of the dimer at the neutral equilibrium separation distance ($\mathbf{F}_{4T,Q}$):

$$H_{AB} = \langle \phi_{4T,LUMO} | \mathbf{F}_{4T,Q} | \phi_{Q,SOMO} \rangle \quad (4.8)$$

The rate at which FRET occurs is given by the following expression.^{18,42}

$$k_{FRET} = \frac{Q_D \kappa^2}{\tau_D R^6} \left(\frac{9000 \ln 10}{128 \pi^5 N n^4} \right) J = \frac{1}{\tau_D} \left(\frac{R_0}{R} \right)^6 \quad (4.9)$$

$$J = \frac{\int_0^\infty F_D(\lambda) \epsilon_Q(\lambda) \lambda^4 d\lambda}{\int_0^\infty F_D(\lambda) d\lambda} \quad (4.10)$$

Here Q_D is the quantum efficiency of the donor (0.01 for P3HT as a thin film⁴³); κ is the dipole orientation factor, which is assumed to be 2/3 for randomly oriented dipoles; τ_D is the excited state lifetime of the donor (400 ps for P3HT as a thin film⁴³); R is the donor-quencher distance; N is Avogadro's constant; n is the refractive index of the medium, and J is the overlap integral. The equation can be simplified by collapsing many of the parameters of the system into a single parameter R_0 , which corresponds to the distance at which the FRET rate is equal to the natural decay rate of the excited state. In Equation 4.10, λ is the photon wavelength, $F_D(\lambda)$ is the relative fluorescence intensity of the donor species at the wavelength (normalized so that $\int_0^\infty F_D(\lambda)d\lambda = 1$), and $\varepsilon_Q(\lambda)$ is the molar absorptivity of the quencher species at the given wavelength.

4.4 Results and Discussion

Fluorescence quenching activity was observed to a variable degree for some, but not all, of the interacting radical-polymer blends evaluated. Figure 4.1 shows a Stern-Volmer plot of the fluorescence intensity of solutions of P3HT and the various radical quencher species versus the concentration of the quencher. For comparison, a solution mixture of P3HT and PCBM is included, as PCBM acts as an efficient fluorescence quencher for a wide variety of conjugated polymers,⁴⁴ including polythiophenes.^{45,46} All solution intensities were corrected for the inner filter effect (see the ESI for details) due to the significant absorption of the quencher species, as shown in Figure 4.S2. Note that the full fluorescence spectra of the different mixtures are shown in Figure 4.S3. The quenching behavior for the galvinoxyl radical is on par with that demonstrated by PCBM, suggesting that the galvinoxyl radical is an effective fluorescence quencher for P3HT. PTIO also shows significant quenching behavior, while TEMPO shows insignificant quenching behavior at the concentrations probed. In particular, PCBM shows a Stern-Volmer constant of 0.56 mM⁻¹, the galvinoxyl radical shows one of 0.46 mM⁻¹, the PTIO radical shows one of 0.29 mM⁻¹, and the TEMPO radical shows one of 0.06 mM⁻¹ (Figure 4.1). It is worth noting that, for diffusion limited quenching, direct comparisons of the Stern-Volmer constants can only be made for molecules of similar sizes. However, theory predicts that larger molecules will react slower in a diffusion-limited regime, due to the increased drag force acting on the molecule.^{47,48} Therefore, the relative trend observed in the quenching behavior would be magnified if molecular size were taken into account.

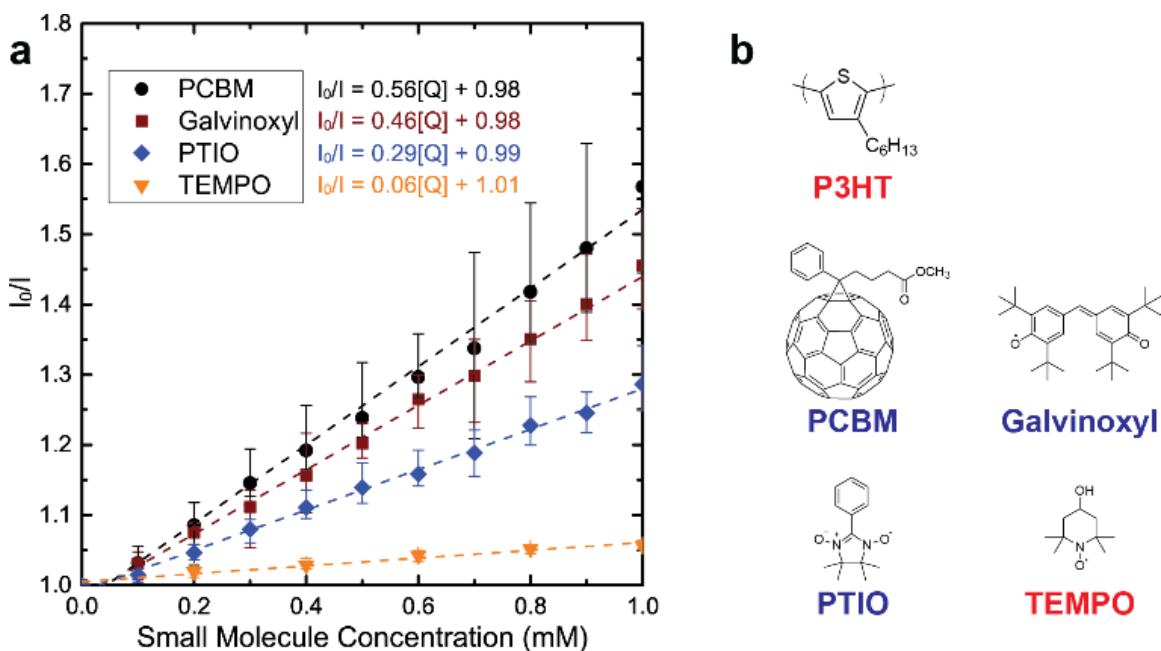


Figure 4.1. (a) Stern-Volmer plots of the corrected fluorescence intensity of P3HT solutions in chloroform (60 μM of thiophene repeat units) and small molecules that serve as quenching sites for the photoexcited P3HT. The vertical axis represents the intensity of a P3HT-only solution divided by the corrected intensity of a solution consisting of P3HT and the quencher at a specific concentration. These data demonstrate that the galvinoxyl and PTIO radical species have nearly the same quenching ability for P3HT as PCBM does in solution; conversely, TEMPO does not demonstrate this property. Error bars show the range of values measured for each concentration of quencher. The excitation and emission wavelengths for all of the measurements were 500 nm and 578 nm, respectively. The raw data were corrected for the inner filter effect. (b) Molecular structures of species used in this work. Electron-donating (p-type) species are indicated in red, while electron-accepting (n-type) species are indicated with blue labels.

A similar trend in relative quenching behavior is seen for thin film composites of P3HT blended with the quencher species (Figure 4.2). This suggests that a similar mechanism is responsible for the quenching behavior in both solution and in thin films, allowing the nature of the quenching interaction to be examined from both experimental platforms. In the interest of translating these results to future device applications, we primarily utilized samples in the thin film state to probe these mechanisms. Absorbance data were used to ascertain the underlying nature of the quenching interaction in these soft materials systems. As can be seen from Figure 4.3, and the inset of Figure 4.3c, there is no apparent shift in the absorbance peaks and an absence of the appearance of any new peaks. This is seen in solution phase as well (Figure 4.S2), and in those measurements, the total absorbance follows the Beer-Lambert law for the absorbance of the

quencher species in a P3HT solution. That is, the final curve is the sum of the two independent absorption spectra, whose magnitude at all points is proportional to the concentration of species present. This suggests that the quenching observed is a dynamic quenching mechanism and not due to the formation of a non-fluorescent supramolecular complex. A blue shift in the peak near 500 nm for P3HT is visible upon the addition of PCBM, as seen in Figure 4.3a, which suggests that PCBM is disrupting the crystalline packing of the P3HT in the solid state, which is consistent with previous reports.⁴⁹

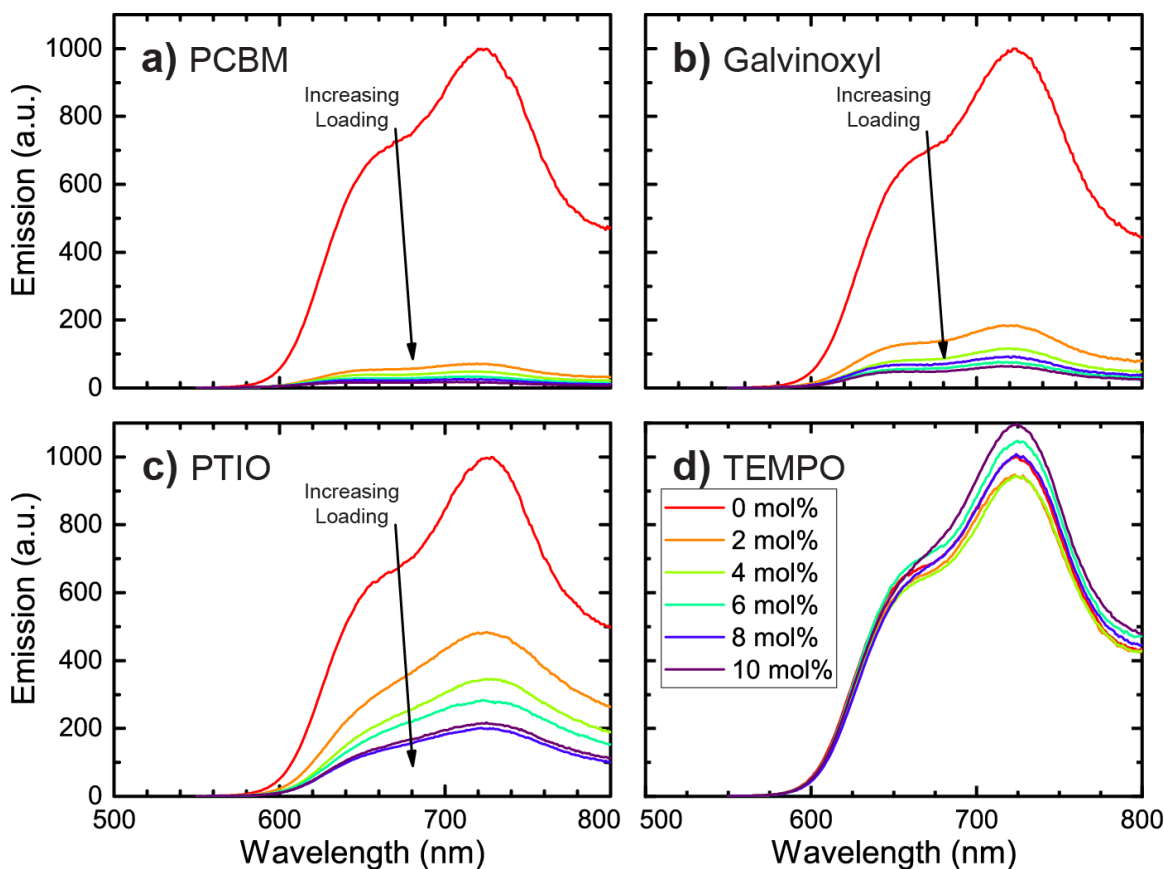


Figure 4.2. Reduction in intensity of fluorescence spectra of P3HT thin films with increasing loadings of (a) PCBM, (b) the galvinoxyl radical, (c) the PTIO radical, and (d) the TEMPO radical. As with the solution-state measurements, the PTIO and galvinoxyl radicals show a reduction in the P3HT fluorescence intensity in the solid state while the TEMPO radical does not. The excitation wavelength was 500 nm.

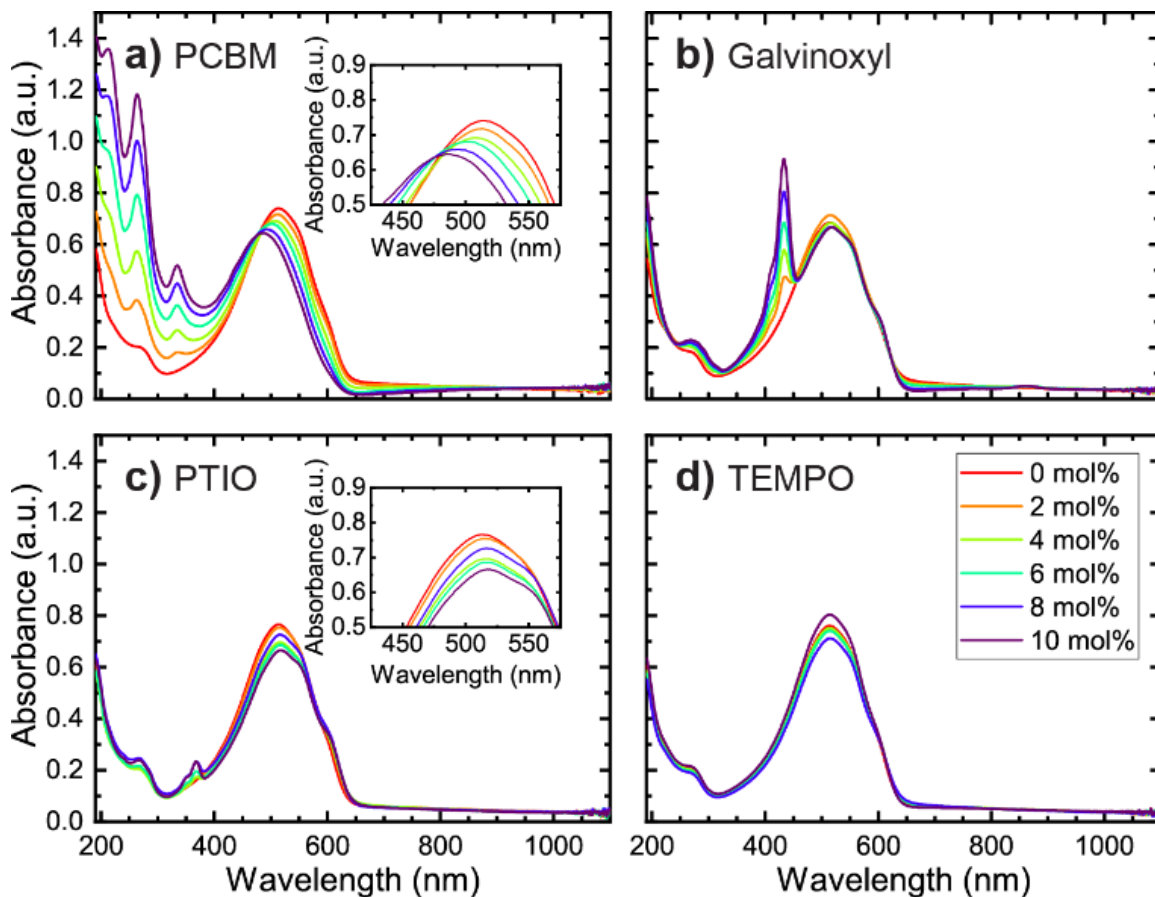


Figure 4.3. Absorbance spectra of P3HT thin films with increasing amounts of (a) PCBM, (b) the galvinoxyl radical, (c) the PTIO radical, and (d) the TEMPO radical. These data demonstrate that no supramolecular complexes are forming in the ground state between P3HT and the radical species, as the peak locations for P3HT and the radical species are unchanged [see inset of (c)]. Moreover, there is no appearance of a lower energy absorption band. PCBM, by contrast, shows a blue-shifting in the P3HT absorption peak [see inset of (a)], most likely because the PCBM disrupts the crystalline packing of the P3HT. The insets show the blue-shift for P3HT-PCBM in greater detail, as compared to P3HT-PTIO, which shows no shift.

Interestingly, this peak shift is not observed in any of the P3HT-radical blends. This is consistent with x-ray diffraction (XRD) measurements, which show that P3HT forms pristine crystalline domains on the nanoscale (Figure 4.4). For the P3HT-radical blends, the (100) and (010) peaks remain in the same location, suggesting that the P3HT crystalline structure is unaffected by the presence of the radical species. A P3HT-PCBM blend, by contrast, shows a suppression of the (010) peak for P3HT with no appearance of the PCBM crystal peaks (Figure 4.4a), which also suggests that PCBM disrupts the crystalline packing of the P3HT, but does not form its own phase at these low loadings of the quenching species. For the P3HT-Galvinoxyl and P3HT-TEMPO

blends, the primary peak corresponding to the radical species is seen in the blended films, suggesting formation of pure crystalline phases for the radical species (Figure 4.4b and d). Interestingly, two new peaks are seen for the P3HT-PTIO blend, which do not correspond to any peaks seen in either pure compound (Figure 4.4c). As the peaks corresponding to the pristine PTIO radical are not seen, this suggests that the crystal structure of the PTIO radical is disrupted. However, as a pristine P3HT phase is present in the blended film, it is still reasonable to conclude that the quenching behavior seen in P3HT-PTIO blends is not due to a change in the crystal structure of the fluorescent species.

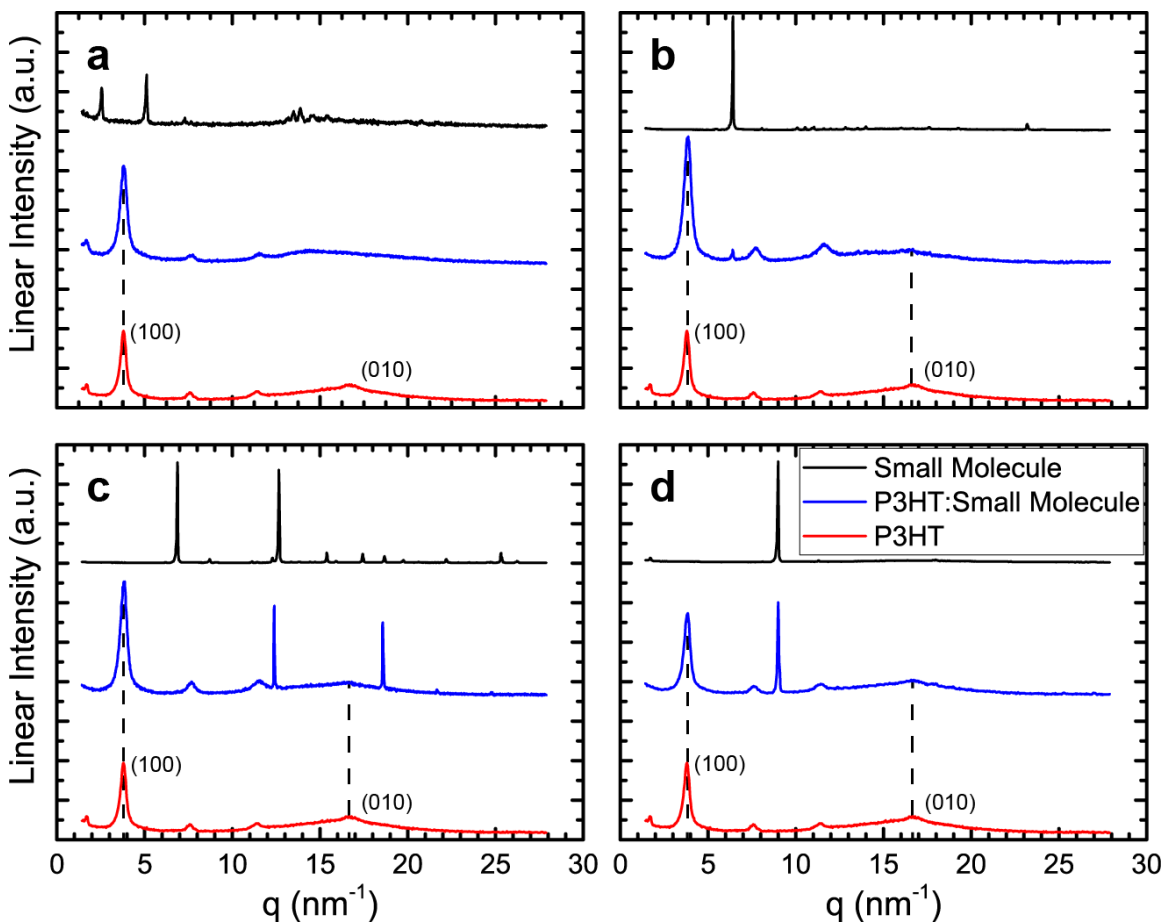


Figure 4.4. XRD data of P3HT thin films with small molecule additives of (a) PCBM, (b) the galvinoxyl radical, (c) the PTIO radical, and (d) the TEMPO radical present at a loading of 10% (on a molar basis), compared to those of pristine P3HT and the pristine small molecule species. For the radical species, peaks corresponding to those seen for pristine P3HT appear in the XRD spectra of the combined films (blue) with minimal shift in peak locations, indicating the existence of a pure P3HT phase in the film. This is in contrast with the P3HT-PCBM film, which shows no (010) peak corresponding to the π - π stacking, most likely because the PCBM disrupts the crystalline packing of the P3HT. The spectra are shifted vertically and the small molecule signals are scaled in order to provide clarity in data presentation.

These trends in quenching data and nanoscale structure are consistent with one of two interaction mechanisms: either (1) photoinduced charge transfer or (2) excited state transfer through a Förster Resonance Energy Transfer (FRET) or Dexter Energy Transfer pathway.¹⁸ The excited state transfer mechanisms are similar in that they both result in the fluorescent molecule, or donor, being returned to the ground electronic state, while the quencher, or acceptor, is promoted to an excited state. Both require an electronic transition for both the donor and acceptor with the same energy change. However, they differ in the mechanism by which they occur. FRET occurs via a resonant interaction between the excitation dipoles,⁴² while Dexter transfer happens due to a concerted electron and hole transfer from the donor to the acceptor.⁵⁰ Two functional differences exist between the two mechanisms. First, as FRET is mediated by dipole interactions its rate is inversely proportional to the distance to the sixth power, while Dexter transfer, which relies on overlap between the frontier molecular orbitals of the donor and acceptor species, shows approximately an exponential dependence on distance. Therefore, FRET is able to operate at large distances, while Dexter transfer is limited to molecules in close proximity. Second, for FRET to occur both excited state transitions require a transition dipole, while Dexter transfer can occur as long as two isoenergetic electronic transitions exist, allowing for the acceptor to be promoted to a non-optically active excited state or one with a different spin state. Because of these two factors, typically if there is an overlap of the fluorescence spectrum of the donor with the absorbance spectrum of the acceptor, FRET is considered to be the dominant mechanism, with Dexter transfer being considered only when FRET is not possible.

Both the galvinoxyl and PTIO radicals show significant absorbance coefficients within the region of the spectrum where P3HT emits, both in solution phase and in solid state (Figure 4.5), due to their extensive π -conjugation. TEMPO, by contrast, shows minimal absorbance in that region. This spectral overlap suggests that FRET may be the mechanism for the observed quenching. Because of the discussion above and because these transitions are dipole-allowed, we will not consider Dexter further, though its contribution could be measured by using covalently-linked P3HT-radical hybrid materials and tracking the distance dependence of the quenching. However, the observed trend in quenching behavior is also consistent with photoinduced electron transfer as a mechanism. In thin films, the fluorescence quenching of P3HT by PCBM is caused by such a mechanism,⁵¹ and based upon the observed redox behavior of the radical species, a photoinduced electron transfer mechanism is energetically viable.

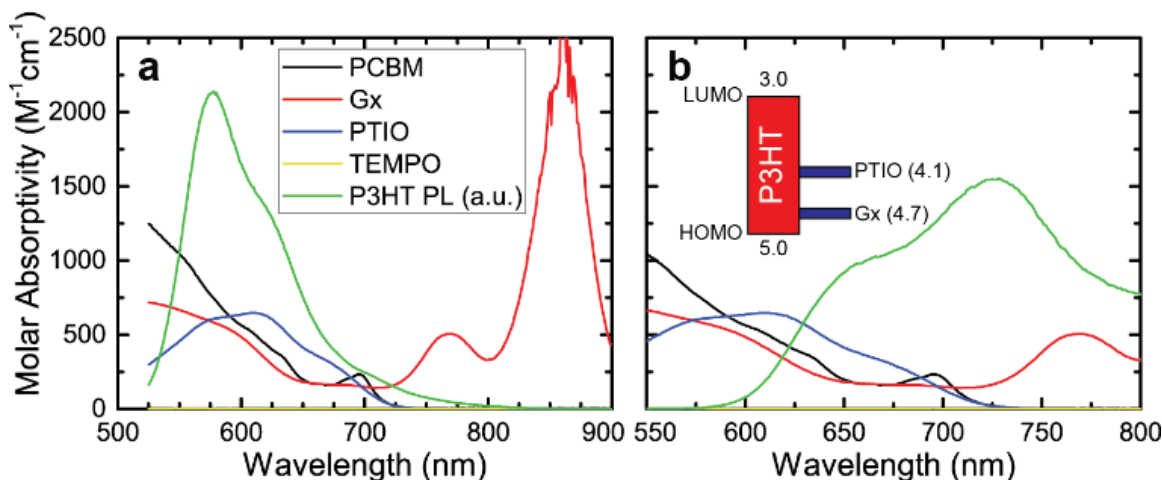


Figure 4.5. Overlap of the P3HT emission spectrum (green line) with the absorbance spectra of the quencher molecules. (a) The emission spectrum of a 60 μM P3HT solution in chloroform, and (b) the emission spectrum of a P3HT thin film. The inset shows the frontier orbital (HOMO and LUMO) energies of P3HT and the reduction potentials, in units of eV removed from free vacuum, of the two n-type open-shell species: the PTIO and galvinoxyl radicals.

The galvinoxyl and PTIO radicals show a reduction potential of 4.7 and 4.1 eV below vacuum, respectively.^{52,53} These values are farther-removed from vacuum than that of the lowest unoccupied molecular orbital (LUMO) energy of P3HT, which is 3.0 eV below vacuum, indicating that an electron transfer from an excited P3HT to one of these radical species could occur (inset of Figure 4.5). The TEMPO radical, by contrast, has never been observed to form a stable anion species, suggesting that it would be unable to act as an electron acceptor. The presence of π -conjugation may also play a role in the stability of the anion species, though introduction of electron-withdrawing groups has also been utilized to design n-type radical species.⁵⁴ Nevertheless, as both mechanisms are consistent with the observed trend, and have similar origins from a molecular structure standpoint, further characterizations are necessary to quantify the relative importance of the different mechanisms.

To uncover which mechanisms are at play in these optoelectronically-active blends, transient absorption spectra of the P3HT-radical blends were compared with the spectrum of pristine P3HT (Figure 4.6). The spectrum of pristine P3HT shows a bleach signal between 500 and 600 nm, corresponding to the ground-state bleach (GSB), as well as a photoinduced absorption between 600 and 700 nm, corresponding to photoinduced absorption of delocalized polarons (i.e., positively-charged P3HT segments within crystalline regions of the thin film).⁵⁵ Comparing this

spectrum with the spectra associated with those of the P3HT-radical blends shows little qualitative difference. That is, no additional signals corresponding to bleaching of the radicals or photoinduced absorption of their anions can be detected. In the case of the galvinoxyl radical, the main absorbance peak is found at 400 nm, outside the range of the detector. The galvinylate anion, however, absorbs strongly at 560 nm, well within the range measured (Figure 4.S4). No clear difference can be seen between the spectra at this point, suggesting that photoinduced charge transfer is not at play, despite the energetic favorability of such a transfer. In the case of PTIO, the main absorbance peak overlaps with that of P3HT, and the anion absorbs around 325 nm, also outside the range that can be measured by the available equipment. Nevertheless, a clear difference is seen between the P3HT-radical blends and the P3HT-PCBM blend, which does show charge transfer. A larger polaron signal is present, and the signal persists for the entire measurement, which is consistent with photoinduced charge separation.^{51,56,57} The lack of similar signals suggests that charge transfer is not occurring in the P3HT-radical blends.

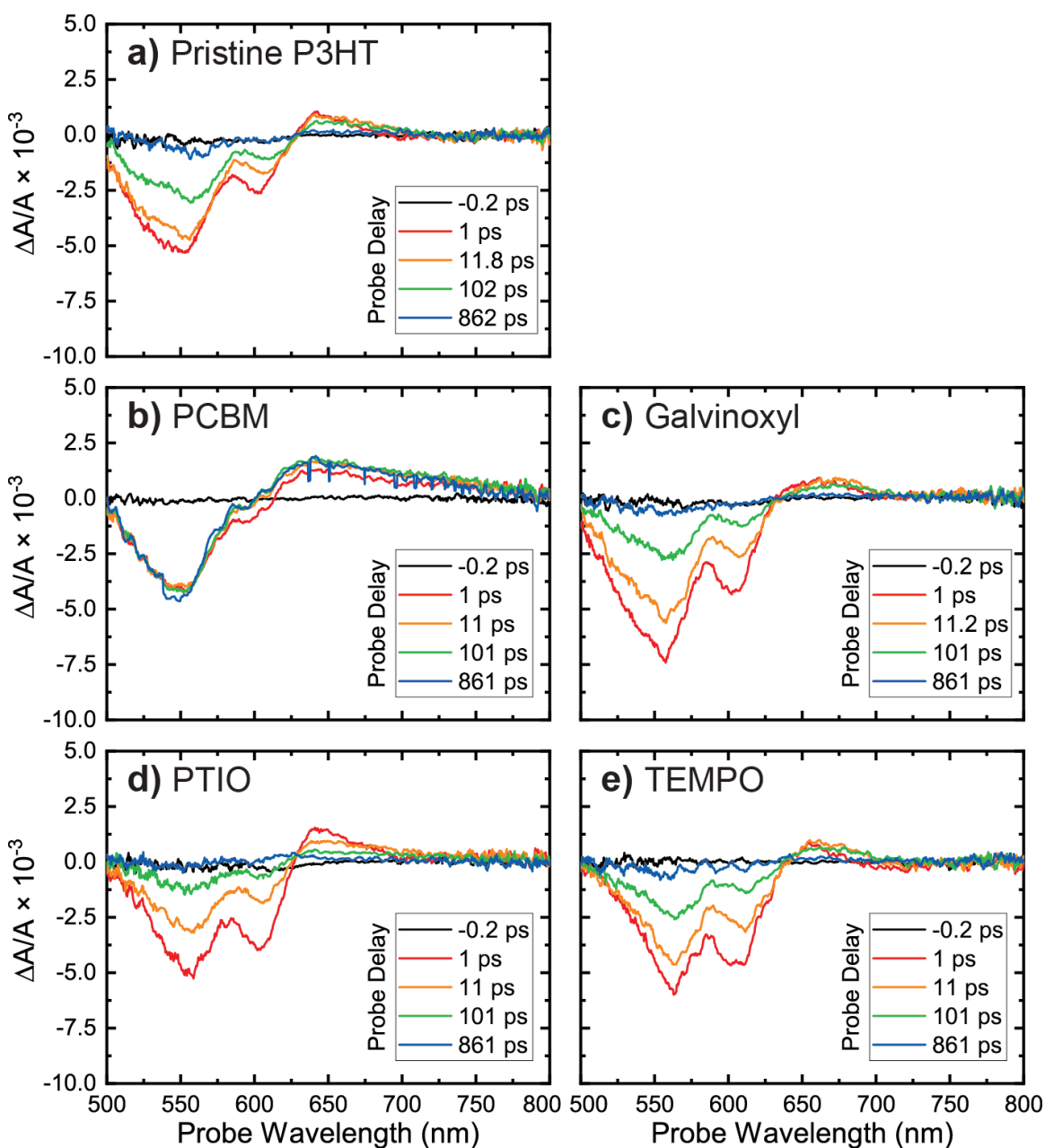


Figure 4.6. Representative transient absorption spectra of a (a) pristine P3HT film, (b) P3HT-PCBM blend, (c) P3HT-Galvinoxyl blend, (d) P3HT-PTIO blend, and (e) P3HT-TEMPO blend at selected delay times. The negative signal from 500 to 625 nm corresponds to the ground-state bleaching of the P3HT film, while the positive signal from 625 to 700 nm corresponds to delocalized polarons in the P3HT film. The pump wavelength was 400 nm. All quencher species were added to the thin films at a 10 mol% loading.

The data in the time domain reveal a clear difference in behavior between the pristine P3HT and the P3HT-radical composite films (Figure 4.7). For the P3HT-radical blends, both the GSB and the polaron signals decay significantly more rapidly than for the pristine film, suggesting that the radicals enhance the rate of ground state recovery. This is in stark contrast to the P3HT-PCBM film, where the ground state bleach and polaron signals persist with minimal decay through the duration of the experiment, due to the long-term charge separation. Additionally, the dynamics of the GSB and polaron signals appear to track each other well for both the pristine and radical-doped films, which suggests that the presence of the radicals has little effect on the formation of polarons within the film.

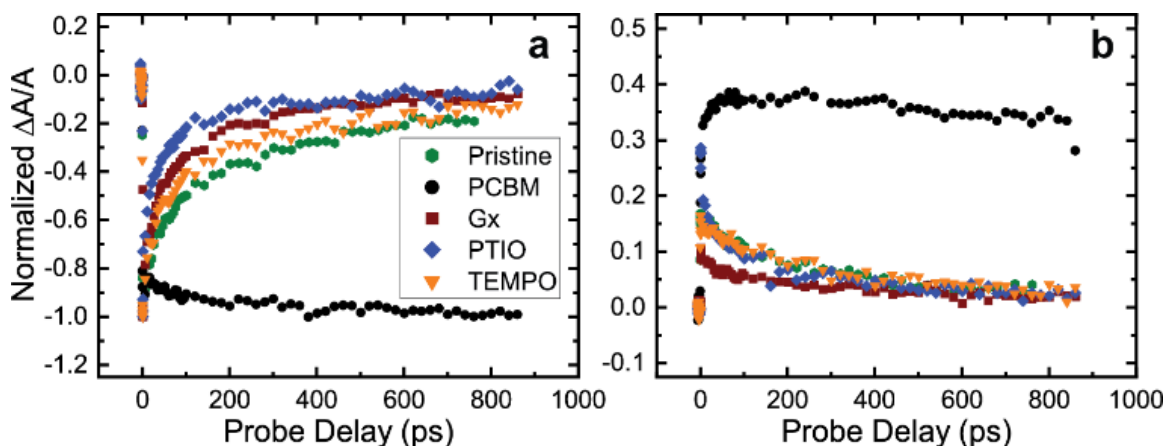


Figure 4.7. Comparison of the dynamics of the transient absorption signals of the P3HT-quencher blends at a probe wavelength of (a) 550 nm (ground-state bleach) and (b) 650 nm (polaron). Each of the radical-containing composites shows a faster decay of both signals over the pristine sample. This is in contrast to the P3HT-PCBM blend, which shows a persistent signal over the course of the measurement that reaches a maximum long after the P3HT-radical blends, due to persistent charge separation. A 10 mol% loading of quencher species was used for the films.

This clear contrast between P3HT-PCBM and the radical signals, as well as the absence of any signals corresponding to the anions of the radical acceptors within the wavelength window probed, suggests that charge transfer is minimal in these blends. However, the increased rate of decay for the GSB is consistent with FRET as a mechanism, as resonant energy transfer results in regeneration of the ground state of the donor. Therefore, FRET appears to be the dominant mechanism behind the observed fluorescence quenching.

To further assist with the determination of the quenching mechanism, computational studies were performed on P3HT in combination with the different quencher species to estimate the rate of the charge transfer reaction and compare this to the FRET rate (see methods section for further details and a description of all the parameters). To reduce the computational time, quaterthiophene (4T) was used as a substitute for P3HT, and the *tert*-butyl moieties on the galvinoxyl radical were replaced with methyl groups, referred hereafter as GxMe. To facilitate a direct comparison, after being oriented in a cofacial manner as described in the ESI, the centroid-centroid distance was set at 4.5 Å. While the equilibrium separation for the 4T-GxMe pair was significantly smaller at 3.9 Å (Figure 4.S1), the reduced steric hindrance of the GxMe molecule compared to Gx means that a larger separation would be expected for a 4T-Gx pairing. This distance is also larger than what is typically seen for studies on photoinduced charge transfer in P3HT-PCBM;^{40,58} again, this is due to the increased steric hindrance from the radical species. The results of the calculations for the charge transfer rates are shown in Table 4.1.

Table 4.1. Calculated Charge Transfer Parameters and Rates for the Radical Species.

Quencher	ΔG_0 (eV)	H_{AB} (meV)	λ_{inner} (eV)	λ_{outer} (eV)	k_{ET} (s ⁻¹)
GxMe	-1.53	-9.2	0.21	0.10	3.8×10^{-8}
PTIO	0.27	-95.6	0.61	0.11	3.7×10^8
TEMPO	0.99	23.2	0.81	0.14	1.9×10^{-4}

As predicted from the orbital energies and the reduction potentials, electron transfer from 4T to GxMe is calculated to be favorable and electron transfer from 4T to TEMPO is unfavorable. Interestingly, electron transfer to PTIO is calculated to be unfavorable, contrary to the predictions from its measured reduction potential. However, this energy is lower than the reorganizational energy. Ultimately, this combined with the large electronic coupling leads to a significant charge transfer rate of 3.7×10^8 s⁻¹. For GxMe, while the electron transfer is energetically favorable, the reaction is significantly within the Marcus inverted region, which results in a negligible charge transfer rate. In the case of TEMPO, the electron transfer is unfavorable and thus the charge transfer rate is also negligible. The insignificant charge transfer rate predicted for the 4T-GxMe pair is inconsistent with charge transfer being the primary mechanism behind the fluorescence quenching interaction.

By utilizing the spectral data and assuming an intermolecular separation of 4.5 Å, the FRET rates can be computed. The calculated values are shown in Table 4.2. As predicted from the spectral overlap, both the galvinoxyl and PTIO radicals show a significant quenching rate through the FRET mechanism. TEMPO, by contrast, gives a rate 4 orders of magnitude slower. Thus, the calculated FRET rates agree with the trend observed in quenching behavior. Additionally, for the PTIO radical, the calculated FRET rate is 3 orders of magnitude faster than the calculated charge transfer rate, which agrees with the lack of observed charge transfer in the experimental results. Therefore, these computational results are consistent with the experimental results and indicate that FRET is the dominant quenching mechanism in the P3HT-radical blends.

Table 4.2. Calculated FRET Parameters and Rates for P3HT-Radical Blends.

Quencher	J ($\text{nm}^4 \text{M}^{-1} \text{cm}^{-1}$)	R_0 (Å)	k_{FRET} (s^{-1})
Galvinoxyl	7.19×10^{13}	13.9	2.2×10^{12}
PTIO	2.95×10^{13}	12.0	9.0×10^{11}
TEMPO	2.34×10^{10}	3.7	7.7×10^8

4.5 Conclusions

The electronic and energetic interactions between open-shell small molecules and a common conjugated polymer, P3HT, in solution and as composite thin films were evaluated in full. Specifically, the fluorescence of P3HT was observed to be effectively quenched by the stable organic open-shell species, the galvinoxyl and PTIO radicals both in solution and as thin films, with quenching performance on par with that of PCBM. The TEMPO radical, by contrast, showed minimal quenching of the P3HT fluorescence. As demonstrated through a combination of computation, steady-state spectroscopy, and ultrafast spectroscopy, the quenching behavior was primarily due to energy transfer between the two species, in contrast to the electron-transfer mechanism that is dominant in the classic closed-shell quencher PCBM. This mechanism was supported by the large spectral overlap between the absorbance spectra of the radical species that acted as quenchers and the emission spectrum of the P3HT donor, as well as the rapid recovery of the ground state observed through transient absorption measurements. Charge transfer, an alternative plausible mechanism, was determined to not be the primary means of fluorescence quenching in the P3HT-radical systems evaluated here as the signal of the quencher anions were

not observed in the transient absorption, as well as through calculations that suggested it would proceed at a far slower rate than through FRET. As FRET is a long-range interaction, this finding has implications for future applications involving energy transfer from a fluorescent conjugated molecule to an open shell species, such as heterojunctions between the two in device applications or in conjugated molecules bearing radical pendant groups. Specifically, the finding suggests that by choosing a radical species that can act as a FRET acceptor for a given conjugated species, greater flexibility in the distance between the two moieties can be achieved. Moreover, it highlights the key need to appropriately and fully evaluate the subtle physical, electronic, and energetic interactions between closed-shell and open-shell organic composite materials.

4.6 Acknowledgements

The work performed by D.A.W. and B.W.B. was made possible through the Air Force Office of Scientific Research (AFOSR) under support provided by the Organic Materials Chemistry Program (Grant Number: FA9550-15-1-0449, Program Manager: Dr. Kenneth Caster), and we gratefully thank the AFOSR for this support. J.M.S and L.H. acknowledge the support from US National Science Foundation through grant NSF-CHE-1555005 for the transient absorption characterization.

4.7 Electronic Supplementary Information

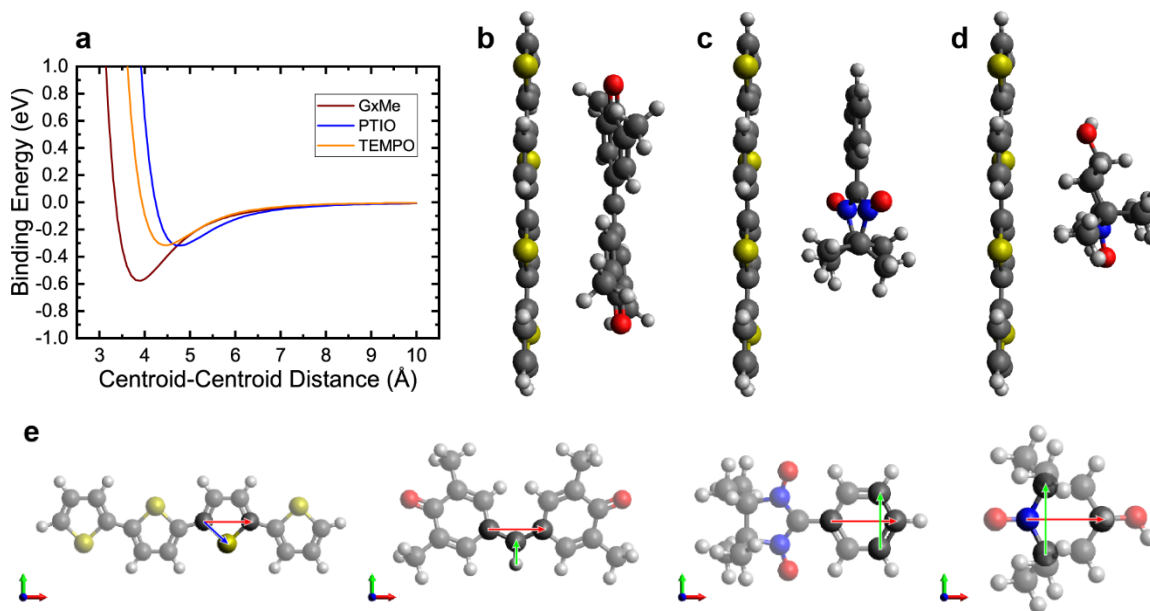


Figure 4.S1. (a) Binding curves for the neutral quaterthiophene (4T) and radical quencher species. Geometries of the (b) 4T-GxMe pair, (c) 4T-PTIO pair, and (d) 4T-TEMPO pair at the equilibrium distances seen looking down on the x-z plane. (e) Orientations of the individual species seen looking down the x-y plane (red: x, green: y, blue: z). The species were aligned in a co-facial orientation in the following manner. For 4T, the 2- and 5- carbons of the thiophene ring nearest the geometric center of the molecule were aligned along the x-axis, and the plane of this thiophene ring was aligned with the x-y plane by orienting the cross product of the x-axis and the C-S bond with the positive z-axis. For GxMe, the C2 axis was aligned with the y-axis, and the two carbons closest to the C2 axis were aligned with the x-axis. For PTIO, the C2 axis was aligned with the x-axis, and the phenyl ring was aligned with the x-y plane by orienting the 3- and 5- carbons of the phenyl ring with the y-axis. For TEMPO, the mirror plane, or the vector between the nitrogen and the 4-carbon, was aligned with the x-axis, and the 2- and 6-carbons were aligned with the y-axis. The TEMPO molecule was oriented so the less sterically-hindered face was facing the negative z-direction. All molecules were translated such that their centroids were aligned with the origin. To generate the 4T-radical pairs, the two molecules were superimposed with their centroids overlapping, and the radical species was displaced a given distance along the positive z-axis.

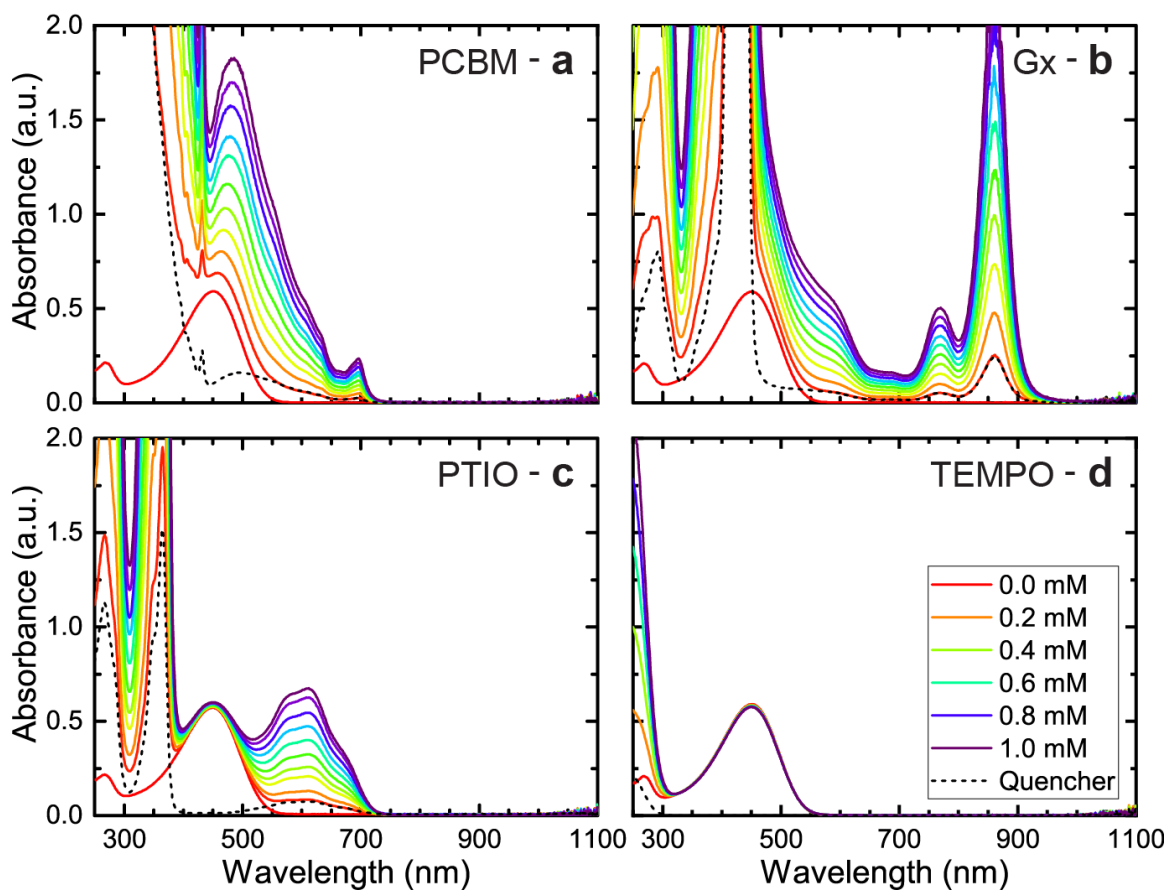


Figure 4.S2. Absorbance spectra of P3HT in solution ($60 \mu\text{M}$ of repeat units in chloroform) blended with varying concentrations of (a) PCBM, (b) the galvinoxyl radical, (c) the PTIO radical, and (d) the TEMPO radical. The absorbance spectra of solutions with 0.1 mM of small molecule and no P3HT are indicated with a dashed line. The spectra are the sum of the spectra of the individual components, indicating that no supramolecular complexes are forming in the ground state when the materials are co-dissolved in solution.

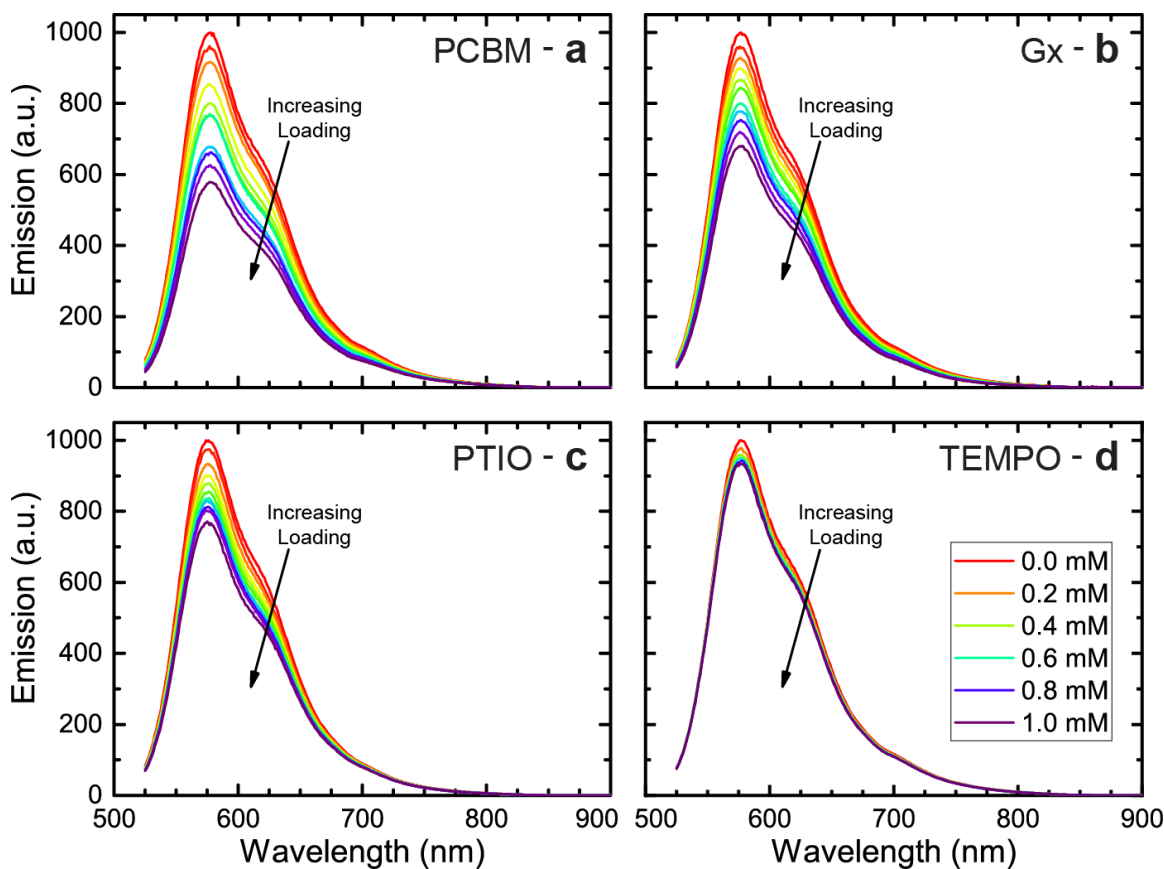


Figure 4.S3. Reduction of the intensity of fluorescence spectra of P3HT in solution ($60\mu\text{M}$ of repeat units in chloroform) upon addition of up to 1 mM of (a) PCBM, (b) the galvinoxyl radical, (c) the PTIO radical, and (d) the TEMPO radical, showing that the galvinoxyl and PTIO radical species act as fluorescence quenchers with nearly the same quenching ability as PCBM, while the TEMPO radical does not show this effect. The excitation wavelength was 500 nm. All spectra were corrected for the inner filter effect.

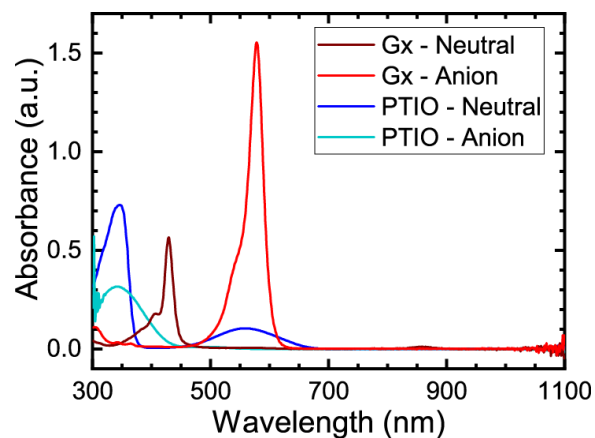


Figure 4.S4. Absorbance spectra of the neutral galvinoxyl and PTIO radicals and the reduced galvinoxylate and PTIO anions. The galvinoxyl species were measured at a 0.01 mM concentration in ethanol, and the PTIO species were measured at a 0.1 mM concentration in water. These concentrations were chosen so that the samples would have similar optical densities for comparison purposes. The galvinoxylate anion shows a strong absorbance near 560 nm, while the PTIO anion shows a broad absorbance near 325 nm.

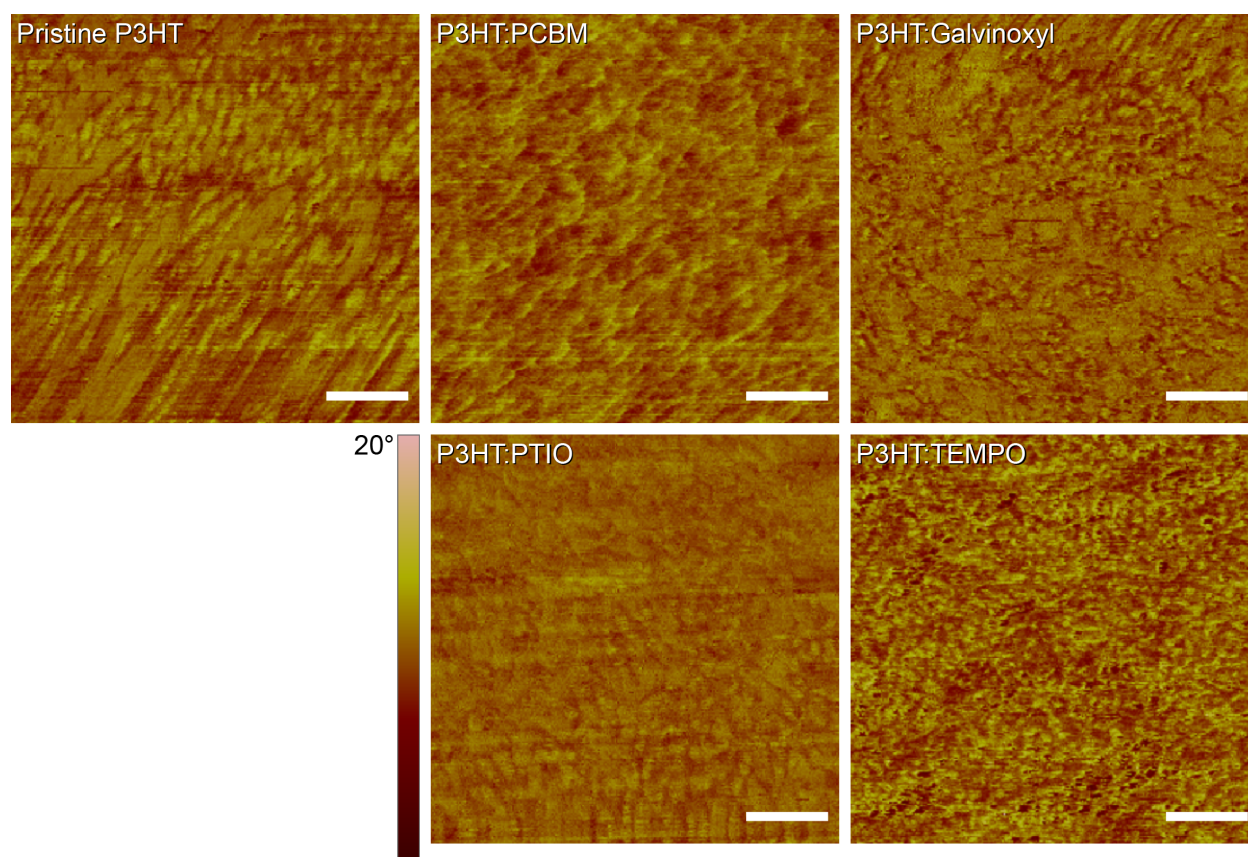


Figure 4.S5. Atomic Force Microscopy (AFM) phase images of P3HT thin films with small molecule additives present at a loading of 10%, on a molar basis. Scale bars represent 50 nm.

4.7.1 Derivation of the Inner Filter Effect Correction Formula

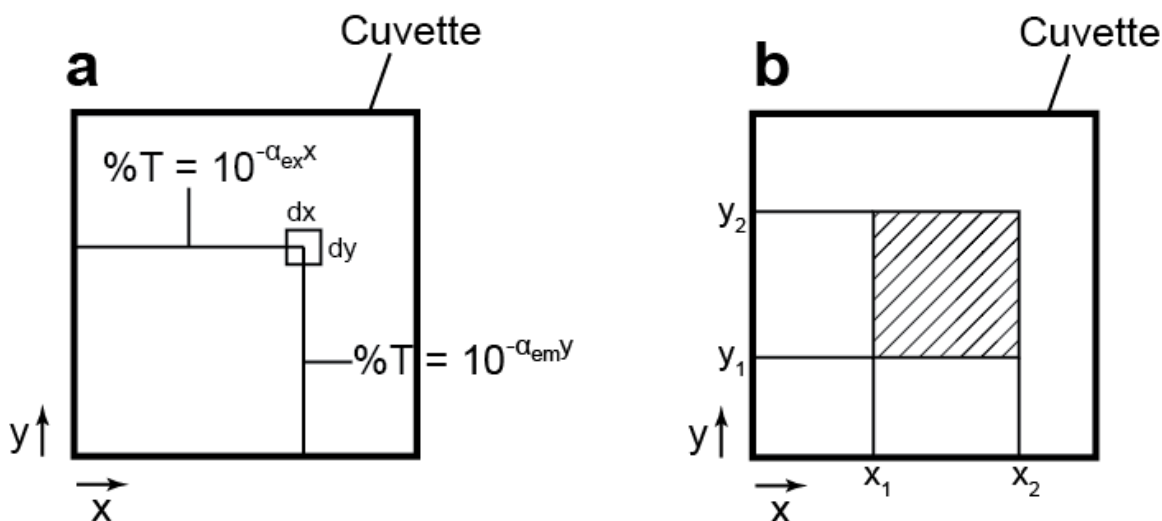


Figure 4.S6. Illustrations for the inner filter effect derivation. (a) Depiction of how the light going to and coming from an infinitesimal area element is attenuated and (b) the definition of the coordinates used in the derivation.

The inner filter effect is composed of two parts, the primary inner filter effect, which is the absorption of the excitation beam, and the secondary inner filter effect, which is the absorption of the fluorescence signal. In a typical fluorimeter, the fluorescence signal is measured at a right (i.e., 90°) angle to the excitation beam, so that the excitation beam does not saturate the photodetector. Thus, the primary and secondary inner filter effects arise from attenuation in perpendicular directions. In the absence of an inner filter effect, the number of photons generated is the product of the photon flux entering the sample, the width of the excitation beam, the fraction of light absorbed by the fluorophore in the sample, and the quantum yield of the fluorophore (number of photons emitted per photon absorbed). This can be expressed with Equation 4.S1.

$$I_{em} = I_{ex}W(1 - 10^{-\epsilon_{F,ex}Lc_F})\Phi_Q \quad (4.S1)$$

Here, I_{em} is the fluorescence intensity, I_{ex} is the emission intensity, $\epsilon_{F,ex}$ is the Beer-Lambert constant of the fluorophore at the excitation wavelength, L and W are the length and width of the sample, c_F is the concentration of the fluorophore, and Φ_Q is the quantum yield. If the inner filter effect is to be taken into account, then we can consider an infinitesimal area over which the attenuation is negligible and integrate over the entire sample. Within the infinitesimal area, the

number of photons generated is given by Equation 4.S1, except with L and W replaced by dx and dy and with the excitation intensity and emission intensity attenuated by the transmittance of the respective wavelengths through the sample to that point (Figure 4.S6a). The equation is as follows.

$$I_{obs}(x, y) = I_{ex}(1 - 10^{-\epsilon_{F,ex}c_F dx})dy\Phi_Q 10^{-\alpha_{ex}x} 10^{-\alpha_{em}y} \quad (4.S2)$$

Here, α_{ex} and α_{em} are the absorbance per unit length at the excitation and emission wavelengths, equal to the sum of the products of the concentration of the absorbing species in the solution and the Beer-Lambert constant for that species at the excitation or emission wavelength.

$$\alpha_{em/ex} = \sum \epsilon_{em/ex,i}c_i \quad (4.S3)$$

In this work, the only absorbing species are the fluorophore and the quencher. Equation 4.S2 can be integrated if the exponential term is replaced with its Taylor series expansion in dx and all terms of second-order and higher are discarded, which is a valid assumption here as dx is infinitesimally small. This gives the following expression.

$$I_{obs}(x, y) = \ln(10) I_{ex}\epsilon_{F,ex}c_F\Phi_Q 10^{-\alpha_{ex}x} 10^{-\alpha_{em}y} dx dy \quad (4.S4)$$

In turn, Equation 4.S4 can be integrated to yield the following.

$$I_{obs} = I_{ex}\epsilon_{F,ex}c_F\Phi_Q \frac{(10^{-\alpha_{ex}x_1} - 10^{-\alpha_{ex}x_2})(10^{-\alpha_{em}y_1} - 10^{-\alpha_{em}y_2})}{\ln(10) \alpha_{ex}\alpha_{em}} \quad (4.S5)$$

In this expression, x_1 , x_2 , y_1 , and y_2 define the width and location of the excitation beam and the area seen by the detector (Figure 4.S6b). For the instrument used, both of these cover the entire cuvette length. Thus x_1 and y_1 are equal to zero, and x_2 and y_2 are equal to the path length of the cuvette. In the interest of generality, this substitution will not be made until the final step.

The corrected intensity is what the intensity would be in the absence of the inner filter effects. This can be found by setting α_{ex} and α_{em} to zero in Equation 4.S5 and integrating. Making this substitution yields the following.

$$I_{corr}(x, y) = \ln(10) I_{ex} \epsilon_{F,ex} c_F \Phi_Q dx dy \quad (4.S6)$$

$$I_{corr} = \ln(10) I_{ex} \epsilon_{F,ex} c_F \Phi_Q (x_2 - x_1)(y_2 - y_1) \quad (4.S7)$$

Dividing Equation 4.S7 by Equation 4.S5 and eliminating the common factor of $I_{ex} \epsilon_{F,ex} c_F \Phi_Q$ gives the proper correction formula.

$$\frac{I_{corr}}{I_{obs}} = \frac{\ln(10)^2 \alpha_{ex}(x_2 - x_1) \alpha_{em}(y_2 - y_1)}{(10^{-\alpha_{ex}x_1} - 10^{-\alpha_{ex}x_2})(10^{-\alpha_{em}y_1} - 10^{-\alpha_{em}y_2})} \quad (4.S8)$$

If the excitation beam width and the detector area both cover the entire cuvette length, then the equation becomes the expression of Equation 4.S9.

$$\frac{I_{corr}}{I_{obs}} = \frac{\ln(10)^2 \alpha_{ex} L \alpha_{em} L}{(1 - 10^{-\alpha_{ex}L})(1 - 10^{-\alpha_{em}L})} \quad (4.S9)$$

By cross-multiplying by I_{obs} and noting that $\alpha_{ex/em}L = A_{ex/em}$, where $A_{ex/em}$ is the total absorbance of the solution at the excitation or emission wavelengths, Equation 4.1 of the main text is recovered.

4.8 Notes and References

- (1) Meller, G.; Grasser, T. *Organic Electronics*; Springer: Heidelberg/New York, 2010.
- (2) Ma, R. In *Handbook of Visual Display Technology*; Chen, J., Cranton, W., Fihn, M., Eds.; Springer, 2016; pp 1799–1820.
- (3) Boudouris, B. W. *Curr. Opin. Chem. Eng.* **2013**, 2 (3), 294–301.
- (4) Facchetti, A. *Chem. Mater.* **2011**, 23, 733–758.
- (5) Mukherjee, S.; Boudouris, B. W. *Organic Radical Polymers: New Avenues in Organic Electronics*; Springer, 2017.
- (6) Wilcox, D. A.; Agarkar, V.; Mukherjee, S.; Boudouris, B. W. *Annu. Rev. Chem. Biomol. Eng.* **2018**, 9, 83–103.
- (7) Joo, Y.; Agarkar, V.; Sung, S. H.; Savoie, B. M.; Boudouris, B. W. *Science* **2018**, 359 (6382), 1391–1395.
- (8) Rostro, L.; Galicia, L.; Boudouris, B. W. *J. Polym. Sci. B Polym. Phys.* **2015**, 53 (5), 311–316.

- (9) Zheng, L.; Mukherjee, S.; Wang, K.; Hay, M. E.; Boudouris, B. W.; Gong, X. *J. Mater. Chem. A* **2017**, *5*, 23831–23839.
- (10) Sung, S. H.; Bajaj, N.; Rhoads, J. F.; Chiu, G. T.; Boudouris, B. W. *Org. Electron.* **2016**, *37*, 148–154.
- (11) Tomlinson, E. P.; Willmore, M. J.; Zhu, X.; Hilsmier, S. W. A.; Boudouris, B. W. *ACS Appl. Mater. Interfaces* **2015**, *7* (33), 18195–18200.
- (12) Tomlinson, E. P.; Mukherjee, S.; Boudouris, B. W. *Org. Electron.* **2017**, *51*, 243–248.
- (13) Joo, Y.; Huang, L.; Eedugurala, N.; London, A. E.; Kumar, A.; Wong, B. M.; Boudouris, B. W.; Azoulay, J. D. *Macromolecules* **2018**, *51* (10), 3886–3894.
- (14) Basel, T. P.; Huynh, U.; Zheng, T.; Xu, T.; Yu, L.; Vardeny, Z. V. *Adv. Funct. Mater.* **2015**, *25*, 1895–1902.
- (15) Li, F.; Gore, D. N.; Wang, S.; Lutkenhaus, J. L. *Angew. Chem. Int. Ed.* **2017**, *56*, 9856–9859.
- (16) Zhang, Y.; Park, A. M.; McMillan, S. R.; Harmon, N. J.; Flatté, M. E.; Fuchs, G. D.; Ober, C. K. *Chem. Mater.* **2018**, *30* (14), 4799–4807.
- (17) Li, F.; Wang, S.; Zhang, Y.; Lutkenhaus, J. L. *Chem. Mater.* **2018**, *30* (15), 5169–5174.
- (18) Lakowicz, J. R. *Principles of Fluorescence Spectroscopy*, 3rd ed.; Springer: New York, 2010.
- (19) Peng, Q.; Obolda, A.; Zhang, M.; Li, F. *Angew. Chem. Int. Ed.* **2015**, *54*, 7091–7095.
- (20) Neier, E.; Arias, R.; Rady, N.; Venkatesan, S.; Hudnall, T. W.; Zakhidov, A. *Org. Electron.* **2017**, *44*, 126–131.
- (21) Green, S. A.; Simpson, D. J.; Zhou, G.; Ho, P. S.; Blough, N. V. *J. Am. Chem. Soc.* **1990**, *112* (20), 7337–7346.
- (22) Kawanaka, Y.; Shimizu, A.; Shinada, T.; Tanaka, R.; Teki, Y. *Angew. Chem. Int. Ed.* **2013**, *52* (26), 6643–6647.
- (23) Hughes, B. K.; Braunecker, W. A.; Ferguson, A. J.; Kemper, T. W.; Larsen, R. E.; Gennett, T. *J. Phys. Chem. B* **2014**, *118*, 12541–12548.
- (24) Zamojć, K.; Wiczak, W.; Zaborowski, B.; Jacewicz, D.; Chmurzyński, L. *Spectrochim. Acta - Part A Mol. Biomol. Spectrosc.* **2015**, *136* (PC), 1875–1880.
- (25) Gustmann, H.; Lefrancois, D.; Reuss, A. J.; Gophane, D. B.; Braun, M.; Dreuw, A.; Sigurdsson, S. T.; Wachtveitl, J. *Phys. Chem. Chem. Phys.* **2017**, *19*, 26255–26264.
- (26) Tansakul, C.; Lilie, E.; Walter, E. D.; Rivera III, F.; Wolcott, A.; Zhang, J. Z.; Millhauser, G. L.; Braslau, R. *J. Phys. Chem. C* **2010**, *114*, 7793–7805.
- (27) Lin, F.; Pei, D.; He, W.; Huang, Z.; Huang, Y.; Guo, X. *J. Mater. Chem.* **2012**, *22* (23), 11801.
- (28) Dutta, P.; Beaulac, R. *Chem. Mater.* **2016**, *28* (4), 1076–1084.
- (29) Marrocchi, A.; Lanari, D.; Facchetti, A.; Vaccaro, L. *Energy Environ. Sci.* **2012**, *5* (9), 8457.
- (30) Fonin, A. V.; Sulatskaya, A. I.; Kuznetsova, I. M.; Turoverov, K. K. *PLoS One* **2014**, *9* (7), e103878.
- (31) Parker, C. A.; Barnes, W. J. *Analyist* **1957**, *82*, 606–618.
- (32) Marcus, R.; Sutin, N. *Biochim. Biophys. Acta-Reviews Bioenerg.* **1985**, *811*, 265–322.
- (33) Grimme, S.; Ehrlich, S.; Goerigk, L. *J. Comput. Chem.* **2009**, *32* (7), 1456–1465.
- (34) Becke, A. D. *J. Chem. Phys.* **1993**, *98* (7), 5648.
- (35) Weigend, F.; Ahlrichs, R. *Phys. Chem. Chem. Phys.* **2005**, *7* (18), 3297.
- (36) Neese, F. *Wiley Interdiscip. Rev. Comput. Mol. Sci.* **2012**, *2* (1), 73–78.
- (37) Petrenko, T.; Kossmann, S.; Neese, F. *J. Chem. Phys.* **2011**, *134* (5), 0–14.

- (38) Pettersen, E. F.; Goddard, T. D.; Huang, C. C.; Couch, G. S.; Greenblatt, D. M.; Meng, E. C.; Ferrin, T. E. *J. Comput. Chem.* **2004**, *25* (13), 1605–1612.
- (39) Sanner, M. F.; Olson, A. J.; Spehner, J.-C. *Biopolymers* **1996**, *38* (3), 305–320.
- (40) Liu, T.; Troisi, A. *J. Phys. Chem. C* **2011**, *115*, 2406–2415.
- (41) Hamnett, A.; Hillman, A. R. *J. Electrochem. Soc.* **1988**, *135* (10), 2517–2524.
- (42) Förster, T. *Radiat. Res. Suppl.* **1960**, *2*, 326–339.
- (43) Cook, S.; Furube, A.; Katoh, R. *Energy Environ. Sci.* **2008**, *1* (2), 294.
- (44) Wang, J.; Wang, D.; Moses, D.; Heeger, A. J. *J. Appl. Polym. Sci.* **2001**, *82* (10), 2553–2557.
- (45) Yamashiro, T.; Aso, Y.; Otsubo, T.; Tang, H.; Harima, Y.; Yamashita, K. *Chemistry Letters*. 1999, pp 443–444.
- (46) Boudouris, B. W.; Molins, F.; Blank, D. A.; Frisbie, C. D.; Hillmyer, M. A. *Macromolecules* **2009**, *42* (12), 4118–4126.
- (47) Umberger, J. Q.; LaMer, V. K. *J. Am. Chem. Soc.* **1945**, *67* (7), 1099–1109.
- (48) Alberty, R. A.; Hammes, G. G. *J. Phys. Chem.* **1958**, *62* (2), 154–159.
- (49) Vanlaeke, P.; Swinnen, A.; Haeldermans, I.; Vanhoyland, G.; Aernouts, T.; Cheyns, D.; Deibel, C.; D’Haen, J.; Heremans, P.; Poortmans, J.; Manca, J. V. *Sol. Energy Mater. Sol. Cells* **2006**, *90* (14), 2150–2158.
- (50) Dexter, D. L. *J. Chem. Phys.* **1953**, *21* (5), 836–850.

5. MODIFYING FIELD-EFFECT TRANSISTOR RESPONSE IN A CONJUGATED POLYMER UPON THE ADDITION OF RADICAL DOPANTS*

5.1 Abstract

As open-shell moieties are increasingly integrated into organic electronic devices, there remains a need to establish the interactions that occur between these oxidation-reduction-active (redox-active) radical species and commonly-used conjugated polymers. In this report, we show that the addition of the stable radical galvinoxyl to the conjugated polymer poly(3-hexylthiophene) (P3HT) alters the thin film transistor response from semiconducting to conducting as well as modestly enhances the electrical conductivity. This interaction is not seen with other radical species. While an increase in charge carrier concentration is observed, the interaction does not seem to be otherwise consistent with a simple charge-transfer doping mechanism, due to the mismatched reduction and oxidation potentials of the two species. Additionally, no freeze-out of charge carriers is observed at lower temperatures. It is also not due to parallel conduction through the radical fraction of the bulk composite, as the radical species is non-conductive. Hole mobility is enhanced at lower concentrations of the radical, but it decreases at higher concentrations due to the reduced fraction of conductive material in the polymer bulk. Despite the increase in mobility at lower concentrations, the activation energy for charge transport is increased by the presence of the radical. This suggests that the radical is not improving the charge transport through filling of deep trap states or by reducing the activation energy for the charge transport reaction; however, the galvinoxyl radical is likely filling shallow trap states within the P3HT for the composite thin film.

5.2 Introduction

Conjugated small molecules and polymers are the leading classes of materials in organic electronic devices. In fact, an impressive range of molecular architectures have been tailored for applications including organic field-effect transistors (OFETs),^{1,2} organic photovoltaics,³⁻⁵ organic light-emitting devices (OLEDs),⁶ and thermoelectric modules.^{7,8} However, conjugated materials

* This work was submitted to Thin Soft Films on June 11, 2020

are not always the optimal materials choice for every application, and many organic electronic technologies have yet to capture a significant share of the commercial market. For this reason, there is interest in developing alternative classes of materials that can complement the strengths of conjugated systems.

One such class is comprised of stable organic radicals.^{9–11} These moieties show excellent charge transfer properties, making them well-suited for organic battery applications,¹² and their open-shell nature makes them useful in spin-manipulation applications.^{13–17} Beyond their usage as small-molecule dopants,^{18,19} polymers containing radicals have shown promise as interfacial modifying layers in organic electronic devices,^{20–22} and proper molecular design allows for impressive intrinsic electronic conductivity values to be had.²³ Additionally, conjugated molecules with covalently-linked radical moieties have been developed for use in battery applications,^{24–31} as well as to protect the conjugated moiety from degradation by manipulating the excited state dynamics.^{32–37} With their potential as next-generation electronic materials, determining how open-shell molecules interact with oft-used conjugated materials in thin films is of prime importance to guide future applications.

The interaction of radicals with materials in their excited states, observed primarily through fluorescence quenching, has been well-documented in the literature,^{33,38–45} and our previous work has established the excited-state interactions between a common conjugated polymer, poly(3-hexylthiophene) (P3HT), and three distinct stable organic radicals.⁴⁶ Despite finding a clear pattern in the excited state interactions, similar considerations have not been given to the interactions in the ground state. Of course, for most organic electronic applications, the ground state interactions are more relevant. Thus, to elucidate the potential effects of introducing open-shell functionalities into thin films of conjugated polymers, the full scope of the interactions between these classes of materials must be established in a complete manner.

One means to examine ground-state interactions that is particularly relevant to device applications is to evaluate the charge transport properties of one material, and how these properties are affected by the presence of another species in thin films. Changes in the electronic structure of the host material, and even formation of charge-transfer complexes, lead to significant changes in the electrical properties even with small quantities of additive,⁴⁷ and this molecular principle is often exploited to develop functional devices (e.g., chemical sensors).^{48,49} A useful device geometry for measuring these charge transport properties is the OFET. OFETs allow the charge

carrier concentration in the material to be modulated through application of a gate voltage, and evaluation of the subsequent response and transfer curves allows for the carrier concentration and mobility values to be determined. Here, we report an interaction between P3HT and the galvinoxyl radical (Gx), which causes a shift from semiconducting to conducting behavior. This is not seen with the other radical species evaluated here, and the P3HT-galvinoxyl radical interaction does not appear to be caused by formation of a charge transfer complex, as seen with many other oft-reported molecular dopants in organic electronics.^{47,50,51} In addition to hinting at the possibility of synergistic interactions between the two classes of material, these results underscore potential pitfalls of incorporating radical functionality into organic electronic devices, and they highlight the need to control the chemistry of the open-shell group in a careful manner when thin film composite considerations are being made. Because many of the potential applications of radicals in conjugated hosts are primarily concerned with either manipulating excited-state behavior of the conjugated material or aim for the electronic properties of the closed- and open-shell components to be decoupled, interactions that alter the electronic structure and semiconducting character of the host material may lead to reduced efficacy in an actual device context. Thus, this work provides the first step in clear molecular design considerations as open-shell materials are further incorporated into conjugated polymer matrices for high-performance organic electronic devices.

5.3 Experimental Details

5.3.1 Materials

The galvinoxyl (Gx) and 4-hydroxy-2,2,6,6-tetramethylpiperidin-1-oxyl (TEMPO) (97%) radicals, hexamethyldisilazane (99%), and anhydrous 1,2-dichlorobenzene (DCB) (99%) were purchased from Sigma-Aldrich. The 2-phenyl-4,4,5,5-tetramethylimidazoline-1-oxyl-3-oxide (PTIO) radical (98%) was purchased from TCI America. P3HT (regioregular electronic grade, $M_n \sim 60 \text{ kg mol}^{-1}$) was purchased from Rieke Metals. Gold (99.99%) and titanium (99.7%) were purchased from Kurt Lesker. Acetone (99.5%), chloroform (99.8%), and isopropanol (99.5%) were purchased from Fisher. Silicon wafers were purchased from Silicon Valley Microelectronics. These metallic silicon wafers were degenerately p-doped with boron, coated with a 300 nm

thermally-grown silicon dioxide layer. Poly(galvinoxystyrene) (PGSt) was synthesized according to a previously reported procedure.⁵² All materials were used as received.

5.3.2 OFET Fabrication

Silicon wafers were diced into 13.6 mm × 15.6 mm chips. These substrates were cleaned by sonication for 10 minutes each in acetone, chloroform, and isopropyl alcohol, in a sequential manner, and dried with compressed nitrogen. The substrates were then loaded into a spincoater. Liquid hexamethyldisilazane (HMDS) was added to the substrate and allowed to rest for 30 seconds. After this time, the sample was spun at 3,000 rpm for 30 s, followed by heating on a hot plate at 100 °C for 30 min under ambient conditions. Then, 10 nm of titanium, followed by 80 nm of gold, were thermally evaporated onto the oxide side of the substrates through a shadow mask to form the source and drain contacts. These contacts formed a channel with a width of 10 mm and a length of 0.1 mm. Afterwards, the active layer solution was spun-coat on the substrates at a rate of 1,500 rpm for 60 s within an inert atmosphere glovebox. The active layer solutions consisted of P3HT and different open-shell dopants blended to give a total solids concentration of 25 mg mL⁻¹ in DCB, and these solutions were stirred overnight at 50 °C prior to being used as active layer coating solutions.

After fabrication, the devices were tested using a Lakeshore Cryotronics Model TTPX vacuum probe station for room temperature measurements, and a Lakeshore Cryotronics Model CRX-VF for variable-temperature measurements. Keithley 2400 SourceMeters, controlled using in-house Labview programs, were used to gather the current-voltage response data for room-temperature measurements, and Keithley 2450 SourceMeters were used for variable-temperature measurements. A diamond-tipped scribe pen was used to remove the oxide, revealing the metallic silicon gate that allowed for contact to be made with the back electrode. Output curves were obtained by sweeping the drain-source voltage from +10 V to -100 V in 2.5 V increments while the gate-source voltage was held constant for a given sweep and stepped from +10 V to -100 V in 10 V increments. Transfer curves were obtained by sweeping the gate-source voltage from +10 V to -100 V in 2.5 V increments and holding the drain-source voltage constant at -100 V. Conductivity responses were obtained by disconnecting the gate electrode and sweeping the drain-source voltage from -50 V to +50 V in 0.5 V increments.

5.4 Results and Discussion

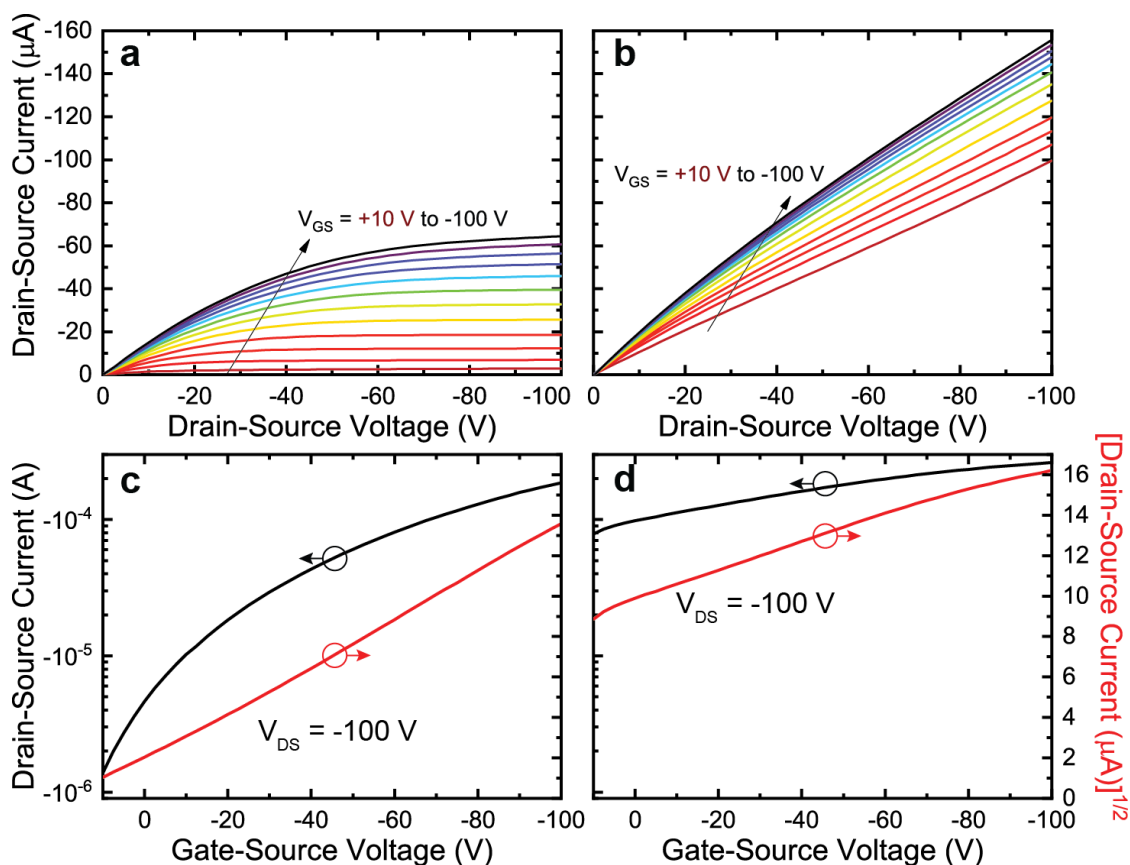


Figure 5.1. Output curves for (a) pristine P3HT transistor and (b) a P3HT-Gx blend transistor with a 5% galvinoxyl (by weight) loading. The corresponding transfer curves are shown in (c) and (d). In the pristine film, the current saturates at high voltage, and the saturation point increases with gate voltage. In the doped film, the current is roughly linear with voltage, and the conductivity dependence on gate voltage is reduced. The differing scale between (a) and (b) vs. (c) and (d) is due to hysteresis.

P3HT is an oft-used organic semiconductor, and it demonstrates a typical response when incorporated into a field-effect transistor (FET) geometry (Figure 5.1a,c). However, upon blending with the galvinoxyl radical, a shift in behavior is seen, where the output characteristics no longer saturate at the measured drain-source voltages (Figure 5.1b,d). This also results in the transistor no longer reaching an OFF state. To verify that this is not due solely to the open-shell nature of the compound, two other radical species are blended at a similar molar ratio.

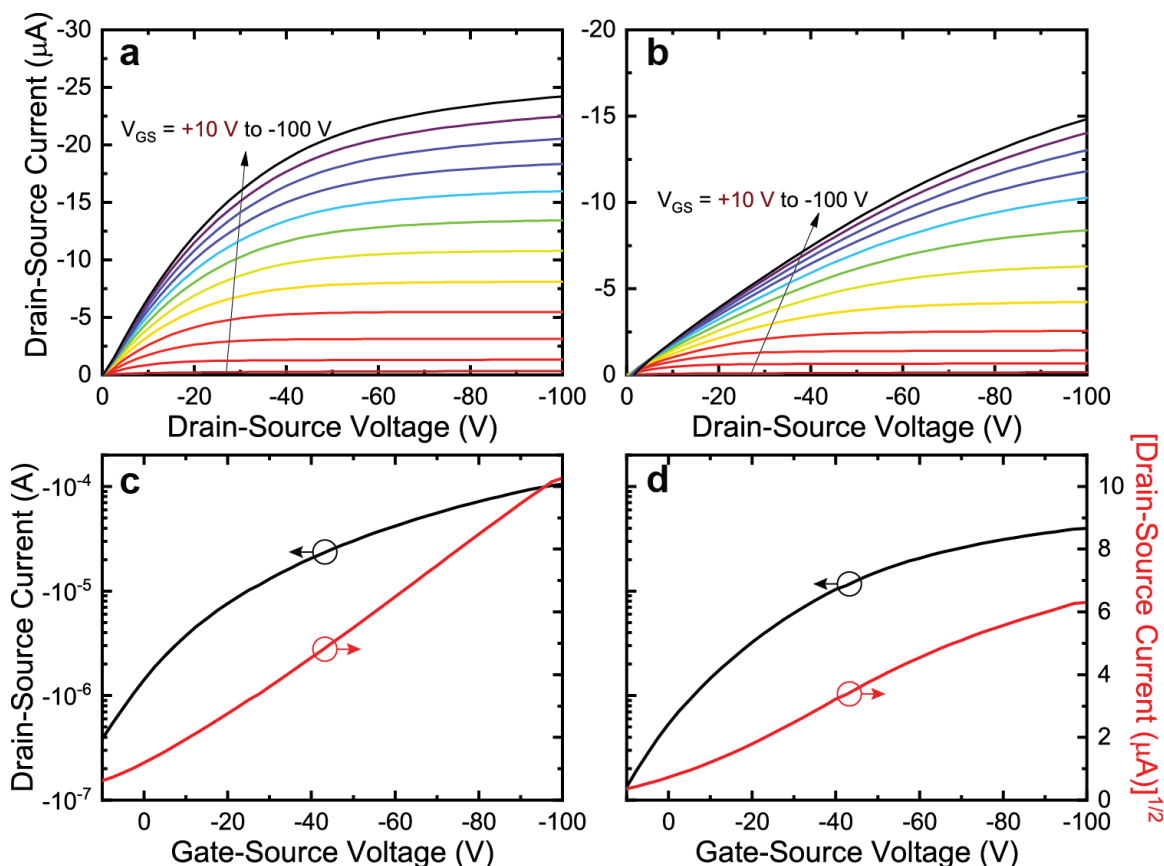


Figure 5.2. Output curves for P3HT transistors with loadings of 2.5% (by weight) of the (a) PTIO and (b) TEMPO radicals. The corresponding transfer curves are shown in (c) and (d). These loadings were selected to have approximately the same molar concentration as the galvinoxyl radical-containing device shown in Figure 5.1b. The qualitative shift in behavior is not observed for these radicals, which contrasts with what was observed for the galvinoxyl radical.

That is, doping the P3HT OFET with PTIO or TEMPO radicals does not show the same behavior as the galvinoxyl radical (Figure 5.2). One potential explanation for this behavior is that the galvinoxyl radical is doping the P3HT polymer through a charge-transfer reaction. In other words, an electron is transferred from the highest-occupied molecular orbital (HOMO) of a P3HT segment to the singly-occupied molecular orbital (SOMO) of a galvinoxyl molecule. For the sake of comparison, the TEMPO and PTIO radicals were chosen to select a wide range of preferred redox behaviors. Whereas the galvinoxyl radical is an n-type radical, meaning that it is preferentially-reduced to form a stable anion, the TEMPO radical is p-type, meaning that it is preferentially-oxidized to form a stable cation, and the PTIO radical is ambipolar, meaning that it can undergo both oxidation and reduction reactions in a facile manner (Figure 5.3).

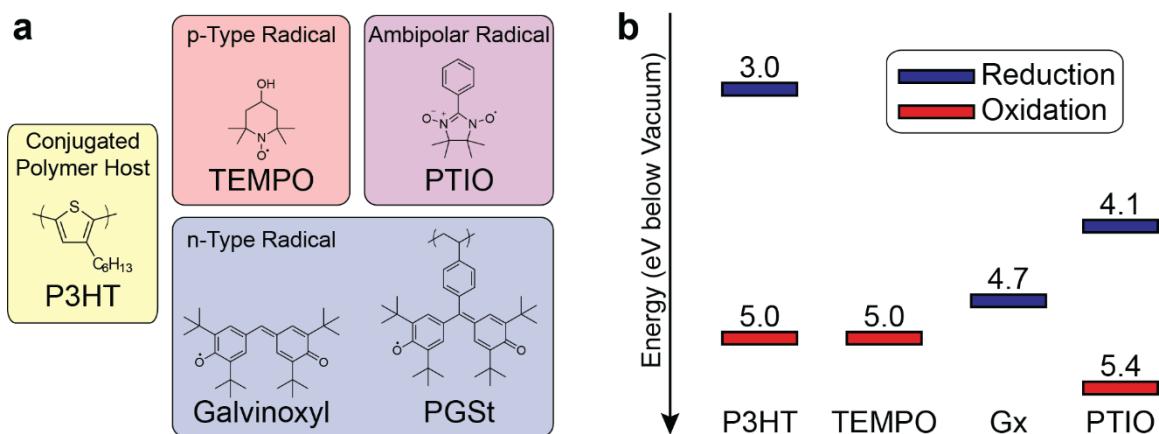


Figure 5.3. (a) Chemical structures of the conjugated polymer (P3HT), radical polymer (PGSt), and small molecule open-shell materials implemented in this work. Radicals are classified according to whether they preferentially reduce (n-type), preferentially oxidize (p-type), or are capable of being oxidized or reduced under normal conditions (ambipolar). (b) Oxidation (red) and reduction (blue) potentials of all molecular species implemented in this work. For P3HT these values are identified with the HOMO and lowest-unoccupied molecular orbital (LUMO) energy. For the radical species, these are identified with the SOMO energy. This identification is ambiguous for ambipolar species, such as the PTIO radical; thus, both its oxidation and reduction potentials are shown.

The galvinoxyl radical, unlike the TEMPO radical, can be reduced to form a stable anion, and its reduction potential of -4.7 eV relative to vacuum,⁵³ is significantly lower than that of the PTIO radical, with a reduction potential of -4.1 eV.⁵⁴ However, the oxidation potential of P3HT is -5.0 eV,¹⁹ which is 0.3 eV below the reduction potential of the galvinoxyl radical. This energy difference is significantly greater than the thermal energy available to the system. Furthermore, our previous study saw no evidence that any supramolecular complexes, such as charge transfer complexes, were formed in P3HT-galvinoxyl radical blends.⁴⁶ By contrast, charge-transfer dopants such as 2,3,5,6-tetrafluoro-7,7,8,8-tetracyanoquinodimethane (F4TCNQ) show a significant change in the absorbance spectrum due to the formation of polarons.^{47,50,55} Therefore, a charge-transfer interaction is unlikely.

To further establish the nature of the P3HT-galvinoxyl radical interaction, the charge transport properties were investigated at higher loadings of the radical (Figure 5.4). While lower loadings can utilize the galvinoxyl radical as a small molecule, higher loadings with a small molecule dopant result in poor film quality. To ensure that the observed behavior at higher loadings was not due to film quality issues, we incorporated the galvinoxyl radical into a macromolecular form. By creating a polymer blend composed of P3HT and poly(galvinoxyl styrene) (PGSt), high-

quality film formation was observed on a consistent basis. Importantly, the same change in behavior is observed when PGSt is incorporated into the P3HT active layer thin films as was observed with the small molecule galvinoxyl radical; this suggests that the presence of the polymer backbone does not affect the observed charge transport behavior. Because the response of the device active layers remained linear, we extracted the electrical conductivity values of the P3HT-PGSt composite films, and we observed a marked increase in conductivity upon radical polymer doping. In fact, a large increase in electrical conductivity is seen going from 0 to 5% PGSt (by weight). The conductivity then decreases upon increasing the loading to 25% PGSt (by weight), and its value levels at even higher loadings. At the highest loadings (i.e., when the active layer film is almost completely composed of PGSt), the conductivity drops dramatically. This is because PGSt is not a good electrical conductor, and these data suggest that a minimum loading of between 1 and 5% P3HT (by weight) is needed for charge transport to occur readily.

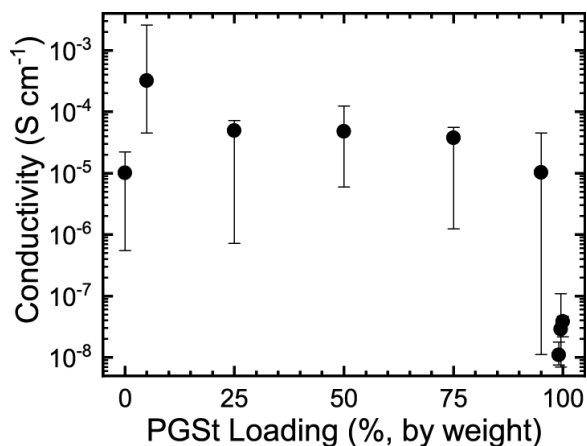


Figure 5.4. Electronic conductivity of the P3HT-PGSt active layer blends as a function of the PGSt loading. Though an increase is seen from 0 to 5% PGSt loadings, the conductivity does not change for loadings from 25% to 75%. No conductivity is observed for blends with extremely high PGSt loadings.

Utilizing the FET geometry allows for the contributions of the charge carrier mobility and charge carrier concentration to the conductivity of the material to be decoupled from one another. If the device is far from saturation, then the charge carrier concentration should be modulated linearly with changes in gate voltage, which will allow for the mobility to be extracted, according to the following equation.

$$I_{DS} = \mu_{lin} C_{ox} \frac{W}{L} \left(V_{DS} V_{GS} - \frac{V_{DS}^2}{2} \right) \quad (5.1)$$

Here, μ_{lin} is the linear regime mobility, C_{ox} is the capacitance per unit area of the gate dielectric, W is the channel width, and L is the channel length. For the saturation regime, the formula is expressed by Equation 5.2.

$$I_{DS} = \mu_{sat} C_{ox} \frac{W}{L} \left(\frac{V_{GS}^2}{2} \right) \quad (5.2)$$

Here, μ_{sat} is the saturation regime mobility. To extract the mobility from the transfer curves measured at $V_{DS} = -100$ V, Equation 5.1 was used for the doped OFETs (as these devices never saturated), and Equation 5.2 was used for the pristine P3HT devices. At low loadings of the galvinoxyl radical and the open-shell PGSt macromolecule, the mobility increases with greater radical doping (Figure 5.5a). However, at loadings beyond $\sim 10\%$, the mobility decreases (Figure 5.5b). This is likely due to an increased fraction of the bulk composite being non-conductive. Note that a similar trend in both the small molecule and radical polymer cases is had because the interaction is with the radical moiety, and the presence of the backbone does not affect the change in mobility.

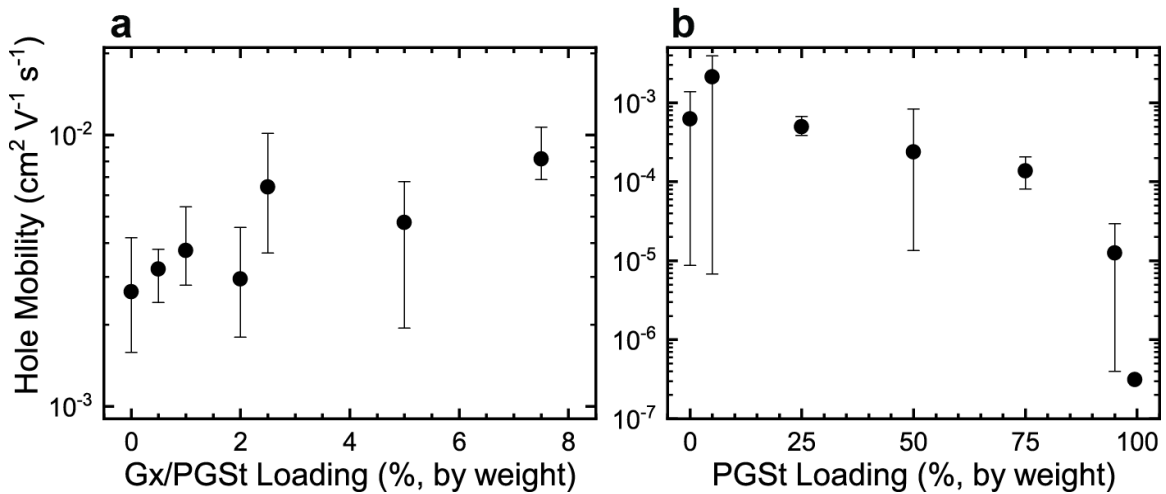


Figure 5.5. Mobility as a function of the galvinoxyl/PGSt loading, ranging from 0 to 100% loading (by weight). (a) Results for low loading. (b) Results for loadings used in Figure 5.4. The mobilities were extracted from the transfer curves assuming saturation for 0% loading and linear regime for higher values. The mobility can be seen to increase slightly at low loadings but decrease at high loadings. At the highest loadings, the mobility decreases dramatically.

The charge carrier concentration can be calculated based on the following equation.

$$\sigma = \mu n_h q \quad (5.3)$$

Here, σ is the conductivity, μ is the mobility, n_h is the concentration of charge carriers, and q is the absolute value of the electron charge. The greater conductivity at intermediate radical loadings implies that the charge carrier density is enhanced by the presence of the radical species (Figure 5.6), despite the fact that a simple charge transfer doping mechanism would be energetically unfavorable.

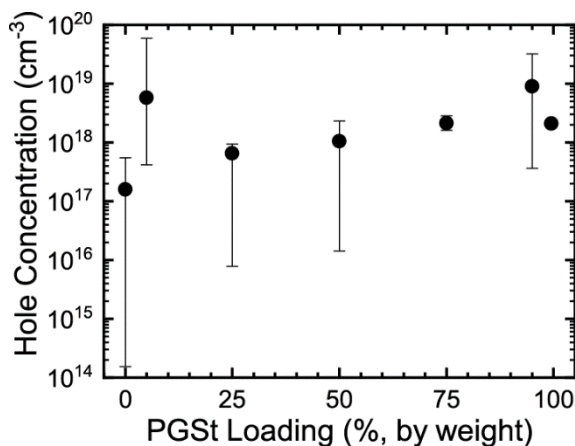


Figure 5.6. Charge carrier concentration found by dividing the conductivity by the mobility as a function of the PGSt fraction. A modest increase is seen at higher loadings.

As expected, the conductivity decreases with decreasing temperature. However, the ON-OFF ratio of the doped device stays nearly constant as temperature is lowered (Figure 5.7a). If the shift in behavior were due to charge transfer doping, lowering the temperature would lead to freeze-out of the charge carriers, which would cause the device to behave as an undoped transistor at lower temperatures. As this is not observed, a charge transfer interaction is most likely not the explanation. An alternative explanation for the observed shift in character of the P3HT is that the galvinoxyl radical is facilitating charge transport. The mobilities of the devices are well-described using an Arrhenius law (Figure 5.7b, Figure 5.7c, and Table 5.1. Arrhenius fitting parameters for doped and undoped P3HT OFETs.). A slight increase in the activation energy can be seen going from the undoped to the doped transistor. If the galvinoxyl radical were facilitating charge

transport, then a decrease in activation energy would be expected, which is the opposite of what is observed. Therefore, a mechanism that involves reducing the activation energy, such as a decrease in the number of deep trap states, is not at play.

Table 5.1. Arrhenius Fitting Parameters for Doped and Undoped P3HT OFETs.

Sample	$\mu - E_A$ (meV)	$I_{ON} - E_A$ (meV)
Undoped - 1	230	250
Undoped - 2	230	210
Doped	260	270

While a modest increase in both the mobility and charge carrier concentration is observed, the data do not provide straightforward evidence for a mechanism of either. No spectroscopic evidence of charge transfer doping is observed, and the lack of a freeze-out response at low temperatures further suggests that an electron transfer from P3HT to the galvinoxyl radical is not responsible. Similarly, the radical is not facilitating charge transport through a reduction in the activation energy or affecting the deep trap states. However, a reduction in the number of shallow trap states would improve the mobility without affecting the activation energy of the deep trap states. Therefore, it is reasonable to conclude that the presence of the radical facilitates charge transport by reducing the number of shallow trap states in the bulk material.

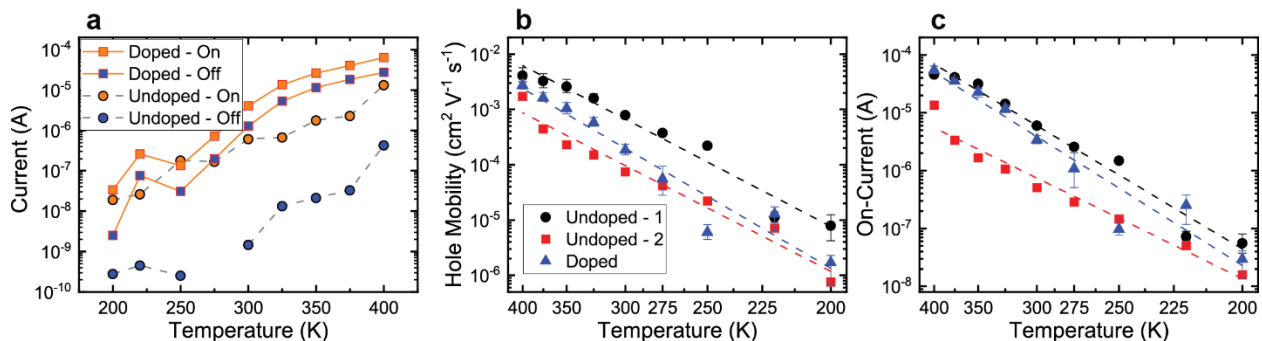


Figure 5.7. (a) Plot of on (orange) and off (blue) currents of a pristine P3HT OFET (circles) and a P3HT OFET blended with 5% PGSt by weight (squares). The current decreases with temperature, but the qualitative behavior does not change. Arrhenius plots of (b) mobility and (c) ON current for undoped P3HT OFETs (black circles and red squares) and a P3HT OFET blended with 5% PGSt by weight (blue triangles). A similar slope can be seen for both undoped devices, despite the difference in magnitude, while the doped device shows a slightly greater slope.

5.5 Conclusions

In summary, the addition of the galvinoxyl radical causes a shift in behavior for P3HT from semiconducting to conducting. This interaction is not observed for two other radical species tested. Previous reports suggest that no supramolecular complex is formed in thin films containing both P3HT and galvinoxyl,⁴⁶ yet the qualitative shift in transistor behavior is clear evidence that an interaction is occurring. The addition of small amounts of the galvinoxyl radical appear to enhance charge carrier concentration and mobility, though mobility decreases at the highest loadings as the conductive fraction of the blend decreases. Despite the increase in apparent carrier concentration, the measured redox potentials of P3HT and the galvinoxyl radical suggest a simple charge transfer is unfavorable, and measurements at lower temperatures do not lead to a freeze-out of carriers. While the galvinoxyl radical does not reduce the number of deep trap sites or catalyze the charge transport mechanism, its presence improves the charge carrier mobility, likely by reducing the number of shallow trap sites. As composites of conjugated materials with radicals become more prevalent in the literature, these results underscore the importance of understanding all the interactions that take place between these classes of materials.

5.6 Acknowledgements

This work was made possible through the Air Force Office of Scientific Research (AFOSR) under support provided by the Organic Materials Chemistry Program (Grant number: FA9550-19-1-0271, Program Manager: Dr. Kenneth Caster), and we gratefully thank the AFOSR for this support. We also gratefully thank Dr. Sanjoy Mukherjee for providing PGSt.

5.7 References

- (1) Bao, Z.; Locklin, J. *Organic Field-Effect Transistors*; CRC Press: Boca Raton, FL, 2007.
- (2) Sirringhaus, H. *Adv. Mater.* **2014**, *26* (9), 1319–1335.
- (3) Collins, S. D.; Ran, N. A.; Heiber, M. C.; Nguyen, T. *Adv. Energy Mater.* **2017**, *7*, 1602242.
- (4) Di, D.; Rasi, C.; Janssen, R. A. J. *Adv. Mater.* **2018**, 1806499.
- (5) Meng, L.; Zhang, Y.; Wan, X.; Li, C.; Zhang, X.; Wang, Y.; Ke, X.; Xiao, Z.; Ding, L.; Xia, R.; Yip, H.; Cao, Y.; Chen, Y. *Science* **2018**, *2612*, 1–10.
- (6) Ma, R. In *Handbook of Visual Display Technology*; Chen, J., Cranton, W., Fihn, M., Eds.; Springer, 2016; pp 1799–1820.
- (7) Russ, B.; Glauddell, A.; Urban, J. J.; Chabinyk, M. L.; Segalman, R. A. *Nat. Rev. Mater.* **2016**, *1* (10).

- (8) Beretta, D.; Neophytou, N.; Hodges, J. M.; Kanatzidis, M. G.; Narducci, D.; Martin-Gonzalez, M.; Beekman, M.; Balke, B.; Cerretti, G.; Tremel, W.; Zevalkink, A.; Hofmann, A. I.; Müller, C.; Dörling, B.; Campoy-Quiles, M.; Caironi, M. *Mater. Sci. Eng. R Reports* **2019**, *138* (July 2018), 210–255.
- (9) Tomlinson, E. P.; Hay, M. E.; Boudouris, B. W. *Macromolecules* **2014**, *47* (18), 6145–6158.
- (10) Mukherjee, S.; Boudouris, B. W. *Organic Radical Polymers: New Avenues in Organic Electronics*; Springer, 2017.
- (11) Wilcox, D. A.; Agarkar, V.; Mukherjee, S.; Boudouris, B. W. *Annu. Rev. Chem. Biomol. Eng.* **2018**, *9*, 83–103.
- (12) Nakahara, K.; Oyaizu, K.; Nishide, H. *Chem. Lett.* **2011**, *40* (3), 222–227.
- (13) Weiss, E. A.; Chernick, E. T.; Wasielewski, M. R. *J. Am. Chem. Soc.* **2004**, *126* (8), 2326–2327.
- (14) Zhang, Y.; Basel, T. P.; Gautam, B. R.; Yang, X.; Mascaro, D. J.; Liu, F.; Vardeny, Z. V. *Nat. Commun.* **2012**, *3*, 1043.
- (15) Basel, T. P.; Huynh, U.; Zheng, T.; Xu, T.; Yu, L.; Vardeny, Z. V. *Adv. Funct. Mater.* **2015**, *25*, 1895–1902.
- (16) Wang, Z.; Zhao, J.; Barbon, A.; Toffoletti, A.; Liu, Y.; An, Y.; Xu, L.; Karatay, A.; Yaglioglu, H. G.; Yildiz, E. A.; Hayvali, M. *J. Am. Chem. Soc.* **2017**, *139* (23), 7831–7842.
- (17) Huang, Y.; Xu, Z.; Jin, S.; Li, C.; Warncke, K.; Evangelista, F. A.; Lian, T.; Egap, E. *Chem. Mater.* **2018**, *30* (21), 7840–7851.
- (18) Tomlinson, E. P.; Willmore, M. J.; Zhu, X.; Hilsmier, S. W. A.; Boudouris, B. W. *ACS Appl. Mater. Interfaces* **2015**, *7* (33), 18195–18200.
- (19) Tomlinson, E. P.; Mukherjee, S.; Boudouris, B. W. *Org. Electron.* **2017**, *51*, 243–248.
- (20) Rostro, L.; Galicia, L.; Boudouris, B. W. *J. Polym. Sci. B Polym. Phys.* **2015**, *53* (5), 311–316.
- (21) Sung, S. H.; Bajaj, N.; Rhoads, J. F.; Chiu, G. T.; Boudouris, B. W. *Org. Electron.* **2016**, *37*, 148–154.
- (22) Zheng, L.; Mukherjee, S.; Wang, K.; Hay, M. E.; Boudouris, B. W.; Gong, X. *J. Mater. Chem. A* **2017**, *5*, 23831–23839.
- (23) Joo, Y.; Agarkar, V.; Sung, S. H.; Savoie, B. M.; Boudouris, B. W. *Science* **2018**, *359* (6382), 1391–1395.
- (24) Li, F.; Zhang, Y.; Kwon, S. R.; Lutkenhaus, J. L. *ACS Macro Lett.* **2016**, *5*, 337–341.
- (25) Casado, N.; Hernández, G.; Veloso, A.; Devaraj, S.; Mecerreyes, D.; Armand, M. *ACS Macro Lett.* **2016**, *5*, 59–64.
- (26) Li, F.; Gore, D. N.; Wang, S.; Lutkenhaus, J. L. *Angew. Chem. Int. Ed.* **2017**, *56*, 9856–9859.
- (27) Zhang, Y.; Park, A. M.; McMillan, S. R.; Harmon, N. J.; Flatté, M. E.; Fuchs, G. D.; Ober, C. K. *Chem. Mater.* **2018**, *30* (14), 4799–4807.
- (28) Schwartz, P. O.; Pejic, M.; Wachtler, M.; Bäuerle, P. *Synth. Met.* **2018**, *243* (January), 51–57.
- (29) Wang, P.; Lin, S.; Lin, Z.; Peeks, M. D.; Van Voorhis, T.; Swager, T. M. *J. Am. Chem. Soc.* **2018**, *140* (34), 10881–10889.
- (30) Li, F.; Wang, S.; Zhang, Y.; Lutkenhaus, J. L. *Chem. Mater.* **2018**, *30* (15), 5169–5174.
- (31) Xie, Y.; Zhang, K.; Monteiro, M. J.; Jia, Z. *ACS Appl. Mater. Interfaces* **2019**, *11* (7), 7096–7103.

- (32) Kawanaka, Y.; Shimizu, A.; Shinada, T.; Tanaka, R.; Teki, Y. *Angew. Chem. Int. Ed.* **2013**, *52* (26), 6643–6647.
- (33) Ito, A.; Shimizu, A.; Kishida, N.; Kawanaka, Y.; Kosumi, D.; Hashimoto, H.; Teki, Y. *Angew. Chem. Int. Ed.* **2014**, *53* (26), 6715–6719.
- (34) Chernick, E. T.; Casillas, R.; Zirzmeier, J.; Gardner, D. M.; Gruber, M.; Kropp, H.; Meyer, K.; Wasielewski, M. R.; Guldi, D. M.; Tykwinski, R. R. *J. Am. Chem. Soc.* **2015**, *137*, 857–863.
- (35) Ito, A.; Hinoshita, M.; Kato, K.; Teki, Y. *Chem. Lett.* **2016**, *45* (11), 1324–1326.
- (36) Shimizu, A.; Ito, A.; Teki, Y. *Chem. Commun.* **2016**, *52* (14), 2889–2892.
- (37) Huang, Y.; Egap, E. *Polym. J.* **2018**, *50* (8), 603–614.
- (38) Green, S. A.; Simpson, D. J.; Zhou, G.; Ho, P. S.; Blough, N. V. *J. Am. Chem. Soc.* **1990**, *112* (20), 7337–7346.
- (39) Tansakul, C.; Lilie, E.; Walter, E. D.; Rivera III, F.; Wolcott, A.; Zhang, J. Z.; Millhauser, G. L.; Braslau, R. *J. Phys. Chem. C* **2010**, *114*, 7793–7805.
- (40) Lin, F.; Pei, D.; He, W.; Huang, Z.; Huang, Y.; Guo, X. *J. Mater. Chem.* **2012**, *22* (23), 11801.
- (41) Hughes, B. K.; Braunecker, W. A.; Ferguson, A. J.; Kemper, T. W.; Larsen, R. E.; Gennett, T. *J. Phys. Chem. B* **2014**, *118*, 12541–12548.
- (42) Żamojć, K.; Wiczak, W.; Zaborowski, B.; Jacewicz, D.; Chmurzyński, L. *J. Fluoresc.* **2014**, *24*, 713–718.
- (43) Zamojć, K.; Wiczak, W.; Zaborowski, B.; Jacewicz, D.; Chmurzyński, L. *Spectrochim. Acta - Part A Mol. Biomol. Spectrosc.* **2015**, *136* (PC), 1875–1880.
- (44) Dutta, P.; Beaulac, R. *Chem. Mater.* **2016**, *28* (4), 1076–1084.
- (45) Gustmann, H.; Lefrancois, D.; Reuss, A. J.; Gophane, D. B.; Braun, M.; Dreuw, A.; Sigurdsson, S. T.; Wachtveitl, J. *Phys. Chem. Chem. Phys.* **2017**, *19*, 26255–26264.
- (46) Wilcox, D. A.; Snaider, J.; Mukherjee, S.; Yuan, L.; Huang, L.; Savoie, B. M.; Boudouris, B. W. *Soft Matter* **2019**, *15*, 1413–1422.
- (47) Pingel, P.; Neher, D. *Phys. Rev. B - Condens. Matter Mater. Phys.* **2013**, *87* (11), 1–9.
- (48) Schroeder, V.; Savagatrup, S.; He, M.; Lin, S.; Swager, T. M. *Chem. Rev.* **2018**, *acs.chemrev.8b00340*.
- (49) Gopalan, A.-I.; Komathi, S.; Muthuchamy, N.; Lee, K.-P.; Whitcombe, M. J.; Lakshmi, D.; Sai-Anand, G. *Prog. Polym. Sci.* **2019**, *88*, 1–129.
- (50) Méndez, H.; Heimel, G.; Winkler, S.; Frisch, J.; Opitz, A.; Sauer, K.; Wegner, B.; Oehzelt, M.; Röthel, C.; Duhm, S.; Többers, D.; Koch, N.; Salzmann, I. *Nat. Commun.* **2015**, *6*, 1–11.
- (51) Lüssem, B.; Keum, C.-M.; Kasemann, D.; Naab, B.; Bao, Z.; Leo, K. *Chem. Rev.* **2016**, *acs.chemrev.6b00329*.
- (52) Mukherjee, S.; Boudouris, B. W. *Mol. Syst. Des. Eng.* **2017**, *2* (2), 159–164.
- (53) Suga, T.; Ohshiro, H.; Sugita, S.; Oyaizu, K.; Nishide, H. *Adv. Mater.* **2009**, *21* (16), 1627–1630.
- (54) Suga, T.; Sugita, S.; Ohshiro, H.; Oyaizu, K.; Nishide, H. *Adv. Mater.* **2011**, *23* (6), 751–754.
- (55) Duong, D. T.; Wang, C.; Antono, E.; Toney, M. F.; Salleo, A. *Org. Electron. physics, Mater. Appl.* **2013**, *14* (5), 1330–1336.

6. INTRODUCTION TO BROADBAND DIELECTRIC SPECTROSCOPY

The twin fields of condensed matter physics and materials science made enormous strides upon development of a consistent first-principles theoretical model of crystalline materials, some of the implications of which were discussed in Chapter 2. However, crystalline materials are only one example of solid materials in practical use. Far more common are disordered solids, and these range from polycrystalline materials, which show order only in disjoint crystalline domains, to fully amorphous solids showing no order whatsoever at scales larger than a few atom lengths. Virtually all polymer materials fall into this category. Unfortunately, the lack of long-range order means that it is difficult to construct a model amorphous system that does reasonably well at capturing the behavior, as opposed to the crystalline phase where considerable insight can be derived from studying a single unit cell. Therefore, much of the physics concerning the amorphous solid phase relies on empirical relationships and heuristics. If a consistent theoretical model of amorphous solid behavior could be achieved, it would be an enormous boon from both a pure science and a practical applications standpoint.

6.1 Relaxation

One commonly studied behavior for amorphous materials is relaxation.^{1,2} Relaxation describes how a system returns to equilibrium (including metastable equilibrium) when perturbed, or how it achieves a new equilibrium when the forces acting on it change. This response will not occur immediately but will do so over a timescale referred to as the relaxation time. For amorphous materials, this is particularly apparent with the transition from liquid to solid. With crystalline materials, there is a clear transition. The material remains solid until its melting temperature, where thermal energy overcomes the binding energy of the crystal. The melting occurs at a single temperature because this binding energy is uniform for each atom in the crystal. In amorphous materials, this distinction is less clear, because each molecule will have a different potential well surrounding it. Each molecule can be thought of as being held in place by a cage formed from its nearest neighbors, but there may be occasional gaps in the cage. These allow the molecule to move more freely, which will make space for another molecule to move in, and so on. Because the energy landscape is not uniform, the number of molecules that can escape their local environment

increases gradually as temperature is raised all the way up to the melting point, such that the solid-liquid transition is a gradual process. Escaping from the cage is a probabilistic affair, and thus, there will be some average time for a molecule to remain trapped at a given temperature. As an example, suppose the timescale were one minute. If the material is observed for a few seconds, all molecules will remain trapped in their cages and the observer will conclude the material is a solid. However, if the observer returns after a few hours, each molecule will have escaped several cages and will seem to have freely diffused through the material (albeit slowly), and the conclusion will be that a liquid is observed. In this case, the state of the material depends on the timescale of the observation. Relaxation of the material will be enabled by molecules escaping from their cages, and the relaxation time is thus related to the average time that it takes for this to occur. In complex molecules, there may be multiple such relaxations. As molecular motion proceeds more rapidly at higher temperatures, the relaxation time decreases as temperature increases.

At low enough temperatures or short enough timescales that all the molecules are frozen, the material is referred to as a glass.³⁻⁵ The term “glassy state” is used, although “state” is a misnomer, at least in the thermodynamic sense as the material is not at equilibrium. At this point all molecules are trapped in their cages and can only vibrate (or perhaps rotate) in place. If the temperature is raised, there will be a point where the relaxation time for molecules moving between their cages becomes faster than the timescale on which the material is measured. At this point, the material will seem significantly less rigid. This temperature is referred to as the glass transition temperature (T_g). T_g , of course, depends on the timescale used for the measurement, with 100-1000 s being a commonly-utilized value.³ Smaller molecules become liquid at this point, but for polymers, the physical entanglements between polymer chains eventually prevent flow. At these temperatures, the polymer remains solid but becomes ductile and elastic, like rubber. The relaxation time for the polymer entanglements then defines the border between the rubbery state and the liquid state. Of course, these are chosen by convention and are not firm borders. A glass will flow provided sufficient time to do so, and a liquid if acted upon quickly enough will seem solid.²

The phenomenon of viscoelasticity observed in materials such as uncrosslinked rubber and in Silly Putty™ is one example of these concepts. These materials can be molded into balls and will bounce if thrown against a surface but can be sheared indefinitely and will slowly flow under their own weight if left undisturbed. In other words, the materials behave as solids on short

timescales, but they behave as liquids on long timescales. Another example is the phenomenon of creep and stress relaxation, seen especially in many polymers when comparing stress (a force applied to a material) and strain (the resulting deformation of the material).⁶ If a constant stress is applied, the material will continue to stretch beyond the initial strain. Removal of the stress will result in only partial recovery of the initial strain. In other words, the material has been permanently stretched out. This can also be observed by keeping the material at a fixed strain. The initial stress will decrease as the material relaxes.

One way to study stress relaxation on multiple timescales is to apply a sinusoidally-varying strain and vary the frequency to observe how the relationship between strain and stress varies. This is referred to as dynamic mechanical analysis or dynamic mechanical spectroscopy.² For a sufficiently small stress and strain where the relationship is linear, this will result in a stress that varies sinusoidally with the same frequency, but with a different amplitude and potentially a different phase. This is useful because it allows elastic and viscous behavior to be decoupled. For an elastic material, stress (σ) and strain (ϵ) are proportional with the proportionality constant being the modulus (G).

$$\sigma(t) = G\epsilon(t) \tag{6.1}$$

For a viscous material, the stress is proportional to the strain rate (i.e., the time derivative of strain) with the proportionality constant being the viscosity (η).

$$\sigma(t) = \eta \frac{d}{dt} \epsilon(t) \tag{6.2}$$

If a sinusoidal strain is applied, the equations for stress with respect to time will look as follows, with $\sigma_E(t)$ being the time-dependent stress for an elastic material and $\sigma_V(t)$ being the time-dependent stress for a viscous material. ϵ_0 is the amplitude of the stress.

$$\epsilon(t) = \epsilon_0 \sin(\omega t) \tag{6.3}$$

$$\sigma_E(t) = G\epsilon_0 \sin(\omega t) \quad (6.4)$$

$$\sigma_V(t) = \frac{\eta}{\omega} \epsilon_0 \cos(\omega t) = \frac{\eta}{\omega} \epsilon_0 \sin\left(\omega t + \frac{\pi}{2}\right) \quad (6.5)$$

Therefore, for a sinusoidal strain the stress will be in-phase with the strain for an elastic material and a quarter-cycle out of phase for a viscous material. For viscoelastic materials, phase shift values anywhere in between are also possible. Therefore, for periodic strains the relationship can be characterized by two factors: the ratio between the maximal stress and strain ($|G| = \sigma_0/\epsilon_0$, where σ_0 is the amplitude of the stress response), and the phase difference between the two (δ) (Figure 6.1). Both factors will depend on frequency.

$$\sigma(t) = |G|(\omega)\epsilon_0 \sin(\omega t + \delta(\omega)) \quad (6.6)$$

For convenience, this is represented using a complex number (G^*), where the magnitude and argument are equal to the stress/strain ratio and the phase difference, respectively.

$$\sigma(t) = G^*(\omega)\epsilon_0 e^{i\omega t} = |G|(\omega)e^{i\delta(\omega)}\epsilon_0 e^{i\omega t} = (G'(\omega) + iG''(\omega))\epsilon_0 e^{i\omega t} \quad (6.7)$$

This allows the elastic modulus and viscosity at different frequencies to be calculated from the real and imaginary components of the complex modulus. Because elastic materials store the energy used to deform them, while viscous materials dissipate it, G' and G'' are referred to as the storage and loss modulus, respectively. These two parameters, as a function of temperature and frequency, characterize the mechanical relaxation behavior of a material. Often times, their ratio, which is equal to $\tan(\delta)$, will be used as well.

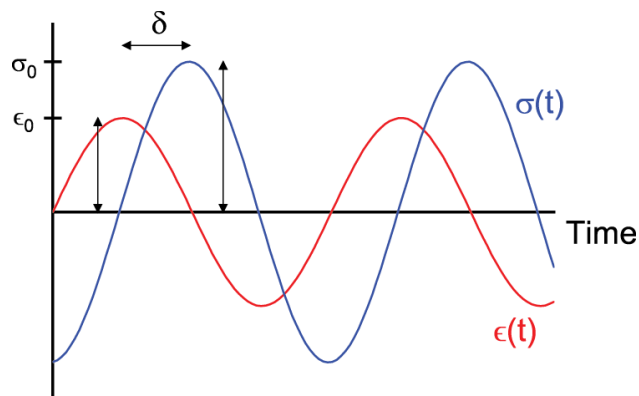


Figure 6.1. Example of mechanical stress (σ) generated in a viscoelastic material in response to a small sinusoidal strain (ϵ). For a complex modulus $G^* = |G|e^{i\delta}$, the magnitude of the complex modulus $|G|$ is equal to the ratio of the amplitudes of the stress and strain functions, while the argument δ is equal to the phase difference between the two.

Dynamic mechanical spectroscopy is widely utilized to characterize materials, as the mechanical properties are often the primary concern for many of these materials. However, a disadvantage of mechanical analysis, particularly for more fundamental studies, is the limited frequency window available to perform measurements. Mechanical systems are typically incapable of reliably actuating at a frequency greater than 10-100 Hz. The lower end of the frequency window is limited by the patience of the experimentalist, but as every order of magnitude of frequency desired increases the measurement time by a factor of 10, it quickly becomes no longer worthwhile to perform the measurement. A solution is to use an alternative means of probing the molecular relaxation that can be done at higher frequencies. One such technique is dielectric spectroscopy.⁷

Any material containing mobile regions of nonzero charge is capable of being polarized. This means that, in the presence of an electric field, the charges will move such that they are aligned with the applied field. Both intramolecular motion of electrons (leading to optical absorption and electronic excitation), and motion of nuclei (leading to infrared absorption and vibronic excitation) are examples, but most relevant to relaxation are the rearrangements of molecular dipoles. Dielectric spectroscopy uses an alternating electric field to drive these motions, and as such, directly probes relaxation on a molecular level. As these motions are ultimately the same ones that give rise to mechanical relaxation, dielectric spectroscopy provides an alternative means to probe these phenomena.⁸

The polarization of a material (\vec{P}) and the electric field (\vec{E}) are both vector quantities. For small electric fields, these values are linearly related through a value known as the dielectric susceptibility (χ_E).

$$\vec{P} = \epsilon_0 \chi_E \vec{E} \quad (6.8)$$

Here, ϵ_0 is the permittivity of free space. The dielectric susceptibility is related to the relative permittivity of the material via $\epsilon = \chi_E + 1$. It is clear that concepts from mechanical relaxation can be applied, with polarization as the analogue of strain and the electric field as the analogue of stress. However, it should be noted that the relationship is inverted here. To directly compare, Equation 6.8 can be inverted with the quantity $1/\epsilon_0 \chi_E$ defined as the dielectric modulus. Alternatively, a “permittivity” (more often called compliance) can be defined for the mechanical system.

As with the complex modulus, the permittivity for a system with a periodic electric field is represented by a complex number, with the real part corresponding to energy storing mechanisms and the imaginary part corresponding to energy dissipating mechanisms. Specifically,

$$\epsilon(\omega) = \epsilon'(\omega) - i\epsilon''(\omega) \quad (6.9)$$

This can be understood by modelling the system as a network of capacitors and resistors. For a parallel plate capacitor, the charge accumulated (Q) per unit area (A) on both electrodes will be proportional to the electric field via the permittivity.

$$\frac{Q}{A} = \epsilon_0 \epsilon \vec{E} \cdot \vec{n} \quad (6.10)$$

Here, \vec{n} is a unit vector perpendicular to both plates. The relation between charge and polarization can be understood in the following way. If no material is present between the parallel plates, the applied electric field will cause some charge to accumulate on both electrodes until the mutual repulsion of the charges counterbalances the electric field. This is accounted for by ϵ_0 , the

permittivity of free space. If a polarizable material is between the plates, the charges on each electrode will lead to the dipoles rotating such that the negative end of the dipole is close to the positive electrode, and vice-versa. These opposite charges will attract more charges and thus allow greater accumulation on each electrode, the effect of which is calculated by the term $\chi_E \epsilon_0$. Because of the proportionality between charge and electric field for a capacitive material, the polarization and electric field will be in-phase yielding a real-valued permittivity. As the charge will flow back upon release of the electric field, this is an energy storing mechanism. In contrast, for a conductive material, charge will not accumulate but will instead flow through the device. For anything less than a perfect conductor, energy will be dissipated as charge passes through the material. In this case the current density (j), which is the time derivative of charge density, will be proportional to the electric field through the conductivity (σ).

$$j = \frac{dQ}{dt A} = \sigma E \quad (6.11)$$

As with viscosity, this leads to an imaginary permittivity for a sinusoidal electric field, though in this case, the loss permittivity is negative, leading to the definition given in equation 6.9.

How should the complex permittivity vary with frequency? Each relaxation will manifest as a sigmoidal decrease in ϵ' with increasing frequency and a peak in ϵ'' at the frequency equal to the inverse of the relaxation time, which is also where the inflection point in ϵ' occurs.

$$\omega_r = 1/\tau_r \quad (6.12)$$

The reason for this is because at frequencies much greater than ω_r , molecular motion is restricted, so the dipoles are unable to fully align themselves with the electric field. At frequencies much lower than ω_r , the dipoles are free to rotate and will fully align themselves. Thus, the polarization is greater at low frequencies. The peak in the loss permittivity occurs due to the fact that the molecules are pushing each other out of the way at ω_r and changing configuration. At higher frequencies, the molecules vibrate in place and do not change configuration, while at lower frequencies, the slower speed of the movement allows the process to occur more reversibly. According to linear response theory, the storage and loss permittivities are tied together

mathematically such that given one, the other can be calculated.⁹ This means that the information contained within them is redundant. Often times, only the loss permittivity is reported, as the peaks in the loss permittivity correspond directly to relaxation events, and the dynamic variation is higher, making it easier to visualize. However, when attempting to mathematically model the relaxation, having both responses can improve the quality of the fit.

Molecules often contain multiple dipoles that will relax independently. Therefore, multiple relaxation events will be observed, each corresponding to a different molecular motion (Figure 6.2). An example from earlier in the text is the glass/rubber transition and the rubber/liquid transition seen in polymers. For most materials, the primary relaxation of concern is the α -process, which corresponds to the glass transition. This indicates the onset of cooperative motion.¹⁰ In the case of macromolecules, an example of cooperative motion is the entire polymer chain moving in a single direction through a process known as reptation (so called because the motion resembles a snake slithering).¹¹ However, relaxations can occur on a smaller scale. For instance, in polymers, a side chain can undergo relaxation without the rest of the polymer needing to move.¹² Linear segments along the polymer backbone can also undergo crankshaft rotation or twisting motions.¹³ Furthermore, even rigid small molecules can show a secondary relaxation, referred to as a Johari-Goldstein β , which is ascribed to isolated motions that would make up the cooperative motion of the α -process on a longer timescale.¹⁴⁻¹⁷ These processes all contribute to one or more relaxations occurring at higher frequencies and lower temperatures than the glass transition, which are typically referred to in order as the β -, γ -, δ -, etc. processes. Additionally, an excess wing is often seen on the high frequency side of the α peak.¹⁸ This leads to ambiguous terminology in the literature, with some reports considering the excess wing part of the α -process and referring to the subsequent peaks as β - and so forth,¹⁹⁻²¹ and others identifying the excess wing as the β -process and referring to the subsequent peaks as γ - and so forth.²²⁻²⁴ Ultimately, while some of the molecular motions that give rise to these high-frequency processes can be identified, there is no consistent picture unifying the properties or behavior of them across different systems.

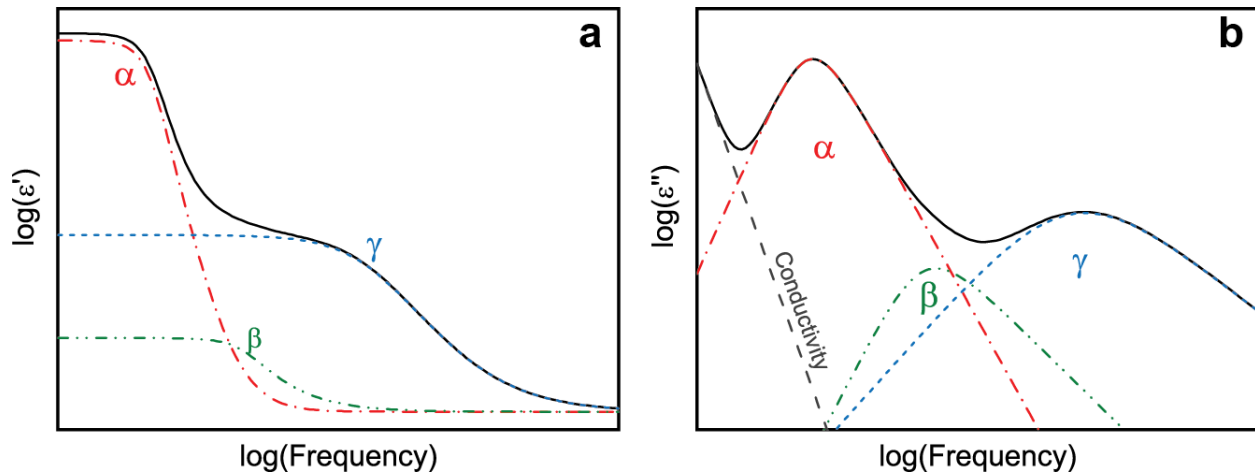


Figure 6.2. Schematic of dielectric relaxation (a) storage and (b) loss response, demonstrating many of the signals often seen in relaxation spectra. The α -process corresponds to the glass transition, while the β - and γ -processes correspond to more localized motions. The infinite-frequency dielectric response is included in each component in (a), while the response due to conductivity is included in (b).

In addition to the α -, β -, and γ -processes, other relaxations are seen. At frequencies lower than the glass transition, there is recent evidence in many materials of another process, referred to as the $\alpha+$ -process.²⁵ The exact origin is unknown, but the process may be related to the rubber/liquid transition or to network formation and dissolution within the material. At frequencies higher than the γ -, δ -, etc. processes, there is a peak referred to as the boson peak around the THz region.²⁴ The boson peak is notable because it does not move with temperature. At still higher frequencies, the IR and UV-Vis absorption modes of the material can be detected. However, these are unrelated to material relaxation, and thus, dielectric spectroscopy is usually concerned with sub-THz frequencies.

A disadvantage of dielectric spectroscopy is that the dielectric response also, at low frequencies, contain an additional signal that is not typically useful. Ionic impurities within the material will, if cooperative motion is permitted, travel freely through the material in response to the electric field. This ionic current acts as an additional loss mode whose intensity is inversely proportional to the frequency. Thus, at low frequencies, the ionic conductivity of the material begins to dominate the loss response (Figure 6.2b).²⁶ While the α -peak can still be resolved in many materials, as the onset of cooperative motions also permits the ions to travel, any larger-scale processes will be unobservable with dielectric spectroscopy. One might think that these relaxations could be observed in the storage permittivity, but the ion motion acts as an extra dipole

polarizing the material, which due to the relatively large distance the ions travel compared to the molecular dipole length, ends up resulting in an enormous polarization at the lowest frequencies.²⁷ Therefore, dielectric spectroscopy is not as well-suited to study the largest-scale relaxations, but it excels below the glass transition.

Little attention has been given to the effect of temperature thus far. As temperature is lowered, decreased molecular motion means that the molecules will not change configuration as frequently, which slows down the relaxation processes, shifting their response functions to lower frequencies. Conversely, higher temperatures cause the state of the system to be jumbled around more frequently, speeding up relaxation. As a result, a given relaxation will occur at higher and higher frequencies as temperature is increased. In this manner, the effect of temperature is to increase the speed of the underlying molecular motions such that relaxation occurs more rapidly. While the frequency range over which a material can be measured is limited, by changing the temperature, relaxations out of the frequency window can be slowed or sped up such that they move within the frequency window, which suggests that if the temperature dependence of the relaxation time shift is known, the relaxation behavior at frequencies well outside the experimental window can be predicted at a given temperature. The simplest case is time-temperature superposition (TTS).¹ In initial experiments on polymers above their T_g values, it was observed that simply shifting the response at different temperatures by introducing a multiplicative factor to the frequency resulted in all of the responses lining up into a master curve.^{28,29} In this way, the effective experimental window could be expanded from 4 orders of magnitude in the frequency domain to over 16. For mechanical relaxation, master curves are widely utilized to predict the response at different frequencies. However, TTS relies on a number of assumptions that are not commonly met. First, it assumes that all relaxations show the same temperature dependence. As different relaxations are governed by different molecular motions, this seems to be an extraordinary assumption, and in fact, it is not generally held. Second, it assumes the shape and height of the relaxation are constant, which again is not often seen. Materials that meet these assumptions are called thermorheologically simple; conversely, those that do not are called thermorheologically complex. TTS is frequently applied to mechanical data, which has a limited experimental frequency window. However, for dielectric data, with its much broader window, TTS is almost never observed.³⁰ In most dielectric datasets, the changing shape of the relaxation peaks is clearly evident, which is illustrated in Figure 6.3. With mechanical datasets, the curves can

almost always be made to overlap over a range of two decades, and the discrepancy at the ends can be ignored. However, with the eight decades that dielectric spectroscopy affords, it becomes obvious that only a limited interval can be made to superimpose. Despite the shortcomings of the theory of TTS, it still remains a useful conceptual tool. However, the complicated temperature dependence of the response requires more sophisticated models to understand.

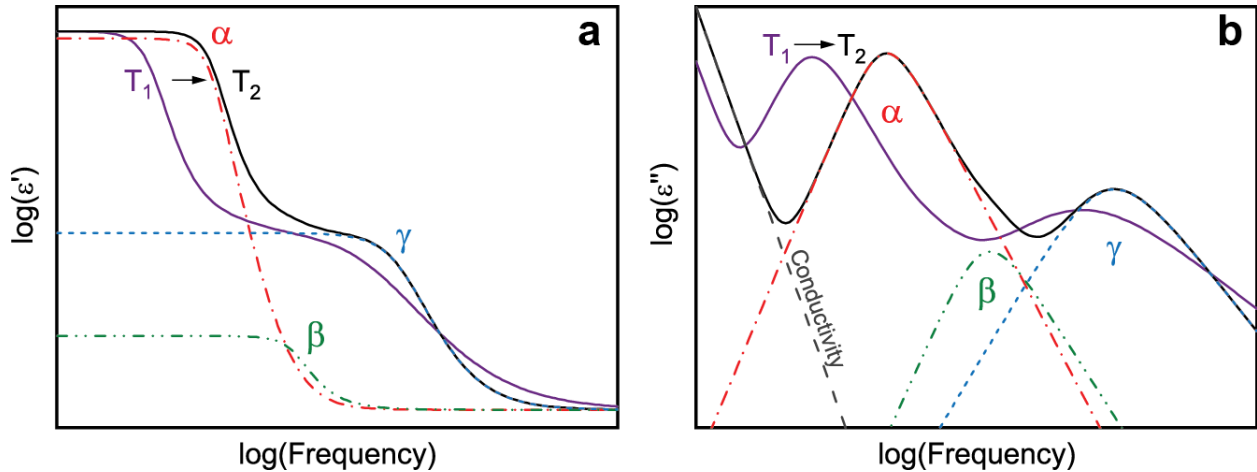


Figure 6.3. Schematic of the effect of increasing temperature on the illustrative dielectric response shown in Figure 6.2. Increasing the temperature causes the individual peaks of the response to shift to higher frequencies. However, the peaks do not all shift by the same amount, nor does their shape necessarily stay fixed as they shift.

6.2 Mathematical Models of Dielectric Relaxation

The simplest quantitative model of dielectric relaxation can be understood if it is assumed to occur exponentially with time. That is to say, if there is a step change in the applied electric field, the difference between the polarization at any given time and the equilibrium polarization will decay exponentially. In more general terms, the autocorrelation function for the dipole polarization, which refers to the correlation coefficient between the orientation of each dipole at $t = 0$ and an arbitrary time in the future, is assumed to decay exponentially. This result can be derived for isolated dipoles that rotate in jumps governed by Brownian motion. If the Fourier transforms of the polarization and electric field are taken, then their quotient will give the following equation.³¹

$$\varepsilon(\omega) = \frac{\Delta\varepsilon}{1 + i\omega\tau_r} + \varepsilon_\infty \quad (6.13)$$

Here, $\Delta\varepsilon$ is the strength of the dielectric response, ε_∞ is the dielectric constant at high-frequencies, and τ_r is the relaxation time, which is equal to the time constant of the exponential decay. This equation is referred to as the Debye function, and it produces the expected qualitative behavior for dielectric relaxation. However, the width of the loss peak is significantly lower than what is seen in actual datasets. Additionally, the Debye model predicts that the loss peak will be symmetric at lower and higher frequencies, whereas a high-frequency wing is often seen.^{18,32} While actual dielectric response data show large deviations from the Debye model except in rare cases, it provides a useful framework for justifying the general shape of the response. In particular, the Debye function demonstrates time-temperature superposition. Of the 3 parameters in the function, only τ_r shows any significant temperature dependence. ε_∞ shows none and $\Delta\varepsilon$, while it is predicted to decrease at higher temperatures as per Onsager theory,³³ is relatively unaffected.

To achieve a more quantitative picture of relaxation, the Debye function is typically modified with stretching exponents providing more flexibility in the shape of the model. The most general form is known as the Havriliak-Negami function.³⁴

$$\varepsilon(\omega) = \frac{\Delta\varepsilon}{(1 + (i\omega\tau_{HN})^\alpha)^\beta} \quad (6.14)$$

Here, α and β are constrained between 0 and 1. Decreasing α leads to a broadening of the response while decreasing β skews the response towards higher frequencies (Figure 6.4). The equation is a combination of two other models: the Cole-Cole function ($\beta = 1$),³⁵ and the Cole-Davidson function ($\alpha = 1$).³² For data in the time-domain, the exponential decay assumed by the Debye model is modified with a stretching exponent. This is referred to as the Kohlrausch-Williams-Watts (KWW) function.³⁶

$$\phi(t) \sim e^{-\left(\frac{t}{\tau_0}\right)^\beta} \quad (6.15)$$

Here, $\phi(t)$ is the autocorrelation function. These functions are broadly applicable to a wide variety of systems, but ultimately they are just empirical relationships (the KWW function can be derived for certain situations, but it is typically utilized as an empirical fit⁴). Furthermore, the dependence of the shape parameters on temperature is inconsistent, and the physical meaning of this temperature dependence is unclear.^{37–39}

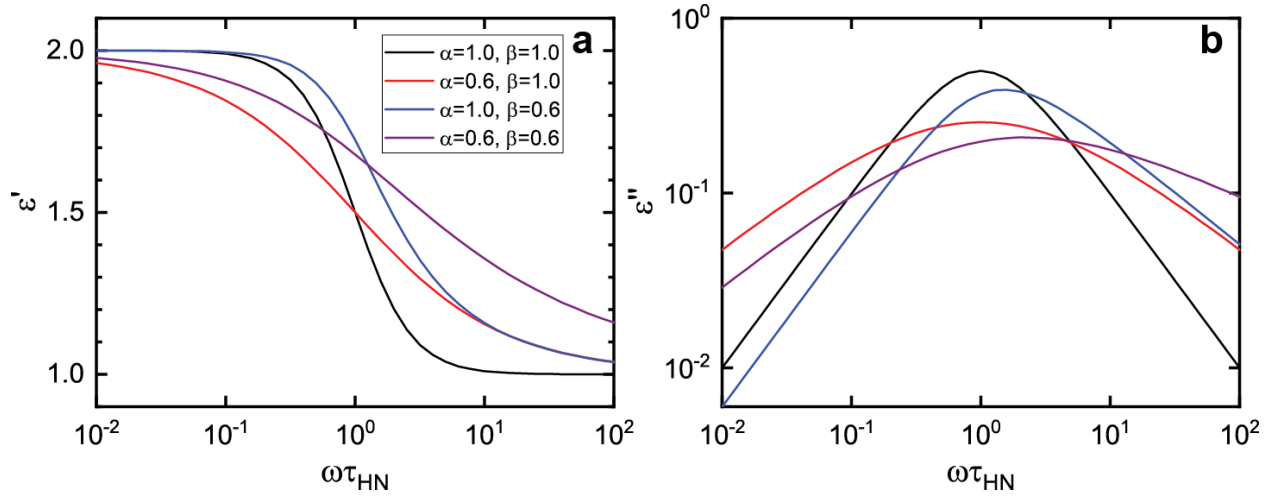


Figure 6.4. Havriliak-Negami function illustration, showing the effects of the stretching exponents α and β on the (a) storage and (b) loss permittivity. Decreasing α leads to a broadening of the response, while decreasing β skews the response towards higher frequencies. The black line is equivalent to a Debye function.

One alternative approach is to represent the response as a spectrum of Debye processes.⁴⁰

$$\varepsilon(\omega) = \varepsilon_{\infty} + \int_0^{\infty} \frac{H(\tau)}{1 + i\omega\tau} d\tau \quad (6.16)$$

$H(\tau)$ is the spectral density function, analogous to $\Delta\varepsilon$ in the Debye model. The standard approach is to numerically fit using the discrete version of the equation, with a regular spacing for $\Delta\tau$.

$$\varepsilon(\omega) = \varepsilon_{\infty} + \sum_i \frac{\Delta\varepsilon_i}{1 + i\omega\tau_i} \quad (6.17)$$

As the Debye model has a theoretical basis behind it, it is hoped that recasting the data in this fashion will lead to greater insights. Unfortunately, the fitting scheme is restricted to using the

same set of τ_i for each isotherm, then allowing $\Delta\varepsilon_i$ to vary as a function of temperature, which is unphysical. Ideally, it would be possible to fix $\Delta\varepsilon$ and let τ_i vary with temperature, but standard numerical fitting procedures do not operate in this manner.

6.3 Model Dielectric Materials

One commonly studied class of materials are the diglycidylether of bisphenol-A (DGEBA) epoxies (Figure 6.5a). DGEBA can be polymerized as a step polymer by reacting with bisphenol-A. The resulting polymer is often called phenoxy.⁴¹ DGEBA can also be crosslinked using a variety of other molecules due to the reactivity of the glycidyl groups. Commonly, a molecule with two primary amine functionalities will be utilized, which can react with four glycidyl groups (Figure 6.5b). This leads to a heavily crosslinked network. Short phenoxy oligomers can be cured as well, which allows the crosslink density to be easily varied.^{42–46} DGEBA is widely utilized in commercial settings as an adhesive, surface coating, or structural material,⁴⁷ and its versatility in terms of molecular architecture make it a very widely studied model material for both mechanical and dielectric relaxation studies.^{37,48–52}

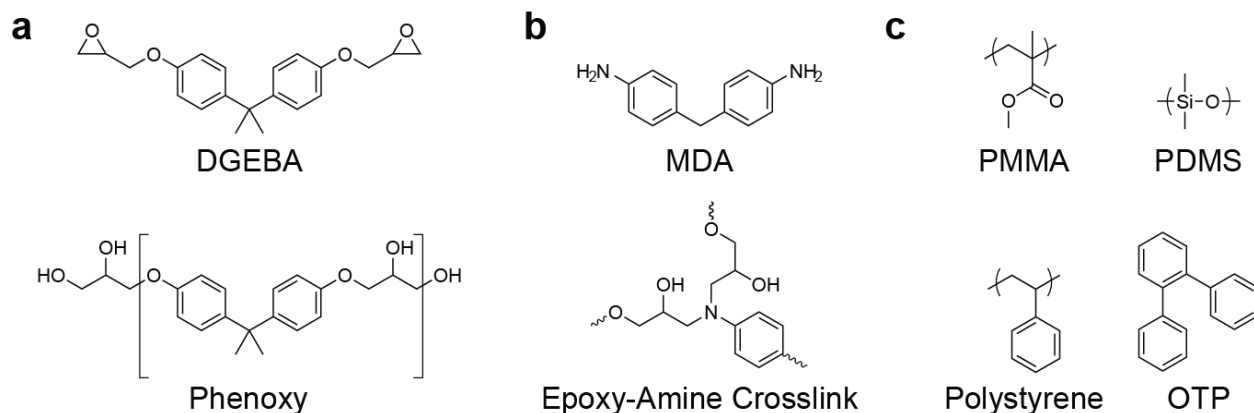


Figure 6.5. Illustrations of model compounds for dielectric spectroscopy. (a) Chemical structure of diglycidylether of bisphenol-A (DGEBA) and of phenoxy, a DGEBA linear polymer. (b) Chemical structure of 4,4'-methylenedianiline (MDA), a commonly used crosslinking agent for DGEBA, and chemical structure of the crosslink between one functional end of an MDA molecule and two DGEBA molecules. (c) Chemical structures of other materials commonly studied with dielectric spectroscopy, including poly(methylmethacrylate) (PMMA), poly(dimethylsiloxane) (PDMS), and *ortho*-terphenyl (OTP).

Other common materials include poly(methylmethacrylate) (PMMA),⁵³ polystyrene,^{10,54} and poly(dimethylsiloxane) (PDMS) (Figure 6.5c).⁵⁵ Small molecule glass formers can also be studied. Most common are large monoalcohols, where the alcohol group imparts polarity allowing the molecule to be measured through dielectric spectroscopy, while the bulk of the molecule prevents crystallization.^{31,56} One of the most commonly studied small molecules, however, is *ortho*-terphenyl.⁵⁷ This molecule is relatively small and rigid but still forms glasses, and its size and rigidity make it useful for theoretical studies.⁵⁸ The use of both small molecules and polymers allows for different regimes of relaxation behavior to be studied. As small molecules typically have very low T_g values, relaxation at timescales much longer than the glass transition can be studied. Small molecules also show greater relaxation strength (compare typical real permittivity values of ~ 40 for alcohols³² with values between 2 and 10 for polymers⁵⁹). Polymers, on the other hand, have a wide range of T_g values depending on their molecular weight and crosslink density.^{2,60} Typically, these will be much larger than those of small molecules, therefore relaxation at timescales shorter than the glass transition can be more easily studied. Additionally, polymers tend to show a richer behavior at these scales, due to their more complex structures.^{12,13} The wide range of materials utilized highlights the versatility of dielectric spectroscopy as an analytical method, and emphasizes the broad-reaching importance that advances in the theory of amorphous solids will have to myriad seemingly-unrelated materials applications.

6.4 References

- (1) Ferry, J. D. *Viscoelastic Properties of Polymers*, 3rd ed.; Wiley, 1980.
- (2) Sperling, L. H. *Introduction to Physical Polymer Science*, 3rd ed.; Wiley-Interscience, 2001.
- (3) Cavagna, A. *Phys. Rep.* **2009**, *476* (4–6), 51–124.
- (4) Ediger, M. D.; Angell, C. A.; Nagel, S. R. *J. Phys. Chem.* **1996**, *100* (31), 13200–13212.
- (5) Debenedetti, P. G.; Stillinger, F. H. *Nature* **2001**, *410* (March), 259.
- (6) Aklonis, J. J. *J. Chem. Educ.* **1981**, *58* (11), 892–897.
- (7) Kremer, F.; Schönhals, A. *Broadband Dielectric Spectroscopy*; Springer-Verlag Berlin Heidelberg: New York, 2003.
- (8) Pakula, T. In *Broadband Dielectric Spectroscopy*; Kremer, F., Schönhals, A., Eds.; Springer-Verlag Berlin Heidelberg: New York, 2003; pp 597–624.
- (9) Böttcher, C. J. F.; Bordewijk, P. In *Theory of Electric Polarization Volume II - Dielectrics in Time-dependent Fields*; Elsevier B.V., 1978; pp 1–44.
- (10) Matsumiya, Y.; Uno, A.; Watanabe, H.; Inoue, T.; Urakawa, O. *Macromolecules* **2011**, *44* (11), 4355–4365.
- (11) De Gennes, P. G. *J. Chem. Phys.* **1971**, *55* (2), 572–579.

- (12) McCrum, N. G.; Read, B. E.; Williams, G. *Anelastic and dielectric effects in polymeric solids*; John Wiley, 1967.
- (13) Schatzki, T. F. *J. Polym. Sci.* **1962**, *57*, 496.
- (14) Johari, G. P.; Goldstein, M. *J. Chem. Phys.* **1970**, *53* (6), 2372–2388.
- (15) Johari, G. P. *J. Phys. Chem. B* **2019**, *123* (13), 3010–3023.
- (16) Paluch, M.; Roland, C. M.; Pawlus, S.; Zioło, J.; Ngai, K. L. *Phys. Rev. Lett.* **2003**, *91* (11), 115701.
- (17) Ngai, K. L.; Capaccioli, S.; Prevosto, D.; Wang, L. M. *J. Phys. Chem. B* **2015**, *119* (38), 12502–12518.
- (18) Leheny, R. L.; Nagel, S. R. *Europhys. Lett.* **1997**, *39* (4), 447–452.
- (19) Johari, G. P. *Ann. N. Y. Acad. Sci.* **1976**, *279*, 117–140.
- (20) Schilling, R. In *Disorder Effects on Relaxational Processes*; 1994; pp 193–231.
- (21) Füllbrandt, M.; Purohit, P. J.; Schönhals, A. *Macromolecules* **2013**, *46* (11), 4626–4632.
- (22) Casalini, R.; Fioretto, D. *Phys. Rev. B - Condens. Matter Mater. Phys.* **1997**, *56* (6), 3016–3021.
- (23) Zajac, M.; Kahl, H.; Schade, B.; Rödel, T.; Dionisio, M.; Beiner, M. *Polymer (Guildf)*. **2017**, *111*, 83–90.
- (24) Lunkenheimer, P.; Loidl, A. In *Broadband Dielectric Spectroscopy*; Kremer, F., Schönhals, A., Eds.; Springer-Verlag Berlin Heidelberg: New York, 2003; pp 131–170.
- (25) Ni, Y.; Medvedev, G. A.; Curliss, D. B.; Caruthers, J. M. *Polymer (Guildf)*. **2020**, *Submitted*.
- (26) Schönhals, A.; Kremer, F. In *Broadband Dielectric Spectroscopy*; Kremer, F., Schönhals, A., Eds.; Springer-Verlag Berlin Heidelberg: New York, 2003; pp 59–98.
- (27) Fricke, H. *London, Edinburgh, Dublin Philos. Mag. J. Sci.* **1932**, *14* (90), 310–318.
- (28) Andrews, R. D.; Hofman-Bang, N.; Tobolsky, A. V. *J. Polym. Sci.* **1948**, *3* (5), 669–692.
- (29) Tobolsky, A. V.; Catsiff, E. *J. Polym. Sci.* **1956**, *19* (91), 111–121.
- (30) Kremer, F.; Schönhals, A. In *Broadband Dielectric Spectroscopy*; Kremer, F., Schönhals, A., Eds.; Springer-Verlag Berlin Heidelberg: New York, 2003; pp 99–130.
- (31) Debye, P. *Polar Molecules*; Chemical Catalogue Company: New York, 1929.
- (32) Davidson, D. W.; Cole, R. H. *J. Chem. Phys.* **1951**, *19* (12), 1484–1490.
- (33) Onsager, L. *J. Am. Chem. Soc.* **1936**, *58* (8), 1486–1493.
- (34) Havriliak, S.; Negami, S. *Polymer (Guildf)*. **1967**, *8*, 161–210.
- (35) Cole, K. S.; Cole, R. H. *J. Chem. Phys.* **1941**, *9*, 341–351.
- (36) Williams, G.; Watts, D. C. *Trans. Faraday Soc.* **1970**, *66*, 80–85.
- (37) Pisignano, D.; Capaccioli, S.; Casalini, R.; Lucchesi, M.; Rolla, P. A.; Justl, A.; Rössler, E. *J. Phys. Condens. Matter* **2001**, *13* (20), 4405–4419.
- (38) Döb, A.; Paluch, M.; Sillescu, H.; Hinze, G. *J. Chem. Phys.* **2002**, *117* (14), 6582–6589.
- (39) Švajdlenková, H.; Ruff, A.; Lunkenheimer, P.; Loidl, A.; Bartoš, J. *J. Chem. Phys.* **2017**, *147* (8).
- (40) Böttcher, C. J. F.; Bordewijk, P. In *Theory of Electric Polarization Volume II - Dielectrics in Time-dependent Fields*; Elsevier B.V., 1978; Vol. 7, pp 45–137.
- (41) Gabriel. Phenoxies | Phenoxy Resin | Amorphous Polymers | Gabriel <https://www.gabrielchem.com/phenoxy-resin/> (accessed Jun 17, 2020).
- (42) Delatycki, O.; Shaw, J. C.; Williams, J. G. *J. Polym. Sci. Part A-2* **1969**, *7*, 753–762.
- (43) Takahama, T.; Geil, P. H. *J Polym Sci Polym Phys Ed* **1982**, *20* (11), 1979–1986.
- (44) Charlesworth, J. M. *Polym. Eng. Sci.* **1988**, *28* (4), 221–229.
- (45) Pogany, G. A. *Polymer (Guildf)*. **1970**, *11* (2), 66–78.

- (46) Urbaczewski-Espuche, E.; Galy, J.; Gérard, J.; Pascault, J.; Sautereau, H. *Polym. Eng. Sci.* **1991**, *31* (22), 1572–1580.
- (47) Penn, L.; Morra, B.; Mones, E. *Composites* **1977**, *8* (1), 23–26.
- (48) Corezzi, S.; Capaccioli, S.; Gallone, G.; Lucchesi, M.; Rolla, P. A. *J. Phys. Condens. Matter* **1999**, *11* (50), 10297–10314.
- (49) Capaccioli, S.; Corezzi, S.; Gallone, G.; Rolla, P. A.; Comez, L.; Fioretto, D. *J. Non. Cryst. Solids* **1998**, *235–237*, 576–579.
- (50) Corezzi, S.; Capaccioli, S.; Gallone, G.; Livi, A.; Rolla, P. A. *J. Phys. Condens. Matter* **1997**, *9* (29), 6199–6216.
- (51) Corezzi, S.; Beiner, M.; Huth, H.; Schröter, K.; Capaccioli, S.; Casalini, R.; Fioretto, D.; Donth, E. *J. Chem. Phys.* **2002**, *117* (5), 2435–2448.
- (52) Hassan, M. K.; Tucker, S. J.; Abukmail, A.; Wiggins, J. S.; Mauritz, K. A. *Arab. J. Chem.* **2016**, *9* (2), 305–315.
- (53) Theobald, S.; Pechhold, W.; Stoll, B. *Polymer (Guildf)*. **2001**, *42*, 289–295.
- (54) Fukao, K.; Miyamoto, Y. *Phys. Rev. E - Stat. Physics, Plasmas, Fluids, Relat. Interdiscip. Top.* **2000**, *61* (2), 1743–1754.
- (55) Kirst, K. U.; Kremer, F.; Litvinov, V. M. *Macromolecules* **1993**, *26* (5), 975–980.
- (56) Böhmer, R.; Gainaru, C.; Richert, R. *Phys. Rep.* **2014**, *545* (4), 125–195.
- (57) Richert, R. *J. Chem. Phys.* **2005**, *123* (15), 2003–2006.
- (58) Kudchadkar, S. R.; Wiest, J. M. *J. Chem. Phys.* **1995**, *103* (19), 8566–8576.
- (59) Nasreen, S.; Treich, G. M.; Baczkowski, M. L.; Mannodi-Kanakkithodi, A. K.; Cao, Y.; Ramprasad, R.; Sotzing, G. In *Kirk-Othmer Encyclopedia of Chemical Technology*; John Wiley & Sons, Inc., 2017.
- (60) Fox, T. G.; Flory, P. J. *J. Appl. Phys.* **1950**, *21*, 581–591.

7. RELAXATION MAP OF GLYCEROL AND SORBITOL IN THE GLASS AND LIQUID STATES*

7.1 Abstract

Recently developed method for obtaining the complete relaxation map from linear relaxation data (Ni et al, *Macromolecules*, **53**, 1867, 2020) has been applied to the molecular glass formers glycerol and sorbitol. For glycerol, dielectric data from Schneider et al (*J. Non-Cryst. Solids*, **235**, 173, 1998) above T_g was augmented with dielectric data below T_g . For sorbitol the broadband dielectric was measured from $T_g-150^\circ\text{C}$ to $T_g+50^\circ\text{C}$ and was used with additional data from Geirhos et al (*Phys. Rev. Lett.*, **120**, 085705, 2018). The new approach differs from the traditional analysis; specifically, (i) the spectrum is inherently discrete, (ii) the spectral strengths of all individual Debye processes are the same, (iii) the density of processes is non-uniform, which is the source of the order-of-magnitude change in the observed dielectric response, and (iv) the individual relaxation times are allowed to shift independently with temperature. Using this approach, new relaxation processes continue to emerge from a short-time source at or near the boson peak as the temperature is decreased. This addition of new processes is the origin of the increase in the static dielectric constant with decreasing temperature. Above T_g the new processes rapidly join the main α -relaxation peak that has the classic VTF temperature dependence. Approaching T_g and below, the newer processes exhibit progressively weaker temperature dependence, where at very low temperature an Arrhenian-like temperature dependence is approached. The classic features of glass forming materials – the α -relaxation, the excess wing, and the β -relaxation are described in terms of the new relaxation map.

7.2 Introduction

Studying the linear relaxation response of glass forming materials is an important path to elucidating the physics of glass formation and the behavior of the resulting glass.^{1,2} Dielectric relaxation occupies a prominent place among relaxation experiments because it enables probing a wide frequency window at a single temperature.³ When several dielectric spectroscopy techniques

* This work was submitted to Journal of Chemical Physics on May 22, 2020 by Medvedev, G. A.; Wilcox, D. A.; Boudouris, B. W.; and Caruthers, J. M.

are combined, that window may span up to fifteen logarithmic decades.⁴ The current challenge is how to analyze the relaxation data to extract information about the underlying molecular processes. One approach is to describe the data in terms of the relaxation spectrum,⁵ where in case of dielectric relaxation the complex permittivity $\varepsilon^*(\omega)$ is represented as

$$\varepsilon^*(\omega) = \varepsilon'(\omega) - i\varepsilon''(\omega) = \varepsilon_\infty + \int_{-\infty}^{\infty} H(\log \tau) \frac{1}{1+i\omega\tau} d\log \tau \quad (7.1)$$

where ω is the frequency, $\varepsilon'(\omega)$ and $\varepsilon''(\omega)$ are storage and loss permittivities, ε_∞ is the infinite frequency permittivity due to atomic and electronic effects and τ is the relaxation time. The function $H(\log \tau)$ is the spectral strength; specifically, the contribution of the processes with the relaxation times lying in the interval from τ to $\tau + d\tau$ to the overall relaxation response. The $(1 + i\omega\tau)^{-1}$ term in Equation 7.1 implies that a given relaxation process is modeled as a Debye process. The spectral approach takes advantage of both the $\varepsilon'(\omega)$ and $\varepsilon''(\omega)$ data in determining the relaxation response, where any inconsistencies in the experimental data readily become apparent. In numerical analysis a discrete analogue of Equation 7.1 is used; specifically,

$$\varepsilon^*(\omega) = \varepsilon'(\omega) - i\varepsilon''(\omega) = \varepsilon_\infty + \sum_k H_k \frac{1}{1+i\omega\tau_k} \quad (7.2)$$

where H_k is the strength associated with the process with the k^{th} relaxation time, τ_k . Implicit in the transition from Equation 7.1 to Equation 7.2 is the assumption that the relaxation times of the Debye processes $\{\log \tau_k\}$ are evenly spaced from $-\infty$ to $+\infty$ along the $\log(\text{time})$ axis, where the arbitrary choice of 5 points per logarithmic decade is common. Once the $\{\log \tau_k\}$ are specified the $\{H_k\}$ are the unknown spectral strengths, where the goal of the analysis is to find a set of $\{H_k\}$ that describe the experimentally measured $\varepsilon'(\omega)$ and $\varepsilon''(\omega)$ data. The problem as formulated in Equations 7.1 and 7.2 is a Fredholm equation of the first kind and consequently mathematically ill-posed, where small fluctuations in the $\varepsilon'(\omega)$ or $\varepsilon''(\omega)$ data can cause large oscillations in $\{H_k\}$. In order to address the issue of fluctuations, various regularization techniques have been developed to enable smooth solutions.⁶⁻⁸

Using the traditional spectral analysis procedure described above, a set of $\{H_k\}$ can be found that fits the data at each temperature. Unfortunately, no further progress is possible for the general case because the spectral strengths for a given discretization of the $\log(\text{time})$ axis, i.e. individual $H_k(T)$, behave with temperature in a non-trivial manner. An exception to this is for the case of thermo-rheologically simple materials, i.e. materials that obey time-temperature superposition. For such materials the set of $\{H_k\}$ shifts as whole along the $\log(\text{time})$ axis with changes in temperature. When the time-temperature (or frequency-temperature) invariance was first observed in viscoelastic experiments on polymers by Tobolsky, Ferry, and co-workers,¹ it was thought to be a generic feature of all glass forming materials – at least in the temperature range above T_g and possibly even in the glassy state, where reports on violations of time-temperature superposition for single-phase materials were dismissed as exceptions to a basically correct rule. This consensus no longer holds. With new experimental techniques like broadband dielectric spectroscopy with a frequency window of seven or more decades as compared to mechanical spectroscopy, where the accessible frequency window is typically three decades or less, thermo-rheological simplicity is now viewed as the exceptional case rather than the rule. Consequently, the brute force approach of extracting the relaxation spectrum from individual isotherms is hardly used in analyzing dielectric relaxation data.

The most common method of analysis in the dielectric relaxation data is the use of empirical functions such as the Cole-Cole,⁹ Cole-Davidson,¹⁰ Havriliak-Negami¹¹ and Kohlrausch-Williams-Watts (KWW)¹² functions, where multiple functions are needed to fit a full set of isotherms.¹³⁻²⁶ For instance, two functions are typically utilized in the temperature region above T_g alone. In case of the type A glass formers,²⁷ i.e. materials that do not exhibit the β -relaxation peak like glycerol, these typically are: a function (usually Cole-Davidson¹⁰ or KWW¹²) to describe the α -relaxation peak proper that is associated with the glass transition and an additional function representing what is known as the ‘excess wing’ of the α -relaxation peak; although, a single complex function such as the generalized Gamma distribution^{27,28} or the Chamberlin cluster model function^{29,30} have also been used. In case of the type B glass formers,²⁷ i.e. materials that exhibit clear β -relaxation peak like sorbitol, the two functions typically are: a Havriliak-Negami function to describe the α -relaxation, including both the peak proper and the excess wing, and either a second Havriliak-Negami function or a Cole-Cole function to describe the β -relaxation. The β -relaxation peak becomes the dominant feature in isotherms below T_g ,

where sometimes additional functions are needed at even lower temperatures and higher frequencies.^{19,20,31} Note that the above description pertains to molecular glass formers, where the picture may become even more complicated in case of polymeric glass formers, which are beyond the scope of this communication. It is implied that each function, although empirical, represents an underlying physical process, where the apparent need for multiple functions implies that there are multiple, independent relaxation mechanisms. If this were true one should see each function shifting more-or-less intact with temperature, although different functions would generally have different shift factors; specifically, each individual function would exhibit frequency-temperature invariance, although the relaxation response would change shape. However, as is commonly seen this is not the case. When several isotherms are fit using the empirical functions, one observes that the parameters in the individual functions are required to change with temperature, where some of these dependencies are not weak and even non-monotonic.^{14-19,22,24} Perhaps the temperature dependence of the shape parameters of the empirical functions can be accepted – narrowing or broadening of a peak is not unreasonable and there could perhaps be an underlying physical reason. However, a change of the spectral strength (i.e., the area) of a given process is more troubling, where a strong temperature dependence of the spectral strength has been reported for both α - and the β -processes.^{15,16,18,19,22,26} The need for increased spectral strength of the α -process with decreasing temperature is driven by the experimentally observed increase in the static dielectric susceptibility defined as $\chi_S = \varepsilon'(\omega \rightarrow 0) - \varepsilon_\infty$, which is a universal feature of glass forming materials.^{21,32-35} An increase in χ_S per se would not be a problem and is expected according to Onsager-Kirkwood theory of dielectric permittivity.^{36,37} However, the Onsager-Kirkwood theory predicts χ_S behaving as aT^{-1} , whereas the experimentally observed behavior is $\chi_S = aT^{-1} + b$ with a large negative intercept b .¹⁹ Even more problematic is the temperature dependence of the spectral strength of the β -process apparently needed to fit the experimental data. As reported for glass forming materials of different chemical structures, the spectral strength of the β -processes rapidly *decreases* with decreasing temperature in the vicinity of Tg then abruptly ceases to depend on temperature several degrees below Tg.^{16,18,19,22} Then, according to some reports, it begins to *increase* with decreasing temperature well below Tg.²² As far as we know, there is no theoretical rationalization for such behavior. To summarize: (i) the empirical functions approach uses a large number of parameters which non-trivially depend on temperature, (ii) there is no theory relating commonly used empirical functions to specific molecular mechanisms, and

(iii) the empirical function approach has not had much success revealing patterns in relaxation response of glass formers of varying chemical structure. Therefore, a different approach to analyzing relaxation behavior of glass forming materials is needed.

Let us revisit the approach based on solving Equation 7.2. In a recent publication we proposed a different method for obtaining spectra from the relaxation data.³⁸ Specifically, in the traditional approach where $\{\log \tau_k\}$ are just a formal discretization of the time axis and the spectral strengths H_k are the physically meaningful quantities that must be determined from the relaxation data. In contrast, we argued that $\{\log \tau_k\}$ are the physically meaningful quantities with the assumption that the spectral strength of each Debye process is constant, i.e. $H_k = \bar{H}$ for all k 's and temperatures. In this alternative approach the locations of the $\log \tau_k$ values are dictated by the experimental data, rather than being evenly spaced, such that the density of the processes is high in the regions where the loss permittivity $\varepsilon''(\omega)$ has a peak and is low in the regions where $\varepsilon''(\omega)$ passes through a minimum. This idea is, in part, inspired by the linear viscoelastic molecular models (e.g., the Rouse³⁹ and reptation⁴⁰ models for polymers) that predict a discrete spectrum of unevenly spaced processes of constant magnitude. In this approach each $\log \tau_k$ has its own temperature dependence, where the complete description of the behavior of the system is contained in a relaxation map that is the set of $\{\log \tau_k(T)\}$ functions. This new approach, which we call the Variable Spacing, Equal Spectral Strength (VASESS, pronounced vases) method. VASESS does not require any *a priori* assumption about the shape of the relaxation spectra, that the spectrum is composed of two or more empirical relaxation functions or that the shift function has a particular shape or functional form. This new approach is just a fair mapping of the experimental data to a set of Debye processes.

In this paper the new method of analyzing the relaxation data is applied to dielectric spectroscopy data for two well-known molecular glass formers, glycerol and sorbitol, where relaxation maps will be constructed for both materials. The choice of glycerol is natural because the set of dielectric relaxation data reported by Schneider et al³³ is the most extensive (in terms of the frequency and temperature range covered) data set reported to date for any material. The Schneider et al data for glycerol will be augmented with new broadband dielectric spectroscopy data below T_g for temperatures they did not measure. The T_g of glycerol is low (190 K); thus, the sub-T_g region accessible by standard experimental equipment using liquid N₂ is relatively narrow from only 120 K to 190 K. To expose more of the sub-T_g behavior, sorbitol (T_g = 268 K) was

chosen as a second material for study, where sub-T_g dielectric behavior from 120 K to 268 K was measured. These data are augmented with the sub-T_g sorbitol data reported recently by Geirhos et al;⁴¹ that includes the temperature range from 10 K to 260 K. The analysis of both glycerol and sorbitol enable the comparison of β -relaxation response for these two materials. For glycerol, the β -relaxation peak is absent while sorbitol exhibits a well-resolved sub-T_g β -relaxation peak. How this difference between the two materials is reflected in their respective relaxation maps will be shown.

The paper is organized as follows: In the next section the experimental methods used for determining the broadband dielectric behavior of glycerol and sorbitol will be given; followed by a section that summarizes the VASESS methodology developed in the paper by Ni et al.³⁸ The Results section will present both experimental data and the VASESS analysis first for glycerol and then sorbitol. Finally, the Discussion section will examine the new perspective that the relaxation maps of glycerol and sorbitol provide with respect to relaxation in glass forming liquids.

7.3 Experimental

Glycerol (99.5%) and D-Sorbitol (99.5%) were purchased from Sigma Aldrich. Glycerol was dried overnight with 4Å molecular sieves, and sorbitol was used with no further purification. Both chemicals were stored in a moisture-free inert atmosphere glovebox prior to use. Data were gathered using a Concept 40 Novocontrol Dielectric Spectrometer with an Alpha ANB Analyzer, ZGS active sample cell, and QUATRO Cryosystem. All samples remained under a nitrogen blanket in the Novocontrol spectrometer for the entire duration of the test, which in addition to providing temperature control also prevented moisture from infiltrating the apparatus and contaminating the hygroscopic samples.

Glycerol samples were measured using a Novocontrol BDS 1307 Cylindrical Liquid Sample Cell with a 22.5 mm inner electrode. The sample cell was disassembled, rinsed with water, acetone, and isopropanol, and allowed to air dry before use. After reassembling, the liquid was slowly added to the cell using a syringe up to the level of the guard ring, with care taken to avoid introducing bubbles. Once filled, the sample holder was removed from the glovebox and quickly loaded in the spectrometer to minimize ambient exposure. Experimental measurements were taken starting at 120 K and increased in discrete temperature steps of 10 K up to a maximum temperature of 300 K. After equilibrating at each temperature, the in-phase and out-of-phase components of

the dielectric response were measured from 10^{-1} Hz to 10^{+7} Hz with a spacing of 5 points per logarithmic decade.

Sorbitol was measured in a parallel plate configuration. The 20 mm diameter plates (Novocontrol BDS 1301 disposable electrodes) were cleaned by sonication for 10 minutes in acetone, chloroform, and then isopropanol before the plates were air dried. The bottom plate, along with two 100 μm -thick silica spacer rods (Novocontrol BDS 1304-100), was placed on a hot plate at 120 °C located inside the glovebox. Sorbitol was added to the bottom plate, melted and then baked for 1 hour to ensure removal of any residual moisture. The preheated top plate was then added and pressed into place using a mechanical assembly with guide posts to ensure alignment. The sample was then allowed to cool to room temperature and excess material was removed from the sides of the plates. Immediately before testing, the sample was removed from the glovebox and quickly loaded in the spectrometer to minimize ambient exposure. The sample was heated to 390 K for 30 minutes to ensure melting, then cooled to the lowest experimental temperature. Experimental measurements were taken starting at 120 K and increased in discrete steps up to 320 K. After the apparatus reached each temperature, the sample was equilibrated for an additional 10 to 150 minutes to minimize any transient relaxation. After equilibration, the dielectric response was measured from 10^{-2} Hz to 10^{+7} Hz with a spacing of 5 points per logarithmic decade for temperatures of 300 K and below. For temperatures 305 K and above, the dielectric response was measured from 10^{-1} Hz to 10^{+7} Hz. This reduced frequency window was used because (i) the material tended to crystallize at these higher temperatures for the long times required to perform the low frequency experiments from 10^{-2} to 10^{-1} Hz and (ii) the low-frequency response at these temperatures was dominated by conductance and electrode polarization making it impossible to determine the dielectric relaxation.

7.4 Method of Analysis

A new approach to analyzing viscoelastic relaxation data called VASESS has been proposed by Ni et al,³⁸ where we will now briefly outline the ideas and implementation methodology as applied to broadband dielectric relaxation. The VASESS method is based on solving Equation 7.2 to obtain the relaxation spectrum; however, unlike in the traditional analysis, the spectral strength is constant and the spectral density is optimized to fit the experimental $\epsilon'(\omega)$ and $\epsilon''(\omega)$ isotherms, where a new solution is obtained at every temperature. A key assumption is

that all spectral components have the same constant strength, \bar{H} , which is temperature independent. With a change in temperature, processes with relaxation times $\{\log \tau_k\}$ may enter or exit the experimental window, but when they exit the experimental window, they will still affect the response and must be taken into account. Specifically, relaxation times that are too short to affect the $\varepsilon''(\omega)$ isotherm, because $\omega\tau_k/(1 + \omega^2\tau_k^2)$ is small when $\omega\tau_k \ll 1$, will still contribute to the $\varepsilon'(\omega)$ isotherm, because $1/(1 + \omega^2\tau_k^2)$ is unity when $\omega\tau_k \ll 1$.

The methodology makes the following assumptions about how the $\{\log \tau_k\}$ behaves with temperature:

1. The temperature dependence for each τ_k is monotonic and increases with a decrease in T . There is no additional specification of the temperature dependence of an individual τ_k – only what is needed to describe the experimental data. Each τ_k can have its own temperature dependence.
2. Processes do not overtake (i.e. cross) each other.
3. New processes can emerge (i.e., they can be born) in the high frequency region of the response, but not at frequencies greater than the boson peak, which has a relaxation time of approximately 10^{-12} s. New processes, including the ones that have not yet entered the experimental window, immediately begin contributing to the static dielectric permittivity ε_S .

It follows from the above assumptions that once a process is born it will move along the time axis with a decrease in temperature. As the temperature is lowered, a process enters the experimental window at the short-time edge of the window and exits at the long-time edge. When a process exits the experimental window, its relaxation time becomes unknowable because it no longer affects the fit to the data. When a fit to data is obtained, the regions on the relaxation time axis (which is the inverse frequency axis) where the experimentally measured loss permittivity $\varepsilon''(\omega)$ is large will have a high density of $\log \tau_k$'s; and conversely, the regions with low $\varepsilon''(\omega)$ will be sparsely populated. Because it is not uncommon to observe $\varepsilon''(\omega)$ change by three orders-of-magnitude, it is clear that thousands of processes are required to describe the large change in the $\varepsilon''(\omega)$ intensity. Straightforward optimization over thousands of unknowns (i.e., $\log \tau_k$'s) is of course not possible. As described in details in Ni et al,³⁸ a smooth function for the density of processes, $\rho(\log \tau)$, is used so that the optimization is carried out over a limited number of parameters in the function rather than the $\log \tau_k$'s themselves. The density $\rho(\log \tau)$ is but a tool for optimization and its exact

functional form is irrelevant; in fact, experimentation with various trial functions shows that the resulting set of $\log \tau_k$'s is the same provided the data being fit are of sufficiently high quality. Different isotherms do not have to be fit using the same $\rho(\log \tau)$ function.

The value of the constant spectral intensity \bar{H} determines the total number of processes required to fit the data. \bar{H} has no lower bound, because replacing each process with a pair of infinitesimally closely spaced processes (each of half strength) preserves the fit, and by repeating this operation \bar{H} can be made arbitrarily small. The upper bound, on the other hand, is dictated by the data. This is illustrated in Figure 7.1 using the 120 K loss permittivity isotherm for sorbitol shown in Figure 7.1B (symbols). When the constant spectral strength is equal to $\bar{H} = 10^{-2}$, then the set of $\log \tau_k$'s shown in Figure 7.1A as blue symbols results in the excellent fit shown in Figure 7.1B as blue solid line. Now if the value of \bar{H} is doubled (i.e., now $\bar{H} = 2 \cdot 10^{-2}$) then the corresponding set of $\log \tau_k$ s shown in Figure 7.1A as magenta symbols results in a good fit to the data almost everywhere except in the $4 < \log f < 6$ range, where small oscillations appears in the magenta curve in Figure 7.1B. This is because the individual Debye processes in the corresponding time range (i.e., $-6 < \log \tau_k < -4$) are now sufficiently far apart to be resolvable. Because no oscillations are seen in the experimental data, the value of $\bar{H} = 2 \cdot 10^{-2}$ exceeds the allowable upper bound for \bar{H} .

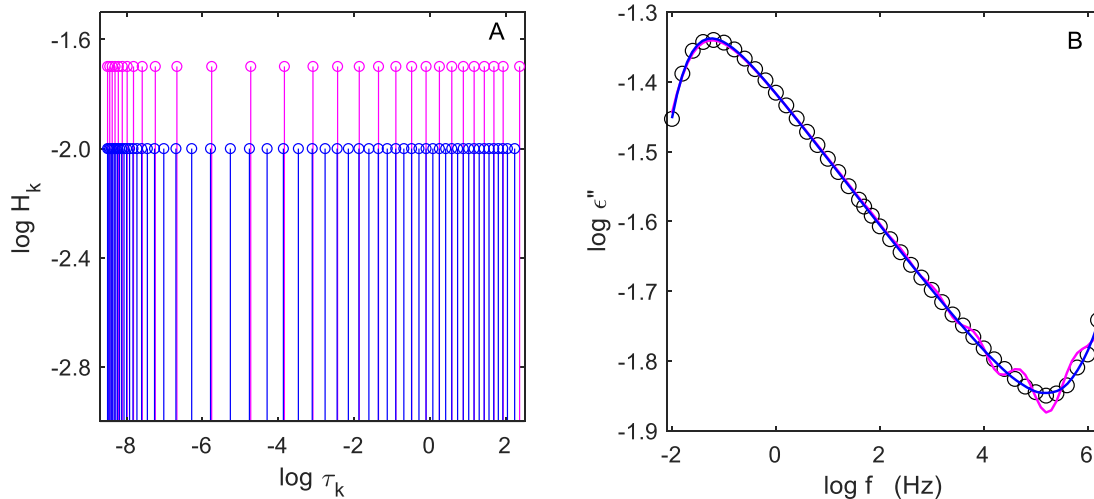


Figure 7.1. Effect of the process strength magnitude \bar{H} . (A) Relaxation spectrum used to fit the loss dielectric permittivity shown in the right panel; $\bar{H} = 10^{-2}$ – blue, $\bar{H} = 2 \cdot 10^{-2}$ – magenta. (B) Sorbitol data for 120 K – markers, solid lines – fits produced by the spectra shown in the left panel.

It should be noted that both $\epsilon'(\omega)$ and $\epsilon''(\omega)$ isotherms are required for the VASESS analysis procedure. Consider a situation where only the $\epsilon''(\omega)$ isotherms are reported, which is unfortunately often the case with the literature data. At a given temperature a fit to the $\epsilon''(\omega)$ isotherm can be obtained using, say, 100 processes within the experimental window, but are these processes from 500 to 600 or from 1000 to 1100 (counting from the shortest time process)? In other words, how many processes are there having relaxation times too short to affect the loss signal within the experimental window? However, these “unseen” processes will still affect the $\epsilon'(\omega)$ isotherm, which enable determination of which processes are in the experimental window. Thus, obtaining the relaxation map requires knowing both the $\epsilon'(\omega)$ and $\epsilon''(\omega)$ response for each isotherm.

7.5 Results

The dielectric loss and storage permittivities for the small molecule glass formers glycerol and sorbitol are analyzed. For glycerol there is an extensive data set from Schneider et al³³ obtained using a combination of several dielectric spectroscopy techniques. This set covers the temperature range from 184 K to 413 K, where the DSC-determined T_g for glycerol is 190 K. To supplement the Schneider et al super-cooled liquid data, dielectric relaxation experiments on glycerol were carried out in the glassy region from 120 K to 250 K. In the region above T_g our data agree with the glycerol data of Schneider et al. With respect to sorbitol, Wagner and Richert⁴² performed dielectric relaxation experiments in the range from 136 K to 302 K, where the DSC-determined T_g for sorbitol is 268 K. Unfortunately, only the loss isotherms were reported in the Wagner and Richert paper, which precludes use of VASESS method as indicated in the previous section. Kastner et al⁴³ measured the dielectric response of sorbitol from 120 K to 400 K, but they also only reported the loss isotherms again precluding use of the VASESS analysis. Geirhos et al⁴¹ reported broadband dielectric $\epsilon'(\omega)$ and $\epsilon''(\omega)$ isotherms for sorbitol from 10 K to 260 K, where we have augmented their sorbitol data with broadband dielectric experiments from 150 K to 320 K. In the temperature region where our data overlap with the data of Geirhos et al the agreement between the two data sets is excellent. In what follows we analyze the Schneider et al, Geirhos et al and our dielectric relaxation data sets using the VASESS method described above.

7.5.1 Glycerol

Above T_g dielectric relaxation data of Schneider, Lunkenheimer, Brand and Loidl

Using various broadband dielectric spectroscopy techniques, Schneider et al³³ obtained an extremely wide set of dielectric permittivity data for glycerol, which is recognized as the gold standard in the field. This set is reproduced in Figure 7.2, where the fits using the VASESS method are also shown.

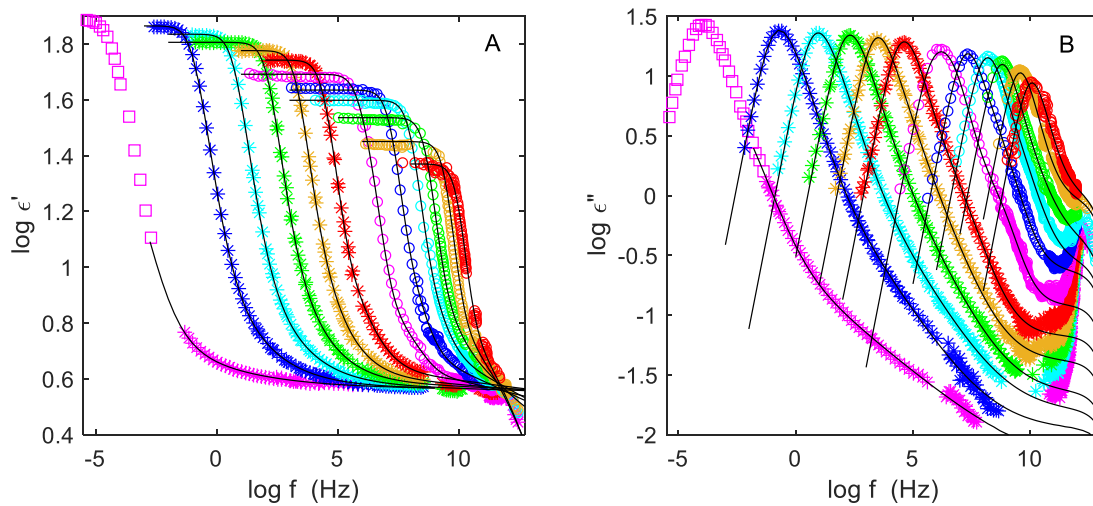


Figure 7.2. Storage (A) and loss (B) dielectric permittivity data of Schneider et al. Symbols corresponds to temperatures (left-to-right): 184 K – magenta squares and stars, 195 K – blue stars, 204 K – cyan stars, 213 K – green stars, 223 K – orange stars, 234 K – red stars, 253 K – magenta circles, 273 K – blue circles, 295 K – cyan circles, 323 K – green circles, 363 K – orange circles, 413 K – red circles. Solid lines – fit using the VASESS method of this paper.

Several comments are in order regarding the data in Figure 7.2:

1. 184 K isotherms. According to the authors,³³ the data were intended to be for material at equilibrium (strictly speaking in a super-cooled liquid state). To achieve this goal, the material at 184 K (i.e., $T_g - 6$ K) was equilibrated for a “long” time that was not specified in the original paper. Also, the lower frequency data (indicated as squares in Figure 7.2) were obtained via a constant field relaxation experiment (rather than dynamic experiment like the rest of the data) that were subsequently converted to the frequency domain. Upon examining the low frequency portion of the 184 K data we found that the data are

inconsistent; specifically, the storage and loss data indicated as squares in Figure 7.2 cannot be represented as a sum of Debye processes. It should be emphasized that we do not mean that the VASESS method employed in this paper fails; rather that no series of Debye processes exists that can simultaneously describe both the $\epsilon'(\omega)$ and $\epsilon''(\omega)$ data. A potential culprit is physical aging, where the material was still changing during the course of the relaxation experiment. Alternatively, there may have been a problem when converting the data from the time domain to the frequency domain. Consequently, we did not attempt to fit the low frequency portion of the 184 K data.

2. Boson peak. A prominent feature of the data is the so-called boson peak appearing at a frequency slightly above 10^{12} Hz. The nature of the boson peak is still a hotly debated topic.⁴⁴⁻⁴⁸ One of the salient features of the boson peak is its sharpness. Specifically, the tails of the peak decrease with the logarithm of frequency more rapidly than would be consistent for even a single Debye process. This shows that the boson peak is not due to a relaxation process in a traditional sense. Consequently, we did not attempt to fit the boson peak; specifically, data at frequencies greater than 10^{11} Hz were not included in the analysis.
3. The gap in the experimental data at the lowest temperatures. It appears that there is a gap between the relaxation portion of the data and the boson peak for three lowest temperatures (i.e., 184, 195, and 204 K), where the loss curves vanish only to re-emerge at the boson peak. This vanishing is not real, being caused by experimental limitations for these low intensity signals. This is confirmed by comparison of the dielectric³³ and light-scattering data⁴⁹ for glycerol, where the light-scattering data exhibit continuous transition between the relaxation and the boson peak portions of the data. Consequently, when fitting the data, the VASESS predicted dielectric response does not decay to zero in the “gap” region as shown in Figure 7.2.

Two assumptions were made in order to fit the dielectric data. First, the boson peak is not due to a relaxation process, because its width is narrower than consistent with a single Debye process, hence, it will not be included in the fitting procedure. Second, the relaxation portion does not decay to zero with increase in frequency; instead, based on the light scattering data, it becomes level, where the level value decreases with temperature. In accordance with the second assumption,

a hyperbolic tangent was used in the empirical density function, ρ , given in the SI to describe the high frequency/short time behavior. This is apparent in the spectra shown in Figure 7.3, where at short times all curves become flat. Even the magenta curve at 184 K eventually becomes flat, but outside the range shown in Figure 7.3.

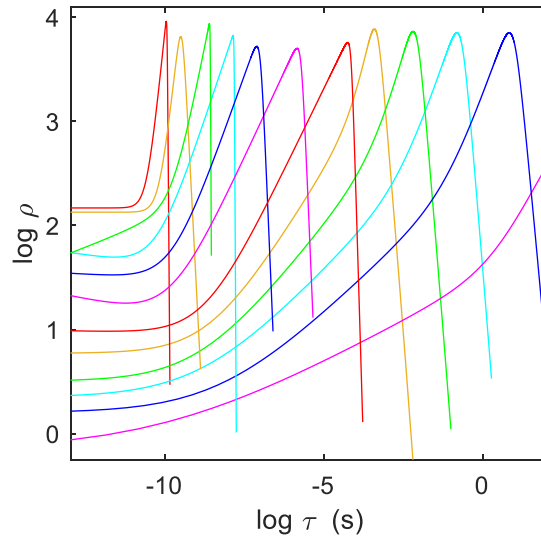


Figure 7.3. Spectral density of processes vs relaxation times of the processes obtained from fitting the dielectric permittivity data of Schneider et al³³ from Figure 7.2. Temperatures are the same as in Figure 7.2, i.e. from 184 K to 413 K going right-to-left. Colors correspond to colors in Figure 7.2.

A judgement call was made concerning the frequency where the relaxation portion becomes polluted by the boson peak, and only the data up to that chosen frequency were fit, where 10^{11} Hz was chosen as the frequency cut-off. A good fit to the highest temperature isotherm in Figure 7.2B (red circles) appears to extend beyond this frequency; however, we believe this to be a coincidence. The behavior above the maximum fitting frequency of 10^{11} Hz is a prediction based on the aforementioned flat spectrum shown in Figure 7.3. Obviously, we have no way of knowing how high in frequency (or short in time) the flat portion of the spectrum reaches. So, another arbitrary assumption is made to end all spectra at 10^{-13} s. Thus, the final decrease in the predicted $\varepsilon''(\omega)$ curves at the highest frequencies seen in Figure 7.2B is a result of this truncation of the spectra.

Using the VASESS analysis described in the Method of Analysis Section with the assumptions described above, the fits to the data in Figure 7.2 were obtained, where deviations occur in the region where the boson peak begins to appear. The corresponding spectra are shown in Figure 7.3. By ‘spectrum’ we here mean the density of processes, ρ , (i.e., number of processes per logarithmic decade of time) plotted versus the logarithm of the relaxation time. A $\log(\rho)$ vs $\log(\tau)$ curve resembles, but is not identical to, the corresponding loss curve flipped horizontally as $\log(\text{frequency})$ is converted to $-\log(\text{time})$. As explained in the Method of Analysis a phenomenological function $\rho(\log \tau)$ is used at each temperature, where optimization is carried out over its parameters to achieve fit to the data. The list of functions with the optimized parameter values for all temperatures is provided in the SI.

The area under the spectrum, which is the total number of processes, monotonically increases with decreasing temperature. Specifically, the number of processes increases from 2160 at 413 K (leftmost red curve) to 7144 at 195 K (rightmost blue curve). The number of processes at 184 K is unknown, as the full spectrum at this temperature cannot be obtained for the reasons explained above. The new processes emerge at the short-time/high-frequency end of the spectrum as the temperature is decreased, which provides a natural explanation for increase in the static dielectric susceptibility χ_S . It should be noted that the spectrum at the highest temperature of 413 K (leftmost red curve) must be considered as approximate, since the separation between the relaxation portion and the boson peak portion of the corresponding isotherms in Figure 7.2 is not robust. Also, the shape of the spectrum for the three lowest temperature isotherms – 184, 195, and 204 K, at the shortest times (i.e., lower left corner of Figure 7.3) is not robustly determined due to the lack of data in the gap region between the relaxation portion and the boson peak portion of the isotherms.

The following information can be ascertained from examining Figure 7.3:

1. Glycerol is known for the absence of the β -relaxation peak. Indeed, the loss isotherms in Figure 7.2 exhibit no discernable high frequency peak.
2. The long-time side of the α -process is steep in agreement with what has been observed for small molecule glass formers and oligomers and in contrast to what has been observed for polymers.⁵⁰⁻⁵² It should be noted, however, that the steepness of the long-time slope of the α -process is not established robustly, because it hinges entirely on the first few low frequency data points for each loss isotherm in Figure 7.2B. For example, the spectrum for

413 K appears much sharper than the spectrum for 195 K. However, we have been able to achieve a seemingly good fit (at least to a human eye, if not the optimizer) to the 195 K isotherm using a spectrum that on the long-time side looks much like the 413 K spectrum, i.e. steeper than the one shown in Figure 7.3. Thus, if the first few low frequency data points are even slightly affected by conduction (which is always the danger at low frequencies), the long-time slope of the optimized spectrum can be significantly impacted. Nevertheless, we did not choose to show the steeper versions of the spectra in Figure 7.3. This is because according to Jensen et al⁵³ the mechanical loss isotherms for glycerol are much broader than the dielectric loss isotherms. So, the conclusion implied by the very steep spectrum that ‘there is nothing beyond the largest relaxation time’ may not hold.

3. Although the shapes of the curves are quite similar, they cannot be superposed, indicating the well-known fact that glass forming materials are not thermo-rheologically simple if a sufficiently wide frequency window is employed.

The culmination of the VASESS analysis is the relaxation map shown in Figure 7.4, where each line refers to the temperature dependence of a distinct relaxation process. Only a few representative processes out of 7144 are shown for clarity (see Figure 7.4 caption for details). The high-density region of processes corresponds to the maximum in the $\epsilon''(\omega)$. It should be noted that the long-time processes at 184 K (the rightmost temperature point in Figure 7.4) are unavailable; hence, most processes end at 195 K creating a gap in the upper right corner of Figure 7.4. Also, the short-time processes cannot be robustly resolved for lowest temperatures due to the aforementioned gap in the data in Figure 7.2; as a result, the relaxation map does not extend to the lower right corner of Figure 7.4. An important feature of the relaxation map in Figure 7.4 is that (i) new processes emerge at high frequencies in the vicinity of the boson peak and (ii) then rapidly coalesce with the existing processes as temperature decreases. From this perspective, the excess wing consists of the processes at various stages of joining in with the processes forming the main collection of processes that forms the α -peak. Once in the main band of processes, the processes all roughly follow the familiar $\log a_T$ curve. Exactly how rapidly do the new processes join the main band after they have emerged from somewhere in the vicinity of the boson peak? The slopes appearing in Figure 7.4 only provide a crude estimate, because they are based on only two points – the temperature spacing is at best every 10 K and at the highest temperatures is 50 K. In order to

resolve the true shape of the temperature dependence of the relaxation processes as they emerge from the vicinity of the boson peak, the dielectric response at intermediate temperatures are needed.

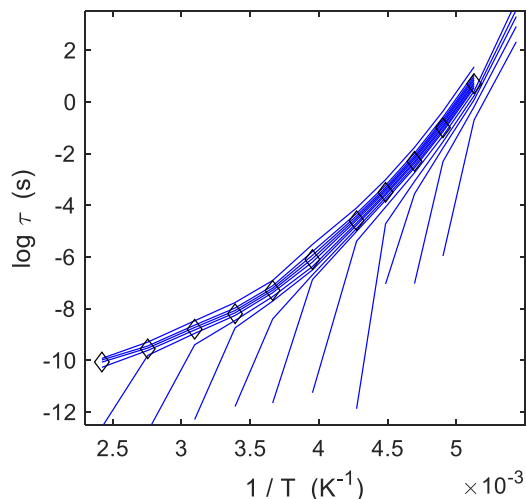


Figure 7.4. Relaxation map for glycerol obtained from fitting the Schneider et al. data in Figure 7.2. Relaxation times for processes from the longest (i.e. at the long-time edge of the spectra in Figure 7.3) to shortest (i.e. at the short-time edge of the spectra in Figure 7.3) are shown, where for clarity only every 500th process (out of the maximum number of 7144 processes) is plotted. Black diamond markers indicate locations of the loss peaks in Figure 7.2 after their conversion from the frequency domain to the time domain.

Additional dielectric relaxation data both below and above T_g

In order to expand the data set of Schneider et al, additional broadband dielectric relaxation experiments were performed on glycerol from 120 K to 250 K with a temperature increment of 10 K. The storage and loss isotherms are shown in Figure 7.5. Our data for temperatures above 200 K agree well with the results of Schneider et al. Unlike in case of Schneider et al, the data at 190 K and 200 K (and certainly for lower temperatures) are not for equilibrated material. This is because according to the protocol described in the Experimental section, the material was quenched from well above T_g to the lowest temperature (i.e., 120 K) and then the temperature was increased in increments of 10 K. The frequency range in Figure 7.5 is from 10^{-1} Hz to slightly above 10^6 Hz, where conduction effects interfere at the lower end of the frequency window and the $\epsilon''(\omega)$ data become noisy at the higher frequency end of the experimental window.

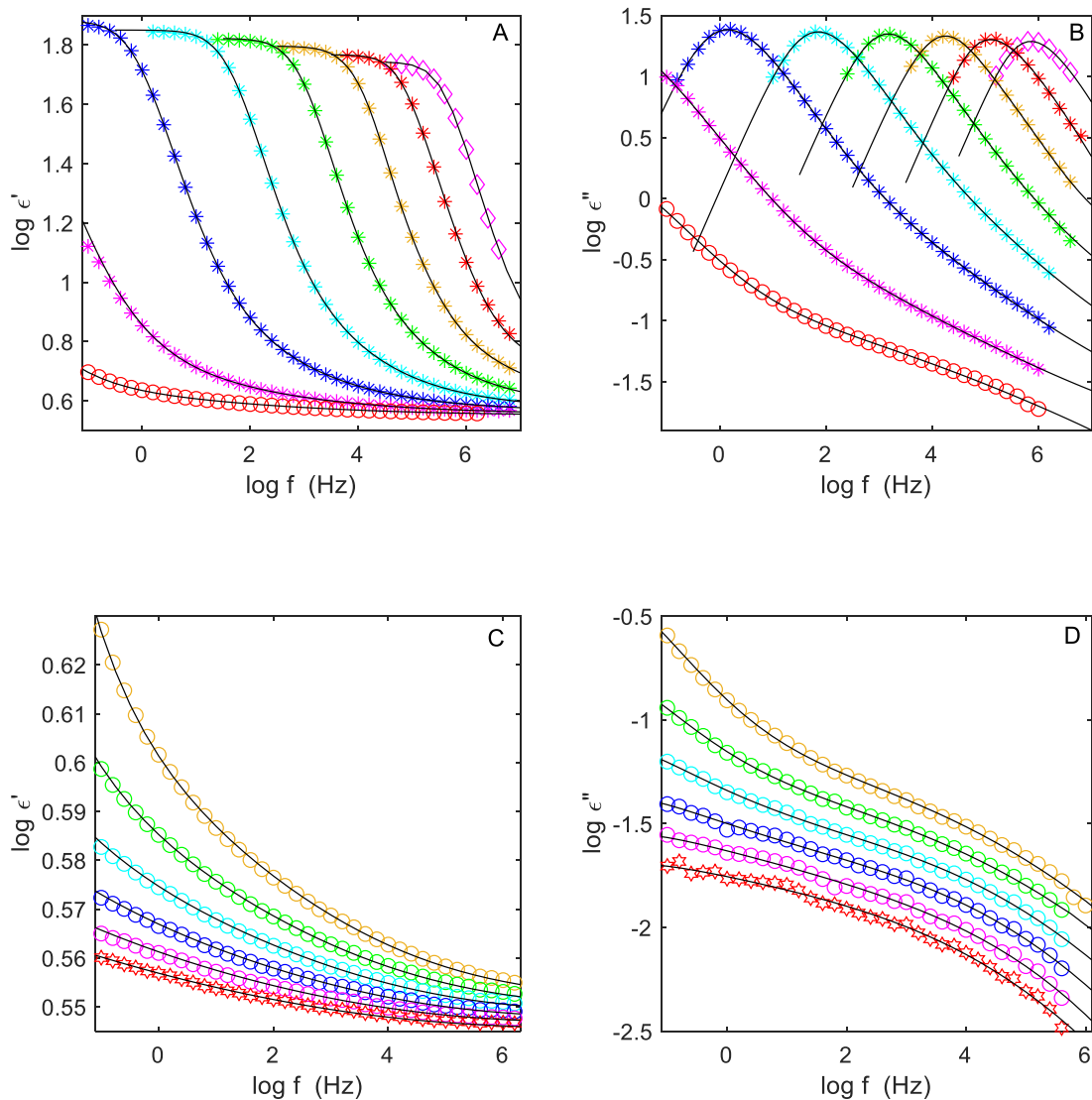


Figure 7.5. Storage (A, C) and loss (B, D) dielectric permittivity for glycerol. Symbols corresponds to temperatures: (A) and (B) (left-to-right) 180 K – red circles, 190 K – magenta stars, 200 K – blue stars, 210 K – cyan stars, 220 K – green stars, 230 K – yellow stars, 240 K – red stars, 250 K – magenta diamonds; (C) and (D) (left-to-right) 120 K – red hexagram, 130 K – magenta circles, 140 K – blue circles, 150 K – cyan circles, 160 K – green circles, 170 K – yellow circles. Solid lines – fits using the spectra shown in Figure 7.6.

The spectra required to produce the fit to data shown in Figure 7.5 are given in Figure 7.6. The list of phenomenological functions $\rho(\log \tau)$ used along with the optimized parameter values for all temperatures is provided in the SI. Just like in the case of the Schneider et al data,³³ the loss isotherms in Figure 7.5 contain no discernable shoulder at high frequencies.

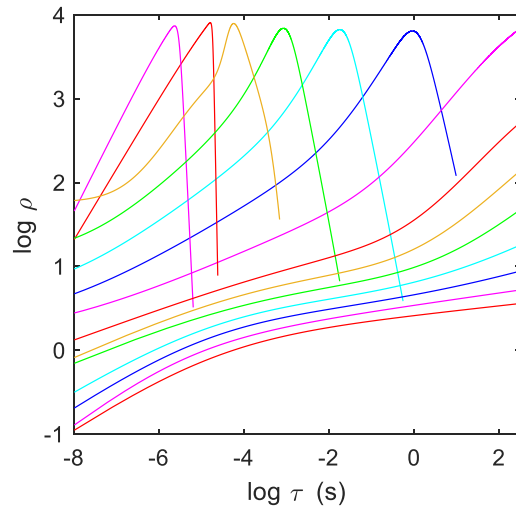


Figure 7.6. Spectra (density of processes vs relaxation times of these processes) obtained from fitting the dielectric permittivity data in Figure 7.5. Temperatures are the same as in Figure 7.5 from 120 K (rightmost curve) to 250 K (leftmost curve) going right-to-left. Colors correspond to those in Figure 7.5.

The relaxation map for the new glycerol relaxation data is shown in Figure 7.7, where only a few representative processes out of 7259 are shown for clarity; specifically: every 500th process is shown for the red curves, every 50th process is shown for the orange curves, and every 5th process for the green curves (see Figure 7.7 caption for details). Specific features of the relaxation map shown in Figure 7.7 are:

1. Although new processes may appear to continue to emerge in the sub-T_g region, the number of emerging processes has decreased significantly. Specifically, there are over 7200 processes in the relaxation map shown in Figure 7.7, where there are only 5 that emerge below T_g; moreover, the last process shown in Figure 7.7 (i.e. the right most green line) may in fact start above T_g if the relaxation time could be extended to 10⁻¹² s into the region of the boson peak like was possible for the relaxation map constructed from the Schneider et al data shown in Figure 7.4. Thus, the data do not permit a definitive statement regarding whether any additional relaxation processes emerge below T_g for glycerol.
2. There is a qualitative difference in the temperature dependence of the relaxation processes above T_g as compared to the temperature dependence below T_g. Above T_g new processes emerge from the region of the boson peak and then rapidly coalesce into the bundle of the α -processes, in which they then all exhibit the same temperature dependence, i.e. the red

curves in Figure 7.7. In contrast, below T_g the processes are concave downward on the $1/T$ plot (i.e. the orange and green curves in Figure 7.7), they remain separated as their slopes becomes less steep, and even possibly spread further apart as the temperature is lowered

3. Above T_g the increase in the number of processes with decreasing temperature causes the increase in the static susceptibility $\chi_0 = \varepsilon'(\omega \rightarrow 0) - \varepsilon_\infty$, where the steady increase in $\varepsilon'(\omega \rightarrow 0)$, i.e., the asymptotic leveling-off value at low frequencies, is seen in Figure 7.5 when temperature is decreased from 250 K to 200 K. Similar behavior is observed over a much wider temperature interval in the Schneider et al. data shown in Figure 7.2. However, at temperatures below 200 K in Figure 7.5A and especially in Figure 7.5C the value of $\varepsilon'(\omega \rightarrow 0)$ is unknown, because its asymptotic behavior has not been reached.
4. The relaxation processes that dominate the region below T_g (i.e. the orange and green curves) start above T_g . The last green curve appears to start below T_g ; however, the shortest relaxation time that could be determined is 10^{-8} s which is three to four orders-of-magnitude longer than the boson peak. It is quite possible that all the relaxation times emerge from the region of the boson peak above T_g . Whether this feature occurs for glass formers other than glycerol remains to be seen.
5. Although the orange and green curves in the Figure 7.7 relaxation map do not go to low-enough times to directly determine if they emerge from the region around the boson peak, they exhibit an increasingly steeper slope with increasing temperature consistent with the Schneider et al. data shown in Figure 7.4. Also, there appears to be a smooth transition towards the temperature dependence of the red lines that are coalescing into the main α -process. The data of Schneider et al.³³ for the α -process clearly does emerge from the region of the boson peak, where it is natural to assume that the orange and green processes in Figure 7.7 also emerge from this region.
6. A key observation is that processes in the sub- T_g region do not exhibit a true Arrhenian temperature dependence, but rather are concave downward, appearing to emerge from the region of the boson peak just like seen earlier in Figure 7.4 at temperatures above T_g .

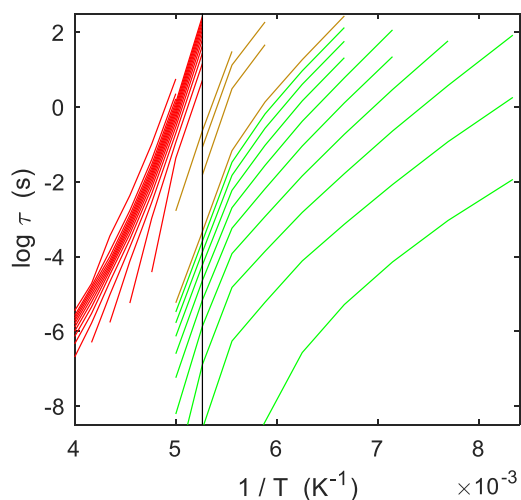


Figure 7.7. Relaxation map for glycerol obtained from fitting the data in Figure 7.5. Relaxation times for processes from the longest (i.e. at the long-time edge of the spectra in Figure 7.6) to shortest (i.e. at the short-time edge of the spectra in Figure 7.6) are shown; processes No 5 to No 45 with an increment of 5 – green, processes No 50 to No 200 with an increment of 50 – orange, No 700 to No 7200 with an increment of 500 – red. Vertical black line indicates T_g .

The relaxation maps for glycerol based on the Schneider et al³³ data shown in Figure 7.4 and the relaxation data from this paper data shown in Figure 7.7 are plotted together in Figure 7.8. The agreement in the above T_g region (i.e. the blue and red curves) is excellent. As mentioned above, the short-time behavior of each process is based on only two temperature points; so, the fact that some curves apparently cross is not real. Some of the green curves in Figure 7.8 were extended to times less than 10^{-8} s, which is an extrapolation because, unlike the Schneider et al data, these data are only for the frequency window reaching up to $10^{6.5}$ Hz. However, we believe that this extrapolation is justified. Specifically, the $\log \tau$ values for the processes in question were determined via extrapolation of the process density function $\rho(\log \tau)$. The process density function for the temperatures from 120 K to 190 K is modeled as a product of two hyperbolic tangent functions (see details in the SI). Thus, the spectra in Figure 7.6, when extrapolated to shorter times, will look like the spectra in Figure 7.3, that is, they will reach an asymptotic value and stop decreasing – extrapolation of a constant is most probably benign even though it may be up to four logarithmic decades.

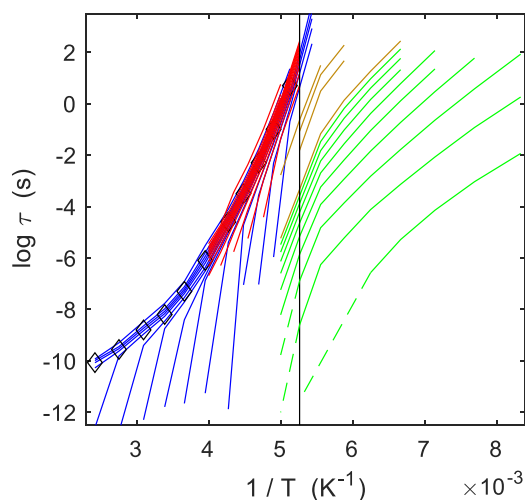


Figure 7.8. Combined relaxation map for glycerol, including results of Figure 7.4 (based on Schneider et al. data) and Figure 7.7 (based on this paper data). Extrapolation of data to shorter relaxation times is shown as dashed lines (see text for details).

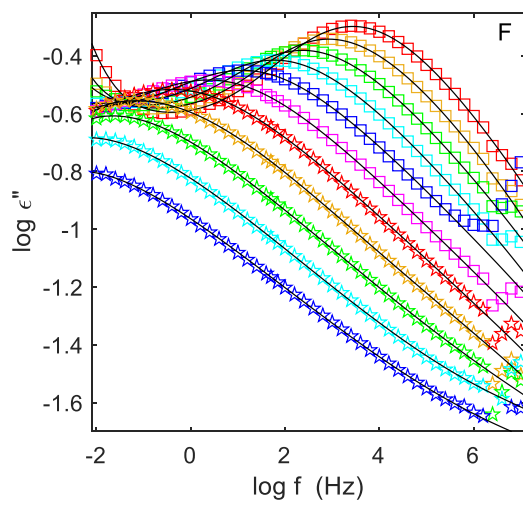
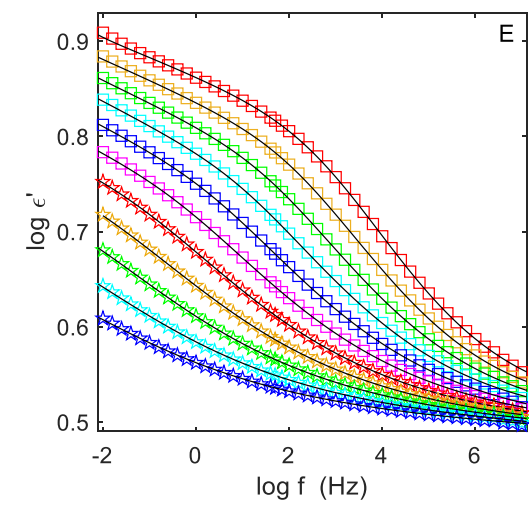
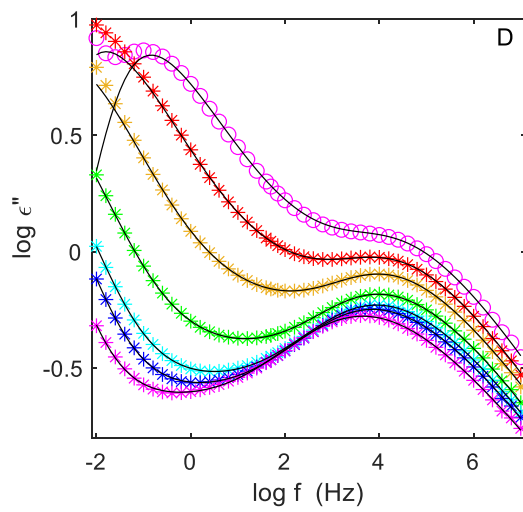
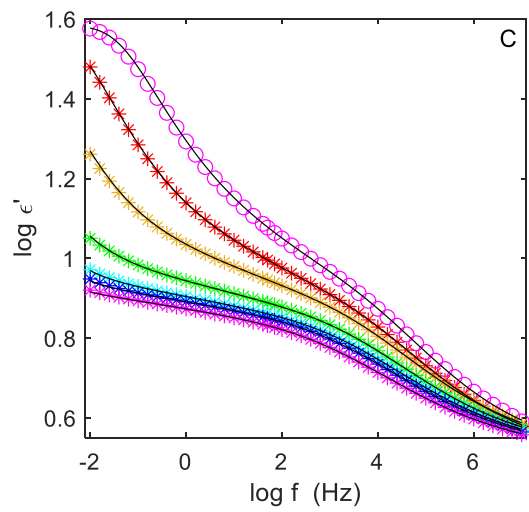
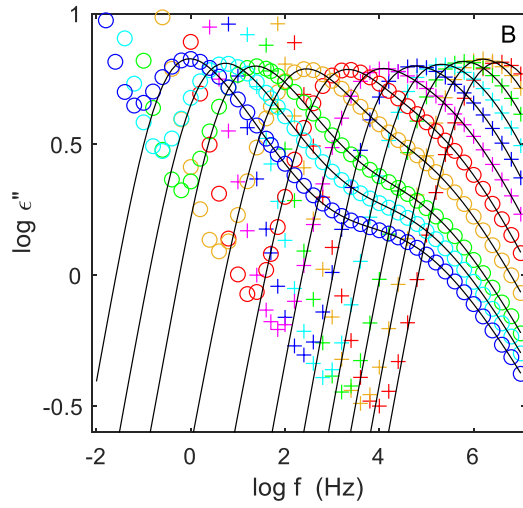
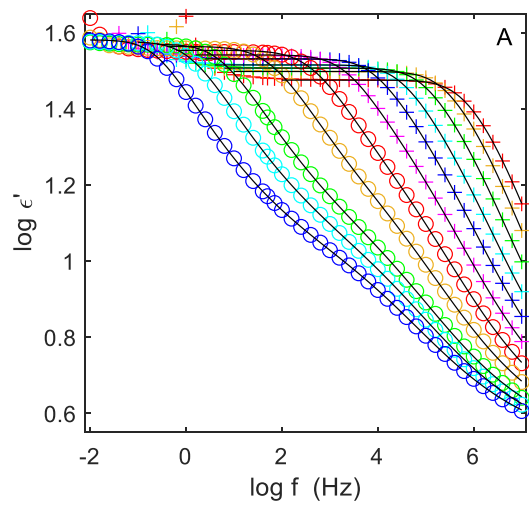
Sub-Tg processes are often described in terms of the Johari-Goldstein postulate, where the sub-Tg process is assigned an Arrhenian activation energy that is extrapolated to high temperatures where it appears to coalesce with the main α -process.^{18,26,54-57} The temperature dependence of the sub-Tg process is typically determined from how the sub-Tg relaxation peak changes with temperature, which would be consistent with the band of green curves located next to the orange curves in Figure 7.8. It is possible to fit the low temperature data of this band of curves with an Arrhenian temperature dependence; however, when analyzing the full relaxation response, the curves most certainly do not remain Arrhenian. The data in Figure 7.8 calls into question the Johari-Goldstein analysis that assumes the Arrhenian dependence of the sub-Tg process can be extrapolated well above Tg.

7.5.2 Sorbitol

In order to assess if the key features of the relaxation map shown in Figure 7.8 for glycerol occur in another glass forming small molecule, broadband dielectric relaxation experiments on sorbitol were performed from 120 K to 320 K; however, experiments at 120 K, 130 K and 140 K appear to have unexplained artifacts and thus they are not reported. Temperature increments of 10 K were employed except in the vicinity of Tg = 268 K where smaller temperature increments

of 2.5 K and 5 K were used. At temperatures above 320 K crystallization begins to occur, as was also reported by Nozaki et al.²⁶ The storage and loss isotherms are shown in Figure 7.9. The loss dielectric permittivity $\epsilon''(\omega)$ agree well with the data published by Wagner and Richert.⁴² The dielectric permittivity data of Wagner and Richert as well as of this paper differ substantially from the data reported by Nozaki et al. It should be noted that the data of Nozaki et al is an amalgamation of the dielectric relaxation data obtained using five different apparatuses, where the mismatch between different subsets of data is clearly visible. (For instance, there is an apparent *decrease* in the “static” permittivity with decrease in frequency, which is unphysical.) The high temperature dielectric relaxation data for sorbitol are affected by conduction and electrode polarization effects more severely than the glycerol data. For glycerol it was possible to unambiguously truncate the raw glycerol data at a frequency where these parasitic effects had not yet polluted the true relaxation response, where this frequency is different for each temperature. The situation is less clear in case of sorbitol, especially so in the region near T_g ; thus, we chose to present the raw data in Figure 7.9. This has important implications from the modeling perspective; specifically, because the portions of the isotherms attributed to conduction and electrode polarization cannot be quantitatively accounted for, we must make an admittedly subjective judgement call as to where the fitted portion ends. In Figure 7.9B and Figure 7.9D deviations occur between the predictions from the spectral density given in Figure 7.10 and the experimental data are where the parasitic conduction and electrode polarization contribution begin. The upturn in the high frequency region seen in Figure 7.9F is most probably experimental artifact.

Figure 7.9. Storage and loss dielectric permittivity for sorbitol. Symbols corresponds to temperatures: (A) and (B) (left-to-right) 275 K – blue circles, 277.5 K – cyan circles, 280 K – green circles, 285 K – orange circles, 290 K – red circles, 295 K – magenta plusses, 300 K – blue plusses, 305 K – cyan plusses, 310 K – green plusses, 315 K – orange plusses, 320 K – red plusses; (C) and (D) (left-to-right) 255 K – magenta stars, 260 K – blue stars, 262.5 K – cyan stars, 265 K – green stars, 267.5 K – orange stars, 270 K – red stars, 272.5 K – magenta circles; (E) and (F) (left-to-right) 150 K – blue pentagrams, 160 K – cyan pentagrams, 170 K – green pentagrams, 180 K – orange pentagrams, 190 K – red pentagrams, 200 K – magenta squares, 210 K – blue squares, 220 K – cyan squares, 230 K – green squares, 240 K – orange squares, 250 K – red squares. Solid lines – fits using the spectra shown in Figure 7.10.



Unlike in case of glycerol, where only the α -relaxation peak and the excess wing are readily identifiable in the $\epsilon''(\omega)$ data, the loss isotherms for sorbitol exhibit a definite β -relaxation process, first appearing as a shoulder at 290 K and then as a separate peak for temperatures from 255 K to 190 K. As the temperature is lowered further only the higher frequency portion of the β -relaxation process is seen in Figure 7.9F.

The spectra required to produce the fits to data shown in Figure 7.9 are given in Figure 7.10. The phenomenological functions $\rho(\log \tau)$ used along with the optimized parameter values are provided in the SI for all temperatures. At the same value of $\bar{H}=10^{-2}$ as for glycerol, the total number of processes needed to fit the sorbitol data is less – only 3517 vs 7259 for glycerol. This is because the value of the static dielectric permittivity for sorbitol is roughly half of that for glycerol (i.e., $10^{1.6}$ vs $10^{1.9}$). Examining Figure 7.10, the following features of the spectral density are observed:

1. The evolution of the α -process for sorbitol is qualitatively similar to that for glycerol shown in Figure 7.3 and Figure 7.6.
2. At the highest temperature (320 K = T_g+50 K) the sorbitol spectrum is broader than the spectrum at the highest temperature for glycerol (413 K = T_g+220 K). However, when spectra are compared at 50 K above their respective T_g 's, then both the glycerol and sorbitol are similar.
3. As the temperature is decreased sorbitol exhibits the beginning of the excess wing, but unlike glycerol, the wing does not exhibit an intensity decay of nearly three orders-of-magnitude due to the appearance of the strong β -relaxation process.
4. The β -relaxation process for sorbitol is much more prominent than in glycerol.
5. An interesting feature of sorbitol spectral density is that the excess wing of the α -process does not shift for a significant temperature interval below T_g from 265 K to 220 K as seen in Figure 7.10B and Figure 7.10C. This contrasts with glycerol, where the excess wing seems to shift with temperature at a steady pace.

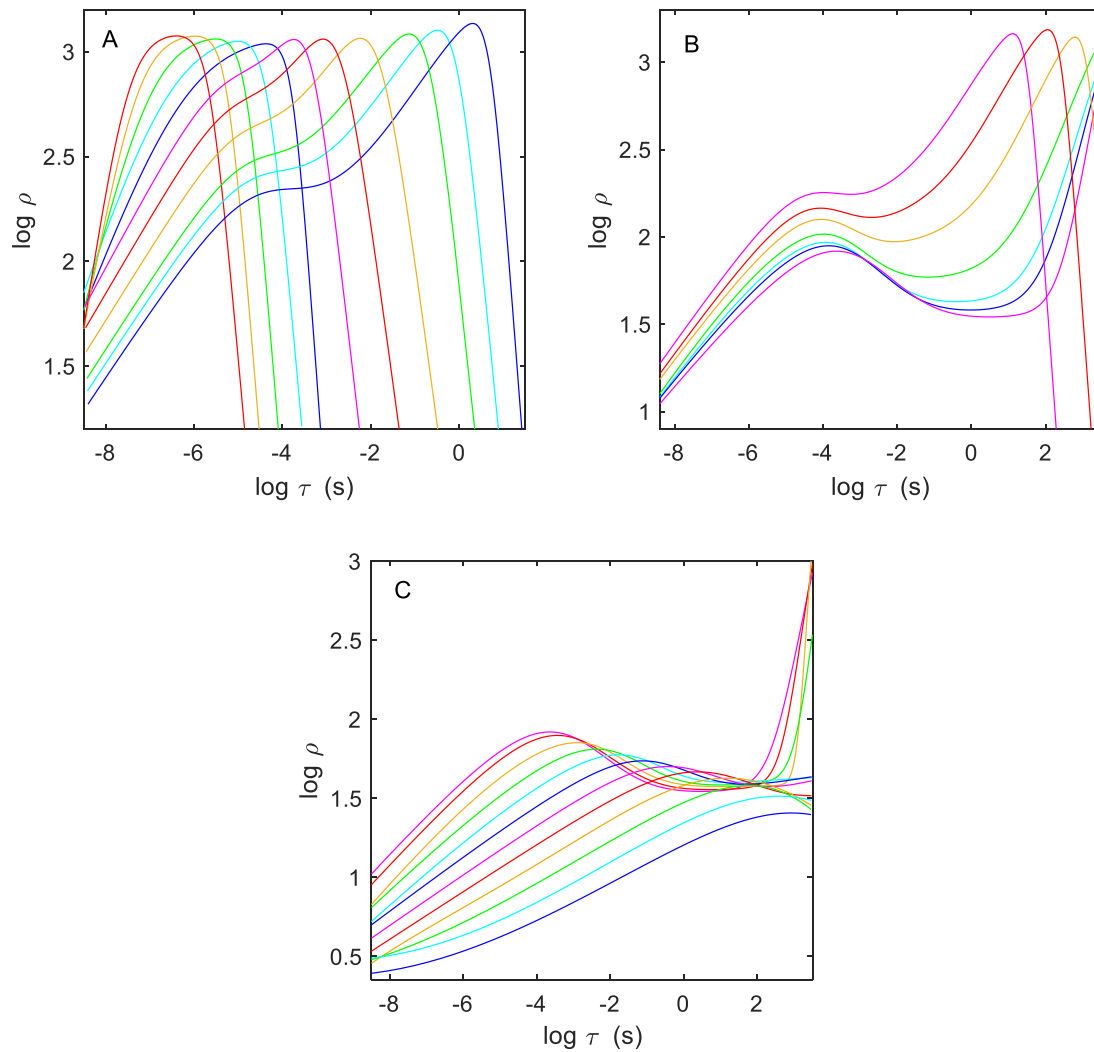


Figure 7.10. Spectra (density of processes vs relaxation times of these processes) obtained from fitting the dielectric permittivity data in: (A) – Figure 7.9A and Figure 7.9B, (B) – Figure 7.9C and Figure 7.9D, (C) – Figure 7.9E and Figure 7.9F. Temperatures are the same as in Figure 7.9 going right-to-left. Colors correspond to those in Figure 7.9.

The dielectric relaxation data of Geirhos et al⁴¹ for sorbitol are shown in Figure 7.11. The data are for the temperature range from 5 K to 260 K; however, the storage permittivity was not reported for all temperatures. The isotherms in Figure 7.11 are the ones for which both storage and loss isotherms were reported (see detailed list in the caption to Figure 7.11). Our data and the data of Geirhos et al generally agree in the range of overlap from 150 K to 260 K, however, there is a 0.05 difference in the value of the logarithm of the storage permittivity. The spectra required to produce the fits to the Geirhos et al data shown in Figure 7.11 are given in Figure 7.12. The phenomenological functions $\rho(\log \tau)$ used along with the optimized parameter values are provided in the SI. Using $\bar{H}=10^{-3}$, the total number of processes needed to fit the data is 14600. A value of $\bar{H}=10^{-3}$ had to be used to fit the data in Figure 7.11; otherwise, waviness would appear in the predicted loss curves at the lowest temperature, as explained in the Method of Analysis section above. At temperatures from 260 K to 150 K the spectra in Figure 7.12 are virtually identical to their counterparts in Figure 7.10, once the order-of-magnitude difference in the relaxation strengths (i.e., $\bar{H}=10^{-3}$ to fit Geirhos et al data vs $\bar{H}=10^{-2}$ to fit our own data) is accounted for by shifting the spectra in Figure 7.12 vertically by -1.

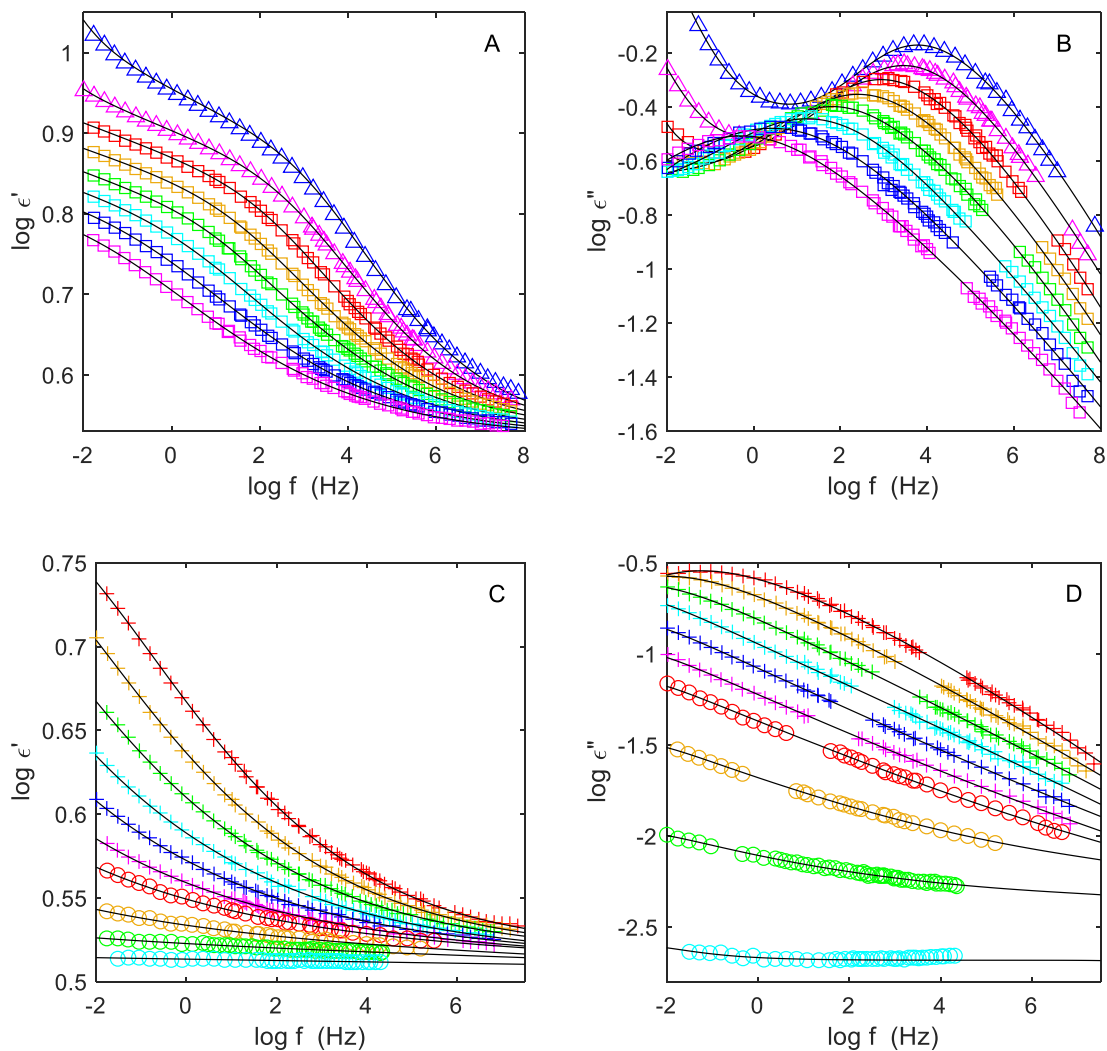


Figure 7.11. Storage (A, C) and loss (B, D) dielectric permittivity data for sorbitol of Geirhos et al.⁴¹ Symbols corresponds to temperatures: (A) and (B) (left-to-right) 190 K – magenta squares, 200 K – blue squares, 210 K – cyan squares, 220 K – green squares, 230 K – orange squares, 240 K – red squares, 250 K – magenta triangles, 260 K – blue triangles; (C) and (D) (left-to-right) 10 K – cyan circles, 70 K – green circles, 100 K – orange circles, 120 K – red circles, 130 K – magenta pluses, 140 K – blue pluses, 150 K – cyan pluses, 160 K – green pluses, 170 K – orange pluses, 180 K – red pluses. Solid lines – fits using the spectra shown in Figure 7.12.

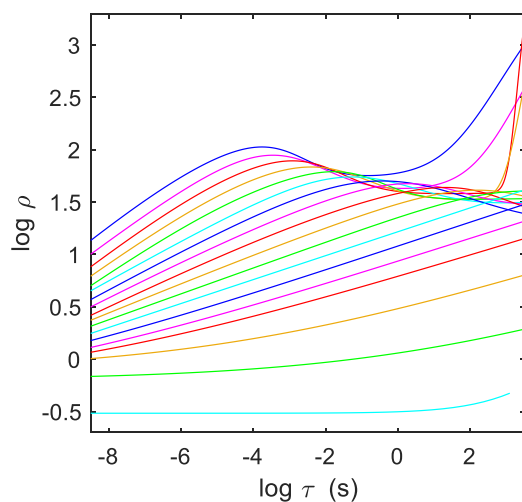


Figure 7.12. Spectral density of processes vs relaxation times of the processes obtained from fitting the dielectric permittivity data of Geirhos et al⁴¹ from Figure 7.11. All curves have been shifted vertically by -1 to facilitate comparison with Figure 7.10. Temperatures are the same as in Figure 7.11, i.e. from 10 K to 260 K going right-to-left. Colors correspond to colors in Figure 7.11.

The relaxation maps for sorbitol are given in Figure 7.13. Specifically, Figure 7.13A displays the combined relaxation map obtained for this paper data (i.e. data given in Figure 7.9) and the Geirhos et al⁴¹ data (i.e. data given in Figure 7.11). For the dielectric data reported in this paper, every 100th process out of a total number of 3517 is shown, i.e. the processes from 50 to 3450, are shown as blue curves. In case of Geirhos et al data every 500th process out of total number of 14600 is shown, i.e. the processes from 500 to 14500, are shown as red curves. There is excellent agreement in the shape of the curves. The envelope of the high temperature processes agrees well with the literature α -relaxation $\log a_T$ shift factor data compiled from various experimental techniques. Also shown in Figure 7.13 are $\log a_T$ shift factors for the β -relaxation as determined by (i) Faivre et al⁵⁸ from the maximum of the loss viscoelastic shear modulus, $G''(\omega)$ and (ii) Kastner et al⁴³ based on fitting the relaxation response to the linear combination of a Havriliak-Negami function for the α -process and a Cole-Cole function for the β -process, where the reported $\log a_T$ is based on the Cole-Cole function time parameter.

The relaxation map for sorbitol is qualitatively similar to that observed for glycerol as shown in Figure 7.7. Specifically, (i) new processes keep emerging from a short-time source with an initially steep slope that eventually becomes less steep; (ii) in the sub-T_g region the splaying of processes is apparent, where the 1st blue line from the bottom in Figure 7.13A (i.e. process No 50)

has a much gentler slope than the 4th blue line (i.e. process No 350); and (iii) the processes that emerge at the lower temperatures, i.e. curves 1 through 4, appear to asymptotically approach Arrhenian behavior as the temperature decreases. The relaxation map for the lowest temperature data of Geirhos et al is shown in Figure 7.13D. As mentioned above, there is a gap between the lowest temperature (i.e. 10 K) and the next (i.e. 70 K) because the storage isotherms between 10 K and 70 K were not reported, precluding use of the VASESS analysis. As a result, the corresponding “curves” in Figure 7.13D based on only two points are inevitably just straight lines.

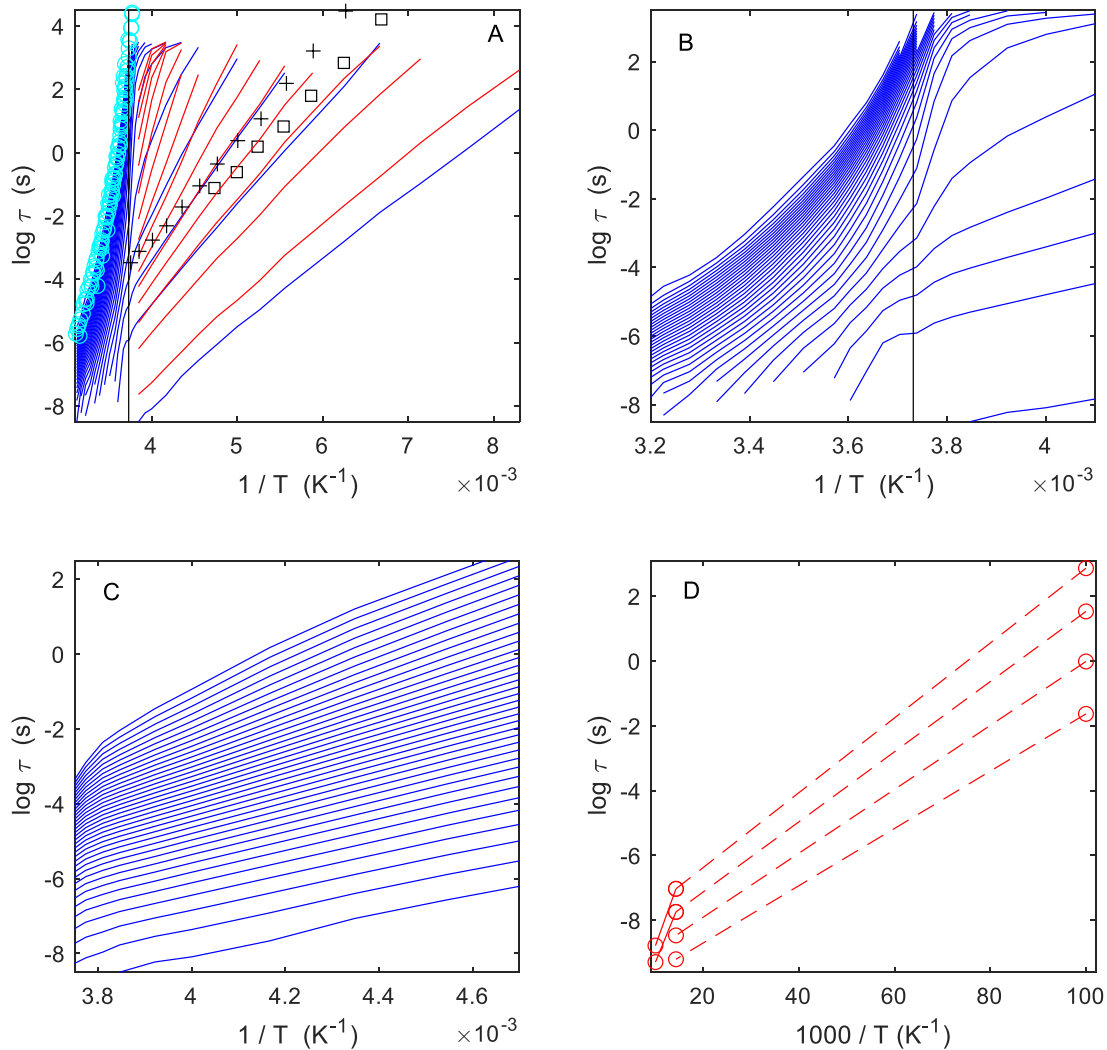


Figure 7.13. (A) Relaxation map for sorbitol obtained from fitting the data in Figure 7.9 and Figure 7.11. Relaxation times from the shortest to the longest (right-to-left): this paper data – blue lines, processes No 50 to No 3450 (total 3517) with an increment of 100; Geirhos et al data – red lines, processes No 500 to No 14500 (total 14600) with an increment of 500. Cyan circles – compilation of literature data for the α -relaxation $\log a_T$ shift factor using various experimental techniques, including viscosity, mechanical relaxation, dielectric relaxation, light scattering, and NMR.^{18,22,26,41,42,58-60} Black squares – mechanical relaxation data of Faivre et al⁵⁸; black pluses – dielectric relaxation data of Geirhos et al⁴¹ and Kastner et al⁴³ for the β -relaxation $\log a_T$ shift factor. Vertical black line indicates T_g . (B) Magnified portions of (A) above and near T_g region; (C) β -relaxation region, relaxation times (right-to-left) for processes No 50 to No 400 with an increment of 10 are shown. (D) Relaxation map obtained from Geirhos et al⁴¹ data at the lowest temperatures. The relaxation strength is set at $\bar{H}=10^{-2}$ for fitting this paper data and at $\bar{H}=10^{-3}$ for fitting Geirhos et al data.

In order to more critically examine the relaxation map for sorbitol, the response shown in Figure 7.13A is expanded in Figure 7.13B. Specific comments from this expanded view of the data are:

1. Examining Figure 7.13B, the upper edge of the group of processes that constitutes the α -relaxation peak looks jagged with some lines abruptly ending. These processes do not disappear; instead, the location of the relaxation times for these processes at the next lower temperature cannot be determined because it is outside the experimental window. Thus, the abrupt end of these lines is an artifact due to the limitations of the experimental data.
2. There is a noticeable kink present in all lines on the high temperature side of the vertical black line indicating T_g . We believe the existence of the kink is an unavoidable effect of thermal history (see Experimental section on how the experiment is performed). At the temperatures above 270 K the material is in equilibrated state and below 270 K it is not; as a result, the two branches of each curve in Figure 7.11B do not exactly match.
3. The initial steep slope of newly emerging processes is seen in the curves in the region where T^{-1} is $3.6 \cdot 10^{-3} \text{ K}^{-1}$. Because more temperature points are available in the sorbitol data as compared to the much wider temperature spacing for glycerol data, one can see that the temperature dependence of a relaxation process is actually a curve on the T^{-1} plot vs the straight line observed for glycerol. However, the glycerol relaxation map included times as small as 10^{-13} s vs only 10^{-7} s for sorbitol, where additional data at higher frequencies with closely spaced isotherms might indicate that the processes emerge from the boson peak region with an Arrhenian temperature dependence.
4. The previously made observation that the excess wing for sorbitol lingers within the experimental window below T_g manifests as a sharp turn to the almost horizontal slope the curves take in the upper right corner of Figure 7.13B.
5. The presence of the β -relaxation peak below T_g is a consequence that curves 2, 3, and 4 (counting from the bottom) in Figure 7.13B are more tightly bunched than (i) curves 1 and 2 and (ii) 4, 5, and 6. This effect is more clearly seen in magnification of the sub- T_g region shown in Figure 7.11C. Examine the spacing of the lines at T^{-1} of $4.6 \times 10^{-3} \text{ K}^{-1}$, where the spacing is denser in the region centered around $\log \tau = 2$ but wider at both shorter and longer relaxation times. It is this higher density of relaxation processes that results in the β -relaxation peak observed in the $\varepsilon''(\omega)$ data. Also, notice that the higher spectral density

region moves to shorter relaxation times as the temperature is increased, which accounts for the temperature dependence of the β -relaxation peak that is consistent with the temperature dependence of the β -relaxation peak determined mechanically by Faivre et al⁵⁸ and dielectrically by Geirhos et al. The key understanding from the data shown in Figure 7.13C is that the β -relaxation peak is not a new relaxation process, but rather just the consequence of the splaying of the temperature dependence of the individual relaxation processes.

6. The processes in the sub-T_g region have an approximate Arrhenian temperature dependence at low temperatures, but exhibit significant downward curvature as they approach T_g. This is especially clear in Figure 7.11B, where the downward curvature continues, presumably down to the region of the boson peak.

7.6 Discussion

The recently developed VASESS method³⁸ has been used to analyze the dielectric relaxation data for the two prototypical glass formers glycerol and sorbitol over a wide temperature range that includes both the super-cooled and glassy state for each material. The essence of the VASESS method is that, unlike in the traditional analysis, the spectral strength is constant, where the spectral density is then optimized to fit the experimental data. The method makes the following assumptions: (i) once a process appears it does not disappear at lower temperatures, but only shifts along the time axis with change in temperature, (ii) the temperature dependence of the process's relaxation time increases monotonically with decreasing temperature, and (iii) processes do not overtake, i.e. crossover, neighboring processes. With these conditions, a set of processes that describes the relaxation data is uniquely and robustly determined for each material (provided the data are sufficiently rich and smooth). The ultimate result of the analysis is a relaxation map that describes how each process behaves with temperature. In the traditional method of determining the relaxation spectra with uniform spacing the problem is ill-posed, requiring the use of regularization methods to determine the spectra; in contrast, the VASESS method of determining the spectral density (vs the spectral strength) does not appear to be ill-posed, although there is no formal proof – perhaps indicating that resulting spectral density has a stronger connection to the underlying physics.

The traditional method of analyzing dielectric spectra by fitting two or more empirical functions (i.e. Cole-Davidson, Havriliak-Negami, etc.) involves a significant number of model parameters – parameters that change, often in complex ways, with temperature and that depend upon the number and functional form assumed for the fitting functions. In contrast, the current approach does not contain fitting parameters, where the relaxation times and their temperature dependencies are extracted directly from the data. Moreover, thermo-rheological complexity is naturally accommodated as different processes are allowed to have different temperature dependencies. More important than the robust fitting of the experimental dielectric data, the new approach provides a different perspective of the relaxation behavior of glass forming materials. Specifically, in the traditional approach of fitting the response with multiple empirical functions the implicit assumption is that each of these functions is associated with a different underlying relaxation mechanism. The relaxation maps shown in Figure 7.8 for glycerol and Figure 7.11 for sorbitol provide a completely different perspective. Specifically, the temperature dependence of all the relaxation processes is remarkably similar:

1. Processes emerge at very high frequencies in the vicinity of the boson peak;
2. Almost all of the processes emerge above T_g ;
3. Above T_g , as the temperature is decreased, each process moves to rapidly coalesce with a main band of processes that have already emerged at higher temperatures, where the temperature dependence during coalescence is even stronger than that exhibited by $\log a_T$ at T_g ;
4. The main band of processes is associated with the α -process, which exhibit the standard $\log a_T$ temperature dependence measured experimentally;
5. The temperature dependencies of the individual processes that comprise the α -band of processes are of similar shape giving rise to the approximate thermo-rheological simplicity observed experimentally in the region above T_g ;
6. At T_g there is a significant change in the slope of temperature dependence of the individual relaxation processes, which become concave downward as a function of T^{-1} ;
7. Below T_g the temperature dependencies of the relaxation processes begin to splay, where at a constant temperature there is a region of higher density of processes at intermediate relaxation times between regions of lower density and high density;

8. At extremely low temperatures the temperature dependence of each process begins to approach Arrhenian behavior.

There is no distinct set of α , β , γ , etc. processes, only a similar temperature dependence for all processes. What appears as a peak or shoulder in the $\epsilon''(\omega)$ dielectric loss permittivity is just the compressing/ decompressing of the temperature dependence of the individual processes shown in the relaxation map, e.g. in Figure 7.13C the β -peak at the lower temperatures is the consequence of the high density of processes with relaxation times of between 10^{-2} to 10^{-3} s as compared to the process density at both shorter and longer relaxation times.

The relaxation maps shown in Figure 7.8 and Figure 7.13 provide a different perspective than the traditional understanding of the relaxation behavior in glass forming materials. The α -relaxation proper is a tightly bunched group of curves that (i) grow in number as the new processes join and (ii) all have a similar temperature dependence that follows the $\log a_T$ temperature dependence determined via the temperature dependence of the $\epsilon''(\omega)$ peak. The excess wing is a train of more recently born processes at various stages of catching up to the main α group. The new result here is that at different temperatures the processes in the excess wing are *not the same* set of processes, so any attempt at shifting the excess wing in the time-temperature superposition fashion is inappropriate. Finally, the β -relaxation group consists of processes that have emerged from the short-time source at lower temperatures than the processes that constitute the initial α -relaxation group – processes that have not yet coalesced into the band of the processes in the main α group. Whether this group manifests as a distinct β -relaxation peak depends on how close to T_g it emerges. Under the glycerol-like scenario, the β group is born sufficiently high above T_g so that it rapidly joins the α group and is never seen in the relaxation data as a separate peak. Under the sorbitol-like scenario, the β group is born closer to T_g so that it is not able to catch up with the α group as the temperature is decreased before its slope sharply decreases at T_g ; thus, the β group will remain separated from the α group and will be seen as a peak at lower temperatures. The β -relaxation peak broadens at still lower temperatures due to the splaying effect, i.e., the slopes of the new processes being less steep the newer the process.

An important feature is the emergence of new processes as temperature is decreased from a source located somewhere in the vicinity of the boson peak. The birth of new processes continues throughout the entire temperature range from the equilibrium liquid into the super-cooled liquid

and perhaps even in the glass, although the density of processes emerging as the temperature is lowered towards T_g and below is small at least for glycerol and sorbitol. The emergence of new processes with decreasing temperature provides a straightforward resolution of the increase in the static dielectric susceptibility with decreasing temperature – a universal feature of glass forming materials.

The sub- T_g relaxation process is often identified as a Johari-Goldstein process.⁶¹ A key postulate in the Johari-Goldstein analysis is that the sub- T_g process decouples from the main α -process at high temperature and short relaxation times, but then remains active and appears as the dominate process well-below T_g . There is a significant body of literature on the molecular interpretation of the Johari-Goldstein postulate.^{54,62-65} The key implicit assumption is that the temperature dependence of the Johari-Goldstein process observed below T_g is Arrhenian and can be extrapolated well-above T_g . The mechanical relaxation response of Faivre et al⁵⁸ and the dielectric relaxation data of Geirhos et al⁴¹ for sorbitol shown in Figure 7.13A are examples of sub- T_g extrapolation of this kind. The relaxation maps in Figure 7.8 for glycerol and Figure 7.13 for sorbitol indicate a completely different picture. Specifically, although the sub- T_g data may be approximately fit to an Arrhenian temperature dependence, the Arrhenian extrapolation of low temperature data to temperatures above T_g is not justified – the data are clearly non-Arrhenian close to T_g and above. The postulate that the sub- T_g process emerges out of the main α -process, i.e. a Johari-Goldstein transition, is qualitatively different from the results in this paper that show that all processes, including the processes responsible for the sub- T_g peak in the dielectric loss spectra, emerge from the region of the boson peak. That data reported in this paper call into serious question the Johari-Goldstein interpretation of the origin of the sub- T_g relaxation peak.

7.6.1 Possible Arrhenian Model

The above picture is based on the assumption that the processes do not overtake each other or, equivalently, that the corresponding lines on the relaxation map do not cross. What are the possibilities if this assumption is jettisoned? The low temperature region of the relaxation maps in Figure 7.8 and Figure 7.13 suggests an intriguing possibility – what if all lines in the map are straight on a T^{-1} Arrhenian plot? If this idea can be made to work, the relaxation response of a glass forming material will be described using exclusively Arrhenian processes. We will now examine this possibility.

One might envision an arrangement of processes as depicted in Figure 7.14. Specifically, a set of Arrhenian processes has activation energies ordered in such a way that the envelope to the set forms the traditional $\log a_T$ shift function for α -relaxation. Processes originating at higher temperatures, i.e. at lower T^{-1} values, and having lower activation energies would describe the β -relaxation as shown in Figure 7.14. If the Arrhenian description is to work, it must reproduce the density of processes at each temperature like that shown in Figure 7.3 and Figure 7.6 for glycerol and Figure 7.10 for sorbitol. Our experimentation with the Arrhenian model indicates that a qualitative, but not a quantitative, fit to the relaxation data can be achieved in the temperature region to the right of the vertical dashed line in the figure, where some curvature in the lines would be required for a quantitative fit. This perhaps is not fatal for the Arrhenian model as a whole where one can postulate that the lines are allowed to bend when the material enters the non-equilibrium state below T_g . The spectral density above T_g , but to the right of the dashed line, has a wedge-like shape that is consistent with the α -peak proper and the excess wing. However, the model fails qualitatively to the left of the dashed vertical line at higher temperatures, where a box-like spectrum for the density of processes is predicted contrary to the experimental data that shows a peak, e.g. see Figure 7.3 for glycerol.

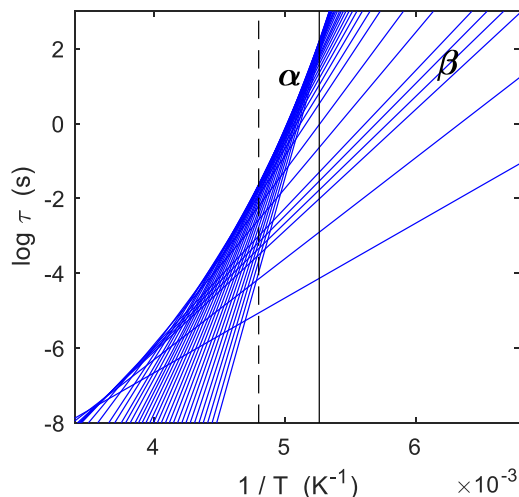


Figure 7.14. A sketch of a relaxation map for the Arrhenian model (see text for details) as an alternative to fit the relaxation data. Vertical solid line is T_g . Vertical dashed line separates high and low temperature regions.

Perhaps a less ambitious model could provide a compromise, where the α -relaxation is described in a traditional way, i.e. as a group of curves (not Arrhenian straight lines) bunched together and following the familiar VTF/WLF temperature dependence, but where the processes responsible for the β -relaxation still look like the ones in Figure 7.14. However, two important issues will still be unresolved: First, the steady increase in the static dielectric susceptibility with decreasing temperature would not be predicted, since the traditional description of the α -processes does not have new processes emerging from the region of the boson peak with decreasing temperature. Second, as we already mentioned, curvature appears necessary to quantitatively fit the β -relaxation data. Thus, as attractive a picture as the set of Arrhenian processes shown in Figure 7.14 might be (or even a reasonable perturbation of the Arrhenian processes), it is unable to describe the full set of dielectric relaxation data. The relaxation maps shown in Figure 7.8 and Figure 7.13 provide a better picture of the overall relaxation process in glass forming materials. Of course, the possibility that some, but not all, relaxation map curves cross cannot be excluded; however, if a simple no-crossing rule is sufficient to fit the data as demonstrated in the Results section, parsimony requires that we choose it over more complicated scenarios.

7.6.2 Possible origin of the processes emerging at short times

If the scenario suggested by the relaxation maps given in Figure 7.8 and Figure 7.13 is correct, then what is the nature of a process and by what mechanism do the new processes emerge from the short-time source? According to linear response theory, the dielectric permittivity is governed by the equilibrium correlation function of microscopic polarization; specifically,^{66,67}

$$\sum_i \langle \boldsymbol{\mu}_i(0) \cdot \boldsymbol{\mu}_i(t) \rangle + 2 \sum_j \sum_{i < j} \langle \boldsymbol{\mu}_i(0) \cdot \boldsymbol{\mu}_j(t) \rangle \quad (7.3)$$

where $\boldsymbol{\mu}_i$ is a molecular dipole, the summation is over all dipoles in volume V and the bracket in Equation 7.3 indicates the equilibrium average. The above expression consists of two terms – the autocorrelator and the cross-correlator. If only the autocorrelator contributes to the permittivity, then the static permittivity is constant and, contrary to the experiment, cannot increase with decrease in temperature faster than $1/T$ with a zero intercept. Thus, the observed change in the static permittivity with temperature is due to the cross-correlator contribution as has been

previously postulated.⁶⁷⁻⁶⁹ If the movement of neighboring particles becomes more correlated with decreasing temperature, which is generally believed to be the underlying physical mechanism of glass formation; then, some cross-correlation terms in Equation 7.3 which averaged to zero at a higher temperature would give a non-zero contribution at a lower temperature. This picture seems to provide a consistent account for emergence of new processes with the decrease in temperature.

7.6.3 Some final questions

The new picture of relaxation behavior in glass forming materials presented here raises some new questions and re-emphasizes some old ones in the field. The most fundamental question is: what is the nature of a process? The best-known example of a process resulting from a molecular level model are the Rouse modes in linear polymers³⁹ (or their analogues in polymer networks^{70,71}), but they are specific motions occurring in chain molecules. As we have shown in a recent paper,⁷² the Rouse modes lie above the α -relaxation envelope on the relaxation map and their number and density are orders-of-magnitude lower than that for the processes in the main α -group of processes. A process occurring in a molecular liquid is still presumably a collective motion, but not a chain motion because there are no chains. The findings of this report perhaps open a possibility for understanding the nature of a process using molecular simulations. According to the relaxation map presented here, new processes emerge from the short-time source located on the time axis in the vicinity of the boson peak, i.e. near 10^{-12} s. This time range is readily accessible by molecular simulations, unlike the time range where the glass transition related effects begin to be seen, which has been a major focus of the molecular simulation efforts to date.

The next set of questions concerns why processes behave with temperature in the way shown in the relaxation maps in Figure 7.8 and Figure 7.13. *First*, initially all processes emerge from the region of the boson peak having very steep slopes, which are even steeper than that of the temperature dependence of $\log a_T$ function at T_g . Perhaps the processes emerge with the same slope, but this will require additional data at frequencies of the order of 10^{12} Hz for more closely spaced isotherms – data that can perhaps be determined using MD simulations. The key questions are: why do processes emerge from the boson peak region, why do they have such a strong temperature dependence, and why does the spectral density decrease with decreasing temperature? *Second*, once a process is born it rapidly merges with a band of process that all have a similar temperature dependence that results in the VTF/WLF-like behavior of the $\log a_T$ function. Why

do all of these processes seem to move as a group? *Third*, processes born only slightly above T_g and at T_g have decreased initial slope and when a process crosses T_g the slope with respect to T^{-1} sharply decreases. Once below T_g each process exhibits its individual slope vs coalescing into a single band of processes as occurs above T_g , where the slopes with respect to T^{-1} are in a decreasing order, i.e. the processes born at lower temperatures have smaller slope values. As a result, the processes in the relaxation map “splay” causing the density of processes at a given temperature, i.e. along a vertical line in a relaxation map, to decrease with decrease in temperature. This behavior is obviously connected to the non-equilibrium nature of material below T_g , but why? *Fourth*, slight differences in the spacing of the relaxation lines give rise to the apparent β -peak (see the low temperature spacing of the relaxation lines for sorbitol in Figure 7.13C). Why are there regions of more densely spaced lines that give rise to apparent peaks and shoulders in the $\epsilon''(\omega)$ data?

Finally, there is the perennial question in the field of glass physics – why all processes, including the long-time Rouse modes in polymers, the main α -group processes, and the newly formed processes with initially steep slopes, all become enslaved by what manifests as the traditional $\log a_T$ temperature dependence above T_g . This paper makes no claim in being able to answer the questions posed in this last section, but we believe that the new perspective that comes from considering the relaxation map as shown in Figure 7.8 and Figure 7.11 provides a more solid foundation to begin addressing the questions of the molecular origins of relaxation behavior in glass forming liquids.

7.7 Acknowledgments

J.M. Caruthers and G.A. Medvedev acknowledge support from the National Science Foundation Grant Number 1761610-CMMI. D.A. Wilcox and B.W. Boudouris were supported by the National Science Foundation through the CAREER Award in the Polymers Program via Award Number: 1554957.

7.8 Supplementary Material

Form of the process density function $\rho(x)$, where $x = \log \tau$, used to obtain fit to the storage and loss permittivity isotherms in the main text.

7.8.1 Glycerol (Schneider et al data)

184 K

$$\rho = \frac{1}{4} \left((1 - v_1) \tanh(s_1(x - x_1)) + 1 + v_1 \right) \left((1 - v_2) \tanh(s_2(x - x_2)) + 1 + v_2 \right) v_3$$

T	s_1	x_1	v_1	s_2	x_2	v_2	v_3
184	0.69	2.90	0.04	0.20	5.10	0.0027	6.44×10^3

195-223 K

$$\rho = \frac{v_1}{4(1 + \exp(s_1(x - x_1)))} \left((1 - v_2) \tanh(s_2(x - x_2)) + 1 + v_2 \right) \left((1 - v_3) \tanh(s_3(x - x_3)) + 1 + v_3 \right)$$

T	s_1	x_1	v_1	s_2	x_2	v_2	s_3	x_3	v_3
195	9.2	0.98	3.90×10^5	0.81	2.55	0.0033	0.34	1.61	0.0012
204	10.4	-0.67	4.57×10^5	0.83	0.91	0.0036	0.375	0.075	0.0014
213	11.0	-2.08	18.88×10^5	0.99	-0.61	0.0054	0.45	0.19	0.0003
223	12.2	-3.33	158.4×10^5	1.38	-2.02	0.0050	0.57	-0.18	0.0001

234-323 K

$$\rho = v_1 \frac{v_2 \exp(-s_2(x - x_2)) + v_3 \exp(s_3(x - x_3)) + \exp(-s_4(x - x_4))}{(1 + \exp(s_1(x - x_1))) (1 + v_4 \exp(-s_4(x - x_4)))}$$

T	s_1	x_1	v_1	s_2	x_2	v_2	s_3	x_3	v_3	s_4	x_4	v_4
234	25	-4.14	1.92×10^4	1.3	-4.37	0.011	0.07	-4.18	17.9	1.25	-7.61	3.76×10^3
253	18	-5.71	1.65×10^4	1.5	-5.65	0.013	0.19	-6.36	17.4	1.33	-9.16	4.79×10^3
273	18	-7.00	1.56×10^4	1.8	-6.23	0.010	0.26	-5.92	15.9	1.74	-10.18	6.30×10^3
295	131	-7.82	1.52×10^4	1.9	-7.00	0.010	0.33	-7.44	13.6	1.82	-10.85	6.10×10^3
323	150	-8.57	1.61×10^4	2.3	-7.21	0.016	0.99	-8.04	30.5	2.65	-9.99	1.27×10^3

363-413 K

$$\rho = \frac{1}{2(1 + \exp(s_1(x - x_1)))} \left((1 - v_2) \tanh(s_2(x - x_2)) + 1 + v_2 \right) v_3$$

T	s_1	x_1	s_2	x_2	v_2	v_3
363	20	-9.5	3.1	-7.7	1.8×10^{-7}	7.5×10^8
413	100	-9.9	3.4	-8.4	3.3×10^{-7}	4.5×10^8

7.8.2 Glycerol (Dielectric data reported in this paper)

150-190 K

$$\rho = \frac{1}{4} \left((1 - v_1) \tanh(s_1(x - x_1)) + 1 + v_1 \right) \left((1 - v_2) \tanh(s_2(x - x_2)) + 1 + v_2 \right) v_3$$

T	s_1	x_1	v_1	s_2	x_2	v_2	v_3
150	0.33	11.0	0.001	0.36	-4.6	0	3.80×10^3
160	0.48	7.1	0.002	0.26	-3.7	0.011	3.60×10^3
170	0.58	4.7	0.006	0.28	-3.6	0.013	1.75×10^3
180	0.68	3.2	0.013	0.23	-1.5	0.003	2.10×10^3
190	0.69	2.6	0.001	0.28	0.6	0.006	19.2×10^3

200-230 K

$$\rho = \frac{v_1}{4(1 + \exp(s_1(x - x_1)))} \left((1 - v_2) \tanh(s_2(x - x_2)) + 1 + v_2 \right) \left((1 - v_3) \tanh(s_3(x - x_3)) + 1 + v_3 \right)$$

T	s_1	x_1	v_1	s_2	x_2	v_2	s_3	x_3	v_3
200	6.9	0.1	8.4×10^5	0.77	2.2	0.0023	0.36	1.0	0.0010
210	7.9	-1.6	11.3×10^5	0.91	0.2	0.0034	0.44	-0.6	0.0010
220	8.9	-3.0	97.4×10^5	1.09	-1.4	0.0067	0.55	0.1	0.0002
230	13.2	-4.3	1642×10^5	4.6	-3.3	0	1.05	-4.7	0.0195

240-250 K

$$\rho = \frac{1}{(1 + \exp(s_1(x - x_1)))} \frac{v_3}{(1 + \exp(-s_4(x - x_4)))}$$

T	s_1	x_1	v_3	s_4	x_4
240	60	-4.7	3.7×10^4	1.9	-4.2
250	25	-5.5	2.7×10^4	2.3	-5.25

7.8.3 Sorbitol (Dielectric data reported in this paper)

150-180 K

$$\rho = \frac{1}{2(1 + \exp(s_1(x - x_1)))} \left((1 - v_2) \tanh(s_2(x - x_2)) + 1 + v_2 \right) v_3 (1 + \exp(-s_4(x - x_4)))$$

T	s_1	x_1	s_2	x_2	v_2	v_3	s_4	x_4
150	0.74	3.8	0.20	4.9	0.0035	111	0.23	-5.8
160	0.69	3.3	0.22	4.4	0.0049	123	0.16	-3.9
170	0.96	2.8	0.21	3.8	0.0047	121	0.11	-6.2
180	0.75	0.9	0.29	4.3	0	504	0.35	-1.6

190-220 K

$$\rho = \frac{1}{2} \left((1 - v_2) \tanh(s_2(x - x_2)) + 1 + v_2 \right) \frac{v_3}{(1 + \exp(-s_3(x - x_3)))}$$

T	s_2	x_2	v_2	s_3	x_3	v_3
190	0.52	0.85	7.1	0.35	6.80	101
200	0.58	0.05	5.3	0.37	3.95	83.1
210	0.65	-0.55	4.1	0.41	0.80	56.6
220	0.78	-1.05	3.0	0.50	-2.05	45.2

230-265 K

$$\rho = \frac{1}{4} \left((1 - v_1) \tanh(s_1(x - x_1)) + 1 + v_1 \right) \left((v_2 - 1) \tanh(-s_2(x - x_2)) + 1 + v_2 \right) \frac{v_3}{(1 + \exp(-s_3(x - x_3)))}$$

T	s_1	x_1	v_1	s_2	x_2	v_2	s_3	x_3	v_3
230	2.3	4.1	0.0063	0.73	-1.65	3.7	0.52	-2.50	6.8×10^3
240	4.7	3.6	0.0084	0.78	-2.10	3.4	0.63	-3.90	4.6×10^3
250	2.1	3.8	0.0096	0.65	-2.90	7.2	0.59	-2.80	4.0×10^3
255	1.6	3.9	0.0100	0.67	-3.10	7.4	0.60	-3.10	3.7×10^3
260	1.2	3.9	0.0117	0.69	-3.30	6.7	0.63	-3.60	3.4×10^3
262.5	1.0	3.9	0.0126	0.75	-3.30	5.0	0.68	-4.30	3.4×10^3
265	0.8	3.8	0.0164	0.86	-3.30	3.4	0.72	-4.70	3.6×10^3

267.5-295 K

$$\rho = \frac{1}{4} \frac{\left((1 - v_2) \tanh(s_2(x - x_2)) + 1 + v_2 \right) \left((v_3 - 1) \tanh(-s_3(x - x_3)) + 1 + v_3 \right)}{(1 + \exp(s_1(x - x_1))) (1 + \exp(-s_4(x - x_4)))} v_4$$

T	s_1	x_1	s_2	x_2	v_2	s_3	x_3	v_3	s_4	x_4	v_4
267.5	7.0	3.1	0.67	3.0	0.03	0.86	-3.7	3.65	0.67	-3.65	3.55×10^3
270	7.0	2.4	0.64	2.0	0.05	0.86	-3.9	3.6	0.69	-3.25	3.15×10^3
272.5	7.0	1.5	0.62	1.0	0.09	0.85	-4.1	3.7	0.70	-2.80	2.90×10^3
275	6.7	0.7	0.55	0.25	0.11	0.80	-4.3	4.5	0.74	-2.70	2.85×10^3
277.5	5.2	-0.05	0.56	-0.45	0.205	0.87	-4.5	4.0	0.74	-2.25	3.0×10^3
280	4.7	-0.7	0.48	-0.8	0.30	0.91	-4.6	3.7	0.76	-1.80	3.65×10^3
285	4.0	-1.8	0.29	-1.25	0.47	0.98	-4.8	3.25	0.71	-1.05	7.25×10^3
290	4.2	-2.7	0.11	-1.65	0.58	1.03	-5.0	2.95	0.81	-0.25	18.8×10^3
295	5.0	-3.35	0	30	0.86	0.96	-5.2	3.75	0.90	0.60	58.6×10^3

300-320 K

$$\rho = \frac{1}{(1+\exp(s_1(x-x_1)))} \frac{v_3}{(1+\exp(-s_4(x-x_4)))}$$

T	s_1	x_1	v_3	s_4	x_4
300	6.8	-3.75	1.22×10^3	1.3	-6.2
305	5.5	-4.35	1.28×10^3	1.45	-6.55
310	5.9	-4.80	1.23×10^3	2.0	-7.0
315	6.0	-5.25	1.24×10^3	2.65	-7.3
320	5.5	-5.65	1.25×10^3	3.2	-7.5

7.8.4 Sorbitol (Geirhos et al data)

Note, $\bar{H} = 10^{-3}$.

10 – 140 K

$$\rho = \frac{1}{2} \left((v_3 - v_2) \tanh(s_2(x - x_2)) + v_3 + v_2 \right)$$

T	s_2	x_2	v_2	v_3
10	0.45	12.8	3.0	11.7×10^3
70	0.13	26.8	6.3	6.6×10^3
100	0.13	21.6	7.6	6.2×10^3
120	0.13	18.1	5.0	5.9×10^3
130	0.13	16.1	4.2	6.0×10^3
140	0.14	14.6	3.6	6.5×10^3

150 – 220 K

$$\rho = \frac{1}{2} \frac{(v_2 - 1) \tanh(-s_2(x - x_2)) + 1 + v_2}{1 + \exp(-s_3(x - x_3))} v_3$$

T	s_2	x_2	v_2	s_3	x_3	v_3
150	0.012	670	15.0	0.26	22.6	4.3×10^3
160	0.42	4.05	12.6	0.28	18.9	4.0×10^3
170	0.52	3.0	4.6	0.33	4.4	0.35×10^3
180	0.68	2.15	2.5	0.38	0.55	0.35×10^3
190	0.60	1.15	3.4	0.41	0.25	0.34×10^3
200	0.40	0.05	10.9	0.43	0.90	0.20×10^3
210	0.49	-0.90	9.3	0.44	1.35	0.39×10^3
220	0.81	-0.80	2.9	0.55	-3.15	0.35×10^3

230 – 260 K

$$\frac{1 \left((1 - v_1) \tanh(s_1(x - x_1)) + 1 + v_1 \right) \left((v_2 - 1) \tanh(-s_2(x - x_2)) + 1 + v_2 \right)}{4 \left(1 + \exp(-s_3(x - x_3)) \right)} v_3$$

T	s_1	x_1	v_1	s_2	x_2	v_2	s_3	x_3	v_3
230	2.5	4.05	0.0051	0.63	-1.55	4.0	0.58	-3.25	6.6×10^4
240	4.7	3.55	0.0081	0.74	-2.10	3.9	0.62	-3.75	4.8×10^4
250	0.88	4.75	0.0012	0.65	-2.90	6.5	0.60	-3.05	3.5×10^4
260	0.78	4.25	0.0136	0.84	-3.05	3.7	0.65	-4.40	4.2×10^4

7.9 References

1. J. D. Ferry, *Viscoelastic Properties of Polymers*, 3rd ed. (John Wiley and Sons, New York, 1980).
2. C. A. Angell, K. L. Ngai, G. B. McKenna, P. F. McMillan and S. W. Martin, *J. Appl. Phys.* **88** (6), 3113-3157 (2000).
3. R. Richert, in *Adv. Chem. Phys.*, edited by S. A. Rice and A. R. Dinner (John Wiley and Sons, New York, 2015), Vol. 156, pp. 101-193.
4. F. Kremer and A. Schonhals, in *Broadband Dielectric Spectroscopy*, edited by F. Kremer and A. Schonhals (Springer-Verlag, Berlin, Heidelberg, 2003), pp. 35-56.
5. A. Schonhals and F. Kremer, in *Broadband Dielectric Spectroscopy*, edited by F. Kremer and A. Schonhals (Springer-Verlag, Berlin, Heidelberg, 2003), pp. 57-97.
6. H. Schäfer, E. Sternin, R. Stannarius, M. Arndt and F. Kremer, *Phys. Rev. Lett.* **76** (12), 2177-2180 (1996).
7. E. Tuncer and J. R. Macdonald, *J. Appl. Phys.* **99** (7), 074106 (2006).
8. A. Y. Zasetsky and R. Buchner, *J. Phys.-Condens. Mat.* **23** (2), 025903 (2010).
9. K. S. Cole and R. H. Cole, *J. Chem. Phys.* **9** (4), 341-351 (1941).
10. D. W. Davidson and R. H. Cole, *J. Chem. Phys.* **19** (12), 1484-1490 (1951).
11. S. Havriliak and S. Negami, *Polymer* **8**, 161-210 (1967).
12. G. Williams and D. C. Watts, *Trans. Faraday Soc.* **66**, 80-85 (1970).
13. P. Lunkenheimer, U. Schneider, R. Brand and A. Loidl, *Contemp. Phys.* **41** (1), 15-36 (2000).
14. J. Bartoš, M. Iskrová, M. Köhler, R. Wehn, O. Šauša, P. Lunkenheimer, J. Krištiak and A. Loidl, *Eur. Phys. J. E* **34** (9), 104 (2011).
15. H. Svajdlenkova, A. Ruff, P. Lunkenheimer, A. Loidl and J. Bartos, *J. Chem. Phys.* **147**, 084506 (2017).
16. G. Power, J. K. Vij and G. P. Johari, *J. Chem. Phys.* **124**, 044513 (2006).
17. F. Qi, T. E. Goresy, R. Bohmer, A. Doss, G. Diezemann, G. Hinze, H. Sillescu, T. Blochowicz, C. Gainaru, E. A. Rossler and H. Zimmermann, *J. Chem. Phys.* **118** (16), 7431-7438 (2003).
18. A. Minoguchi, K. Kitai and R. Nozaki, *Phys Rev E* **68**, 031501 (2003).
19. D. Pisignano, S. Capaccioli, R. Casalini, M. Lucchesi, P. A. Rolla, A. Justl and E. Rössler, *J. Phys.-Condens. Mat.* **13** (20), 4405-4419 (2001).
20. S. Capaccioli, D. Prevosto, M. Lucchesi, P. A. Rolla, R. Casalini and K. L. Ngai, *J. Non-Cryst. Solids* **351** (33), 2643-2651 (2005).

21. R. Casalini, D. Fioretto, A. Livi, M. Lucchesi and P. A. Rolla, *Phys. Rev. B* **56** (6), 3016-3021 (1997).
22. G. Power, G. P. Johari and J. K. Vij, *J. Chem. Phys.* **119** (1), 435-442 (2003).
23. C. Hansen, F. Stickel, T. Berger, R. Richert and E. W. Fischer, *J. Chem. Phys.* **107** (4), 1086-1093 (1997).
24. A. Döb, M. Paluch, H. Sillescu and G. Hinze, *J. Chem. Phys.* **117** (14), 6582-6589 (2002).
25. C. León, K. L. Ngai and C. M. Roland, *J. Chem. Phys.* **110** (23), 11585-11591 (1999).
26. R. Nozaki, D. Suzuki, S. Ozawa and Y. Shiozaki, *J. Non-Cryst. Solids* **235-237**, 393-398 (1998).
27. A. Kudlik, S. Benkhof, T. Blochowicz, C. Tschirwitz and E. A. Rossler, *J. Mol. Struct.* **479**, 201-218 (1999).
28. T. Blochowicz, C. Tschirwitz, S. Benkhof and E. A. Rössler, *J. Chem. Phys.* **118** (16), 7544-7555 (2003).
29. R. V. Chamberlin, R. Böhmer, E. Sanchez and C. A. Angell, *Phys. Rev. B* **46** (9), 5787-5790 (1992).
30. C. Hansen, R. Richert and E. W. Fischer, *J. Non-Cryst. Solids* **215** (2-3), 293-300 (1997).
31. K. Adrjanowicz, K. Kaminski, P. Włodarczyk, K. Grzybowska, M. Tarnacka, D. Zakowiecki, G. Garbacz, M. Paluch and S. Jurga, *Mol. Pharmaceutics* **10** (10), 3934-3945 (2013).
32. P. K. Dixon, L. Wu and S. R. Nagel, *Phys. Rev. Lett.* **65** (9), 1108-1111 (1990).
33. U. Schneider, P. Lunkenheimer, R. Brand and A. Loidl, *J. Non-Cryst. Solids* **235-237**, 173-179 (1998).
34. U. Schneider, P. Lunkenheimer, R. Brand and A. Loidl, *Phys Rev E* **59** (6), 6924-6936 (1999).
35. M. Nakanishi and R. Nozaki, *Phys Rev E* **83** (5), 051503 (2011).
36. L. Onsager, *J. Am. Chem. Soc.* **58** (8), 1486-1493 (1936).
37. J. G. Kirkwood, *J. Chem. Phys.* **7** (10), 911-919 (1939).
38. Y. Ni, H. Song, D. A. Wilcox, G. A. Medvedev, B. W. Boudouris and J. M. Caruthers, *Macromolecules* **53** (5), 1867-1880 (2020).
39. P. E. Rouse Jr., *J. Chem. Phys.* **21** (7), 1272-1280 (1953).
40. M. Doi and S. F. Edwards, *The Theory of Polymer Dynamics*. (Clarendon Press, 1988).
41. K. Geirhos, P. Lunkenheimer and A. Loidl, *Phys. Rev. Lett.* **120** (8), 085705 (2018).
42. H. Wagner and R. Richert, *J. Non-Cryst. Solids* **242** (1), 19-24 (1998).
43. S. Kastner, M. Köhler, Y. Goncharov, P. Lunkenheimer and A. Loidl, *J. Non-Cryst. Solids* **357** (2), 510-514 (2011).
44. T. S. Grigera, V. Martín-Mayor, G. Parisi and P. Verrocchio, *Nature* **422** (6929), 289-292 (2003).
45. J. D. Stevenson, J. Schmalian and P. G. Wolynes, *Nat. Phys.* **2** (4), 268-274 (2006).
46. W. Schirmacher, G. Ruocco and T. Scopigno, *Phys. Rev. Lett.* **98** (2), 025501 (2007).
47. D. A. Parshin, H. R. Schober and V. L. Gurevich, *Phys. Rev. B* **76** (6), 064206 (2007).
48. A. I. Chumakov, G. Monaco, A. Monaco, W. A. Crichton, A. Bosak, R. Ruffer, A. Meyer, F. Kargl, L. Comez, D. Fioretto, H. Giefers, S. Roitsch, G. Wortmann, M. H. Manghnani, A. Hushur, Q. Williams, J. Balogh, K. Parliński, P. Jochym and P. Piekarczyk, *Phys. Rev. Lett.* **106** (22), 225501 (2011).
49. A. Brodin and E. A. Rössler, *Euro. Phys. J. B* **44** (1), 3-14 (2005).

50. S. Kariyo, A. Brodin, C. Gainaru, A. Herrmann, J. Hintermeyer, H. Schick, V. N. Novikov and E. A. Rossler, *Macromolecules* **41** (14), 5322-5332 (2008).
51. A. Herrmann, S. Kariyo, A. Abou Elfadl, R. Meier, J. Gmeiner, V. N. Novikov and E. A. Rössler, *Macromolecules* **42** (14), 5236-5243 (2009).
52. M. Hofmann, B. Kresse, A. F. Privalov, L. Willner, N. Fatkullin, F. Fujara and E. A. Rössler, *Macromolecules* **47** (22), 7917-7929 (2014).
53. M. H. Jensen, C. Gainaru, C. Alba-Simionesco, T. Hecksher and K. Niss, *Phys. Chem. Chem. Phys.* **20** (3), 1716-1723 (2018).
54. H.-B. Yu, R. Richert and K. Samwer, *Science Advances* **3** (11), e1701577 (2017).
55. A. Kudlik, C. Tschirwitz, T. Blochowicz, S. Benkhof and E. A. Rossler, *J. Non-Cryst. Solids* **235-237**, 406-411 (1998).
56. A. Mandanici, R. Richert, M. Cutroni, X. Shi, S. A. Hutcheson and G. B. McKenna, *J. Non-Cryst. Solids* **352**, 4729-4734 (2006).
57. A. Mandanici, W. Huang, M. Cutroni and R. Richert, *J. Chem. Phys.* **128**, 124505 (2008).
58. A. Faivre, G. Niquet, M. Maglione, J. Fornazero, J. F. Jal and L. David, *Euro. Phys. J. B* **10**, 277-286 (1999).
59. C. A. Angell, R. C. Stell and W. Sichina, *J. Phys. Chem.* **86** (9), 1540-1542 (1982).
60. F. Migliardo, C. A. Angell and S. Magazù, *Biochim. Biophys. Acta, Gen. Subj.* **1861** (1, Part B), 3540-3545 (2017).
61. G. P. Johari and M. Goldstein, *J. Chem. Phys.* **53** (6), 2372-2388 (1970).
62. S. Capaccioli, M. Paluch, D. Prevosto, L.-M. Wang and K. L. Ngai, *J. Phys. Chem. Lett.* **3** (6), 735-743 (2012).
63. Y. Cohen, S. Karmakar, I. Procaccia and K. Samwer, *Europhys. Lett.* **100** (3), 36003 (2012).
64. D. Bock, R. Kahlau, B. Micko, B. Pötzschner, G. J. Schneider and E. A. Rössler, *J. Chem. Phys.* **139** (6), 064508 (2013).
65. M. T. Cicerone, Q. Zhong and M. Tyagi, *Phys. Rev. Lett.* **113** (11), 117801 (2014).
66. C. J. F. Bottcher and P. Bordewijk, *Theory of Electric Polarization, Vol. 2: Dielectrics in Time-Dependent Fields*, 2nd ed. (Elsevier, Amsterdam, 1978).
67. G. Williams, *Adv. Polym. Sci.* **33**, 59-92 (1979).
68. A. Schonhals and F. Kremer, in *Broadband Dielectric Spectroscopy*, edited by F. Kremer and A. Schonhals (Springer-Verlag, Berlin, Heidelberg, 2003), pp. 1-32.
69. M. Cook, D. C. Watts and G. Williams, *Trans. Faraday Soc.* **66**, 2503-2511 (1970).
70. A. A. Gurtovenko and Y. Y. Gotlib, *Macromolecules* **31** (17), 5756-5770 (1998).
71. A. A. Gurtovenko and Y. Y. Gotlib, *Macromolecules* **33** (17), 6578-6587 (2000).
72. Y. Ni, G. A. Medvedev, D. B. Curliss and J. M. Caruthers, *Polymer* **submitted** (2020).

8. CONCLUSIONS, ONGOING, AND FUTURE WORK

The work presented in Chapters 4 and 5 establishes the interactions between a model conjugated polymer, poly(3-hexylthiophene) (P3HT), and three radical species that exhibit a range of optical properties and oxidation and reduction behaviors. Through these, a clear trend in both the excited-state and ground-state interactions is observed, with the p-type and optically-inactive TEMPO radical showing no interactions, and the optically-active PTIO and galvinoxyl radicals both interacting in the excited state. For the n-type galvinoxyl radical, additional interactions are seen in the ground state that cause the organic semiconductor P3HT to change in character to a conductor. As stable radical moieties see further inclusion into device application spaces traditionally dominated exclusively by conjugated polymers, an awareness of the nature of these interactions is essential to ensure they are applied in the appropriate context.

While this work has examined radicals primarily as small molecules blended into a conjugated polymer matrix, many applications see them incorporated as pendant groups on a macromolecule. The value of these radical polymers for charge transport applications has been demonstrated, but a fundamental understanding of this charge transport in the solid state is lacking. To complement the understanding of the interactions with conjugated polymers, it is also important to elucidate how charge and energy are transformed within the radical bulk. Insights into these phenomena are needed to bring these materials to their full potential.

The work presented in Chapter 7 discusses a new analysis technique for dielectric spectroscopy that addresses some of the shortcomings of traditional analysis techniques. A clear and comprehensive theoretical understanding of amorphous solid and viscoelastic liquid behavior has yet to emerge, in contrast with the crystalline solid and gaseous phases of matter. While amorphous solids have nearly universal applications, this problem is particularly relevant to the field of organic electronics. Many organic electronic materials take the form of amorphous or polycrystalline polymers. Thus, the field would benefit greatly from an improved understanding of the amorphous solid phase. In particular, understanding relaxation behavior will give insights into the optimal device fabrication conditions and the phenomena leading to effects such as hysteresis that are commonly observed in organic electronic devices.

To address these points, several ongoing and potential future applications are proposed here. In addition to next steps for furthering the understanding gained by the work completed in

this dissertation, these projects aim to practically apply the results to many situations. In particular, the proposed work in Section 8.3 aims to apply the insights from dielectric spectroscopy towards understanding the high conductivity state of a radical polymer and how to bring about the high conductivity on a larger scale. Additionally, the proposed work in Section 8.5 aims to practically apply the results of Chapters 4 and 5 to improve the environmental resilience of a conjugated polymer. Pursuit of these projects will further establish the picture of how two important classes of conducting polymer, one established and one emerging, can be synergistically utilized to improve the performance of organic electronic devices.

8.1 Protected PTEO Copolymers

Radical polymers show significant potential for organic electronic applications, most notably with regards to the intrinsic conductivity of poly(4-glycidyoxy-2,2,6,6-tetramethylpiperidin-1-oxyl) (PTEO), which demonstrates an electrical conductivity of 0.2 S cm^{-1} , albeit at a maximum channel length of 600 nm.¹ Despite samples showing no long-range order, computational studies suggested that this high conductivity was due to favorable aggregation of the TEMPO moieties. This aggregation occurs if sufficient molecular motion is permitted, which can be achieved by heating the material above its glass transition temperature. By simulating a collection of TEMPO molecules, allowing them to aggregate, and measuring the size of the percolating network, estimates were computationally obtained for the minimum required density of TEMPO molecules as well as the maximum concentration of defect sites (i.e., electronically-inactive sites) for high conductivity to occur. While preliminary experimental results suggested that the critical value was located between 70 and 90% active radical sites, it is necessary to establish the precise value for the purposes of providing a quality control standard for the material. Additionally, the precise interactions that give rise to the electrical conductivity in the material are poorly understood. Therefore, observing how the interactions change near this critical value could provide valuable insight into their nature.

Electron paramagnetic resonance (EPR) spectroscopy is a widely utilized tool for studying open-shell systems.² This technique exploits the Zeeman effect (i.e., the splitting of electron energy levels in the presence of a magnetic field) to provide a unique fingerprint of a molecular system that describes the interaction between the different spins in the system. Specifically, application of a magnetic field to an open-shell molecule will create two quantum states where the unpaired

electron is aligned either with or against the magnetic field, and the energy required to transition between these states (i.e., to flip the electron such that it is aligned against the field) corresponds to photons in the microwave region of the spectrum. The magnetic field from nuclear spins will serve to alter the effective field acting on the electrons, which allows EPR spectroscopy to identify these unique effects for given chemical species. Additionally, the effect is quantitative, so by comparing the signal strength to that of a known standard, the precise concentration of radicals in a sample can be determined.

EPR spectroscopy is also an ideal tool for characterizing interactions between the open-shell moieties.³ For pairs of radicals brought into close proximity, further energy splitting will occur due to the interaction of the two spins. This effect depends heavily on distance, which can be exploited to study changes in molecular configurations due to temperature and chemical environment.⁴⁻⁶ However, because of the effect of distance, when multiple spins are present without any spatial order, the end result will be a broadening of the peaks in the isolated molecule into a single peak. The extent of this broadening can be used to quantify the extent to which the radicals interact.^{7,8} Previous work specifically on radical polymers looked at the effects of radical density on conductivity for a radical polymer with a norbornene backbone.⁹ In particular, the radical density was modified by blending a fully-active polymer with a polymer where the nitroxide radicals had been chemically reduced to hydroxylamine moieties. Specifically, hydrogen atom transfer would occur between hydroxylamine and nitroxide radical moieties, allowing a homogenous mixture of copolymers to be generated from two homopolymers.¹⁰ In this case, EPR spectroscopy was used both to quantify the number of radical sites in a given blend and to verify that hydrogen atom transfer had occurred by monitoring the splitting. While this approach demonstrated an exponential dependence of conductivity on radical density, the polymer that was studied does not show the same aggregation behavior as PTEO, so understanding how the radical density affects conductivity in the aggregated state remains an open question.

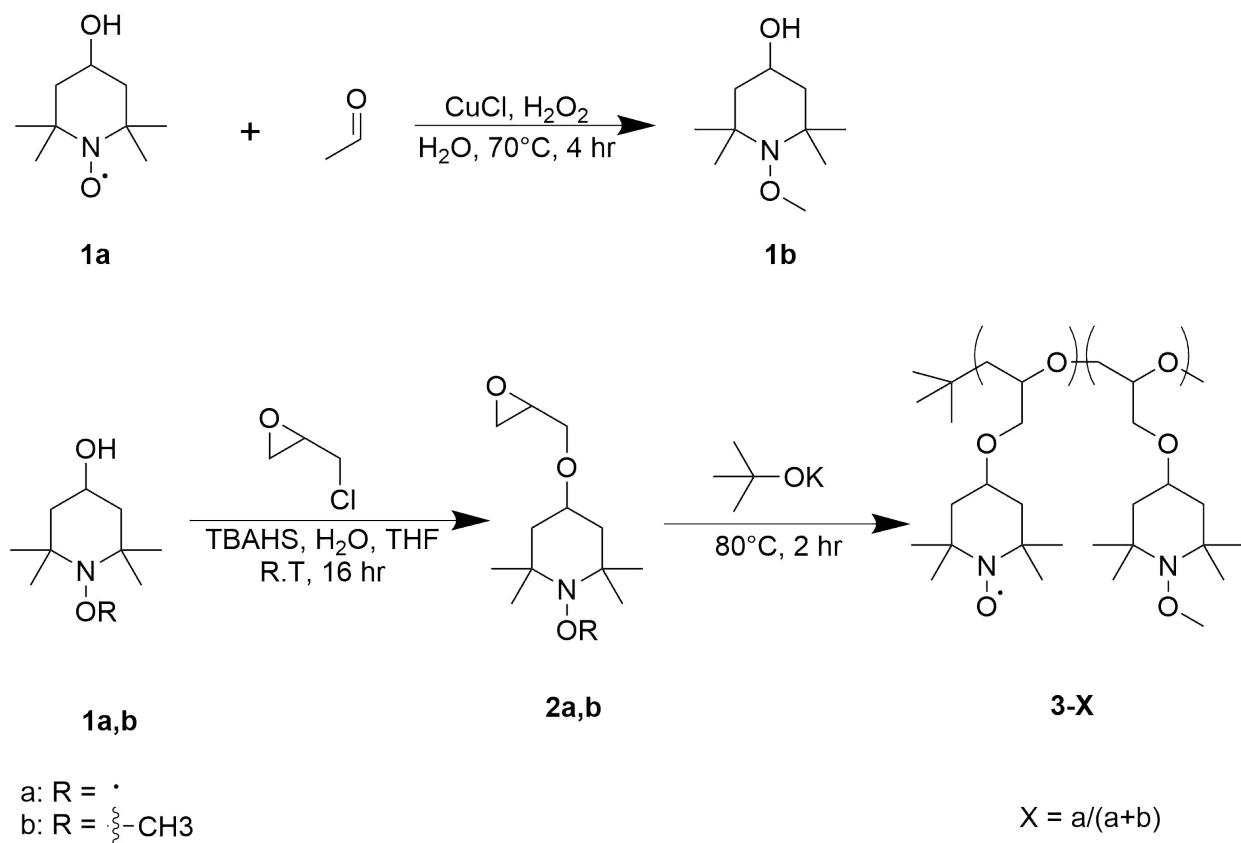
Specifically, this study aims to examine PTEO copolymerized with deactivated radical moieties to determine how the EPR signals correspond to the observed trends in conductivity. That is, copolymers with precisely chosen radical loadings will be synthesized, EPR spectroscopy will be utilized to confirm their radical loadings as well as qualitatively observe the emergence of the splitting pattern, and the conductivities will be measured. Additionally, computational studies will be performed to theoretically calculate the EPR spectra of the copolymers, associate them with a

spatial configuration, and then model the charge transport of the system. By doing this, we anticipate being able to better relate the spin interactions of the radical moieties to the observed conductivity, which will offer insights that will allow further improvements in electrical performance to be realized.

8.1.1 Materials and Methods

Materials

4-hydroxy-2,2,6,6-tetramethylpiperidin-1-oxyl (TEMPO-OH) (97%), hydrogen peroxide (H₂O₂) (30%, by weight, in water), acetaldehyde (99.5%), (±)-epichlorohydrin (99%), tetrabutylammonium hydrogensulfate (TBAHS) (99%), inhibitor-free tetrahydrofuran (THF) (99.9%), potassium tert-butoxide (99.9%), copper (I) chloride (CuCl) (97%), and silica gel (60 Å pore, 230–400 mesh) were all purchased from Sigma Aldrich. Sodium hydroxide (NaOH) (97%), sodium chloride (99%), toluene (99.5%), ethyl acetate (99.5%), hexanes (98.5%), and dichloromethane (99.5%) were purchased from Fisher Scientific. Potassium tert-butoxide was purified via sublimation at 205°C and 0.5 torr and stored under inert atmosphere. All other chemicals were used as received. Water was obtained from a building-wide reverse osmosis system (Marlo Inc. MRO-1500-2.5).



Scheme 8.1. Synthesis of TEMPO-M (1b), TEO/TEO-M (2), and PTEO-X (3)

Synthesis of 1-methoxy-4-hydroxy-2,2,6,6-tetramethylpiperidine (TEMPO-M)

Synthesis of the methyl-protected TEMPO-OH was performed following a procedure from the literature.¹¹ 10 g of TEMPO-OH were dissolved in 40 mL of water in a 3-neck round-bottom flask, followed by 114 mg of CuCl. 15 mL of acetaldehyde were added, and the flask was immediately attached to a condenser cooled to 10 °C to prevent evaporation of the acetaldehyde. The contents of the flask were then heated to 70 °C and 18 mL of a 30% hydrogen peroxide in water solution were added dropwise over a period of 30 mins using a syringe pump (New Era Pump Systems Inc. NE-4000). This reaction was then allowed to proceed for 4 hours before slowly cooling to room temperature. Then, 200 mL of a 10% sodium carbonate solution were added to raise the pH of the solution to 8, and the mixture was further cooled using an ice bath. The mixture was then poured into a vacuum filter and washed with 300 mL of a 10% (by weight) ascorbic acid solution followed by water that had both been cooled with an ice bath. The remaining filter cake was dissolved in toluene and washed with water followed by a saturated sodium chloride in water

solution. The organic phase was dried with magnesium sulfate and filtered, then boiled off under vacuum to yield a tan residue. This residue was then sublimated at 125°C and 0.5 torr three times to yield an off-white solid.

Synthesis of 4-glycidyloxy-2,2,6,6-tetramethylpiperidin-1-oxyl (TEO) and 1-methoxy-4-glycidyloxy-2,2,6,6-tetramethylpiperidine (TEO-M)

A similar procedure was followed for the synthesis of both monomers, following a previous report.¹ First, 8 g sodium hydroxide were dissolved in 8 mL of water in a round-bottom flask while it was cooled under an ice bath. To this, 1.5 g tetrabutylammonium hydrogensulfate (TBAHS) and 10 mL epichlorohydrin were added and allowed to stir until combined. Followed by this, a solution of either 4.1 mg TEMPO-OH or 4.5 mg TEMPO-M (24 mmol) in 30 mL tetrahydrofuran was added dropwise to the aqueous reaction mixture, which was then removed from the ice bath and allowed to react overnight at room temperature. The reaction mixture was then dissolved in 200 mL of water, and it was extracted with 600 mL ethyl acetate. The organic layer was then washed with water followed by a saturated sodium chloride in water solution. The organic layer was then dried with magnesium sulfate, filtered, and then evaporated to yield a red liquid. This liquid was dried under vacuum while being heated to 60 °C until bubbling ceased. Following this, the product was purified using column chromatography with a silica gel column and an 8:1 (by volume) hexanes/ethyl acetate mixture as the eluent. For TEO, the eluent was collected as soon as a red color appeared and then for 400 mL afterwards. The product was dried in a vacuum oven overnight to yield a crystalline red solid. For TEO-M, the first 100 mL of eluent were collected and dried in a vacuum oven overnight to yield a colorless liquid.

Synthesis of poly(4-glycidyloxy-2,2,6,6-tetramethylpiperidin-1-oxyl-co-1-methoxy-4-glycidyloxy-2,2,6,6-tetramethylpiperidine) (PTEO, PTEO-X, and PTEO-M)

5.0 mg of potassium tert-butoxide were massed in a 7 mL vial in a nitrogen atmosphere glovebox. To this, an appropriate mixture of TEO and TEO-M totaling 250 mg were added. This was allowed to stir at room temperature for 5 minutes, followed by 80°C for 2 h inside the glovebox. After the reaction was finished, the product was removed from the glovebox and the reaction mixture was dissolved in dichloromethane. The dissolved reaction mixture was washed with water followed by a saturated sodium chloride in water solution. The organic phase was then dried using

magnesium sulfate, filtered, and evaporated under vacuum to yield an oily residue (varying in color from red to colorless with decreasing TEO/TEO-M ratio). Following this, a mixture of 5 mL water and 400 mL inhibitor-free tetrahydrofuran was prepared (inhibitor-free THF must be used as the inhibitors commonly used in THF will react with the TEMPO moieties). Approximately 5 mL of this solution were added to the raw product and it was dissolved. The product solution was then added to a membrane filter bag (1 kDa cutoff) which was then placed in a jar with the rest of the THF/water mixture. Up to 2 bags were placed in each jar. This was allowed to stir gently for 24 hrs. After this, the liquid outside the membrane was exchanged for fresh liquid. This was repeated a total of 3 times. After this, the liquid in the membrane bag was transferred to a vial, the solvent was removed, and the product dried overnight in a vacuum oven to yield the final polymer product.

Nuclear Magnetic Resonance (NMR) Spectroscopy

¹H NMR spectra were obtained using a Bruker DRX500 spectrometer. Samples were dissolved in either deuterated chloroform or deuterated dimethyl sulfoxide at a concentration of 8 mg sample in 0.5 mL solvent (~1% polymer, by weight).

Differential Scanning Calorimetry (DSC) Measurements

DSC measurements were performed using a TA Instruments Q20 Series differential scanning calorimeter. Hermetically-sealed pans for differential scanning calorimetry were obtained from Fisher Scientific (product number NC9553081). To prepare the sample, approximately 5 mg of polymer were massed into a sample pan, which was then outfitted with a lid and sealed using a TA Instruments Tzero sample press as per the standard procedure. An empty pan was also prepared as a reference sample. For the actual measurement, the sample was heated to 100 °C, held isothermally for 5 minutes, then cooled to -50 °C at a rate of 10 °C min⁻¹ while the heat flow was monitored. A second heating and cooling cycle was performed, followed by the sample being returned to room temperature. The precise glass transition temperature (T_g) was determined by fitting the second scan using TA Analysis software.

Size-Exclusion Chromatography (SEC) Measurements

SEC measurements were carried out using an Agilent Technologies 1260 Infinity chromatograph equipped with a HP G1362A refractive index detector and a set of PLgel 5 μm MIXED-C columns. Polystyrene standards obtained from Agilent with known molecular weight values ranging from 1 to 200 kg mol^{-1} were used to calibrate the SEC. The mobile phase was THF at a temperature of 35 $^{\circ}\text{C}$ flowing at a rate of 1 mL min^{-1} . Samples for SEC analysis were prepared by dissolving 10 mg of polymer in 1 mL of inhibitor-free THF followed by filtration.

Electron Paramagnetic Resonance (EPR) Spectroscopy

EPR spectroscopy was carried out using a Bruker EMX EPR spectrometer with 4 mm \times 250 mm quartz tubes acquired from Wilmad-Labglass (prod# 707-SQ-250M). Solutions of the PTEO polymers were mixed in chloroform at a concentration of 10 mg polymer per 1 mL solvent, then diluted to a concentration of 1 mg mL^{-1} . Then, 0.2 mL of each of the resulting solutions were measured using a syringe and added to separate EPR tubes. As a comparison, a solution with a final concentration of 0.754 mg mL^{-1} TEMPO-OH, which gives the same molar concentration of TEMPO moieties as the polymer solutions, was also prepared. These solutions were measured at a microwave frequency of approximately 9.85 GHz (X-band) with a power of 10 mW, a center field of approximately 3515 G, a receiver gain of approximately 50, a modulation frequency of 100 kHz, a modulation amplitude of 5 G, a conversion time of 20 ms, and a time constant of 5.12 ms.

Electrical Conductivity Measurements (still to be performed)

Boron-doped silicon wafers with a 300 nm thermally-grown layer oxide obtained from Silicon Valley Microelectronics were diced into 13.6 mm \times 15.6 mm chips. Within a cleanroom, these substrate chips were cleaned by immersing in a 2:1 v/v mixture of sulfuric acid and 30 wt% hydrogen peroxide solution for 20 minutes to remove any organic residues. The substrates were then rinsed with deionized water and allowed to dry on a hot plate set to 100 $^{\circ}\text{C}$ for 60 s. A poly(methyl methacrylate) (PMMA) electron-beam resist (Kayaku Advanced Materials product number 495k A4) was spun-coat onto the substrates at a speed of 2000 rpm for 60 s followed by annealing at 180 $^{\circ}\text{C}$ for 5 minutes on a hot plate to create a 200 nm thick film as verified by

profilometry measurements. These substrates were then removed from the clean room and patterned using a Raith eLINE Plus electron beam writer. The patterning parameters were as follows: energy = 20 keV, aperture width = 30 μm , area dose = 250 $\mu\text{C cm}^{-2}$, working area = 100 μm , area step size = 10 nm \times 10 nm. The substrates were patterned such that a channel width of 500 μm and a channel length of 500 nm were achieved. Following patterning, the e-beam resist was developed by immersing the samples in a 3:1 v/v mixture of isopropanol and methyl isobutyl ketone for precisely 60 s, followed by rinsing in isopropanol and drying. Using an MBraun thermal evaporator, titanium (5 nm) and gold (45 nm) layers were deposited on the developed substrates. The residual resist was then removed via ultrasonication in acetone for 30 min to yield substrates with gold bottom contacts patterned in the appropriate shape. The dimensions of the individual channels were verified using scanning electron microscopy, and the conductivity of the bare patterned electrodes were checked to verify that no conductivity was seen.

To measure the electrical conductivity using the patterned electrodes, solutions of 50 mg PTEO-X per 1 mL chloroform were prepared in an inert atmosphere glovebox and allowed to stir for at least an hour. Following this, the solutions were each spun-coat onto a patterned substrate at 2000 rpm for 60 s. The samples were annealed at 80 $^{\circ}\text{C}$ for 2 h, following which the conductivity was measured under vacuum in a Lakeshore Cryotronics Model TTPX probe station with a Keithley 2400 Sourcemeter. To do this, the voltage across the channel was swept from -1 V to $+1$ V and the current recorded, with the conductivity calculated using these data.

8.1.2 Results and Discussion

Synthesis of the protected species was successful, as indicated by the NMR spectra shown in Figure 8.1. Polymerization of TEO-M was also successful, as well as copolymerization with TEO. However, consistency in the polymerization was lacking. It can be seen from the SEC traces shown in Figure 8.2 that the molecular weights vary rather significantly between batches. This does not appear to be a result of any interaction between the radicals, as the molecular weight is uncorrelated with the active fraction (Figure 8.2b). Significant variance was also seen in the glass transition temperatures measured for selected copolymers (Figure 8.3). However, in all cases, the molecular weight was at least as high as what was observed in previous reports, which would indicate that the fully active polymer should show a single peak. Additionally, the glass transition temperature remains below room temperature, meaning that the materials can be thermally

annealed without degradation. Therefore, the material synthesized should be sufficient for studying the effects of radical density on the given polymers. All results are compiled in Table 8.1.

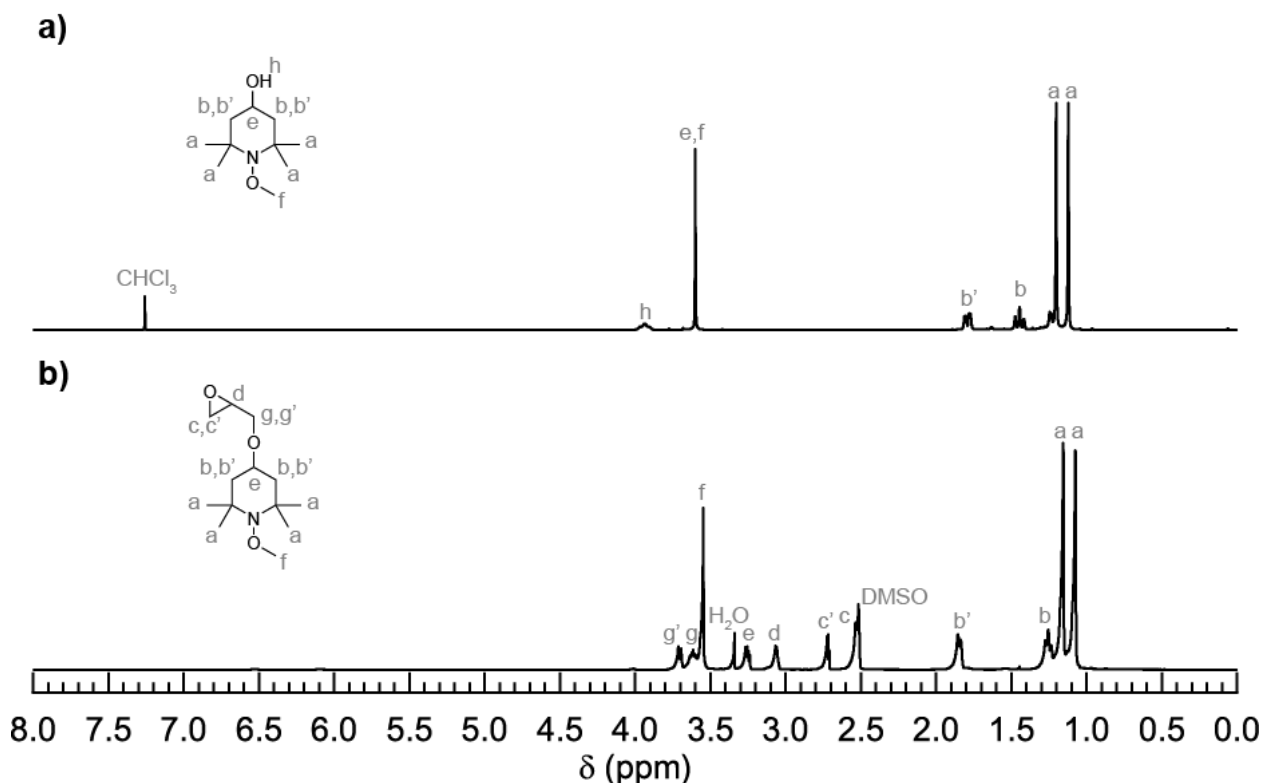


Figure 8.1. ^1H -NMR Spectra of (a) TEMPO-M and (b) TEO-M.

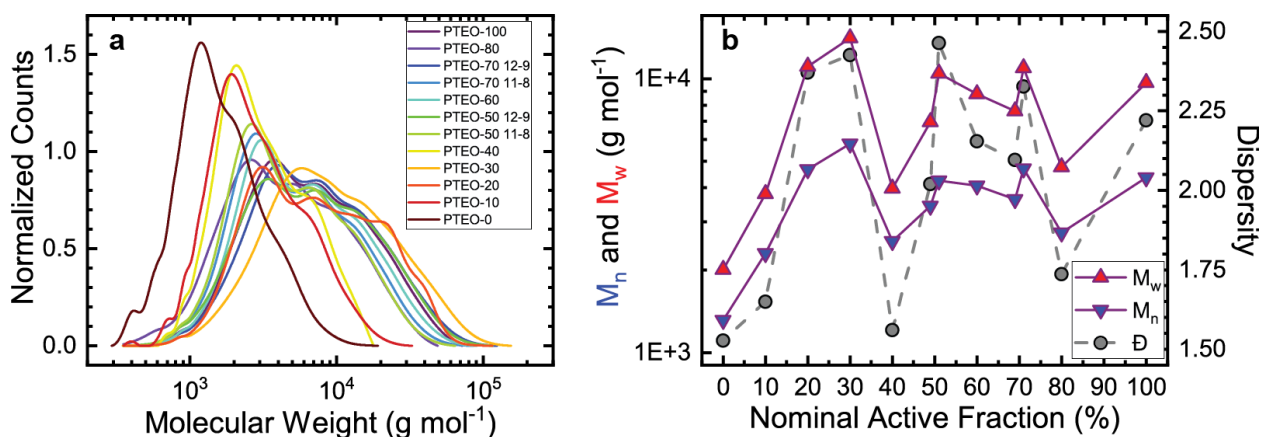


Figure 8.2. (a) Molecular weight distributions of all PTEO copolymers derived from SEC traces. (b) Number-average and weight-average molecular weights (M_n and M_w , respectively) and dispersity (\mathcal{D}) values of all copolymers.

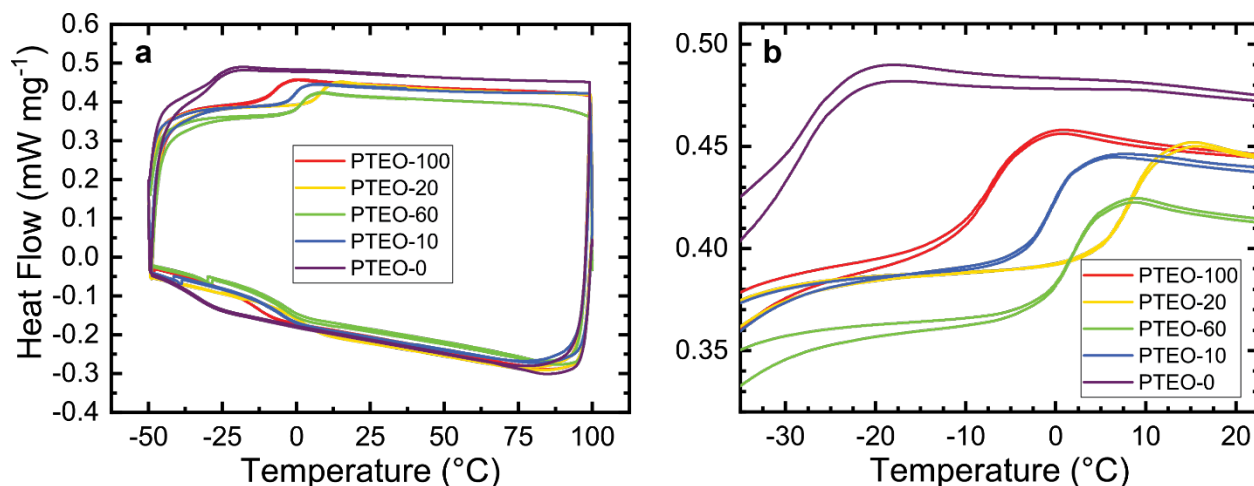


Figure 8.3. Differential Scanning Calorimetry data of PTEO copolymer blends. (a) full data range showing heat flow between -40 °C and 100 °C. (b) Zoomed in data showing glass transition temperature (T_g).

Table 8.1. Summary of Synthesis Information.

Nominal Percent	EPR Integration (/TEMPO)	EPR Integration (/PTEO-100)	Mn (g/mol)	Mw (g/mol)	Dispersity	T_g (°C)
0	0%	0%	1313	2007	1.528	-27.5
10	9%	11%	2302	3797	1.65	-0.3
20	18%	22%	2737	4755	1.737	
30	25%	31%	5795	14060	2.427	
40	30%	37%	2550	3980	1.561	
50 (A)	42%	52%	3437	6947	2.021	
50 (B)	35%	44%	4243	10460	2.465	
60	49%	60%	4073	8778	2.155	-0.6
70 (A)	47%	58%	3633	7620	2.097	
70 (B)	48%	59%	4694	10930	2.327	
80	53%	65%	4671	11080	2.371	8.6
90	57%	70%				
100	81%	100%	4357	9675	2.221	-7.4

Figure 8.4a shows the EPR spectra of the observed polymers. As the radical content is decreased, the single peak corresponding to the polymer decreases in intensity giving way to the triple peak associated with the isolated monomer, starting between a nominal radical concentration of 70-80%. As with other reports in the literature, the intermediate shapes appear to be a sum of contributions from the monomer and polymer components.⁸ However, as seen in Figure 8.4b, the actual radical concentrations appear to be significantly lower than the nominal values (see second

column in Table 8.1). This is seen even for the nominally 100% active radical, suggesting that the radical content is decreasing during the synthesis, and it is due to something other than the presence of the quenched species.

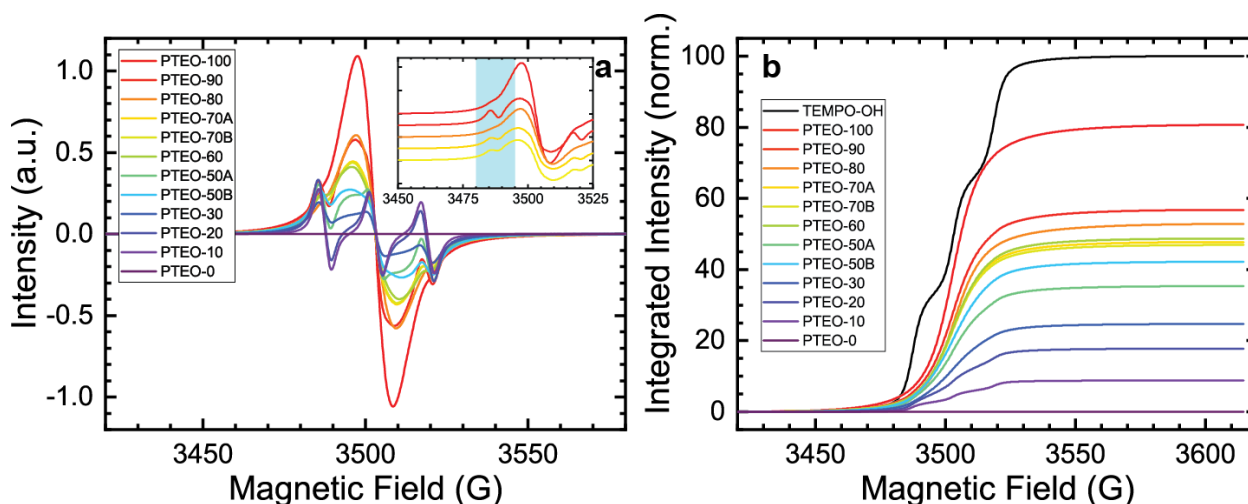


Figure 8.4. (a) EPR derivative spectra of the PTEO copolymers. Here, the transition from a primarily Lorentzian lineshape of the polymer to the triple Lorentzian lineshape of the monomer can be observed. The inset shows the monomer signal is visible as a shoulder on the main polymer peak at nominal concentrations below 80%, with some seen in 90% due to monomer impurity. (b) Integrated EPR spectra normalized to the integration of an equimolar TEMPO solution.

Unfortunately, attempts to measure the conductivity of the copolymers have been unsuccessful. This is likely due to the actual radical content being lower than the nominal value. As mentioned before, the previous report suggests the critical concentration of active radical sites needed to observe high conductivity lies somewhere between 70 and 90%.¹ These results suggest 81% as a new lower bound. However, this concentration must be surpassed in order to find the appropriate cutoff point, as well as to ensure that the EPR data truly reflect the radical content seen. The synthesis procedure follows that described in literature reports where nearly 100% of the radical sites survive the polymerization.^{1,12,13} At present, the cause of this discrepancy is not understood. Therefore, troubleshooting of the synthesis procedure needs to occur to ensure that the necessary radical content is achieved. When this is accomplished, resynthesizing the copolymers and measuring their conductivity according to the outlined procedure will complete the experimental work for this study.

The ultimate goal of this study is to compare the electronic interactions that govern the change in the observed EPR spectrum with those that govern charge transport in the polymer. Therefore, this project will also include a significant theoretical component. Using computational chemistry tools, the EPR spectrum for a given configuration of TEMPO moieties can be predicted. Matching these predicted spectra with experimental data will provide insight into the molecular configuration of the polymer. This will allow for two potential routes towards improving the computational predictions of the high conductivity state. First, the electron transfer rates between the radical sites can be calculated, which will allow the effect on the charge mobility as the density of these sites decreases to be quantified. Second, a more accurate picture of the behavior of the defect sites will be achieved. This will further elucidate the role that the defect sites play in ultimately breaking the charge transport network. With these tools, it will be possible to undertake computational studies of a wide range of novel molecular systems, allowing for more precise design of next-generation high-performance conducting open-shell polymers to be realized.

8.2 Dielectric Spectroscopy of Model Compounds

The novel analysis technique described in Chapter 7 of this manuscript has the potential to offer greater insight that will bridge the macroscopic and microscopic views of glassy relaxation. At present, however, the technique is merely a new lens through which to view the data. A theoretical model describing what these results mean and how they tie into microscopic phenomena has not yet been developed. For that to occur, it is essential to understand how changes in the molecular structure of a material will manifest themselves in the calculated relaxation spectrum. By making these changes in a systematic way, it may be possible to isolate which parts of the spectrum are related to which parts of the molecule, which is an important first step in developing a theory.

The analysis technique described in Chapter 7 has been applied to a loosely-crosslinked bisphenol-A thermoset epoxy.¹⁴ The molecular feature that arguably has the greatest impact on the mechanical properties of a thermoset is the crosslink density. The epoxide component is commercially available in a wide variety of molecular weights, which makes altering the crosslink density a straightforward procedure. Therefore, understanding the impact of crosslink density on the observed relaxation spectra is the logical next step for understanding the material. Previous reports have implicated crankshaft motion of the hydroxyether linkages between bisphenol-A units

as well as distortion of the diphenylpropane moieties as contributing to the γ process using a similar procedure.^{15,16} However, these reports only utilized mechanical relaxation spectroscopy at a single frequency to measure the response. As the response shows significant variation at differing frequencies, the wider frequency window granted by dielectric spectroscopy will give a much broader view on the effect that varying crosslinking density has on the relaxation processes. Combined with the novel analysis technique, there is the potential to gain a much richer view of the microscopic processes underlying relaxation behaviors seen in the epoxy networks.

One significant issue that was encountered when measuring the dielectric response of the epoxy series was the ionic conductivity of the material. Unfortunately, the response due to the alpha process was drowned out by the conductance, which made it impossible to perform the highly quantitative analysis. Efforts to purify the material were unsuccessful. Further attempts to subtract off the conductance response from the response curves were also unsuccessful, as the signal-to-noise ratio was far too high. Therefore, to get a clear picture of the dielectric alpha response, it is necessary to investigate materials where the conductance is low enough so as to not interfere with the alpha response. Fortunately, poly(propylene sulfide) has been observed to show very low ionic conductance.¹⁷ While synthesis has proven challenging, we have successfully gathered preliminary data that confirms the separation. This material will allow the alpha response to be characterized in full, and therefore prove invaluable for guiding future theoretical efforts.

8.3 Impedance Spectroscopy of PTEO

The high conductivity of PTEO comes with the caveat that it is only observed over distances of 600 nm or less.¹ Not much is known about what limits the extent of the highly conductive region, aside from the fact that the highly conductive region contains an aggregation of TEMPO moieties that is likely disrupted after some characteristic length. Gaining a better understanding of the nature of these aggregates, such as how long they take to form, how dense they are throughout the material, and whether or not they can be made larger would prove invaluable for fully realizing the potential of radical polymers as electronically conductive materials. Both dielectric spectroscopy and impedance spectroscopy potentially provide a tool for examining these effects. By studying conduction on a variety of timescales during formation of these aggregates, it may be possible to observe their formation in real time as well as the heterogeneity in the charge transport of the material.

Dielectric spectroscopy provides a means by which the material's frequency-dependent impedance can be characterized on the 100 μm length scale. However, probing scales significantly smaller than that is problematic for the standard parallel plate geometry utilized in dielectric spectroscopy, due to a lack of robust spacers of that size. Therefore, the most practical route forward is to perform similar measurements on a sample using an in-plane geometry with a probe station. While such a measurement will not provide the same level of precision as a parallel plate sample in a sample holder with active electronics, it will allow for considerably greater flexibility in terms of the device geometry. By patterning contacts using the standard electron beam lithography procedure, any length scale or device setup can be probed. This will enable the dielectric and conductive responses to be observed on many length and time scales, which will hopefully provide insight into the microscopic phenomena that result in the high conductivity.

Some practical considerations exist for this experiment. Standard Si/SiO₂ wafers will not work for this measurement. The reason is that an alternating current in the conductive silicon layer will be generated driven by the applied alternating voltage and, due to the high capacitance of the SiO₂ layer and higher conductivity of silicon versus that of PTEO, will significantly contaminate the measurement. Therefore, the substrate must be an insulator whose dielectric properties are relatively invariant with temperature, such as glass. The issue with using an insulating substrate is that it complicates electron-beam patterning, as the charges cannot dissipate and build up, quickly preventing precise imaging on the surface. Fortunately, addition of a conductive material to the surface of the resist allows for patterning. While many practical issues must be resolved with the introduction of an extra layer in the sample, fabrication of a PTEO device on an insulating substrate would allow for impedance spectroscopy to be performed on the material, which would provide insights into the formation of its conductive aggregates.

8.4 Intramolecular Fluorescence Quenching Experiments

The results described in Chapter 4 have established the mechanism of fluorescence quenching of a model conjugated polymer by various radical species. However, many questions remain. Precise quantitative comparison of the quenching constants for each radical species was impeded by the inner filter effect, which required significant correction. This effect also precluded the use of solution-phase transient absorption measurements to compare the quenching effect in solution and in the thin film phase. Furthermore, while the quenching mechanism was assigned to

an energy transfer, no explicit effort was made to distinguish between Förster Resonant transfer and Dexter transfer, which would require controlling the distance between the radical and quencher and observing its effect on quenching. Finally, no effort was made to control the thin-film morphology of the solid-state P3HT-radical blends, which could potentially have a large impact on the observed results. One way to accomplish all of these goals is to covalently link the radical quencher molecules to the fluorophore, which could be accomplished by end-capping the polymer with a radical-labelled molecule. This methodology has been used in the past to study P3HT-PCBM interactions,¹⁸⁻²⁰ as well as for distinguishing different quenching mechanisms.^{21,22} In addition to facilitating and controlling the interactions between P3HT and the quencher radicals, the morphology of the P3HT-Quencher molecules in a thin film can be more easily controlled, allowing for a variety of nanostructures to be generated with improved properties for device applications. Further study of these covalently linked pairs would enrich the understanding of the interactions and provide a means by which they could potentially be controlled and adapted to a variety of situations.

8.5 Protecting P3HT Transistors from Photodegradation with the PTIO Radical

P3HT, like many other conjugated materials, is known to be photosensitive, and its sensitivity to oxygen is greatly increased in the presence of light.²³ As practical applications of organic electronics require environmental stability, it is essential that materials and composites which are resistant to photodegradation be developed. One potential approach is through quenching the excited state of the material. This approach has been exploited for Pentacene, where the material's lifetime under illumination can be increased from a few minutes to over a day in solution.^{24,25} With this approach and the results from Chapter 4 of this work, it is reasonable to hypothesize that a P3HT film doped with either the galvinoxyl or PTIO radicals would show greater photostability than a pristine film. However, the results from Chapter 5 of this work show that doping with the galvinoxyl radical affects the charge transport properties of the P3HT polymer. Therefore, the choice of radical should be informed by considerations of the radical's effectiveness at preventing photodegradation as well as its effects on the end use application of the material.

While doping with the galvinoxyl radical changes the electronic behavior of P3HT, the presence of the PTIO radical is benign. Therefore, for OFET applications, this presents a clear way to enhance the photostability of the material without negating its performance as a transistor. That

is, the PTIO radical, by quenching the excited states in the P3HT, should act to protect it from photodegradation. Testing this hypothesis will be straightforward. Simply comparing the performance of a pristine P3HT OFET with a P3HT OFET doped with the PTIO radical over the course of several days will allow the degree to which the radical protects the host material to be ascertained. Additionally, the effect at different concentrations of the radical should be determined, so that the optimal loading of the radical that will enhance the stability without unacceptably harming the performance can be established. While this approach will likely require a greater loading than covalently bonding the radical moiety, it is also more facile to implement, and potentially applicable to a variety of conjugated polymer systems. Furthermore, as the compatibility of each radical species with different conjugated polymers may differ, this approach will provide a methodology for screening the radicals and quickly testing out new combinations as new materials continue to be developed.

8.6 References

- (1) Joo, Y.; Agarkar, V.; Sung, S. H.; Savoie, B. M.; Boudouris, B. W. *Science* **2018**, *359* (6382), 1391–1395.
- (2) Nordio, P. L. In *Spin Labeling: Theory and Applications*; Berliner, L. J., Ed.; Academic Press, Inc., 1976; pp 5–52.
- (3) Kocherginsky, N.; Swartz, H. M. *Nitroxide Spin Labels: Reactions in Biology and Chemistry*; CRC Press, 1995.
- (4) Glarum, S. H.; Marshall, J. H. *J. Chem. Phys.* **1967**, *47* (4), 1374–1378.
- (5) Parmon, V. N.; Zhidomirov, G. M. *Mol. Phys.* **1974**, *27* (2), 367–375.
- (6) Parmon, V. N.; Kokorin, A. I.; Zhidomirov, G. M.; Zamaraev, K. I. *Mol. Phys.* **1975**, *30* (3), 695–701.
- (7) Bosman, A. W.; Janssen, R. A. J.; Meijer, E. W. *Macromolecules* **1997**, *30* (12), 3606–3611.
- (8) Chechik, V.; Wellsted, H. J.; Korte, A.; Gilbert, B. C.; Caldararu, H.; Ionita, P.; Caragheorghopol, A. *Faraday Discuss.* **2004**, *125* (1), 279–291.
- (9) Hay, M. E.; Wong, S. H.; Mukherjee, S.; Boudouris, B. W. *J. Polym. Sci. Part B* **2017**, *55*, 1516–1525.
- (10) Wu, A.; Mader, E. A.; Datta, A.; Hrovat, D. A.; Borden, W. T.; Mayer, J. M. *J. Am. Chem. Soc.* **2009**, *131* (33), 11985–11997.
- (11) Schoening, K. U.; Fischer, W.; Hauck, S.; Dichtl, A.; Kuepfert, M. *J. Org. Chem.* **2009**, *74* (4), 1567–1573.
- (12) Endo, T.; Takuma, K.; Takata, T.; Hirose, C. *Macromolecules* **1993**, *26* (12), 3227–3229.
- (13) Suga, T.; Yoshimura, K.; Nishide, H. *Macromol. Symp.* **2006**, *245–246*, 416–422.
- (14) Ni, Y.; Song, H.; Wilcox, D. A.; Medvedev, G. A.; Boudouris, B. W.; Caruthers, J. M. *Macromolecules* **2020**, *53*, 1867–1880.
- (15) Takahama, T.; Geil, P. H. *J Polym Sci Polym Phys Ed* **1982**, *20* (11), 1979–1986.
- (16) Charlesworth, J. M. *Polym. Eng. Sci.* **1988**, *28* (4), 221–229.

- (17) Nicol, E.; Nicolai, T.; Durand, D. *Macromolecules* **1999**, *32* (22), 7530–7536.
- (18) Boudouris, B. W.; Molins, F.; Blank, D. A.; Frisbie, C. D.; Hillmyer, M. A. *Macromolecules* **2009**, *42* (12), 4118–4126.
- (19) Healy, A. T.; Boudouris, B. W.; Frisbie, C. D.; Hillmyer, M. A.; Blank, D. A. *J. Phys. Chem. Lett.* **2013**, *4* (20), 3445–3449.
- (20) Banerji, N.; Seifert, J.; Wang, M.; Vauthey, E.; Wudl, F.; Heeger, A. J. *Phys. Rev. B - Condens. Matter Mater. Phys.* **2011**, *84* (7), 1–14.
- (21) Hassoon, S.; Lustig, H.; Rubin, M. B.; Speiser, S. *J. Phys. Chem.* **1984**, *88* (25), 6367–6374.
- (22) Oevering, H.; Verhoeven, J. W.; Paddon-Row, M. N.; Cotsaris, E.; Hush, N. S. *Chem. Phys. Lett.* **1988**, *143* (5), 488–495.
- (23) Reese, M. O.; Nardes, A. M.; Rupert, B. L.; Larsen, R. E.; Olson, D. C.; Lloyd, M. T.; Shaheen, S. E.; Ginley, D. S.; Rumbles, G.; Kopidakis, N. *Adv. Funct. Mater.* **2010**, *20*, 3476–3483.
- (24) Kawanaka, Y.; Shimizu, A.; Shinada, T.; Tanaka, R.; Teki, Y. *Angew. Chem. Int. Ed.* **2013**, *52* (26), 6643–6647.
- (25) Ito, A.; Shimizu, A.; Kishida, N.; Kawanaka, Y.; Kosumi, D.; Hashimoto, H.; Teki, Y. *Angew. Chem. Int. Ed.* **2014**, *53* (26), 6715–6719.

VITA

EDUCATION

Ph.D. in **Chemical Engineering** at **Purdue University** West Lafayette, IN
Thesis Advisor: Dr. Bryan Boudouris GPA: **3.95/4.0** *Anticipated Graduation Date: Aug 2020*

B.S. in **Chemical Engineering** at **The University of Arizona** Tucson, AZ
Graduated with Honors Minors: **Electrical Eng. and Chemistry** GPA: **4.0/4.0** May 2015

RESEARCH EXPERIENCE

Graduate Research Assistant

Dr. Bryan Boudouris, Purdue University, West Lafayette, IN *August 2015–Present*

- Designed and performed experiments and computational studies to characterize the optoelectronic properties of conducting polymers in collaboration with experts in organic chemistry, computational chemistry, ultrafast spectroscopy, and polymer physics, as well as published and presented the results
- Oversaw maintenance and repair of nine experimental apparatuses and coordinated the acquisition and installation of new equipment and recommissioning of long-unused equipment
- Led the research group to ensure compliance with university and state safety and environmental regulations
- Supervised four undergraduate and M.S. students, and mentored junior graduate students

NASA Space Grant Researcher/Lab and Field Assistant

Dr. Shirley Papuga, University of Arizona, Tucson, AZ *June 2013–May 2015*

- Coordinated the collection, organization, and analysis of hourly meteorological data and photographs from Critical Zone Observatory research sites
- Programmed and optimized MATLAB scripts to analyze images and track yearly green-up of forest undergrowth
- Pursued an independent research project concerning the application of LiDAR to the tracking of understory growth in forest ecosystems in collaboration with a postdoctoral scientist

Undergraduate Research Assistant

Dr. Anthony Muscat, University of Arizona, Tucson, Arizona *Fall 2012–Spring 2013*

- Researched effective methods of producing self-assembled monolayers on silicon wafers
- Stressed safety while working with corrosive and toxic chemicals such as various acids and solvents
- Used an ellipsometer to determine the molecular-level thickness of experimental samples and a goniometer to measure the contact angle for water droplets on the surface of the samples

INDUSTRY EXPERIENCE

Metallurgical Intern

Freeport McMoRan Inc. – Henderson Operations: Empire, Colorado *June-August 2015*

- Evaluated the effects of particle size distribution of feed ore on the recovery of metal within the plant
- Communicated research and experimental objectives to plant operators, engineers, and laboratory scientists
- Emphasized safe work practices and took action by suggesting safety improvements in the plant

Metallurgical Intern

Freeport McMoRan Inc. – Sierrita Operations: Green Valley, Arizona

May-August 2014

- Designed experiments to vary process control parameters and optimize molybdenum recovery
- Liaised with plant operators, engineers, and laboratory scientists to orchestrate experiments
- Ensured safety while performing job duties such as gathering and preparing samples

SKILLS

- Programming in MATLAB, Excel VBA, Python, Java, C, C#, and Visual Basic
- Organic electronic device fabrication and testing techniques including cleanroom experience, thin-film coating, thermal evaporation, electron beam lithography, inert atmosphere glovebox usage, and vacuum probe station usage
- Characterization of material surfaces using profilometry, ellipsometry, goniometry, scanning electron microscopy, and atomic force microscopy
- Characterization of material optoelectronic properties using IR spectroscopy, UV-Vis light absorption and fluorescence spectroscopy, transient absorption spectroscopy, electron paramagnetic resonance spectroscopy, and dielectric and impedance spectroscopy
- Computational chemistry using ORCA, NWChem, and Gaussian09
- Polymer synthesis and characterization through FTIR, titrations, size-exclusion chromatography, differential scanning calorimetry, and thermogravimetric analysis

EXTERNAL PRESENTATIONS

- Oral presentation: “Deciphering Low-Temperature Dielectric Relaxation of a Series of Amorphous Polymers” – American Physical Society (APS) Frank J. Padden Jr. Award Virtual Symposium, March 2020.
- Oral presentation: “Tuning Charge and Energy Transfer Interactions in Open-Shell Molecules” – American Institute of Chemical Engineers Annual Meeting, Excellence in Graduate Polymer Research, November 2019.
- Oral presentation: “Deciphering Relaxation Spectra of Amorphous Polymers through Dielectric Spectroscopy of an Epoxy” – American Physical Society (APS) March Meeting, March 2019.
- Poster presentation: “Tuning the Interfacial and Energetic Interactions between a Photoexcited Conjugated Polymer and Open-Shell Small Molecules” – Materials Research Society (MRS) Spring Meeting and Exhibit, April 2019.
- Poster presentation: “Organic Radicals and Radical Polymers for Organic Electronic Applications” – Notre Dame-Purdue Symposium on Soft Matter & Polymers, September 2017.
- Poster presentation: “Manipulating Energy Transfer in Conjugated Polymers using Radical Mediators” – APS March Meeting, March 2017.
- Poster presentation: “Understory Growth Dynamics Following a High-Severity Burn in a Mixed-Conifer Forest” – School of Natural Resources and the Environment EarthWeek Conference, University of Arizona, April 2015, where it was awarded best undergraduate poster.

AWARDS AND HONORS

- American Physical Society (APS) Padden Award Finalist 2020
- American Institute of Chemical Engineers Excellence in Graduate Polymer Research Finalist 2019
- Purdue Bilsland Dissertation Fellowship 2019–2020
- Purdue School of Chemical Engineering Travel Grant 2017
- NSF Graduate Research Fellowship Program Honorable Mention 2016
- Purdue Davidson School of Chemical Engineering Ross Fellowship 2015
- National Merit Scholarship (Undergraduate) 2011–2015

PUBLICATIONS

1. “Modifying Field-Effect Transistor Response in a Conjugated Polymer upon the Addition of Radical Dopants.” **Wilcox, D. A.**; Boudouris, B. W. **2020**, Submitted.
2. “Relaxation Map of Glycerol and Sorbitol in the Glass and Liquid States.” Medvedev, G. A.; **Wilcox, D. A.**; Boudouris, B. W.; Caruthers, J. M. **2020**, Submitted.
3. “Rethinking the Analysis of the Linear Viscoelastic Behavior of an Epoxy Polymer near and above the Glass Transition.” Ni, Y.; Song, H.; **Wilcox, D. A.**; Medvedev, G. A.; Boudouris, B. W.; Caruthers, J. M., *Macromolecules* **2020**, *53*, 1867–1880
4. “Tailored Thioxanthone-based Photoinitiators for Two-Photon-Controllable Polymerization and Nanolithographic Printing.” Chi, T.; Somers, P.; **Wilcox, D. A.**; Iyer, V.; Le, R.; Gengler, J.; Ferdinandus, M.; Liebig, C.; Pan, L.; Xu, X.; Boudouris, B. W., *J. Polym. Sci. B Polym. Phys.* **2019**, *57*, 1462–1475.
5. “Tuning the Interfacial and Energetic Interactions between a Photoexcited Conjugated Polymer and Open-Shell Small Molecules.” **Wilcox, D. A.**; Snaider, J.; Mukherjee, S.; Huang, L.; Savoie, B. M.; Boudouris, B. W. *Soft Matter* **2019**, *15*, 1413–1421.
6. “Stable Radical Materials for Energy Applications.” **Wilcox, D. A.**; Agarkar, V.; Mukherjee, S.; Boudouris, B. W. *Annu. Rev. Chem. Biomol. Eng.* **2018**, *9*, 83–103.